Fast pyrolysis of biomass at high temperatures

Trubetskaya, Anna

Publication date:
2016

Fast pyrolysis of biomass at high temperatures

Anna Trubetskaya

Ph.D. Thesis
2016

Combustion and Harmful Emission Control
Department of Chemical and Biochemical Engineering
Technical University of Denmark
2800 Kgs. Lyngby
Denmark

Preface

This thesis was carried out at Combustion and Harmful Emission Control (CHEC) centre, Department of Chemical Engineering, Technical University of Denmark. The PhD project has been carried out in close collaboration with Dong Energy and Vattenfall. The project is part of the "GREEN" project, financially supported by the Technical University of Denmark, Dong Energy, Vattenfall and The Danish National Advanced Technology Foundation. Professor Peter Glarborg, Professor Anker Degn Jensen and Senior Researcher Peter Arendt Jensen were the advisors of the project.

Dong Energy and Vattenfall are greatly acknowledged for the financial support during the course of this thesis. I would like to thank Peter Glarborg, Anker Degn Jensen and Peter Arendt Jensen for many fruitful discussions throughout the work and for making this project even more exciting than it was initially planned. Special thank you to Anker for his invaluable constructive criticism, encouragement and bringing so much patience into the project. I wish thank Peter Glarborg for the excellent management through the whole PhD project. Thanks also to Peter Arendt Jensen for taking so much time for the project and technical inspiration for the experimental work. I wish also acknowledge Associate Professor Alexander Shapiro for his help with the modeling.

I would further like to express my gratitude to Associate Professor Kentaro Umeki and Angel David Garcia Llamas for the great support during drop tube reactor investigations. I am so thankful for all your time, very nice working atmosphere and many fruitful discussions during the external stay at LTU. Thanks also to Professor Hartmut Spliethoff and Markus Steibel for all your scientific and technical support at TU Munich. Associate Professor Flemming Hofmann Larsen, Professor Mogens Larsen Andersen and Associate Professor Søren Talbro Barsberg at University of Copenhagen are greatly acknowledged for the large interest and enormous amount of time spent on our project.

Special thank you goes to Gert Beckmann and Dr. Jürgen Pankratz (Retsch Technology) for the help with the 2D dynamic imaging instruments. Thanks also to Dr. Jens-Kai Holm (Dong Energy) and Dr. Johan Wadenback (Vattenfall) for the support on the biomass particle characterization. I would like to thank Dr. Francesco Patuzzi and Professor Marco Baratieri (Free University of Bozen) for the help with FTIR-TGA measurements. Thanks goes to Professor Andy Horsewell, Berit Wenzell, Dr. Jens Kling, Diego Gardini (DTU CEN) for the help with ESEM and TEM microscopy analysis. I wish to acknowledge Associate Professor Kenny Ståhl (DTU Chemistry) for the help with X-ray diffraction analysis.

Thanks to my collegues, especially Dominik Bjørn Rasmussen, Morten Nedergaard Pedersen and Sunday Chukwudi Okoro, for all possible help during this project. I wish to express my gratitude

to Morten Søe Jepsen for the experimental results on the fast pyrolysis in a single particle reactor. Special thank you goes to all technical personal at KT workshop. I would like to thank Gerrit Ralf Surup for the fruitful discussions about gasification and thermogravimetric experimental work. Thanks also my family and friends for their support during this PhD project.

Anna Trubetskaya
Lyngby, November 2015

This work is dedicated to the memory of Professor Michael Antal Jr.

Abstract

This Ph.D. thesis describes experimental and modeling investigations of fast high temperature pyrolysis of biomass. Suspension firing of biomass is widely used for power generation and has been considered as an important step in reduction of greenhouse gas emissions by using less fossil fuels. Fast pyrolysis at high temperatures plays a significant role in the overall combustion process since the biomass type, the reaction kinetics and heat transfer rates during pyrolysis influence the volatile gas release. The solid residue yield and its properties in suspension firing, including particle size and shape, composition, reactivity and burnout depend significantly on the operating conditions of the fast pyrolysis.

Biomass fast pyrolysis experiments were performed in a laboratory-scale wire mesh reactor and bench scale atmospheric pressure drop tube / entrained flow reactors with the aim to investigate the effects of operating parameters and biomass types on yields of char and soot, their chemistry and morphology as well as their reactivity using thermogravimetric analysis. The experimental study was focused on the influence of a wide range of operating parameters including heat treatment temperature, heating rate, particle size, residence time, inorganic matter and major organic biomass compounds. Woody and herbaceous biomass were used as fuels. Char yields from the drop tube and entrained flow reactors were lower than those obtained in the wire mesh reactor, emphasizing the importance of heating rate on the product yields. The char yield decreased significantly between 10 and 600 K s^{-1}, but continued to decrease with increasing heating rate, and was lowest for the drop tube / entrained flow reactors with estimated heating rate of $> 10^4$ K s^{-1}. The heat treatment temperature and potassium content affected the char yield stronger than the heating rates and differences in the plant cell wall compounds between 600 and 3000 K s^{-1}. The heat treatment temperature affected more the herbaceous biomass char yield compared with wood.

The differences in the char yield for particle size fractions in the range of 0.05 mm $< d_p <$ 0.425 mm were negligible, leading to the conclusion that the biomass particle can be assumed isothermal, when its size did not exceed 0.425 mm. Compared to smaller particles, the larger pinewood particles ($d_p >$ 0.85 mm) required more than 1 s holding time for the complete conversion at intermediate and fast heating rates. The influence of heating rate on the char yields was less pronounced for larger particles (from 0.85 to 4 mm) obtained at temperatures > 1250°C in the wire mesh reactor, single particle burner and drop tube reactor, due to the predominance of internal heat transfer control within the large particles.

Potassium compared to all other ash elements in the fuels had the highest influence on the char yield. The effect of potassium on the char yield was stronger at low and intermediate heating rates where potassium catalyzed the repolymerization and cross-linking reactions, leading to higher char yields. Silicon compounds abundant in herbaceous biomass had a negligible influence on the

char yield and reactivity. However, a very high content of silicon oxides in biomass ($> 50\,\%$ of the overall biomass inorganic matter) significantly affected the char morphology, as observed for rice husk. For this fuel, the high content of low-temperature melting amorphous silicon oxides led to the formation of a glassy shell on rice husk chars at 1000-1500°C. The ability of char to melt in fast pyrolysis followed the order pinewood $>$ beechwood, straw $>$ rice husk, and was related to the formation of metaplast. Different particle shapes of beechwood and leached wheat straw chars produced in the drop tube reactor which have similar potassium content suggested a stronger influence of the major biomass cell wall compounds (cellulose, hemicellulose, lignin and extractives) and silicates on the char morphology than alkali metals.

In this study, potassium lean pinewood (0.06 wt. %) produced the highest soot yield (9 and 7 wt. %) at 1250 and 1400°C, whereas leached wheat straw with the higher potassium content (0.3 wt. %) generated the lowest soot yield (2 and 1 wt. %). Soot yields of wheat and alfalfa straw at both temperatures were 5 % points lower than wood soot yields and 3 % points higher than leached wheat straw soot yield, indicating that potassium plays a minor role on the soot formation. The leaching of alkali from wheat straw additionally resulted in a removal of lignin, leading to the decreased formation of polycyclic aromatic hydrocarbon precursors, and thereby to lower soot yields.

Pinewood soot particles generated at 1250°C were significantly larger (77.7 nm) than soot particles produced in pinewood (47.8 nm) pyrolysis at 1400°C, beechwood (43 nm) and wheat straw (30.8 nm) devolatilization at both temperatures. The larger pinewood soot particles were related to the formation of tar balls known from smoldering combustion. The major difference in nanostructure of pinewood, beechwood and wheat straw soot was in the formation of multi and single core particles. Pinewood soot particles generated at 1250°C were mainly multi core structures compared to pinewood soot generated at 1400°C, combining both single and multi core particles. Beechwood and wheat straw soot samples had multi and single core particles at both temperatures. In thermogravimetric analysis, the maximal reaction rate of pinewood soot was shifted to temperatures about 100°C higher than for the other samples in both oxidation and CO_2 gasification, indicating a significantly lower reactivity. Soot samples produced at 1400°C were more reactive than soot generated at 1250°C. The beechwood and wheat straw soot samples were more graphitic than pinewood soot based on the electron energy loss spectroscopy (EELS) analysis. In contrast to expectations of graphitic structures to react slower than amorphous samples, beechwood and wheat straw soot were 35 and 571 times more reactive than pinewood soot prepared at 1400°C. The presence of potassium in wheat straw soot mainly as water-soluble KCl, KOH, $KHCO_3$ and K_2CO_3 and to a minor extent bonded to the soot matrix in oxygen-containing surface groups (e.g. carboxyl, phenolate) or intercalated in soot graphene layers led to a higher reactivity in CO_2 gasification compared to low-alkali containing pinewood soot. The results showed that potassium has a dominating effect on the soot reactivity compared to nanostructure and particle size.

A mathematical model of biomass fast pyrolysis was developed to predict the gas and char yields of wood and herbaceous biomass at heating rates $> 600\,\mathrm{K\,s^{-1}}$. The model includes both kinetics and external and internal heat transfer assuming that mass transfer is fast. The model relies on the concept applied in fast pyrolysis of cellulose through the formation of an intermediate liquid (so called metaplast) which reacts further to form char and gas. The kinetics of the fast pyrolysis was described through the Broido-Shafizadeh scheme for biomass. The catalytic effect of potassium which is a major ash element influencing the char yield was included in the model.

Resume (Danish)

Denne Ph.d. afhandling beskriver eksperimentelle og modelbaserede undersøgelser af pyrolyse af biomasse ved høje opvarmningsarter og høje temperature. Suspensionsfyring af biomasse er bredt anvendt i kraftværker til at generere strøm og varme, og substitutionen af fossile brændsler med biomasse ses som et vigtigt led til at reducere udledningen af drivhusgasser. Hurtig pyrolyse ved høje temperaturer spiller en signifikant rolle i forbrændingsprocessen på suspensionsfyrede kedler, da biomassetypen, reaktionshastighed samt varmeoverførsel under pyrolysen påvirker frigivelsen af flygtige stoffer. I suspensionsfyrings anlæg afhænger den dannede mængden af koks og koksens egenskaber, herunder partikelstørrelse og form, sammensætning, reaktivitet og udbrænding, af forholdende under pyrolysen.

Hurtig pyrolyse af biomasse blev undersøgt, ved anvendelse af en trådnets reaktor i laboratorieskala, en drop tube reaktor og entrained flow reaktorer. Formålet med undersøgelserne var at bestemme indflydelsen af biomassetype og driftsforhold på produktudbyttet af koks og sod, samt deres egenskaber med hensyn til kemi, morfologi, og reaktivitet. Kinetik undersøgelser af sod og koks blev bestemt ved termogravimetrisk analyse. Det eksperimentelle studie fokuserede på indflydelsen af en bred vifte af driftsforhold og biomasse karakteristika, som pyrolysetemperatur, opvarmningshastighed, partikelstørrelse, opholdstiden samt uorganiske stoffer i biomassen. Træ og halm biomasse blev brugt som brændsler. Koksudbyttet fra drop tube og entrained flow reaktorerne var lavere end udbyttet i trådnets reaktoren, hvilket understreger opvarmningshastighedens betydning på koksudbyttet. Koksudbyttet faldt betydeligt mellem 10 and 600 K s^{-1}, men fortsatte med at falde med stigende opvarmningshastighed og var lavest i drop tube og entrained flow reaktorerne, hvor den estimerede opvarmningshastighed var $> 10^4$ K s^{-1}. Mellem 600 and 3000 K s^{-1} havde pyrolysetemperaturen og kaliumindholdet en større påvirkning på koksudbyttet end opvarmningshastigheden og forskelle i planternes biopolymer sammensætning. Pyrolysetemperaturen havde en større effekt på koksudbyttet fra halm biomasser end på træ.

Indflydelse af partikelstørrelsen på koksudbytte var ubetydelig for partikler af størrelsen 0,05 mm $< d_p <$ 0,425 mm, og det kan konkluderes at partiklerne kan antages at være isoterme, så længe størrelsen er under 0,425 mm. For de større fyrretræspartikler (dp $>$ 0,85 mm) var det nødvendigt med en opholdstid på mere end 1 sekund for at opnå en fuldstændig omsætning. I forhold til de små partikler var opvarmningshastighedens indflydelse på koksudbyttet mindre for partikler af størrelsen (fra 0,85 til 4 mm). Dette skyldtes den indre varmediffusions indflydelse på den lokale opvarmningsrate for de store partikler.

Af biomassens indhold af uorganiske elementer havde kalium den største indflydelse på koksudbyttet. Kaliums indflydelse var størst ved de lave og mellemliggende opvarmningshastigheder, hvor kalium katalyserede repolymerisering og tværbindingsreaktioner, hvilket resulterede i et

større koksudbytte. Siliciumforbindelser, som findes i store mængder i halm biomasse, havde en ubetydelig effekt på koksudbyttet. Det blev dog observeret at et meget højt indhold af siliciumoxid ($> 50\,\%$ af det uorganiske indhold) påvirkede koksmorfologien. For risskaller betød det høje indhold af lavt smeltende amorfe siliciumoxider at koksen blev omsluttet af en skal af glas ved temperaturer mellem 1000 og 1500°C. Koksens smeltevne under pyrolysen kan rangeres som følgende: fyrretræ $>$ bøgetræ og halm $>$ risskaller, og kan kædes sammen med dannelsen af "metaplast". Forskellige partikelformer af koks fra bøg og udvasket halm, som blev produceret i drop tube reaktor og havde samme kaliumindhold, antydede at sammensætningen af plantens cellevæg (cellulose, hemicellulose, lignin og ekstrakter) havde en større indflydelse på koksens morfologi end indholdet af alkalimetaller.

I dette studie blev også undersøgt dannelsen af sod under pyrolyse processen. Det blev fundet at fyrretræ med et lavt indhold af kalium (0,06 wt. %) gav den højeste produktion af sod (9 og 7 wt. % relativt til den indfødte biomasse) ved henholdsvis 1250 og 1400°C. Udvasket hvedehalm, som har et højere kaliumindhold end fyrretræ (0,3 wt. %) gav den laveste produktion af sod (2 og 1 wt. %). Sodudbyttet af hvede- og alfalfahalm ved begge temperaturer var 5 procentpoint lavere end for træ og 3 procentpoint højere end for udvasket hvedehalm, hvilket indikerer at kalium kun spiller en mindre rolle i dannelsen af sod. Udvaskningen af alkali fra hvedehalm fjernede også lignin, hvilket betød at der blev dannet færre polyaromatiske kulbrinter "forløbere", som derved gav et lavere sodudbytte.

Sodpartikler fra fyrretræ, som blev dannet ved 1250°C, var betydeligt større (77,7 nm) end sodpartikler som blev dannet under pyrolyse ved 1400°C (47,8 nm). De var også større end sodpartikler fra bøgetræ (43 nm) og hvedehalm (30,8 nm) som blev dannet ved både 1250 og 1400°C. De større sodpartikler fra fyrretræ var forbundet til dannelsen af tjærebolde, som også kendes fra ulmende forbrænding. Den største forskel i nanostrukturen mellem sodpartiklerne fra bøg, fyr og hvedehalm var forskellig dannelsen af fler- og enkeltkerne partikler. Sodpartikler fra fyrretræ som blev dannet ved 1250°C var primært flerkernede sammenlignet med soden dannet ved 1400°C, hvor der var en blanding af fler- og enkeltkerne partikler. Bøgetræ og hvedehalm dannede både fler- og enkeltkerne partikler ved begge temperaturer.

Sodprøvernes reaktivitet overfor ilt og CO_2 blev undersøgt ved termogravimetrisk analyse. Den maksimale reaktionshastighed for fyrretræssod lå omkring 100°C over den for de andre typer sod, både ved oxidation og CO_2 forgasning, hvilket indikerer en betydelig lavere reaktivitet for fyrretræssod. Sod, som var dannet ved 1400°C, var mere reaktivt end sod dannet ved 1250°C. Electron energy loss spectroscopy (EELS) analyse viste at soden fra bøg og hvedehalm havde en struktur som mindede mere om grafit end soden fra fyrretræ. Selvom det var forventet at grafitstrukturen ville have en lavere reaktivitet end en amorf struktur, blev det fundet, at sod fra bøgetræ og hvedehalm var henholdsvis 35 og 571 gange mere reaktivt end fyrretræssod dannet ved 1400°C.

Forekomster af kalium i hvedehalm, primært som vandopløseligt KCl, KOH, $KHCO_3$ og K_2CO_3 og i en mindre grad bundet til sodmatrixen i oxygenholdige overfladegrupper (f.eks. carboxyl, phenolat) eller indføjet i sodens grafen-lag, resulterede i en højere reaktivitet ved CO_2 gasificering for hvedesoden end fyrretræssoden, som havde et lavt indhold af alkalimetaller. Resultaterne viste at kalium har en dominerende indflydelse på sodens reaktivitet i forhold til andre faktorer som nanostruktur og partikelstørrelse.

En matematisk model er blevet udviklet som kan beskrive gas- og koksudbyttet under hurtig pyrolyse ved opvarmningshastigheder over $600\,\mathrm{K\ s^{-1}}$. Modellen indeholder både kinetik samt ekstern og intern varmeledning og antager at massetransporten er hurtig. Modellen bygger på konceptet som bruges ved hurtig pyrolyse af cellulose, hvor der dannes en midlertidig væske (såkaldt metaplast), som siden reagerer og danner koks og gas. Kinetikken af den hurtige pyrolyse blev beskrevet vha. Broido-Shafizadeh metoden for biomasse. Den katalytiske effekt af kalium, som er den askekomponent med størst indflydelse på koksudbyttet, blev inkluderet i modellen.

Contents

1 Introduction **5**

1.1 Background 5

1.2 Project objectives and scope 6

2 Literature survey **9**

2.1 Introduction 9

2.2 Biomass structure and composition 9

2.2.1 Wood 9

2.2.2 Wheat straw 11

2.2.3 Biomass composition 12

2.3 Pyrolysis 13

2.3.1 Introduction 13

2.3.2 Pyrolysis mechanism 14

2.4 Effect of operating conditions on pyrolysis 15

2.4.1 Heat treatment temperature 15

2.4.2 Heating rate 15

2.4.3 Particle size and shape 16

2.4.4 Organic matter 17

2.4.5 Inorganic matter 18

2.5 Modeling biomass pyrolysis 19

2.5.1 Kinetic modeling 19

2.5.2 Superposition models 21

2.6 Biomass solid residue: structure and morphology 22

2.6.1 Char morphology 22

2.6.2 Soot morphology 25

2.7 Biomass reactivity 27

2.7.1 Char reactivity 27

2.7.2 Soot reactivity 29

2.7.3 Comparison of low and high temperature kinetics 30

2.8 Current state of knowledge 30

3 Fuels, reactors and characterization techniques **40**

3.1 Introduction 40

3.2 Materials and methods 42

3.2.1 Raw samples 42

3.2.2 Biomass compositional analysis . . . 43
3.3 Reactors used in this thesis . . . 44
3.3.1 Wire mesh reactor . . . 45
3.3.2 Tubular furnace . . . 46
3.3.3 Single particle reactor . . . 47
3.3.4 Drop tube reactor . . . 48
3.3.5 Entrained-flow reactor . . . 49
3.4 Solid residue characterization . . . 51

4 Experimental investigations on biomass fast pyrolysis 61
4.1 Introduction . . . 61
4.2 Effect of operational conditions on the pyrolysis in a wire mesh reactor . . . 61
4.2.1 Fuels and operating parameters . . . 61
4.2.2 Effect of temperature . . . 63
4.2.3 Effect of heating rate . . . 64
4.2.4 Effect of holding time . . . 65
4.3 Effect of operational conditions on the pyrolysis in a drop tube reactor . . . 68
4.3.1 Fuels and operating parameters . . . 68
4.3.2 Carbon and hydrogen balances . . . 69
4.3.3 The solid product yield . . . 70
4.3.4 Volatile gas composition . . . 73
4.3.5 Alkali transformations of herbaceous biomasses . . . 75
4.4 Effect of particle size on pinewood pyrolysis . . . 77
4.4.1 Carbon and hydrogen balances . . . 77
4.4.2 Volatile gas composition . . . 79
4.4.3 The solid product yield . . . 79
4.5 Conclusion . . . 81

5 Solid residue characterization and structural transformations 86
5.1 Introduction . . . 86
5.2 Characterization of char . . . 86
5.2.1 Char morphology at slow and intermediate heating rates . . . 86
5.2.2 Char morphology at fast heating rates in the DTF . . . 90
5.2.3 Particle size and shape characterization . . . 94
5.2.4 N_2 adsorption measurements . . . 95
5.3 Structural char differences of wheat straw and rice husk . . . 96
5.3.1 Introduction . . . 96

5.3.2 Ash analysis . . . 96
5.3.3 X-ray diffraction . . . 97
5.3.4 ^{29}Si solid-state NMR analysis . . . 98
5.3.5 Electron spin resonance spectroscopy analysis . . . 102
5.3.6 Particle size and shape characterization . . . 104
5.4 Conclusion . . . 107

6 A comparison of char and soot reactivity determined from thermogravimetric experiments 114
6.1 Introduction . . . 114
6.2 Reaction kinetics of solid residues . . . 114
6.3 Reactivity of char . . . 115
6.3.1 Materials and methods . . . 115
6.3.2 Reactivity of char prepared at low and intermediate heating rates . . . 115
6.3.3 Reactivity of char prepared at fast heating rates . . . 117
6.3.4 Silicates effect on the char reactivity at fast heating rates . . . 120
6.3.5 Conclusion . . . 122
6.4 Reactivity of soot . . . 123
6.4.1 Materials and methods . . . 123
6.4.2 Reactivity . . . 124
6.4.3 X-ray diffraction of soot . . . 127
6.4.4 Soot yield and inorganic matter effect . . . 129
6.4.5 Particle size analysis . . . 132
6.4.6 Surface structure . . . 135
6.4.7 TEM-EELS Measurements . . . 137
6.4.8 Discussion . . . 138
6.4.9 Conclusion . . . 139
6.5 Conclusion on soot and char reactivity . . . 140

7 Fast pyrolysis model 146
7.1 Introduction . . . 146
7.2 Model development . . . 146
7.2.1 Heat transfer equations . . . 148
7.2.2 Method of lines . . . 151
7.2.3 Biomass particle properties . . . 151
7.2.4 Overview of performed experiments . . . 152
7.3 Results . . . 152

7.3.1 Kinetic parameters 152
7.3.2 Biomass shape representation 156
7.3.3 Particle size effect on devolatilization time 157
7.4 Discussion 158
7.5 Conclusion 159

8 Conclusion **164**

9 Suggestions for future work **167**

Appendices **169**

1 Introduction

1.1 Background

Biomass and waste combustion are significant sources of renewable electricity supply in Denmark. Currently, Danish pulverized fuel fired power plants (PF) are in a transition to 100 % biomass firing to reduce the emission of greenhouse gases [1]. The pulverized biomass combustion is a dominating technology for electricity production. The utilization of biomass leads to a range of major technical challenges for the boiler and flue gas cleaning units, due to different chemical and physical properties compared to coal, reducing reliability and efficiency of power plants and creating limits for the amount of biomass that can be supplied to the power plant. Compared to coal, biomass has a much higher amount of volatile matter (approximately 80 % and more), resulting in a dominating role of devolatilization stage in the combustion of biomass particles [2].

Unlike coal, biomass is difficult to mill to $< 100\,\mu$m due to its fibrous structure, resulting in higher energy consumption for the comminution process. The shape and size distribution of obtained biomass particles consists of a larger fraction of flake- and cylinder-like particles with a particle size $> 300\,\mu$m. In biomass suspension firing, it is a challenge to achieve high fuel conversion at the short residence time while minimizing the energy input for milling used to obtain small particles. An increased energy input into the biomass comminution process affects the total efficiency of a power plant, and large particle sizes may cause additional problems with flame stability and burnout. This is further challenged by application of a broad biofuel range to obtain high operational flexibility at power plants. The biomass utilization at Danish power plants highly focuses on wood pellets, but introduction of new solid fuels such as waste products from agriculture and energy crops, will increase the operational flexibility. Moreover, the quality of agricultural wastes is lower than that of wood due to a higher ash content that may cause deposition and corrosion of the boiler units.

Fast devolatilization at high temperatures and heating rates is the initial step of the pulverized biomass combustion, where the biomass particles are heated up fast to high temperatures as they enter the boiler and thereby volatilize and leave a solid residue called char. Similar to coal combustion, the biomass burn out is known to be influenced by the yield and reactivity of chars, produced during pyrolysis [3]. The morphology and chemical composition of the char are strongly influenced by the pyrolysis conditions and the biomass properties. A low heating rate alters the morphological structure of biomass less than high heating rates [4].

The remaining char after pyrolysis undergoes oxidation that represents the slowest stage in the overall combustion process and strongly depends on the char reactivity and external and internal transport processes. The conversion rate during char oxidation is influenced by the diffusion of oxygen to the particle surface, through the pores and by the intrinsic reactivity [4]. The char morphology generated during pyrolysis affects the particle diffusion properties. Previous investigations showed that the plasticization at high heating rates is stronger than at low heating

rates [3, 5, 6]. A stronger plasticization at high heating rates could increase the biomass reactivity due to the higher total surface area of chars. The intrinsic reactivity can be additionally increased by the catalytic influence of ash elements (K and Ca). The reactivity can decrease when chars are exposed to high temperatures due to the thermal deactivation.

The extensive research efforts have been made to understand the fundamental descriptors of char reactivity and morphology to establish a model for the char conversion. The widely different char properties generated under various pyrolysis condition lead to a range of challenges in a modeling of biomass conversion. The pyrolysis of biomass involves many complex subprocesses, which require many assumptions and simplifications. A single particle model represents a well-defined system for the prediction of the char burnout and the energy release profile in a pulverized biomass boiler.

The optimization of pulverized power plants (PF) has deserved much attention in the recent years, which are directed to extend boiler lifetimes, obtain stable operation, improve thermal efficiency and reduce pollutant emissions. Through improved characterization of the original biomass and char properties, it will be possible to improve the predictive options of biomass conversion models.

1.2 Project objectives and scope

The work presented in this thesis is a part of the GREEN project whose aim was to develop a novel scientific framework for the efficient conversion of existing coal-fired power plants to biomass. The aim of this PhD project has been 1.) to investigate the influence of devolatilization operating parameters (heating rate, temperature, particle size, biomass origin) on the char yield and morphology, in particular at high heating rates using lab and pilot scale reactors 2.) to improve the understanding of char and soot reactivity in dependence of alkali content and organic biomass composition 3.) to develop a simple mathematical model of fast pyrolysis for the char yield prediction. The following chapters of this thesis describe the main results.

- ⋆ Chapter 2 is a brief literature review of different aspects related to biomass combustion.
- ⋆ Chapter 3 describes lab and pilot plant-scale reactors and instrumentation for the solid residue (char + soot) characterization.
- ⋆ Chapter 4 concerns fast pyrolysis experiments performed in a wire-mesh reactor, single-particle burner, drop-tube reactor and entrained flow system with the aim of testing the effects of biomass types and operational conditions on the pyrolysis products.
- ⋆ Chapter 5 deals with char morphology and structural composition.
- ⋆ Chapter 6 describes the relations between solid residue morphology, organic structure, inorganic matter content and its reactivity under oxidation and gasification conditions.

- ⋆ Chapter 7 presents the 1D mathematical model of biomass fast pyrolysis to predict the char yield on the basis of the obtained experimental results.
- ⋆ Chapter 8 summarizes the results of the preceding chapters.
- ⋆ Chapter 9 gives suggestions for the future work.

The manuscript is based on five articles submitted to scientific journals. However, with the intention to keep a consistent structure of the thesis, the information from all articles was distributed according to the chapter thematic, and enriched with the additional results which will be published at a later point of time. Each chapter can be read independently of the others. The articles used in the preparation of this manuscript are listed below.

1.) 'Effect of fast pyrolysis conditions on biomass solid residues at high temperatures (1000-1400°C)' by A Trubetskaya[1], PA Jensen[1], AD Jensen[1], M Steibel[2], H Spliethoff[2] and P Glarborg[1] published in *Fuel Processing Technology* (2015)

2.) 'Influence of fast pyrolysis conditions on yield and structural transformation of biomass char' by A Trubetskaya[1], PA Jensen[1], AD Jensen[1], AD Garcia Llamas[3], K Umeki[3] and P Glarborg[1] published in *Fuel Processing Technology* (2016)

3.) 'Comparison of high temperature chars of wheat straw and rice husk with respect to chemistry morphology and reactivity' by A Trubetskaya[1], PA Jensen[1], AD Jensen[1], F Hofmann Larsen[4] and P Glarborg[1] published in *Biomass & Bioenergy* (2016)

4.) 'Characterization of free radicals in biochars from fast pyrolysis at high temperatures (1000-1500)°C' by A Trubetskaya[1], PA Jensen[1], AD Jensen[1], P Glarborg[1], F Hofmann Larsen[4] and M Larsen Andersen[4] published in *Biomass & Bioenergy* (2016)

5.) 'Impact of fuel on the yield, nanostructure and reactivity of soot from fast biomass pyrolysis at high temperatures' by A Trubetskaya[1], PA Jensen[1], AD Jensen[1], AD Garcia Llamas[3], K Umeki[3], D Gardini[5], J Kling[5], RB Bates[6] and P Glarborg[1] published in *Applied Energy* (2016)

[1]Department of Chemical and Biochemical Engineering, DTU, Søltofts Plads, Bygning 229, 2800 Lyngby, Denmark
[2]Institute for Energy Systems, TU Munich, Boltzmannstr. 15, 85747, Garching, Germany
[3]Energy Engineering, LTU, 97187, Luleå, Sweden
[4]Department of Food Science, University of Copenhagen, Rolighedsvej 26, 1958 Copenhagen, Denmark
[5]CEN Center for Electron Nanoscopy, Technical University of Denmark, 2800 Kgs. Lyngby, Denmark
[6]Department of Mechanical Engineering, MIT, 02139 Cambridge, MA, USA

References

[1] Lin W, Jensen PA, and Jensen AD. Biomass Suspension Combustion: Effect of Two-Stage Combustion on NO_x Emissions in a Laboratory-Scale Swirl Burner. *Energy Fuels*, 23(3):1398–405, 2009.

[2] Yin C, Rosendahl L, Kær S, and Condra TJ. Use of numerical modeling in design for co-firing biomass in wall-fired burners. *Chem Eng Sci*, 59(16):3281–92, 2004.

[3] Cetin E, Moghtaderi B, Gupta R, and Wall TF. Influence of pyrolysis conditions on the structure and gasification reactivity of biomass chars. *Fuel*, 83(16):2139–50, 2004.

[4] Dall'Ora M, Jensen PA, and Jensen AD. Suspension combustion of wood: Influence of pyrolysis conditions on char yield, morphology, and reactivity. *Energy Fuels*, 22(5):2955–62, 2008.

[5] Cetin E, Moghtaderi B, Gupta R, and Wall TF. Biomass gasification kinetics: influences of pressure and char structure. *Combust Sci Technol*, 177(4):765–91, 2005.

[6] Biagini E, Simone M, and Tognotti L. Characterization of high heating rate chars of biomass fuels. *Proc Combust Inst*, 32(2):2043–50, 2009.

2 Literature survey

2.1 Introduction

This Chapter is a brief literature review of different aspects relevant to wood combustion. Section 2.2 gives an overview of wood and herbaceous biomass structure and composition. In section 2.3 pyrolysis as the first step in biomass combustion is discussed. Chapter 2.5 is dedicated to the modeling of biomass pyrolysis. The chemical composition and morphology of solid residues (char and soot) are outlined in section 2.6. The reactivity of original biomass and solid residues generated during pyrolysis is highlighted in section 2.7.

2.2 Biomass structure and composition

The biomass type, its physical characteristics and chemical composition influence the whole process of biomass utilization. In Denmark, the biomass combustion is becoming more extensive, thus requiring a broad biofuel range to obtain high operational flexibility at power plants. Presently, the Danish power plant supply is largely limited to imported wood pellets, but introduction of new solid fuels such as waste products from agriculture and energy crops is desired. The quality of biofuel depends on many characteristics like the fraction of bark, geographic origin, etc. In this section, biomass structure and chemical composition are discussed, which vary among different wood and straw.

2.2.1 Wood

Wood can be considered as a mixture or polymers combined with minerals. Figure 1 shows the structure of a tree trunk including wood layers in the radical direction (bark, phloem, cambium, sapwood and heartwood).

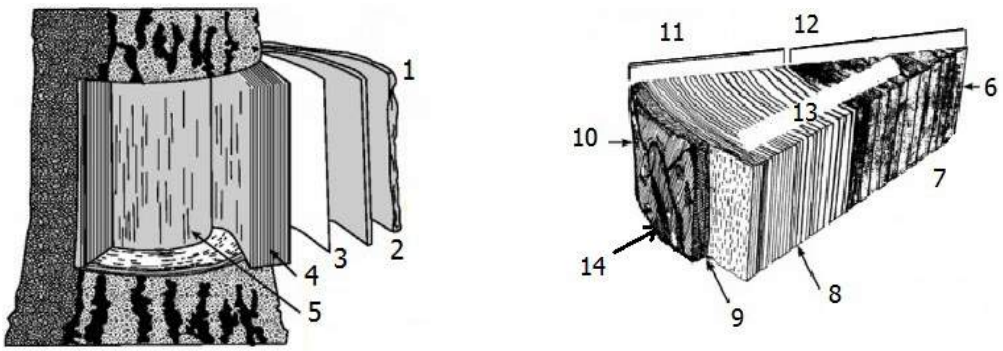

1(a): Main structure of the wood stem

1(b): Three primary planes of wood

Figure 1: Structure of tree trunk, and three primary planes of wood: (1) bark (2) phloem (3) cambium (4) sapwood (5) heartwood (6) pith (7) radial surface (8) annual ring (9) inner bark (10) outer bark (11) sapwood (12) heartwood (13) transverse surface (14) tangential surface [1, 2].

The bark consists of the inner bark (phloem) and the outer bark. The inner bark is a narrow layer of living cells which transport sap to provide the tree with energy, whereas the outer bark consists of dead cells with a high fraction of extractives which protect tree. Cambium is a thin layer between the sapwood and bark where new wood cells are formed. Sapwood is the outer section of wood which consists of dead cells which provide support to the tree, act as nutrient storage reservoir and transport water from roots to the tree crown [3]. Heartwood is the inner section of the wood that consists of dead cells with the main function to provide support.

Wood can be classified into two major groups termed softwoods (gymnosperms) and hardwoods (angiosperms) [3] as shown in Figure 2. The major difference with regard to wood anatomy is the presence of vessels in hardwoods for the water conduction. Moreover, hardwood consists of shorter cells, more parenchyma and a more variable arrangement of cell types occur. Softwoods lack vessels but have cells termed longitudinal tracheids which perform a dual role of conduction and support [3].

Softwood is composed of tracheids (≈90 %), which conduct water and nutrients and support structure, and paranchyma cells (≈10 %) which store nutrients [4]. These two cell types can be classified according to the longitudinal or transverse orientation. The longitudinal cells are orientated parallel to the vertical axis of the tree trunk, whereas the transversely orientated cells have a long axis parallel at right angles to the vertical axis of the tree trunk [3].

Hardwood has a more complex anatomy, containing vessel segments, fibers, transverse and axial parenchyma (up to 40 %). Vessels are designed to carry out the conduction function, whereas fibers play a supporting role. In hardwood, vessels are larger in diameter than the cells, known as tracheids, in softwoods. Hardwoods are commonly referred to porous woods, and softwoods to non-porous woods.

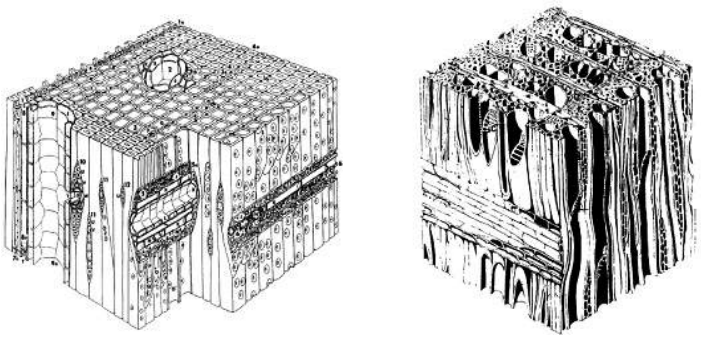

2(a): Softwood 2(b): Hardwood

Figure 2: Softwood and heartwood structure [5].

Figure 3 shows an example of a porous hardwood with large vessel elements which are filled with tyloses. The major function of tyloses is to block the flow of water through the vessels. These are filled with the large quantity of phenolic compounds, lignin, and aromatic substances. The formed phenolic compounds polymerize in insoluble forms, for example in a non-lignin related

bio-polymer suberin which makes a wood particle more stable at high heat treatment temperatures [6, 7].

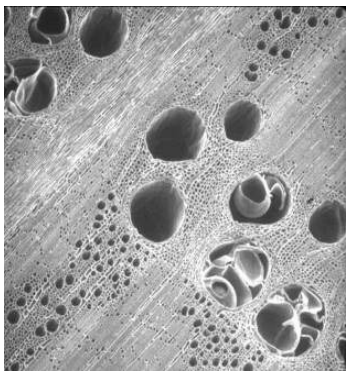

Figure 3: Vessels with tyloses in hardwood [6, 7].

2.2.2 Wheat straw

Straw (gramineae) is a type of monocots or also called a herbaceous biomass. A fundamental difference in the anatomical structure of monocots from dicots (wood) is mainly in a cadmium absence. Grasses have instead of a stem structure with numerous vascular bundles scattered in a ground tissue of parenchymatic storing cells, surrounded by an epidermis [8]. The vascular bundles are formed from the roots, leading to the absence of the conducting tissue. Figure 4 shows structural parts of straw.

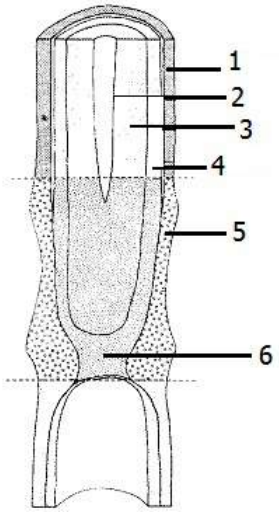

Figure 4: Structure of wheat straw: 1.) lead sheath 2.) lumen 3.) pith 4.) vascular tissue 5.) leaf base 6.) true node [8].

The stem is a hollow cylindrical supporting structure to which leaves are attached at the nodes and thus, divide the stem into internodes. The grass leaves consist of the leaf sheath and blade. The vascular bundles and associated fibres in the bundle sheath of the leaves, internodes and nodes

are embedded in a non-lignified fundamental tissue covered by the epidermis.

2.2.3 Biomass composition

Biomass has a different chemical composition than coal. Biomass contains three distinctly different building blocks, i.e. cellulose, hemicellulose and lignin. The cellulose and hemicellulose are quite different from coal structures while the lignin has more resemblance with coal, containing aromatic moieties [9, 10].

Cellulose consists largely of anhydroglucose held together in a giant straight-chain molecule bound by β-(1,4)-glycosidic linkages [4]. Unlike cellulose, hemicellulose consists of different monosaccharides. The polymer chains of hemicellulose have short branches and are amorphous, leading to the partial water solubility.

Lignins are polymers of aromatic compounds, which provide structural strength and sealing of the water-conducting system that links roots with leaves, and protect plants from degradation. Lignin occurs throughout the plant cell wall, yet is largely concentrated in the primary cell wall and middle lamella as shown in Figure 5 [11].

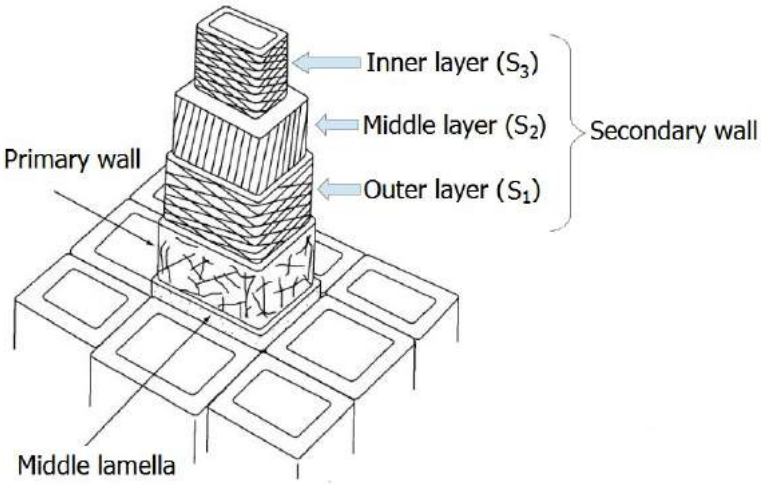

Figure 5: Schematic of cell wall layers within cellular structure [12].

Lignin is a macromolecule, which consists of alkylphenols and has a complex three-dimensional structure, consisting primarily of three units: guaiacyl (G), sinapyl (S), and p-hydroxyphenyl (H) units linked by aryl ether or C-C bonds [13]. Grass lignin has been justified as GSH-lignin, which is different from those of softwood (G-lignin) or hardwood (GS-lignin). Furthermore, hydroxycinnamic acids, mainly p-coumaric and ferulic acids can be present in grasses [14].

Additionally, wood and herbaceous biomasses may contain high amounts of extractives, which affect the biomass mechanical strength. In grasses, waxes (up to 30 %, db) [15] are located in the plant's cuticula, whereas softwood may incorporate sterols, resin acids, fatty acids and alcohols and rest compounds (2-15 %, db) [16]. Wood and grasses contain the lipid and protein fractions in a lower concentration than the carbohydrate components. The protein fraction in

herbaceous biomasses (up to 12.3 %, db) is higher than in wood (up to 2.1 %, db) [17].

Besides the organic components in biomass, the inorganic matter is dispersed throughout the cells. Coal contains a high level of transition metals, while biomass incorporates more alkali and alkali-earth metals, usually in the form of salts. Herbaceous biomasses contain significantly higher amounts of potassium and chlorine than wood and coal. The high presence of KCl in herbaceous biomass could cause high-temperature corrosion that limits the super-heater temperature and decrease thereby the power plant efficiency. Biomass contains less sulfur than coal, leading to lower sulfur emissions. The proximate, ultimate and ash compositional analysis to describe differences between coal and biomass properties are shown in Table 1.

Table 1: Proximate and ultimate analysis of wood and herbaceous biomass and coal (on % dry basis) and ash analysis (in wt. %, dry basis). The symbols ar and db stay for as received and dry basis.

Fuel	Pinewood [18]	Beechwood [19]	Wood chips [20]	Wheat straw [20]	Miscanthus [21]	Coal [22]
Proximate and ultimate analysis (% db)						
Moisture, wt. % (ar)	7.1	7	45	14	1.9	5.3
Ash (550 °C)	0.5	0.4	1	4.5	2.1	10.4
Volatiles	85	85.3	81	78	74.2	34
LHV (MJ kg^{-1})	17.6 [5]	17.1 [23]	9.5	14.9	17.1	26.5
C	49.7	50.8	50	47.5	46.3	71
H	6.3	5.9	5.8	5.9	5.6	4.9
O	43.5	42.9	42.9	42	41.8	12.2
N	0.1	0.3	0.3	0.15	0.6	1.5
S	0.02	0.04	0.05	0.15	0.2	0.7
Ash compositional analysis (wt. % db)						
Cl	0.01	-	0.02	0.4	0.3	0.03
Ca	0.13	0.35	0.2	0.4	0.2	0.2
K	0.03	0.2	0.1	1	0.5	0.2
Mg	0.03	0.1	0.04	0.07	0.05	0.15
Si	0.07	0.1	0.1	0.8	0.1	3

The low heating values (LHV) of pinewood and beechwood were taken from different publications only for the estimation to compare with the coal LHV.

2.3 Pyrolysis

2.3.1 Introduction

Numerous industrial applications dedicated to the conversion of biomass into heat and power include a pyrolysis step under severe thermal conditions. Pyrolysis processes are conducted under an inert atmosphere for the production of charcoal, liquids (bio-oils) or high heating values gases. Their relative fractions depend on the operating conditions. Depending on the reaction temperature, heating rate and residence time, pyrolysis can be classified into slow, intermediate and fast.

Slow pyrolysis has been mainly used for the production of charcoal [24–26]. Biomass is heated up to $< 700°C$ at slow heating rates (up to 10-20 K min^{-1}) with the residence time (5-30 min), leading to the formation of solid char and liquid. In intermediate pyrolysis, reaction

occurs at controlled heating rates in a temperature range of 450-550°C to produce condensable vapors and gas. Heating rates relevant to the pyrolysis of solid fuels during pulverized combustion or fluidized bed gasification are far higher (usually $> 1000\,\mathrm{K\ s^{-1}}$) and residence time is significantly shorter ($< 0.5\,\mathrm{s}$). In pulverized combustion, biomass particles are heated fast to high temperatures as they fall through the boiler and thereby pyrolyze and leave a solid residue called char, gas and vapors. At high temperatures, fast pyrolysis is considered as the initial step of the pulverized biomass combustion. At temperatures around 500°C and with short vapor residence time to minimize secondary reactions, larger fractions of liquids can be obtained. At pulverized fuel-fired power plants the solid fuel is exposed to very high temperatures (up to 1400°C), resulting in heating rates (up to 10^4-$10^5\,\mathrm{K\ s^{-1}}$) and low residence times.

Several types of reactors are most frequently used in determining the pyrolytic behavior of solid fuels. These include wire-mesh, single-particle and entrained-flow / drop tube reactors, fixed (hot-rod) and fluidized-bed reactors. The first step in the combustion is pyrolysis, which is the release of volatiles from a solid fuel at high heating rates in a range of 10^4-$10^5\,\mathrm{K\ s^{-1}}$. The wire-mesh and entrained flow reactors are of interest for combustion at full-scale plants as they can attain high heating rates.

2.3.2 Pyrolysis mechanism

After the heating and drying steps similarly to coal, the biomass undergoes a pyrolysis with rupture of organic chemical bonds and the vaporization of light gases and tars and to the formation of char during primary pyrolysis, whereas the weakest bridges break producing molecular fragments (depolymerization) [9]. These fragments abstract hydrogen from hydroaromatics and aliphatic components, and are released as tar to the gas phase if they are small enough to vaporize and be transported out of the char particle [27]. Additionally, due to the decomposition of functional groups permanent gases (CO_2, H_2, CO, CH_4, C_3H_8, C_2H_4, C_2H_2) are released during char condensation. The tar species can be converted to char, light gas and soot via secondary reactions [28]. The cross-linking reactions (repolymerization) permit the solidification of the metaplast, which is formed due to the bond cleavage in the form of a melted material, to the infinite char matrix. The depolymerization reactions compete with condensation and cross-linking reactions, responsible for the formation of tar with larger aromatic sites [29]. The condensation is assumed to act on species which are still connected to the fuel matrix, while the cross-linking disconnect bonds with the fuel matrix [28]. During condensation and cross-linking reactions, aliphatic chains form light gases and aliphatic compounds. Char is formed from the unreleased or recondensed fragments.

Under fast heating in a pulverized biomass flame, pyrolysis is generally completed in a very short time, and during this period, char oxidation is prevented by the volatile release and the flame formation that stop the oxygen diffusion to the particle [30, 31]. The volatile oxidation occurs via homogeneous reactions. The rate of char oxidation is lower than that of the devolatilization.

Therefore, char oxidation is the time limiting step controlled by the chemical kinetics and external diffusion of oxygen [31]. The pyrolysis conditions affect the char yield and its reactivity. A lower char yield and higher reactivity are beneficial for the fast fuel conversion in the boiler. The influence of heat treatment temperature, heating rate, fuel particle size, residence time, organic and inorganic composition on the char yield and morphology will be investigated in this section.

2.4 Effect of operating conditions on pyrolysis

2.4.1 Heat treatment temperature

Figure 6 shows the mass loss of wood plotted against the final temperature. Devolatilization of biomass starts at lower temperatures than that of coal (500-550°C) and the volatile yield increases with the final temperature up to approximately 80 %.

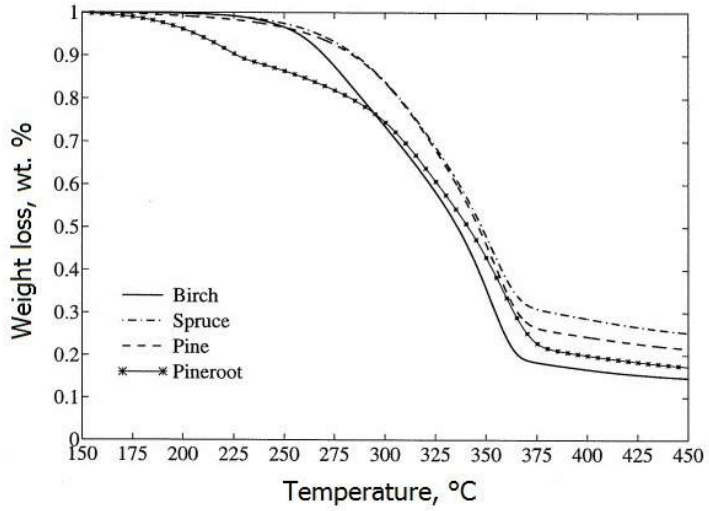

Figure 6: Thermal behavior of birch, spruce, pine and pineroot, 5 K min^{-1} [5].

A higher reaction temperature favors the formation of tar components with higher volatilities and lower molecular weights. The volatile matter yield obtained in a pulverized fuel boiler is dependent upon the temperature history of the particle. A reliable estimation of particle devolatilization temperature requires knowledge of particle shape, thermal properties for high heating rates, chemical kinetics and heat of devolatilization. The effect of heating rate on the volatiles yield is difficult to study independently of final temperature. The calculations made by the chemical percolation devolatilization model (CPD) [32] showed that with the increasing temperature at which the reactions occur at faster heating rates a higher volatile yield is expected.

2.4.2 Heating rate

Heating rate has a stronger effect on biomass pyrolysis than on that of coal, which may be attributed to the cellulose content of the biomass [26, 33]. Heating rates affect the melting

and swelling behavior of both biomass and coal and thereby how the competing processes of tar formation (bond-breaking, cross-linking, internal mass transport) change with the temperature. The heating rates determine the temperature at which the reactions occur [34].

Significant differences in the char yield and morphology were observed between the results corresponding to slow and fast heating rate pyrolysis [35–37]. Zanzi et al. [38] compared the yields and reactivities of chars produced in slow (20 K min^{-1}) and fast heating ($\approx 10^4$ K s^{-1}) pyrolysis. The rapid heating rates caused lower char yield than under the slow heating. Furthermore, the chars generated at fast heating rates were more reactive in gasification than those produced under the slow heating, and had a high porosity. The secondary reactions under the slow heating in TG experiments favored the char formation in contrary to the fast pyrolysis where the secondary reactions were limited.

2.4.3 Particle size and shape

Biomass particles commonly have more irregular shapes and much larger sizes than pulverized coal [39]. A very important issue in the combustion of solids in a suspension fired boiler is particle size and uniformity. Large biomass particles can be incompletely converted due to heat transfer limitations, thus reducing the efficiency of the process, and causing the formation of a high carbon content in the bottom and fly ash.

At high temperatures ($> 1000°C$), the heat flux in smaller biomass particles is higher than in larger particles, leading to the low char yields. The effect of larger particle size on the char yield and morphology at temperatures $< 1000°C$ was studied in the literature [19, 40–43]. They observed that the larger particles cannot be completely pyrolyzed in a temperature range of 700-1000°C, leading to higher char yields in the entrained flow reactor. Bitowft et al. [44] studied fast pyrolysis of small (250-355 mm) and large sawdust particles (500-630 mm) in a temperature range of 1000-1400°C in a drop tube reactor, and observed completely pyrolyzed particles with a similar char yield of $\approx 17\,\%$ above 1000°C. Septien et al. [19] concluded that in a temperature range of 1000-1400°C the effect of a particle size on the char yield is negligible based on the similar char yields of 0.35 and 0.8 mm beechwood particles. Zanzi et al. [38, 40, 45] suggested that the condensable gases escape from smaller biomass particles to surroundings before they undergo secondary reactions, while the larger particles facilitate secondary cracking reactions due to the higher thermal resistance, hindering primary pyrolysis products from release.

Biomass particles are characterized by the fibrous structure, non-spherical shapes and higher aspect ratios (length/width) than pulverized coal. This is especially pronounced for the large solid fuel particles [39]. A large particle size allows secondary reactions to occur within the particle, leading to different product yields compared to smaller biomass particles [46]. The surface area and volume of the particle are the main parameters of interest since this determines the area over which reactions will occur and the residence time of a particle in the combustion process. Various biomass shapes result in different surface area to volume ratios, which are essential to heat and

mass transfer. Spheres represent the lowest surface area to volume ratios of any shape, which makes an assumption of spherical particles in combustion modeling rather conservative. Lu et al. [39] showed that the flake-like and cylinder-like particles have larger surface areas and smaller thicknesses, which result in higher heating rates and faster heat and mass transfer to the particle than in the near-spherical particles. Moreover, the mass loss rate differences between the near-spherical and non-spherical particles increases with increasing size [39, 47, 48].

2.4.4 Organic matter

Biomass is a mixture of structural constituents (cellulose, hemicellulose, lignin) and minor amounts of extractives. Lignin decomposes over a wider temperature range compared to cellulose and hemicellulose, which degrade over narrower temperature ranges [49]. The hemicelluloses break down first, at temperatures of 200 to 260°C and cellulose follows in the temperature range 240 to 350°C, with lignin being the last component to devolatize in a temperature range of 230 to 500°C [26]. Previously, Bradbury et al. [50] and Antal et al. [51] suggested that char formation might result from the repolymerization of volatile material such as levoglucosan. The higher char yield obtained at low heating rate and low temperature due to the predominance of dehydration reactions, leading to the formation of more stable anhydrocellulose [52]. At higher temperatures and higher heating rates cellulose depolymerizes producing mainly levoglucosan which is a more unstable material left for depolymerization to primary volatiles, leading to a lower char yield [38].

Hemicelluloses are the most reactive major component of hemicelluloses due to less crystalline structure. Decomposition of hemicellulose under pyrolytic conditions is postulated to occur due to the polymer breakdown into water soluble fragments, followed by decomposition to monomeric units, and finally decomposition of these fragments to volatiles [53]. The devolatilization of hemicellulose mainly occurs at low temperatures (500°C), leading to a high tar yield. At higher temperatures hemicelluloses produce more gas than tar without levoglucosan formation in comparison to cellulose. Wu et al. [54] observed that higher temperatures favor the cracking and reforming of the volatiles, and thus, increase CO and H_2 formation. Furthermore, hemicelluloses produce more methanol and acetic acid than cellulose. Lignocellulosic materials with a high hemicellulose content have a lower solid product yield compared with that of the biomass with a low hemicellulose content. At high temperature pyrolysis (200-900°C), hemicellulose showed a larger CO_2 yield based on the high carboxyl content, whereas cellulose obtained a high CO yield due to the higher carbonyl content than in hemicelluloses [55].

The decomposition of lignin starts at relatively low temperatures in a range of 200-275°C, the main process occurring around 400°C, with the formation of aromatic hydrocarbons, phenolics, hydroxyphenolics and guaiacyl-/syringyl-type compounds [56]. The reaction between cellulose and lignin during biomass pyrolysis showed that the lignin contributed to the decrease in tar yields and increase in char yield [57]. Lignin inhibits the levoglucosan polymerisation and enhances the formation of low molecular weight products from cellulose, leading to a higher char yield.

Cellulose co-currently decreases the secondary reactions of lignin and enhances the formation of lignin-derived products including guaiacol, 4-methyl-guaiacol and 4-vinyl-guaiacol [58]. Furthermore, a type of lignin compound (guaiacyl, syringyl, phenolics, hydroxyphenolics, etc.) affects the biomass char yield. The highly cross-linked structure of lignin may decompose at low temperatures with a predominance of cross-linking reactions and favors higher char yields due to formation of more resistant condensed structures [59]. At temperatures $< 230°C$ the mass loss of lignin is largely caused by the cracking of hydroxyl groups in lateral chains. At higher temperature CO_2 and CO are released from the cleavage of C-C bonds. The light hydrocarbons (mainly CH_4 and H_2) are released from primary lignin pyrolysis between 350 and 460°C, which at higher temperature is ascribed to secondary degradation of primary unstable volatile species [60]. Avni et al. [61] observed that up to 900°C lignin decomposition leads to CO_2 release from the carboxyl groups, H_2O from the hydroxyl groups, CO from the weakly bound oxygen groups and H_2 from the aliphatic and methoxy groups. Tertiary reactions at higher temperatures may involve breakage and rearrangement of stronger bonds in aromatic rings, with the evolution of additional H_2 and CO from the tightly bound oxygen functional groups. The high temperatures $> 500°C$ and high heating rates lead to higher volatiles yield and lower char yields during lignin pyrolysis [61]. The higher lignin content in olive waste in comparison to wheat straw, increases the char yield as it was observed by Demirbas [26].

2.4.5 Inorganic matter

The product yields and their properties are affected by the amount and type of embedding of the present inorganic elements [18, 62–65]. Biomass inorganic constituents mainly involve potassium, silicon and calcium [66]. The majority of investigations about the inorganic matter influence on the char yield is focussed on biomass, pyrolyzed under slow heating rates and long holding time. Little is know on transformation and release of volatile matter at high heating rates and high temperatures $> 1000°C$.

DeGroot and Shafizadeh [67, 68] investigated the effect of calcium and potassium cations on the wood decomposition, and observed that the Ca and K cations and adsorbed salts increased the char yield. Furthermore, DeGroot and Shafizadeh [68] suggested that due to the close dissociation of inorganic species with the hemicelluloses through ion exchange on glucuronic acid groups, it is most likely that devolatilization of hemicelluloses contributes significantly to the formation of wood char. Jensen et al. [64] and Nik-Azar et al. [69] suggested that the char yield decrease of leached wheat straw compared to untreated wheat straw is due to the K catalytic effect on the repolymerization and cross-linking reactions to char. The high level of potassium in the wheat straw catalyzes the conversion of bridges into char, promoting faster devolatilization rates and surpressing tar formation [70], and lead to the higher char yields. Nik-Azar et al. [69] concluded that at intermediate heating rate ($1000\,K\,s^{-1}$) sodium and potassium cations showed a stronger catalytic effect on the beechwood char yield than calcium cations. The investigations of Dall'Ora

et al. [18, 71] at fast heating rates ($\approx 10^4$ K s^{-1}) in an entrained-flow reactor and in a temperature range of 1000-1400°C showed that Ca and K catalyze cross-linking, leading to higher char yields and less severe morphological changes of beechwood (high K content) compared to pinewood (low K content).

Raveendran et al. [62] investigated the effect of silicon on the char yield under the slow heating, and suggested that the higher char yield of rice husk is related to the presence of silicon in the fuel. Link at al. [72] observed at 800°C at slow heating rate that the low-ash containing pinewood pellets obtained lower char yield (daf) than reed and Douglas fir with the higher silicon content [73].

2.5 Modeling biomass pyrolysis

2.5.1 Kinetic modeling

In spite of numerous studies existing on biomass devolatilization mechanisms, there is no generally accepted model that can estimate the reaction rate and provide information about final conversion and product yields over a wide range of operating conditions. Many kinetic models have been proposed to describe biomass devolatilization [74]. However, the previously developed kinetic models [75–81] were often based on experimental data using particular samples in specific reaction condition. Moreover, these models based on the kinetics derived at lower temperatures, creat challenges for the data extrapolation to higher temperatures in combustion / gasification processes. Early kinetic models of wood char combustion used integral thermogravimetric dynamic data to estimate the kinetic parameters based on the one-step global reaction characterized by the underestimated values of the activation energy [82]. Stenseng et al. [83] compared several single-first-order-reaction kinetics for the wood devolatilization from literature and shown in Figure 7, which shows a wide range of wood devolatilization reactivities with the various activation energies from 68 to 140 kJ mol^{-1} and pre-exponential factors in a range of $8.5{\cdot}10^2$-$1{\cdot}10^8$ s^{-1}. A broad variation of kinetic parameters was probably caused by the differences between wood species and operating conditions [18]. In addition, Nik-Azar et al. [69] reported large uncertainties in the kinetic parameters based on sample mass differences so that heat and mass transfer limitation must be taken into consideration.

The way to avoid the dependency of kinetic parameters on heating rates is the application of a distributed activation energy model as shown for the coal devolatilization by Solomon et al. [84]. This model considers the variety of biomass decomposition reactions. The reactions are shown with the same pre-exponential factor, while the activation energy changes as a continuous distribution, and satisfy the equation 1:

$$\int_0^\infty f(E)dE = 1 \tag{1}$$

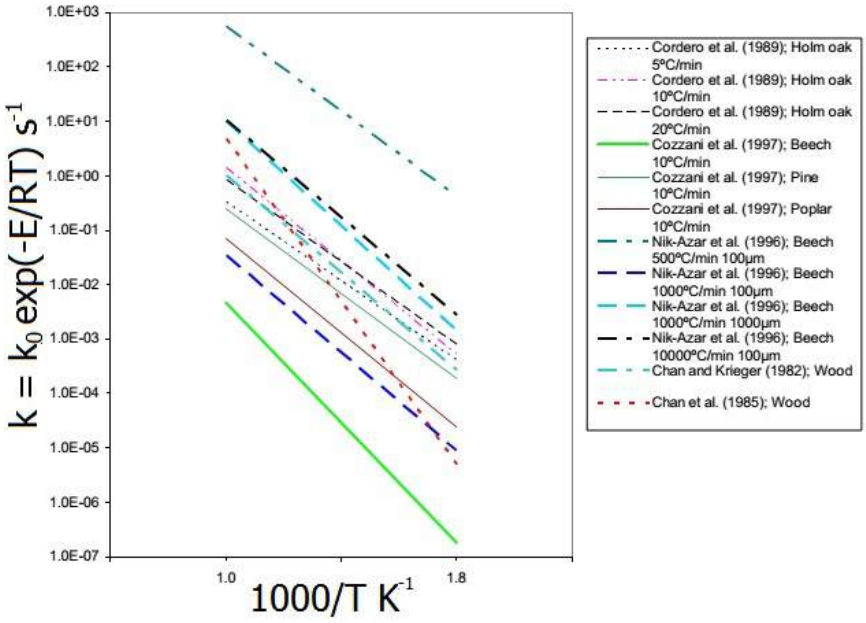

Figure 7: Single-first-order-reaction kinetics for the wood devolatilization at different operating conditions [83].

Dall'Ora et al. [18] simplified the equation 1 for the amount of volatiles released over the time as shown in equation 2:

$$V = V^* \cdot \left[1 - \int_0^\infty exp\left(\int_0^t k_0 e^{-\frac{E}{RT}}\right)\right] \cdot f(E)dE \tag{2}$$

Many kinetic models for wood pyrolysis have been reported in the literature [85]. The simplest models are based on a single decomposition reaction, and they do not allow to estimate the influence of heating conditions on the product yields accurately [86].

$$Fuel\ particle \longrightarrow Volatiles \cdot (1-\gamma) + \gamma \cdot Char$$

Figure 8: One-step global model [74].

Other models assume competing parallel reactions to estimate the production kinetics of gas, tar and char, which is often valid only over a narrow temperature range [77, 87].

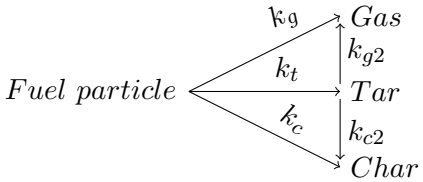

Figure 9: Competing step global model with k_g - rate constant of gas release, k_c - rate constant of char formation, k_t - rate constant of tar formation, k_{g2} - rate constant for the formation of gas from tar and k_{c2} - rate constant for the formation of char from tar [77].

The competing parallel reactions are mainly applicable at low heating rate and for specific fuels, which may create additional challenges for the modeling of fast pyrolysis at high temperatures [74, 88, 89]. More complex modeling ways were also implemented, which involve additional steps for the tar decomposition in the gas phase [90] or an intermediate product deriving from primary decomposition of biomass [50, 52, 91]. The proposed models mostly can be applied only for a particular type of biomass. Moreover, neither of the discussed models included the catalytic alkali effect on the biomass devolatilization, whereas the inorganic matter influences both yields and product release rates significantly [18, 64, 92]. Therefore, consideration of catalytic alkali effect in devolatilization models is desired to specify structural differences between fuels more accurately.

2.5.2 Superposition models

Recently, several studies attempted to develop more general models by extending macromolecular network models (FG-DVC model, CPD model and FLASHCHAIN) of coal devolatilization [93–96]. These models describe the devolatilization behavior of rapidly heated biomass/coal particles on the chemical structure of the parent fuel [97]. Despite the fact that biomass devolatilization releases gas, tar and leaves a solid char, similar to low rank coal devolatilization, the chemical structures of biomass and coal are different. Coal is predominantly an aromatic material, while in biomass only lignin has a relatively similar aromatic structure.

Superposition model theory described by Fletcher et al. [97] is based on the assumption of a base structural unit, which for coal is an aromatic cluster connected to other clusters by labile and char bridges. In addition, side chains are attached to the aromatic cluster and appear to be precursors for light gases and tar. The labile bonds between the aromatic clusters are cleaved, generating fragments of finite molecular weight, whereas fragments with low molecular weights vaporize and escape the fuel particle. The high molecular weight fragments with the low vapor pressure tend to reattach to the lattice. The residual lattice and high molecular weight compounds form a metaplast which determines the degree of fuel plasticization during pyrolysis. Superposition models are based on a mechanism described in Figure 10.

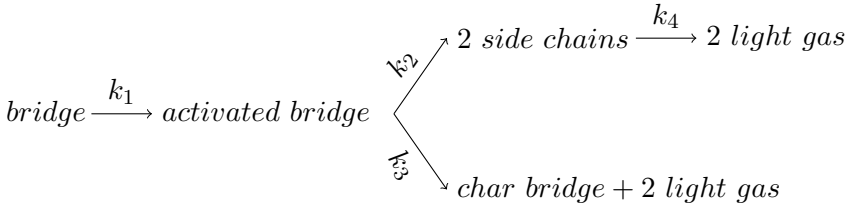

Figure 10: Model description [98].

Bridges between fragments are activated when particles are heated up. The activated bridge or metaplast can either break into two light gas components or form a stable char linkage, while releasing part of the bridge is a light gas. In superposition models, tar and gas yields are not input parameters, but a function of kinetic mechanism, structural parameters and temperature-dependent vapor-liquid-equilibrium [34]. A detailed chemical model for the release of both tar

and light gases during devolatilization has been discussed by Solomon et al. for coal [29, 34] and for lignin [61, 99].

In biomass superposition models the four main chemical components (cellulose, hemicellulose, lignin and extractives) are considered. Serio et al. [99–101] based devolatilization model (FG-DVC) only on lignin transformation. Niksa et al. [70] applied the bio-FLASHCHAIN to model pyrolysis of cellulose and lignin, while xylans and hemicelluloses were ignored. Biagini et al. [102] proposed new structural and chemical parameters for cellulose and hemicellulose and introduced secondary reactions for tar-cracking in their cellulose-hemicellulose-lignin model (CHL). Another devolatilization model of Biagini et al. [103] includes besides the main chemical components also extractives. The cellulose-hemicellulose-lignin-extractives (CHEL) model can accurately estimate the secondary reactions. Macromolecular network models can accurately describe the chemistry of devolatilization of various biomass samples at high heating rates [104]. However, neither of the discussed models included the catalytic alkali effect on the biomass devolatilization. The alkali influences both yields and product release rates significantly, therefore consideration of the catalytic effect of alkali in devolatilization models is desired to specify structural differences between fuels more accurately.

2.6 Biomass solid residue: structure and morphology

The chemical transformations of fuel at the devolatilization stage are accompanied by complex morphological changes which influence the reactivity of the produced chars during the subsequent oxidation or gasification stage [105, 106]. It is well know that the yield and morphology of char depend strongly on pyrolysis conditions. The literature available about characterization of char and soot generated at high-temperatures and fast pyrolysis is not extensive.

Two different solid residues can be distinguished during fast pyrolysis at high temperature ($> 1000°C$), namely char and soot. Char is the fraction of non-devolatilized solid from the initial biomass, consisting of mainly of carbon and ash with minor presence of hydrogen and oxygen. Soot is formed based on reaction mechanisms, consisting of devolatilization, homogeneous formation of precursors such as C_2H_2 and polycyclic aromatic hydrocarbons (PAH) and heterogeneous formation of soot (particle inception, surface growth, coagulation and oxidation) [107, 108].

2.6.1 Char morphology

There is wide agreement in the literature on the conclusion that heating rate has a significant effect on the char morphology [19, 36, 92, 109]. Cetin et al. [36] recalled the occurrence of biomass plastic deformation as an effect of a high heating rate and rated this phenomena in terms of char ability to melt (softwood $>$ hardwood $>$ bagasse). The effects of heating rate and temperature on the morphological transformations at both slow ($< 10\,\mathrm{K\ s^{-1}}$) and intermediate and fast pyrolysis environments ($> 100\,\mathrm{K\ s^{-1}}$) of the same feedstock have rarely been studied. Moreover, little is known about the influence of biomass composition on the char morphology.

Figures 11(a) and 11(b) show SEM images after Cetin et al. [36], where the structural evolution of pine sawdust from original fuel to the char produced at 1000°C in a drop tube furnace (DTF) was investigated. It is evident that the pinewood particle underwent severe transformations under the fast heating, forming a near-spherical char shape. In contrast, SEM images after Septien et al. [19] indicated that the beechwood char produced at 1200°C in an entrained flow reactor (EFR) preserved the original morphology of the biomass as shown in Figure 11(c).

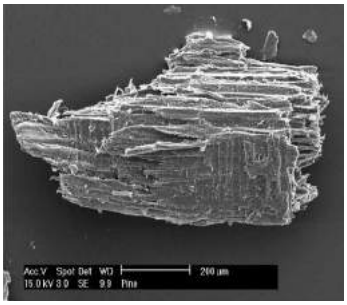

11(a): Original pinewood [36]

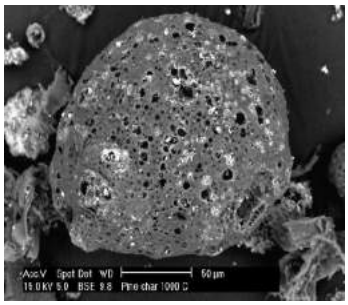

11(b): Pine char (1000°C; DTF) [36]

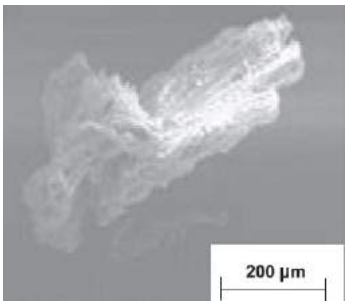

11(c): Beechwood char (1200°C; EFR) [19]

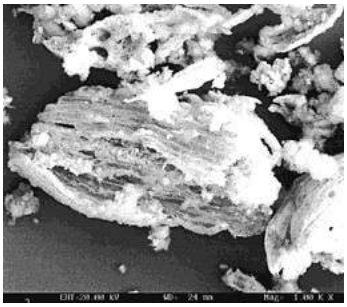

11(d): Wheat straw char (1340°C; EFR) [110]

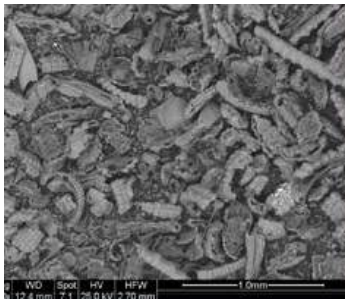

11(e): Wheat straw char (1300°C; DTF) [109]

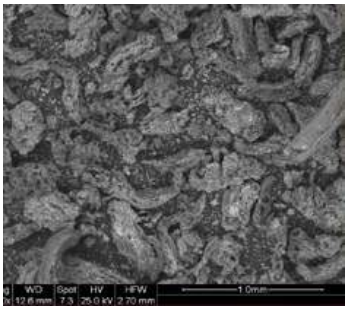

11(f): Rice husk char (1300°C; DTF) [109]

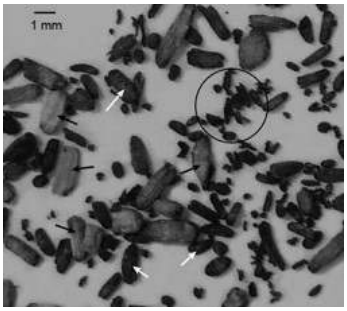

11(g): Pine char (0.5-1 mm; 1000°C; L-EFR) [92]

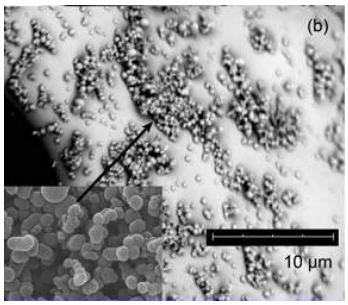

11(h): Pine char surface [92]

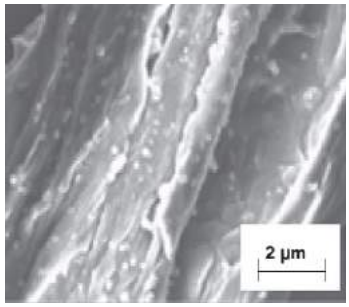

11(i): Beechwood char surface [19]

Figure 11: Scanning electron microscopy (SEM) images of original biomass and chars, prepared at high temperatures, and intermediate (1000 K s^{-1}) and fast heating rates ($\approx 10^4$-10^5 K s^{-1}) [19, 36, 92, 109].

SEM image of char particles obtained by Zolin et al. [110] using an EFR reactor as shown in Figure 11(d) indicates that the wheat straw chars prepared in a temperature range of 1000-1340°C passed through a plastic stage during pyrolysis. The wheat straw char shape varied from spherical to nearly similar to the original fuel. Pottmaier et al. [109] showed that at all heat treatment

temperatures and heating rates, resulting wheat straw and rice husk chars retained most of the features of parental fuels according to Figures 11(e) and 11(f). Umeki et al. [92] investigated the particle size effect on char morphology in a laminar drop tube reactor at 1000°C, and observed the incompletely pyrolyzed particles of sizes between 0.5 and 1 mm with the short residence time (< 1.5 s). The pinewood char particles obtained broad size and shape distributions. Some char particles were significantly smaller than the original fuel particles, whereas other particles preserved the original biomass structure as shown in Figure 11(g). Septien et al. [19] investigated beechwood structural transformations of larger particle size (0.85-1 mm) pyrolyzed in a temperature range of 1000-1400°C and holding time of 2-4 s in an EFR. The beechwood char particles preserved the initial fibrous structure of original fuel. Figure 11(h) obtained by Umeki et al. [92] shows a pinewood char surface with attached small grains. SEM/EDX analysis indicated that smaller grains mainly consists of Mg, Fe, K and Ca, and associated the formation of grains with the vaporized and re-adsorption of the minerals on the char surface. In opposite, Septien et al. [19] observed very small amount of soot and inorganic particles present on the beechwood char surface as shown in Figure 11(i).

Cetin et al. [36, 111] also studied the influence of pressure on the char morphology, and concluded that melting has a stronger effect on char structural transformation compared to swelling as pyrolysis pressure increases. Solomon et al. [27, 99] suggested that at high heating rates, biomass behaves similarly to the bituminous coals and undergoes significant bridge-breaking before it starts to cross-link and therefore becomes fluid, whereas under slower heating conditions, char plasticization is hindered by cross-linking prior to bridge-breaking. The char fluidity of coal and lignin during pyrolysis was described by the FG-DVC model (Functional Group - Depolymerization, Vaporization and Cross-linking model) of Solomon et al. [27, 99]. They pointed out that small differences in the cross-linking rate affect drastically the fluidity of the resulting metaplast.

The morphological changes of biomass during pyrolysis were associated in the literature with the degradation of different plant components that affect the metaplast formation [36, 80, 91, 99, 103, 112, 113]. Cellulose forms a depolymerized liquid intermediate, similar to ice or meltable polymers under the fast heating as shown in Figure 12(a) [114–116]. High heat flux has a stronger effect on the cellulose decomposition compared to slow heating rates [115] by the formation of intermediate liquid species. At slow heating rates, cellulose was not a true liquid but more likely resembles a high viscosity type material, and obtained a higher char yield compared to cellulose pyrolyzed at high heating rates [117].

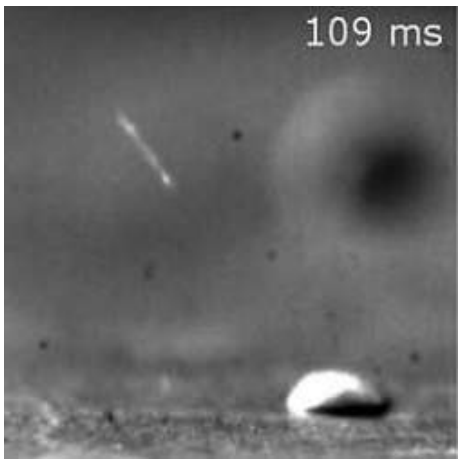

12(a): Cellulose intermediate formation [116]

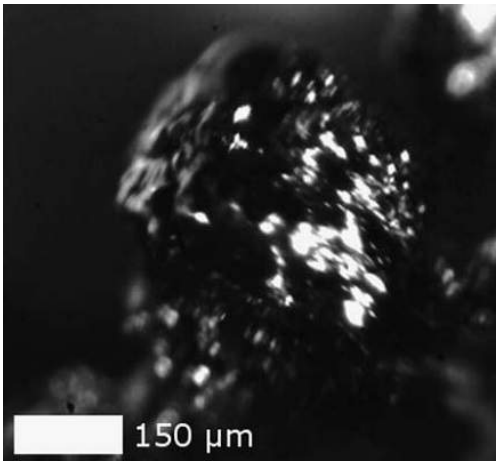

12(b): Molten hardwood lignin [116]

Figure 12: High speed photos of cellulose and hardwood lignin on the heated surface.

Hemicellulose degradation is known to occur over a relatively broad range of temperatures, and it forms more char than cellulose [113]. Sharma et al. [112] observed that at 350°C under the slow heating molten clusters of pectin char were formed with vesicles. Dauenhauer et al. [116] observed the formation of an intermediate liquid with bursting bubbles under the fast heating using high speed photography experimental setup as shown in Figure 12(b). Lignin tends to be less volatile than cellulose and hemicellulose, leading to the formation of higher char yields [118]. Moreover, the inorganic matter, that resides as minerals in coal, may influence the pyrolysis behavior in a different way than in the case of biomass, where potassium and calcium play a role as active catalysts that may additionally affect the metaplast formation [70, 119, 120]. However, it is not well known to what extent the formation of a metaplast depends on the presence of alkali, and how this influence is changed with a heating rate.

2.6.2 Soot morphology

Soot structure and composition have a strong impact on its reactivity. Properties such as particle size, crystallinity, nanostructure affect the reactivity of soot particles [121, 122]. Soot nanostructure depends on the conditions of its formation (temperature, residence time, fuel type, etc). The term nanostructure is used to characterize the graphene layer plane dimensions, their tortuosity and relative orientation [123, 124]. Variations in these properties may affect the soot sample reactivity among other properties. Moreover, the differences in primary particle size from 30 to 300 nm and incorporation of inorganic matter with soot particles may significantly influence its reactivity in combustion and gasification [125, 126]. Little is known about soot formation and properties of soot obtained from the pyrolysis of solid fuels. The literature results are mainly addressed to characteristics of soot generated by combustion or in pyrolysis of liquid or gaseous hydrocarbons.

Ruiz et al. [121] investigated the effect of heat treatment temperature in the formation and

yield of soot from acetylene pyrolysis in a temperature range of 1000 and 1200°C, and observed that the reactivity of soot samples is related to the formation temperature and its nanostructure. Figure 13 shows that soot obtained at 1400°C has a more ordered structure than soot prepared at 1000°C, which suggests that a higher temperature during soot formation leads to a higher structure ordering of soot particles. The size distribution of the soot prepared in fast pyrolysis in a temperature range of 1000-1400°C varied broadly from several nanometers to several hundreds of nanometers [19]. No significant difference with respect to soot nanostructure was observed between soot samples obtained at different temperatures. Septien et al. [126] observed that the soot samples formed from the 0.35 mm and 0.8 mm beechwood particles have a similar composition with regard to carbon and hydrogen. Vander Wal et al. [123, 124] concluded that the structural variations in the graphene layer place dimensions affect the soot reactivity. The large interlayer distances and strongly curved graphene sheets may lead to higher soot reactivity in oxidation. High temperatures lead to lower reactivity.

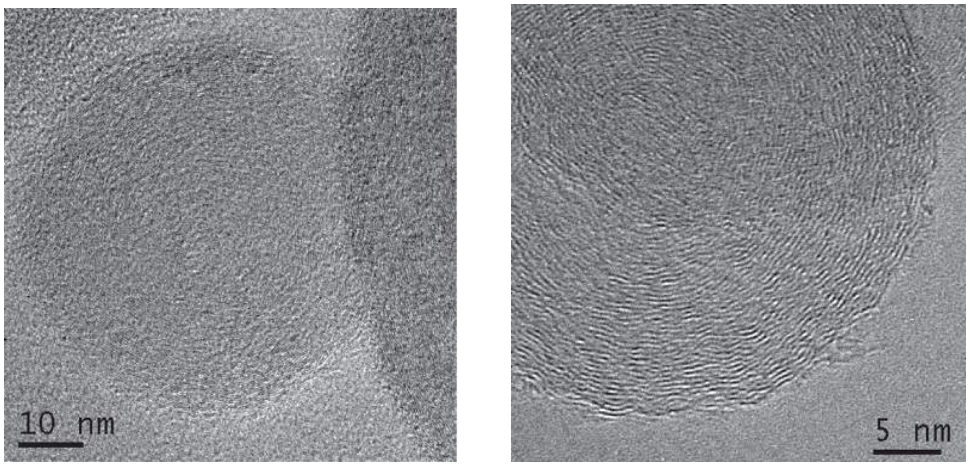

13(a): Soot formed at 1000°C [126]

13(b): Soot formed at 1400°C [126]

Figure 13: HTEM images of beechwood soot generated at 1000 and 1400°C in the entrained-flow reactor under pyrolysis conditions [126].

Wiinikka et al. [125] investigated the influence of pressurized gasification conditions on the soot morphology when using stem wood as a fuel. Based on analysis of the collected particles with HRTEM/EDS techniques two types of soot particles were formed during gasification of the low ash-containing stem wood. Fine soot particles obtained a primary particle size between 30 and 50 nm and large soot particles were between 100 and 300 nm. The presence of large primary soot particles has not been extensively discussed in the literature. Chen et al. [127] identified soot particles of a larger size ($>$ 100 nm) in the pulverized coal combustion, and related their nanostructure to commercially available pristine carbon nano-spheres. The nanostructure of fine and large soot particles is similar, yet with small differences in its ordering. The larger soot particles obtained a less ordered graphitic structure than the smaller spherules as shown in Figure 14.

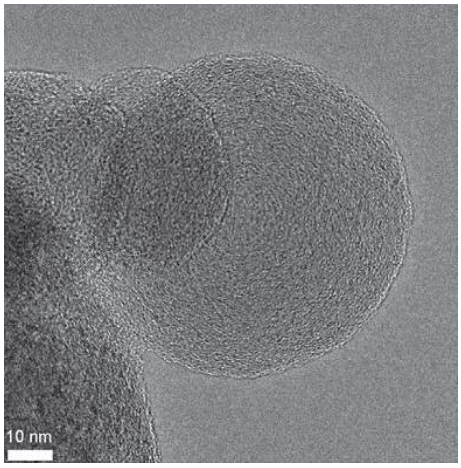

14(a): Fine soot particles [125]

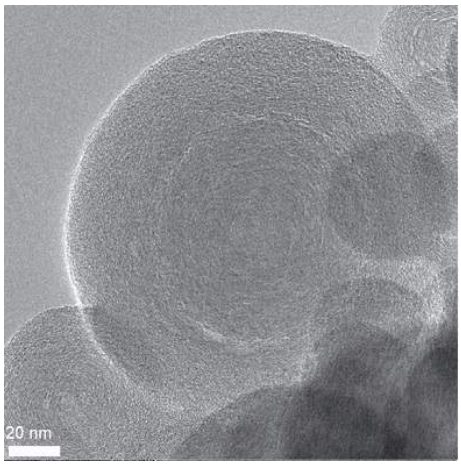

14(b): Large soot particles [125]

Figure 14: HTEM images of stem wood soot generated in a temperature range of 1200 and 1500°C during pressurized entrained-flow gasification.

Moreover, in addition to carbon, traces of volatile ash forming elements (K, S, Cl and Zn) and traces of refractory elements (Si, Ca, Mg and Fe) were detected in the soot particles. They concluded that smaller particle sizes in the particle mass size distribution obtain a higher concentration of ash forming elements compared to larger particle sizes.

2.7 Biomass reactivity

2.7.1 Char reactivity

Similar to coals, the efficient and stable operation of power plants is known to be influenced by the reactivity of chars obtained by devolatilization. Char oxidation and gasification is slower than devolatilization and is the rate liming step in the overall process. Char reactivity is affected by its morphology, annealing of the organic matter and alkali. There are no investigations, suggesting a relation between the combustion or gasification rate of chars originated from biomass and the main plant cell wall components (cellulose, hemicellulose, lignin) [82].

As it is known that wood char is more reactive to oxygen than coal char, which contains lower oxygen and higher hydrogen levels. Wornat et al. [106] showed using high-resolution micrographs that the bituminous coal char obtained a higher degree of structural order than the wood chars, which contained a higher proportion of edge carbons, resulting in a higher char reactivity. The pyrolysis conditions and composition and properties of the biomass influence the char reactivity. High char reactivity is favored when the volatiles are rapidly removed from the fuel particle, facilitated under the fast heating and smaller particle sizes. Under slow heating, volatile products are released through the natural porosity of a fuel particle [128], while at fast heating rates the original biomass structure is lost due to the particle softening and melting, leading under internal overpressure to formation of the micropores and larger internal cavities [37]. For both coal and biomass the impacts of pyrolysis operating conditions on the char reactivity have been studied by

many researchers [35, 38, 110, 111, 129, 130].

Janse et al. [130] investigated the effect of heat treatment temperature, heating rate and devolatilization time on the pinewood, and reported that wood chars generated by flash pyrolysis (500-600°C; 1-300 K s^{-1}; 20-100 s) are significantly more reactive than lower heating rates chars, probably due to a relatively high H/C ratio of the wood chars prepared in flash pyrolysis. The reactivity of char increases when the residence time decreases due to the reduced secondary reactions [38]. At lower heating rates, the prolongated reaction time between tars and char decreases its reactivity. Moreover, Zanzi [38] suggested that the secondary char produced from reactions between the primary char and tars encapsulates the ash, and may eliminate the catalytic effect of alkali on the char reactivity.

Mermoud et al. [119] observed that the steam gasification reactivity of chars generated at high heating rates was affected stronger by the char ash content (mainly K and Ca) than by the pyrolysis time. They suggested that the beechwood char was more reactive than pinewood char due to the higher K content compared to the pinewood. Wornat et al. [106] believed that well-dispersed distributions of alkali (Na, Ca and K) in the biomass improve their catalytic activities in combustion. Pottmaier et al. [109] reported that the high Si content in rice husk may affect the char reactivity at both low and high heating rates, leading to the reactivity decrease in oxidation and gasification compared to that of wheat straw char. The heating rate and inorganic matter content turned out as predominating parameters influencing the char reactivity. Branca et al. [131] investigated the oxidation kinetics of several wood chars, and concluded that the heat treatment temperature and heating rate influence the char reactivity stronger than the organic compositional differences among the wood species.

Zolin [132] observed that the char reactivity decreases as the heat treatment temperature increases. At higher temperatures the carbon matrix of a char is more ordered approaching the graphitic structure and thereby loses its active sites. The compositional differences among biomass species may also influence the char reactivity and graphitization [133, 134]. FTIR spectra and elemental ratios suggest that the decomposition of herbaceous biomass occurs at slightly lower temperatures than that of wood [134]. Generally, decomposition of hemicellulose and cellulose in biomass occurs at low temperatures (between 230 and 400°C), while lignin decomposes over a broader temperature range (160-900°C) [55]. This suggests that the required activation energy for grass decomposition is lower, probably due to higher contents of thermally labile hemicelluloses, than for the more complex structure of wood. Therefore, the relative quantities of biopolymers in the original biomass determine the conditions under which biomass is transformed to chars with a different degree of cross-linking. The structure of carbon can be differentiated into graphitizing and non-graphitizing classes [135]. Oberlin [136] and Kurasaki et al. [137] related the properties of the wood char to the non-graphitizing carbon, which may obtain less cross-linking in pyrolysis than herbaceous biomass. The cross-linking is preserved during heating to the high temperatures, and keeps neighboring crystallites apart with a random orientation as shown in Figure 15.

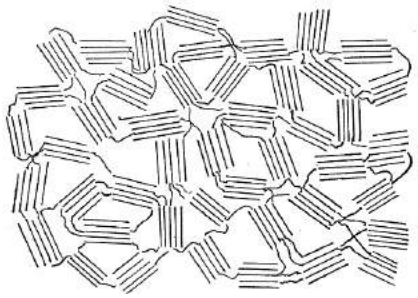

Figure 15: Schematic representation of non-graphitzing carbon structure [135].

The cross-linking hinders the coalescence of crystallites, leading to graphitization. In biochars a cross-linking is influenced by the high fraction of oxygen that immobilize the layer-planes and hinder crystallite growth. The crystallite growth in the herbaceous biomass is hindered by a stronger cross-linking, leading to a less graphitized structure due to a higher oxygen content remaining in the char [135].

Septien et al. [126] investigated the influence of heat treatment temperature (1000-1400°C), residence time (2-4 s) and particle size with mean diameters of 0.35 mm and 0.8 mm in an entrained flow reactor. They concluded that the heat treatment temperature and residence time have a more pronounced effect on the char reactivity in gasification due to the char annealing. The particle size had nearly negligible influence on the beechwood char reactivity.

2.7.2 Soot reactivity

The morphology of primary soot particles including their size and shape, internal structure, surface functionality (nanostructure) influences soot oxidative / gasification behavior significantly [122, 138, 139]. A higher proportion of larger primary soot particles, more graphitic structure, shorter graphene layers, formation of multi-core particles may decrease the soot reactivity, whereas a transformation of graphene lamellae from curved to flat lowers its reactivity [122]. Little is known about the influence of biomass soot nanostructure on its reactivity obtained by fast pyrolysis at temperatures > 1000°C.

The biomass char is more reactive than soot both at oxidation and gasification conditions due to a less ordered structure of carbon in the char compared to the soot. The oxidation reaction of char obtained at 1000°C in an entrained flow reactor and oxidized in 10-20 % volume fraction O_2 at 5-10 K min^{-1} in a TG instrument reaches a maximum rate at $\approx$400°C, which is lower than for soot as Qin et al. [140] observed. Char gasification in 10-90 % volume fraction CO_2 reaches a maximum rate at 760-780°C, while the maximum rate of soot gasification shifted to higher temperatures between 820 and 880°C. Septien et al.[19] and Qin et al. [140] observed that the soot produced at a lower temperature (1000°C) is less reactive than soot generated at 1400°C in opposite to results of Abian et al. [141], indicating a dominating role of inorganic matter and the soot generation process on its reactivity. Septien et al. [126] concluded the ordered structure

of soot does not necessarily decrease the soot reactivity. They suggested that the soot reactivity in gasification may be influenced by the mineral content composed mainly of potassium. Qin et al. [140] related the increasing soot reactivity with higher temperature to a high content of KCl and K_2SO_4 deposited on its surface.

2.7.3 Comparison of low and high temperature kinetics

At high-temperatures, thermogravimetric (TG) analysis has severe limitations in establishing oxidation and gasification kinetics in the temperature range where the reaction rate is high. These limitations are related to the mass transfer control because the residence time for the char conversion is less or in the same order of magnitude as the time required to supply the reactant gas to the sample. The literature on biomass char reactivity at high temperatures is not extensive. The entrained flow [142] or a drop tube reactor [143] are typically used to investigate the reaction of coal char gasification with carbon dioxide or steam. However, solid fuel sampling is usually problematic for high-temperature reactions, especially at a high degree of wood char conversion, where it is difficult to collect all generated solid particles for analysis [144]. Moreover, the complexity of the gasification reactions creates additional difficulties to obtain the solid carbon conversion separately from the overall carbon balance. The aerosol-based method characterizes the conversion of suspended char particles (0.5-10 μm) by on-line measuring the aerodynamic diameter of the particles [145].

Lin et al. [146] compared the validity of low-temperature kinetics obtained using TG instrument with the kinetic parameters provided by the aerosol method in a temperature range of 1100 and 1300°C and fitted by the random pore model (RPM) to the experimental data. Their results showed that the reactivity estimation by extrapolation of the low TG temperature kinetic data to higher temperatures in gasification should be carefully applied. Woody and herbaceous chars showed a similar reactivity in a low temperature range, whereas at higher temperatures in a pre-heated tubular reactor the differences in reactivity of wood and herbaceous biomass using aerosol-based method were more obvious.

More comprehensive investigations are needed to highlight the validity of low-temperature kinetics obtained by the thermogravimetric analysis to the higher temperatures. The kinetic contribution is taken into account by all reactivity models. The accuracy of kinetic data extrapolation obtained from low to higher temperatures may significantly affect the model parameters and numerical estimations.

2.8 Current state of knowledge

The literature provides information for wood in relation to both devolatilization product yields and composition of products whereas considerable less work has been carried out with respect to herbaceous fuels. The majority of investigations on the fuel potential of agricultural waste is focussed on chars, pyrolyzed under the slow heating rate (1-50 K min^{-1}) and long hold-

ing time (1-4 h). The effects of heating rate and temperature on the morphological transformations at both slow ($< 10\,\mathrm{K\ s^{-1}}$) and intermediate and fast pyrolysis environments ($> 100\,\mathrm{K\ s^{-1}}$) of wood and herbaceous biomass have rarely been studied. The larger biomass char particles of size up to 1.5 mm typically used in suspension fired biomass boilers have not been characterized with respect to their size, shape and structural transformations. However, the effect of particle size from 0.5 mm to 1.5 mm on the char morphology, reactivity and product yields is important for the flame stability and burnout at power plants.

More research on different biomass types is required to fill a gap about the effect of biomass origin type on the soot yield and the formation during fast pyrolysis. The influence of biomass soot nanostructure and inorganic compounds (K, Cl, S) on the reactivity of soot from fast pyrolysis at temperatures $> 1000^{\circ}$C has been investigated only by a few authors. Little is known about the influence of temperature, heating rate, particle size, residence time, inorganic matter and major organic components on biomass char yield and morphology. The information about structural biomass char transformations, particularly char fluidity, may be obtained from the equivalent work on low-rank coals. However, the situation with biomass structural changes is complicated by the fact that it contains three distinctly different building blocks, i.e. cellulose, hemicellulose and lignin, which can influence the char particle morphology and thereby the char reactivity.

Many kinetic models have been proposed to describe biomass devolatilization. These kinetic models were based on experiments performed at low temperatures and low heating rates. The empirical models cannot cover the various mechanisms involved in biomass devolatilization, and are applicable only to the particular samples and limited temperature ranges. A relatively simple model is desired to estimate with sufficient accuracy both the reaction rate and solid residue yields. The catalytic effect of alkali has not been included in the existing biomass devolatilization models, which is of primary importance for the accurate description of biomass devolatilization.

References

[1] Alen R. *Chapter 1. Structure and chemical composition of wood. In: P Stenius (ed.), Forest Products Chemistry*. Papermaking Sci Tech, 2000.

[2] Lumiainen J. *Refining of chemical pulp. In: H Paulapuro (ed.), Papermaking Part 1, Stock Preparation and Wet End*. Papermaking Sci Tech, 2000.

[3] Thomas RJ. *Wood: Structure and Chemical Composition. Chapter I. Wood: Structure and Chemical Composition*. ACS Symposium Series, 1977.

[4] Demirbas A. *Biohydrogen*. Springer, 2009.

[5] Grønli MG. A Theoretical and Experimental Study of the Thermal Degradation of Biomass. PhD thesis, Norwegian University of Science and Technology, 1996.

[6] Pearce RB and Holloway PJ. Suberin in the sapwood of oak (Quercus robur L.): its composition from a compartmentalization barrier and its occurrence in tyloses in undecayed wood. *Physiol Plant Path*, 24(1):71–81, 1984.

[7] Pouzoulet J, Pivovaroff AL, Santiego LS, and Rolshausen PE. Can vessel dimension explain tolerance toward fungal vascular wilt diseases in woody plants? Lessons from Dutch elm disease and esca disease in grapevine. *Front Plant Sci*, 253(5):1–11, 2014.

[8] Harper SHT and Lynch JM. The Chemical Components and Decomposition of Wheat Straw Leaves, Intermodes and Nodes. *J Sci Food Agric*, 32(11):1057–62, 1981.

[9] Solomon PR, Hamblen DG, Serio MA, Yu ZZ, and Charpenay S. A characterization method and model for predicting coal conversion behaviour. *Fuel*, 72(4):469–88, 1993.

[10] Bassilakis R, Carangelo RM, and Wojtowicz MA. TG-FTIR analysis of biomass pyrolysis. *Fuel*, 80(12):1765–86, 2001.

[11] Fengel D, Przyklenk M, and Wegener G. Hydrolysis von Polysacchariden mit Trifluoressigsäure. *Das Papier*, 30(6):240–3, 1976.

[12] Adler DC and Buehler MJ. Mesoscale mechanics of wood cell walls under axial strain. *Soft Matter*, 9:7138–44, 2013.

[13] Zeng Y, Zhao S, Yang S, and Ding SY. Lignin plays a negative role in the biochemical process for producing lignocellulosic biofuels. *Curr Opinion Biotech*, 27:38–45, 2014.

[14] Sun S, Tian H, Zhao Y, Sun R, and Zhou H. Experimental and numerical study of biomass flash pyrolysis in an entrained flow reactor. *Bioresour Technol*, 101(10):3678–84, 2010.

[15] Thammasouk K, Tandjo D, and Penner MH. Influence of Extractives on the Analysis of Herbaceous Biomass. *J Agric Food Chem*, 45(2):437–43, 1997.

[16] Ross K, Leung A, Godfrey D, and Mazza G. Evaluation of Thermal Decomposition and Antioxidant Activity of Crop Residues and Ionic Liquid Extracted Lignin. *World Appl Sci J*, 16(2):160–78, 2012.

[17] Klass D. *Biomass for Renewable Energy, Fuels, and Chemicals*. Academic Press, 1998.

[18] Dall'Ora M, Jensen PA, and Jensen AD. Suspension combustion of wood: Influence of pyrolysis conditions on char yield, morphology, and reactivity. *Energy Fuels*, 22(5):2955–62, 2008.

[19] Septien Stringel S. High temperature gasification of millimetric wood particles between 800°C and 1400°C. PhD thesis, Institut National Polytechnique de Toulouse, 2011.

[20] Sander B. Properties of Danish biofuels and the requirements for power production. *Biomass Bioenergy*, 12(3):177–83, 1997.

[21] Ross AB, Jones JM, Kunacki ML, and Bridgeman T. Classification of macroalgae as fuel and its thermochemical behaviour. *Bioresour Technol*, 99(14):6494–504, 2008.

[22] Wu H, Glarborg P, Frandsen FJ, Dam-Johansen K, Jensen PA, and Sander B. Co-combustion of pulverized coal and solid recovered fuel in an entrained flow reactor - General combustion and ash behaviour. *Fuel*, 90(5):1980–91, 2011.

[23] Gucho EM, Shahzad K, Bramer EA, Akhtar NA, and Brem G. Experimental Study on Dry Torrefaction of Beech Wood and Miscanthus. *Energies*, 8(5):3903–23, 2015.

[24] Antal M, Michael J, Mok WSL, Varhegyi G, and Szekely T. Review of methods for improving the yield. *Energy Fuels*, 4(3):221–5, 1990.

[25] Antal M, Croiset E, Dai XY, DeAlmeida C, Mok WSL, and Norberg N. High-yield biomass charcoal. *Energy Fuels*, 10(3):652–8, 1996.

[26] Demirbas A. Effects of temperature and particle size on bio-char yield from pyrolysis of agricultural residues. *J Anal Appl Pyrolysis*, 72(2):243–8, 2004.

[27] Solomon PR, Serio MA, and Suuberg EM. Coal pyrolysis: experiments, kinetic rates and mechanisms. *Prog Energy Combust Sci*, 18(2):133–220, 1992.

[28] Migliavacca G, Parodi E, Bondanti L, Pierucci S, and Ranzi E. A general mathematical model of solid fuels pyrolysis. *Energy*, 30(8):1453–68, 2005.

[29] Zhao Y, Serio MA, and Solomon PR. A general model for devolatilization of large coal particles. *Symp Int Combust*, 26(2):3145–51, 1996.

[30] Li J, Bonvicini G, Tognotti L, Yang W, and Blasiak W. High-temperature rapid devolatilization of biomasses with varying degrees of torrefaction. *Fuel*, 122:261–9, 2014.

[31] Li J, Bonvicini G, Biagini E, Yang W, and Tognotti L. Characterization of high-temperature rapid char oxidation of raw and torrefied biomass fuels. *Fuel*, 143:492–8, 2015.

[32] Fletcher TH and Kerstein AR. Chemical Percolation Model for Devolatilization. 2. Temperature and Heating Rate Effects on Product Yields. *Energy Fuels*, 4(1):54–60, 1990.

[33] Niksa S, Heid LE, Rusel WB, and Saville DA. On the role of heating rate in rapid coal devolatilization. *Symp Int Combust*, 20(1):1445–53, 1984.

[34] Solomon PR, Hamblen DG, Carangelo RM, Serio MA, and Deshpande GV. General Model of Coal Devolatilization. *Biomass Bioenergy*, 2(4):405–22, 1988.

[35] Guerrero M, Ruiz MP, Alzueta MU, Bilbao R, and Millera A. Pyrolysis of eucalyptus at different heating rates: studies of char characterization and oxidative reactivity. *J Anal Appl Pyrolysis*, 74(1-2):307–14, 2005.

[36] Cetin E, Moghtaderi B, Gupta R, and Wall TF. Influence of pyrolysis conditions on the structure and gasification reactivity of biomass chars. *Fuel*, 83(16):2139–50, 2004.

[37] Biagini E, Simone M, and Tognotti L. Characterization of high heating rate chars of biomass fuels. *Proc Combust Inst*, 32(2):2043–50, 2009.

[38] Zanzi R. Pyrolysis of biomass. PhD thesis, Royal Institute of Technology, 2001.

[39] Lu K, Ip E, Scott J, Foster P, Vickers M, and Baxter LL. Effects of particle shape and size on devolatilization of biomass particle. *Fuel*, 89(5):1156–68, 2010.

[40] Zanzi R, Sjöström K, and Björnbom E. Rapid high-temperature pyrolysis in a free-fall reactor. *Fuel*, 75(5):545–50, 1996.

[41] Wei L, Xu S, Zhang L, Zhang H, Liu C, and Zhu H. Characteristics of fast pyrolysis of biomass in a free fall reactor. *Fuel Process Technol*, 87(10):863–71, 2006.

[42] Dupont C, Commandre JM, Gauthier P, Boissonnet G, Salvador S, and Schweich D. Biomass pyrolysis experiments in an analytical entrained flow reactor between 1073 K and 1273 K. *Fuel*, 87(7):1155–64, 2008.

[43] Chen L, Dupont C, Salvador S, Grateau M, Boissonnet G, and Schweich D. Experimental study on fast pyrolysis of free-falling millimetric particles between 800°C and 1000°C. *Fuel*, 106:61–6, 2013.

[44] Bitowft B, Andersson LA, and Bjerle I. Fast pyrolysis of sawdust in an entrained flow reactor. *Fuel*, 68(5):561–6, 1989.

[45] Zanzi R, Sjöström K, and Björnbom E. Rapid pyrolysis of agricultural residues at high temperature. *Biomass Bioenergy*, 23(5):357–66, 2002.

[46] Miller RS and Bellan J. Tar Yield and Collection from the Pyrolysis of Large Biomass Particles. *Combust Sci Tech*, 127(1-6):97–118, 1997.

[47] Momeni M. Fundamental Study of Single Biomass Particle Combustion. PhD thesis, Aalborg University, 2012.

[48] Nørskov LK. Combustion of solid alternative fuels in the cement kiln burner. PhD thesis, Technical University of Denmark, 2012.

[49] Pandey A. *Handbook of plant-based biofuels*. CRC Press, 2009.

[50] Bradbury AGW, Sakai Y, and Shafizadeh F. A kinetic model for pyrolysis of cellulose. *J Appl Pol Sci*, 23(11):3271–80, 1979.

[51] Antal MJ and Varhegyi G. Cellulose pyrolysis kinetics: the current state of knowledge. *Ind Eng Chem Research*, 34(3):703–17, 1995.

[52] Shafizadeh F and Bradbury AGW. Thermal Degradation of Cellulose in Air and Nitrogen at Low Temperatures. *J Appl Pol Sci*, 23(5):1431–42, 1979.

[53] Soltes E and Elder T. *Pyrolysis. In: IS Goldstein (ed.), Organic Chemicals from Biomass*. CRC Press, 1981.

[54] Lu GJ, Wu SB, and Lou R. Characteristics of corn stalk hemicellulose pyrolysis in a tubular reactor. *BioResources*, 5(4):2051–62, 2010.

[55] Yang H, Yan R, Chen H, Lee DH, and Zheng C. Characteristics of hemicellulose, cellulose and lignin pyrolysis. *Fuel*, 86(12-13):1781–8, 2007.

[56] Rodrigues J, Graca J, and Pereira H. Influence of tree eccentric growth on syringyl/guaiacyl ratio in Eucalyptus globulus wood lignin assessed by analytical pyrolysis. *J Anal Appl Pyrolysis*, 58-59:481–9, 2001.

[57] Worasuwannarak N, Sonobe T, and Tanthapanichakoon W. Pyrolysis behaviors of rice straw, rice husk, and corncob by TG-MS technique. *J Anal Appl Pyrolysis*, 78(2):265–71, 2007.

[58] Hosoya T, Kawamoto H, and Saka S. Cellulose-hemicellulose and cellulose-lignin interactions in wood pyrolysis at gasification temperature. *J Anal Appl Pyrolysis*, 80(1):118–25, 2007.

[59] Demirbas A. Effect of lignin content on aqueous liquefaction products of biomass. *Energy Conv Manage*, 41:1601–7, 2000.

[60] Giudicianni P, Cardone G, and Ragucci R. Cellulose, hemicellulose and lignin slow steam pyrolysis: Thermal decomposition of biomass components mixture. *J Anal Appl Pyrolysis*, 100:213–22, 2013.

[61] Avni E, Coughlin RW, Solomon PR, and King HH. Mathematical modelling of lignin pyrolysis. *Fuel*, 64(11):1495–501, 1985.

[62] Raveedran K, Ganesh A, and Khilart KC. Influence of mineral matter on biomass pyrolysis characteristics. *Fuel*, 74(12):1812–22, 1995.

[63] Di Blasi C, Branca C, and Derrico G. Degradation characteristics of straw and washed straw. *Thermochimica Acta*, 364(1-2):133–42, 2000.

[64] Jensen AD, Dam-Johansen K, Wojtowicz MA, and Serio MA. TG-FTIR Study of the Influence of Potassium Chloride on Wheat Straw Pyrolysis. *Energy Fuels*, 12(5):929–38, 1998.

[65] Wang Z, Wang F, Cao J, and Wang J. Pyrolysis of pine wood in a slowly heating fixed-bed reactor: Potassium carbonate versus calcium hydroxide as a catalyst. *Fuel Process Technol*, 91(8):942–50, 2010.

[66] Reichel D, Klinger M, Krzack S, and Meyer B. Effect of ash components on devolatilization behaviour of coal in comparison with biomass - Product yields, composition, and heating values. *Fuel*, 114:64–70, 2013.

[67] DeGroot WF and Shafizadeh F. Kinetics of gasification of Douglas Fir and Cottonwood chars by carbon dioxide. *Fuel*, 63(2):210–6, 1984.

[68] DeGroot WF and Shafizadeh F. The influence of exchangeable cations on the carbonization of biomass. *J Anal Appl Pyrolysis*, 6(3):217–32, 1984.

[69] Nik-Azar M, Hajaligol MR, Sohrabi M, and Dabir B. Mineral matter effects in rapid pyrolysis of beechwood. *Fuel Process Technol*, 51(1-2):7–17, 1997.

[70] Niksa S. Predicting the rapid devolatilization of diverse forms of biomass with bio-Flashchain. *Proc Combust Inst*, 28(2):2727–33, 2000.

[71] Dall'Ora M. Reactivity and burnout of wood fuels. PhD thesis, Technical University of Denmark, 2011.

[72] Link S, Arvelakis S, Hupa M, Yrjas P, Külaots I, and Paist A. Reactivity of the Biomass Chars Originating from Reed, Douglas Fir, and Pine. *Energy Fuels*, 24(12):6533–9, 2010.

[73] Zevenhoven-Onderwater M, Backman R, Skrifvars BJ, and Hupa M. The ash chemistry in fluidised bed gasification of biomass fuels. Part I: predicting the chemistry of melting ashes and ash-bed material interaction. *Fuel*, 80(10):1489–502, 2001.

[74] Di Blasi C. Modeling and Simulation of Combustion Processes of Charring and Non-Charring Solid Fuels. *Prog Energy Combust Sci*, 19(1):71–104, 1993.

[75] Tran DQ and Rai C. Pyrolytic Gasification of Bark. *AIChE*, 75(184):41–9, 1979.

[76] Roberts AF. A Review of Kinetic Data for the Pyrolysis of Wood and Related Substances. *Combust Flame*, 14(2):261–72, 1970.

[77] Thurner F and Mann U. Kinetic Investigation of Wood Pyrolysis. *Ind Eng Chem Process Des Dev*, 20(3):482–8, 1981.

[78] Jegers HF and Klein MT. Primary and Secondary Lignin Pyrolysis Reaction Pathways. *Ind Eng Chem Process Des Dev*, 24(1):173–83, 1985.

[79] Shafizadeh F. Introduction to Pyrolysis of Biomass. *J Anal Appl Pyrolysis*, 3(4):283–305, 1982.

[80] Sheng C and Azevedo JLT. Modeling biomass devolatilization using the chemical percolation devolatilization model for the main components. *Proc Combust Inst*, 29(1):407–14, 2002.

[81] Elfasakhany A, Klason T, and Bai XS. Modelling of pulverized wood combustion using a functional group model. *Combust Theory Modelling*, 12(5):883–904, 2008.

[82] Di Blasi C. Combustion and gasification rates of lignocellulosic chars. *Prog Energy Combust Sci*, 35(2):121–40, 2009.

[83] Stenseng M. Pyrolysis and Combustion of Biomass. PhD thesis, Technical University of Denmark, 2001.

[84] Solomon PR, Best PE, Yu ZZ, and Charpenay S. An empirical-model for coal fluidity based on a macromolecular network pyrolysis model. *Energy Fuels*, 6(2):143–54, 1992.

[85] Di Blasi C. Modeling chemical and physical processes of wood and biomass pyrolysis. *Prog Energy Combust Sci*, 34(1):47–90, 2008.

[86] Di Blasi C. Comparison of semi-global mechanisms for primary pyrolysis of lignocellulosic fuels. *J Anal Appl Pyrolysis*, 47(1):43–64, 1998.

[87] Chan WR, Kelbon M, and Krieger BB. Modelling and experimental verification of physical and chemical processes during pyrolysis of a large biomass particle. *Fuel*, 64(11):1505–13, 1985.

[88] Nunn TR, Howard JB, Longwell JP, and Peters WA. Product composition and kinetics in the rapid pyrolysis of sweet gum hardwood. *Ind Eng Chem Process Des Dev*, 24(3):836–44, 1985.

[89] Hajaligol MR, Howard JB, Longwell JP, and Peters WA. Product composition and kinetics for rapid pyrolysis of cellulose. *Ind Eng Chem Process Des Dev*, 21(3):457–65, 1982.

[90] Liden AG, Berruti F, and Scott DS. A kinetic model for the production of liquids from the flash pyrolysis of biomass. *Chem Eng Comm*, 65(1):207–21, 1988.

[91] Koufopanos CA, Maschio G, and Lucchesi A. Kinetic Modelling of the Pyrolysis of Biomass and Biomass Components. *Can J Chem Ing*, 67(1):75–84, 1989.

[92] Umeki K, Kirtania K, Chen L, and Bhattacharya S. Fuel Particle Conversion of Pulverized Biomass during Pyrolysis in an Entrained Flow Reactor. *Ind Eng Chem Res*, 51(43):13973–9, 2012.

[93] Gavalas GR. *Coal pyrolysis: Coal science and technology*. Elsevier, 1982.

[94] Niksa S and Kerstein AR. Flashchain Theory for Coal Devolatilization Kinetics. 1 Formulation. *Energy Fuels*, 5(5):647–65, 1991.

[95] Fletcher TH, Kerstein AR, Pugmire RJ, Solum MS, and Grant DM. Chemical Percolation Model for Devolatilization: 3. Direct Use of 13-C NMR Data to Predict Effects of Coal Type. *Energy Fuels*, 6(4):414–31, 1992.

[96] Grant DM, Pugmire RJ, Fletcher TH, and Kerstein AR. A Chemical Model of Coal Devolatilization Using Percolation Lattice Statistics. *Energy Fuels*, 3(2):175–86, 1992.

[97] Fletcher TH, Kerstein AR, Pugmire RJ, and Grant DM. A chemical percolation model for devolatilization. 2. Temperature and heating rate effects. *Abst Papers Am Chem Soc*, 198:79–81, 1989.

[98] Fletcher TH, Pond HR, Webster J, Wooters J, and Baxter LL. Prediction of Tar and Light Gas during Pyrolysis of Black Liquor and Biomass. *Energy Fuels*, 26(6):3381–7, 2012.

[99] Serio MA, Charpenay S, Bassilakis R, and Solomon PR. Measurement and modeling of lignin pyrolysis. *Biomass Bioenergy*, 7(1-6):107–24, 1994.

[100] Serio MA, Wojtowicz MA, Chen Y, Charpenay S, Jensen A, and Bassilakis R et al. A Comprehensive Model of Biomass Pyrolysis. US: East Hartford, Advanced Fuel Research Inc.; Report No. Contract 96-33610-2675.

[101] Chen Y, Charpenay S, Jensen A, Wojtowicz MA, and Serio MA. Modeling biomass pyrolysis in combustion. *Proc Combust Inst*, 27:1327–34, 1998.

[102] Biagini E, Falcitelli M, and Tognotti L. A structural model for biomass devolatilization. *Proc* 18^{th} *EUBCE*, pages 923–30, 2010.

[103] Biagini E and Tognotti L. A Generalized Procedure for the Devolatilization of Biomass Fuels Based on the Chemical Components. *Energy Fuels*, 28(1):614–23, 2014.

[104] De Jong W, Di Nola G, Venneker BCH, Spliethoff H, and Wojtowicz MA. TG-FTIR pyrolysis of coal and secondary biomass fuels: Determination of pyrolysis kinetic parameters for main species and NO_x precursors. *Fuel*, 86(15):2367–76, 2007.

[105] Zygourakis K. Effect of Pyrolysis Conditions on the Macropore Structure of Coal-Derived Chars. *Energy Fuels*, 7(1):33–41, 1993.

[106] Wornat MJ, Hurt RH, Yang NYC, and Headley TJ. Structural and compositional transformations of biomass chars during combustion. *Combust Flame*, 100(1-2):131–43, 1995.

[107] Agafonov GL, Vlasov P, and Smirnov VN. Soot Formation in the Pyrolysis of Benzene, Methylbenzene, and Ethylbenzene in Shock Waves. *Kinet Catal*, 52(3):358–70, 2011.

[108] Ranzi E, Frassoldati A, Grana R, Cuoci A, Faravelli T, and Kelley AP. Hierachical and Comparative Kinetic Modeling of Laminar Flame Speeds of Hydrocarbon and Oxygenated Fuels. *Prog Energy Combust Sci*, 38(4):468–501, 2012.

[109] Pottmaier D, Costa M, Farrow T, Oliveira AAM, Alarcon O, and Snape C. Comparison of Rice Husk and Wheat Straw: From Slow and Fast Pyrolysis to Char Combustion. *Energy Fuels*, 27(11):7115–25, 2013.

[110] Zolin A, Jensen AD, Jensen PA, Fradsen F, and Dam-Johansen K. The Influence of Inorganic Materials on the Thermal Deactivation of Fuel Chars. *Energy Fuels*, 15(5):1110–22, 2001.

[111] Cetin E, Moghtaderi B, Gupta R, and Wall TF. Biomass gasification kinetics: influences of pressure and char structure. *Combust Sci Tech*, 177(4):765–91, 2005.

[112] Sharma RK, Wooten JB, Baliga VL, and Hajaligol MR. Characterization of chars from biomass-derived materials: pectin chars. *Fuel*, 80(12):1825–36, 2001.

[113] Sharma RK, Wooten JB, Baliga VL, Lin X, Chan WG, and Hajaligol MR. Characterisation of chars from pyrolysis of lignin. *Fuel*, 83(11-12):1469–82, 2004.

[114] Lede J, Li HZ, and Villermaux J. Fusion-Like Behaviour of Wood Pyrolysis. *J Anal Appl Pyrolysis*, 10(4):291–308, 1987.

[115] Dauenhauer PJ, Colby JL, Balonek CM, Suszynski WJ, and Schmidt LD. Reactive boiling of cellulose for integrated catalysis through an intermediate liquid. *Green Chem*, 11(10):1555–61, 2009.

[116] Teixeira AR, Mooney KG, Kruger JS, Williams CL, Suszynski WJ, and Dauenhauer PJ et al. Aerosol generation by reactive boiling ejection of molten cellulose. *Energy Environ Sci*, 4(10):4306–21, 2011.

[117] Lede J. Cellulose pyrolysis kinetics: An historical review on the existence and role of intermediate active cellulose. *J Anal Appl Pyrolysis*, 94:17–32, 2012.

[118] Orfao JJM, Antunes FJA, and Figueiredo JL. Pyrolysis kinetics of lignocellulosic materials - three independent reactions model. *Fuel*, 78(3):349–58, 1999.

[119] Mermoud F, Salvador S, van de Steene L, and Glofier F. Influence of the pyrolysis heating rate on the steam gasification rate of large wood char particles. *Fuel*, 85(10-11):1473–82, 2006.

[120] Jones JM, Darwell LI, Bridgeman TG, Pourkashanian M, and Williams A. An investigation of thermal and catalytic behaviour of potassium in biomass combustion. *Proc Combust Inst*, 31(2):1955–63, 2007.

[121] Ruiz MP, Guzman de Villoria R, Millera A, Alzueta MU, and Bilbao R. Influence of different operation conditions on soot formation from C_2H_2 pyrolysis. *Ind Eng Chem Res*, 46(23):7550–60, 2007.

[122] Liati A, Eggenschwiler PD, Schreiber D, Zelenay V, and Ammann M. Variations in diesel soot reactivity along the exhaust after-treatment system, based on the morphology and nanostructure of primary soot particles. *Combust Flame*, 160(3):671–81, 2013.

[123] Vander Wal RL and Tomasek AJ. Soot oxidation: dependence upon initial nanostructure. *Combust Flame*, 134(1-2):1–9, 2003.

[124] Vander Wal RL, Tomasek AJ, Street K, Hull DR, Thompson WK, and Stjernberg J. Carbon Nanostructure Examined by Lattice Fringe Analysis of High-Resolution Transmission Electron Microscopy. *Appl Spectroscopy*, 58(2):230–7, 2004.

[125] Wiinikka H, Weiland F, Pettersson E, Öhrman O, Carlsson P, and Stjernberg J. Characterisation of submicron particles produced during oxygen blown entrained flow gasification of biomass. *Combust Flame*, 161(7):1923–34, 2014.

[126] Septien S, Valin S, Peyrot M, Dupont C, Salvador S, and Stjernberg J. Characterization of char and soot from millimetric wood particles pyrolysis in a drop tube reactor between 800°C and 1400°C. *Fuel*, 121:216–24, 2014.

[127] Chen Y, Shah N, Braun A, Huggins FE, and Huffman GP. Electron microscopy investigation of carbonaceous particulate matter generated by combustion of fossil fuels. *Energy Fuels*, 19(4):1644–51, 2005.

[128] Della Rocca PA, Cerrella EG, Bonelli PR, and Cuckertman AL. Pyrolysis of hardwoods residues: on kinetics and char characterization. *Biomass Bioenergy*, 16(1):79–88, 1999.

[129] Hurt RH and Gibbins JR. Residual carbon from pulverized coal fired boilers: 1. Size distribution and combustion reactivity. *Fuel*, 74(4):471–80, 1995.

[130] Janse AMC, de Jonge HG, Prins W, and van Swaaij WPM. Combustion Kinetics of Char Obtained by Flash Pyrolysis of Pine Wood. *Ind Eng Chem Res*, 37(10):3909–18, 1998.

[131] Branca C and Di Blasi C. Combustion kinetics of secondary biomass chars in the kinetic regime. *Energy Fuels*, 24(10):5741–50, 2010.

[132] Zolin A. Reactivity of solid fuels. PhD thesis, Technical University of Denmark, 2001.

[133] Meszaros E, Jakab E, Varhegyi G, Bourke J, Manley-Harris M, and Nunoura T et al. Do All Carbonized Charcoals Have the Same Chemical Structure? 1. Implications of Thermogravimetry - Mass Spectrometry Measurements. *Ind Eng Chem Res*, 46(18):5943–53, 2007.

[134] Keiluweit M, Nico PS, Johnson MG, and Kleber M. Dynamic Molecular Structure of Plant Biomass-Derived Black Carbon (Biochar). *Environ Sci Technol*, 44(4):1247–53, 2010.

[135] Franklin RE. Crystallite Growth in Graphitizing and Non-graphitizing carbons. *Proc Royal Soc London Ser A*, 209(1097):196–218, 1951.

[136] Oberlin A. Carbonization and graphitization. *Carbon*, 22(6):521–41, 1984.

[137] Kurosaki F, Ishimaru K, Hata T, Bronsveld P, Kobayashi E, and Imamura Y. Microstructure of wood charcoal prepared by flash heating. *Carbon*, 41(15):3057–62, 2003.

[138] Messerer A, Niessner R, and Pöschl U. Comprehensive kinetic characterization of the oxidation and gasification of model and real diesel soot by nitrogen oxides and oxygen under engine exhaust conditions: Measurement, Langmuir-Hinshelwood, and Arrhenius parameters. *Carbon*, 44(2):307–24, 2006.

[139] Song J, Alam M, and Boehman AL. Impact of Alternative Fuels on Soot Properties and DPF Regeneration. *Combust Sci Tech*, 179(9):1991–2037, 2007.

[140] Qin K, Lin W, Fæster S, Jensen PA, Wu H, and Jensen AD. Characterization of Residual Particulates from Biomass Eintrained Flow Gasification. *Energy Fuels*, 27(1):262–70, 2012.

[141] Abian M, Jensen AD, Glarborg P, and Alzueta MU. Soot Reactivity in Conventional Combustion and Oxy-fuel Combustion Environments. *Energy Fuels*, 26(8):5337–44, 2012.

[142] Kajitani S, Suzuki N, Ashizawa M, and Hara S. CO_2 gasification rate analysis of coal char in entrained flow coal gasifier. *Fuel*, 85(2):163–9, 2006.

[143] Matsumoto K, Takeno K, Ichinose T, Ogi T, and Nakanishi M. Gasification reaction kinetics on biomass char obtained as a by-product of gasification in an entrained-flow gasifier with stem and oxygen at 900-1000°C. *Fuel*, 88(3):519–27, 2009.

[144] Zhao Y, Sun S, Tian H, Qian J, Su F, and Ling F. Characteristics of rice husk gasification in an entrained flow reactor. *Bioresour Technol*, 100(23):6040–4, 2009.

[145] Lin L, Gustafsson E, and Strand M. Aerosol-based method for investigating biomass char reactivity at high temperatures. *Combust Flame*, 158(7):1426–37, 2011.

[146] Lin L and Strand M. Investigation of the intrinsic CO_2 gasification kinetics of biomass char at medium to high temperatures. *Appl Energy*, 109:220–8, 2013.

3 Fuels, reactors and characterization techniques

3.1 Introduction

The initial decomposition stages of most solid fuel utilization paths involve chemical and physical processes that are reasonable similar [1]. The course of fuel thermal decomposition depends on the particular operating condition, reactor design and fuel type. A number of reactors have been used to provide a wide range of experimental conditions to understand the pyrolysis behavior of biomass. A wire mesh reactor and a drop tube reactor have been extensively used in many combustion related studies during the past two decades. Data from both reactor types have been used in mathematical simulations of pulverized combustion [2].

Bench-scale experiments can be rapid and relatively inexpensive, and may help in the design, development and operation of larger scale equipment as well as provide input information on fuel behavior. Fast pyrolysis experiments using a wire mesh reactor have been used before in different studies [3–9]. Experiments with a wire mesh reactor can be performed at heating rates between 0.5 and 10^3 K s^{-1} with pyrolysis occurring during heating and/or during an isothermal hold period [10]. Pyrolysis mass loss is obtained by weighting the solid fuel particles prior to pyrolysis and the char left in the mesh after pyrolysis. The material balance may be completed by collecting and weighting the tars and by analyzing the evolved gases [3]. The advantage of the wire mesh reactor is a well-controllable heating rate, and prevention of secondary reactions by sweeping the mesh with a gas flow. Due to the inaccuracy of mass balance closures and char recovery using entrained-flow systems, the wire mesh reactor appears as a more reliable instrument for measuring char yields as the effect of secondary reactions in the sample and over the grid can be minimized [2]. One of the disadvantages of the wire mesh reactor is the not well-known temperature of a sample, which can not be easily measured. Prins et al. [11] reported that the temperature of the grid can differ from the that of the thermocouple because of poor heat transfer or heat loss to the thermocouple. The low heat capacity of the grid could lead to a non-homogeneous temperature profile of the wire mesh. Other drawback of the system is a limited amount of char that can be produced, limiting the post-processing analysis of chars.

Another important apparatus used for solid fuel pyrolysis are entrained flow or drop tube reactors. A Drop Tube Furnace (DTF) is capable of creating an environment that closely simulates industrial conditions during pulverized combustion (short residence times, fast heating rates up to 10^4-10^5 K s^{-1}, high temperatures, dilute particle phases). This reactor can be used to prepare chars in reasonable amounts for the later investigations such as structural characterization and reactivity measurements. The advantage of a drop tube reactor is the relatively well-defined residence time obtained by moving the fuel injection tube or an extraction probe at different positions along the reactor's axis. In addition, the particle size and heating rates can be of the same range as in industrial boiler units. One clear disadvantage of the apparatus is the uncertain fate of tars evolved, which could affect the accuracy of carbon and hydrogen balances due to the remaining hot volatile

products which undergo secondary reactions [1]. Other drawback of the drop tube reactors is related to the accurate particle temperature-time histories which are difficult to obtain [12]. In most of the reported investigations [10], the solid fuel particle temperatures were calculated, and not experimentally determined. However, the exact details of the mixing of the solid fuel and carrier gas with the pre-heated gas, which are not very well-known, are important for the precise prediction of temperatures.

Biomass pyrolysis at intermediate heating rates (10-200 K s^{-1}) can be investigated in a single-particle reactor (SPR) for simultaneous measurement of mass loss, diameter, and internal and surface temperatures and char morphology [13–15]. Such an reactor is designed as an electrical heated or gas flame heated furnace with a number of viewing ports. A fuel particle may be suspended on a thermocouple measuring the internal temperature and connected to a microbalance to determine a particle mass loss. A CCD camera is installed to record, the combustion process and particle diameter and surface temperature may be measured with an optical pyrometer. The particle size for the experiments in a SPR ranges typically between 1.5 and 15 mm, and at temperatures up to 2000°C. High temperatures and intermediate heating rates in a range of 10^2-10^3 K s^{-1} are applied to obtain conditions which are reasonably close to those in actual pulverized combustion units. Single-particle experiments have the advantage of well-controlled atmospheres in which it is possible to gain a sufficient knowledge of the phenomena related to biomass pyrolysis for particles of a larger size, whereas the investigations with the drop tube and entrained flow reactors are limited to smaller particle sizes.

Table 2 provides an overview of previous studies on fast pyrolysis of biomass and major organic biomass components, mainly, at high-temperatures and high heating rates > 200 K s^{-1}. The majority of these investigations is referred to low-ash containing feedstocks (softwood, hardwood). The effects of heating rate and temperature on the morphological transformations at both slow (< 10 K s^{-1}) and intermediate and fast pyrolysis environments (> 100 K s^{-1}) of the same feedstock were rarely studied.

Char reactivity experiments are usually performed in thermogravimetric analyzers at heating rates between 3-1000 K min^{-1} and peak temperature below 1400°C. The advantage of TG experiments is the precisely known residence times and particle temperatures. The chief disadvantage is that the kinetics derived at low heating rates is applicable to low temperatures and extrapolation to high temperatures is not accurate [16, 17]. Lin et al. [16] reported that the reaction rates determined using TG instrument showed large discrepancies than those tested at higher temperatures. The reaction rates were at least two orders of magnitude between each configuration, whereas Wells et al. [18] and Hargrave et al. [19] reported that the reaction rates differed by at least one order of magnitude for coal char subjected to the thermogravimetric analysis and compared with those obtained from reactors operating at high temperatures.

Table 2: Review of previous studies on biomass high-temperature fast pyrolysis.

Fuel[a]	Reactor[b]	Temp.	Heating rate	Ref.
		[°C]	[K s^{-1}]	
HW, BG	WMR	1000	300-900	[20]
cel	WMR	400-1100	1000	[21]
HW	SPR	350-900	-[c]	[22]
OW, S	EFR	800-1000	10^4	[22]
HW, cel, lig, hem	SPR	200-650	-[c]	[23]
SW, EC, BG	WMR, EFR, TB	1000	1-10^5	[24]
HW	WMR	500-1300	10^2	[25]
SD	EFR	600-1400	10^4	[26]
SW, BW	EFR	1000-1450	10^4	[27]
P, S	WMR	500-1300	600-1000	[28]
SD	EFR, SPR	600-1400	10^3-10^4	[29]
SD	EFR	600-1400	10^4	[30]
SD, RH	EFR	700-1000	10^4	[31]
SWB, MDF, cel	PR	435-1100	1000	[32]
SW	EFR	800-1000	10^4	[33]
HW	EFR	1000-1400	10^4	[34]

[a]Biomass: HW=hardwood, BG=bagasse, cel=cellulose, hem=hemicellulose, lig=lignin, OW=olive waste, S=straw, SW=softwood, EC=eucalyptus, SD=sawdust, P=poultry, S=slaughter, RH=rice husk, SWB=softwood bark, MDF=medium density fiberboard. [b]Reactor: WMR=wire mesh reactor, EFR=entrained-flow reactor, SPR=single particle reactor, PR=plate reactor. [c] Undefined high heating rate

The behavior of biomass and plant cell wall compounds during pyrolysis under different heating conditions has been extensively studied and reviewed over the past few decades [25, 29, 35–38]. This chapter reviews reactors which were used to study the effect of operational conditions on the product yields and morphology. In this study, experiments at various heat treatment temperatures and heating rates using biomass particles of different size and structural composition were performed to produce the chars for the investigations of fuel kinetics and morphology.

3.2 Materials and methods

3.2.1 Raw samples

Pinewood, beechwood, Danish wheat straw, leached Danish wheat straw, alfalfa straw and rice husk were used in this work to represent softwood, hardwood and agricultural residues. The low-ash containing wood (pinewood, beechwood) of syringyl (S) or guaiacyl-syringyl (GS) lignin types and grass (wheat straw, alfalfa straw, rice husk) of hydroxy phenol-guaiacyl-syringyl (HGS) lignin type, which are rich in K, Ca and Si elements, were selected to investigate the effect of differences in ash composition and organic matter (cellulose, hemicellulose, lignin) on the char yield and structural transformations.

Table 3: Proximate and ultimate analysis of fuels (on % dry basis) and ash analysis (on mg kg^{-1} on dry basis). The symbols ar and db stay for as received and dry basis.

Fuel	Pine-wood	Beech-wood	Wheat straw	Leached wheat straw	Alfalfa straw	Rice husk	Lignin wheat straw	Lignin softwood	Pine-wood*	Beech-wood*
Proximate and ultimate analysis (% db)										
Moisture[a]	5.1	4.5	5.5	4.3	5.2	4.5	4.4	6.1	5.1	5.1
Ash (550°C)	0.3	1.4	4.1	2	7.4	21.7	3.6	1.3	0.3	1.5
Volatiles	86.6	79.4	77.5	84.2	75.9	64.3	66.3	67.3	84.9	79.3
HHV[b]	21.6	20.2	18.8	18.7	19.7	15.5	26.7	26.4	20.3	20.3
LHV[b]	20.2	19	17.5	17.4	16.9	14.5	25.5	25.2	19	19
C	50.5	46.7	42.4	45.7	42.5	35.5	61.8	64.6	50.1	50
H	6.8	6.3	6.3	6.6	6.1	5.5	3.8	5.3	6	5.8
O	42.3	45.3	46.2	45.4	40.7	37.2	29.4	28	43.5	42.6
N	0.1	0.3	1	0.3	3.3	0.1	1.4	0.8	0.05	0.08
S	<0.01	0.02	0.1	0.02	0.03	0.03	0.8	0.1	0.01	0.02
Cl	0.01	0.02	0.1	0.01	0.5	0.05	0.03	0.5	0.01	0.02
Ash compositional analysis (mg kg^{-1} db)										
Al	10	10	150	100	600	70	300	100	8.3	15.9
Ca	600	2000	2500	1300	12900	750	200	250	620	2090
Fe	20	10	200	350	-	80	1400	600	8	10
K	200	3600	11000	1300	28000	2500	270	80	250	3700
Mg	100	600	750	350	1400	400	40	<30	120	610
Na	30	100	150	50	1000	70	6800	4100	60	150
P	6	150	550	80	1900	600	30	30	25	120
Si	50	200	8500	6200	2000	98500	4000	900	33	200
Ti	2	<8	10	10	30	5	100	50	1	4

[a] wt. % (ar) [b] in MJ kg^{-1} *proximate and ultimate analysis after extraction

The fuels were milled on a Retsch rotor mill RZ200 and sieved to particle size fractions of 0.05-0.2 mm, 0.25-0.355 mm, 0.355-0.425 mm, 0.425-0.6 mm, 0.425-0.6 mm, 0.6-0.85 mm and 0.85-1 mm. Two types of Organosolv lignin made from softwood and wheat straw (purity > 94 %) were provided by BOC Sciences. Cellulose Avicel$^{\mathbb{R}}$ (purity > 99.9 %) and xylan from beechwood (purity > 90 %) were supplied by Sigma-Aldrich. The purity of xylan was additionally improved from 90 % to 96.6 % by a three step procedure involving a strong alkali treatment, bleaching and acetylation. The proximate and ultimate analyses of the fuels are shown in Table 3.

The wheat straw was leached in deionized water (room temperature) by continuous stirring for 12 h, followed by drying at 30°C in an oven desiccator without any ventilation. The mineral content after biomass leaching was determined by ash analysis. Due to the wheat straw leaching, the metal content was reduced to ≈ 60 % of the original value and the Cl, S, K, Na and P contents were strongly reduced.

3.2.2 Biomass compositional analysis

The compositional analysis of biomasses (cellulose, hemicellulose, acid-soluble lignin, acid-insoluble lignin, protein and extractives) was conducted according to NREL technical reports [39–

44] and Thammasouk et al. [45], and shown in Table 4.

Table 4: Biomass feedstock composition, calculated in percentage based on dry weight (% w w^{-1}).

Biomass	**Cellulose**	**Hemi-cellulose**	**Lignin**		**Total lignin**	**Extrac-tives**	**Protein**
			acid insoluble	**acid soluble**			
Pinewood	38.3	17.8	29.6	1.8	31.4	8.8*	0.6
Beechwood	35	19.2	32	1.5	33.5	7.5*	1.9
Wheat straw	35.9	18	19.2	6.5	25.7	10.1**	6.3
Leached wheat straw	32.1	23.5	13.8	2	15.8	13.3**	1.3
Alfalfa straw	18.8	12	14.7	6.8	21.5	39.6**	5.1
Rice husk	36.7	17.7	21.6	1.2	22.8	1**	-

* acetone extraction ** ethanol-water extraction

Two different extractions were performed on the fuels using acetone or ethanol-water as a solvent (room temperature). The long extraction with acetone removes efficiently resin and fatty acids, waxes, phytosterols, but it may also undesirably extract sugars, starches and proteins, that are not part of the wood structure [42–44]. The lipophilic extractives in wood samples were quantified using traditional Soxhlet extraction [40]. The homogenized biomass samples of particle size $<70\,\mu$m were freeze-dried in a thimble at -20 °C and extracted 8 h with an excess of HPLC grade acetone (Fischer Scientific) in a Soxhlet extractor. Once the sample was extracted, the solvent was evaporated to dryness under vacuum in a rotary evaporator. The dried extractives were stored in a freezer before the gravimetric analysis.

The water-ethanol extraction was performed on wheat straw, alfalfa straw and rice husk which contain a high level of hydrophilic and lipophilic extractable compounds [45]. The extraction comprised of a water extraction after which the remaining solid was extracted in 95 % ethanol, as described by Thammasouk et al. [45]. In addition, the original sample was also extracted using 95 % ethanol. These operations allowed for the determination of the total amount of water-soluble extractives, ethanol-soluble extractives, and water-insoluble but ethanol-soluble extractives, as well as the total extractives removed under a sequential extraction using water.

3.3 Reactors used in this thesis

Wire mesh reactor (WMR) at TU Munich and Drop Tube Reactor (DTF) at Luleå University of Technology were selected as the main reactors for the fast pyrolysis investigation. The effect of silicon bearing compounds on the herbaceous biomass morphology and char yield were studied using entrained-flow reactor (BabiTER) at TU Munich. The slow and intermediate heating rates influence on the yield and morphology of biomass char was studied using a single particle reactor (SPR) and a tubular reactor (TR).

3.3.1 Wire mesh reactor

The effects of the particle size and holding time on the biomass char yield were studied on the wire mesh reactor at TU Munich [46]. A reconstructed version of the reactor was used to study the influence of the temperature and the heating rate on the char yield and the structural transformation of biomasses as shown in Figure 16.

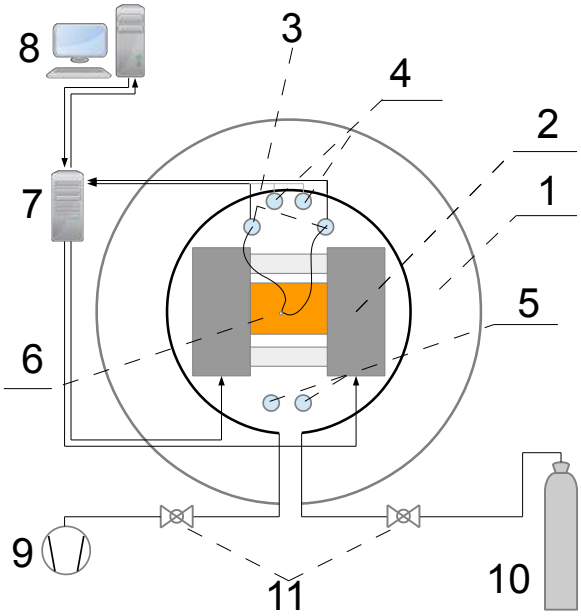

16(a): Wire mesh reactor at TU Munich

16(b): Photo of WMR before reconstruction

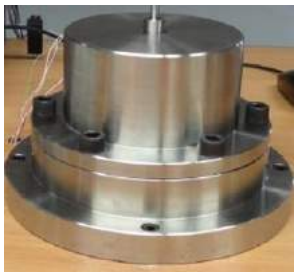

16(c): Photo of WMR after reconstruction

Figure 16: Wire mesh reactor at TU Munich: (a) Schematic top view of the wire mesh reactor at TU Munich: 1. Reactor steel casing; 2. Electrodes and holder of the wire mesh with a sample; 3. Thermocouples B-type; 4. Thermocouples S-type; 5. Thermocouples K-type; 6. Wire mesh with a sample; 7. Intensifier; 8. PC with LabVIEW software; 9. Vacuum pump; 10. Gas bottle; 11. Valves; (b) Photo of WMR before reconstruction; (c) Photo of WMR after reconstruction.

The reconstructed wire mesh reactor could be operated at temperatures up to 1700°C, heating rates up to 5000 K s^{-1}, and pressures up to 50 bar, whereas the original WMR could be operated at temperatures up to 1400°C, heating rates up to 3000 K s^{-1}. The reconstructed wire mesh reactor encloses a tar collection filter at the top of the casing. The optical ports of the original wire mesh

reactor were replaced with the cylindrical chamber to ensure a better sealing.

The cylindrical reactor chamber was enclosed into a stainless steel casing by six bolts. The welded stainless steel mesh (316L, TWP Inc., mesh width of 0.042 mm) was bended in two equal-length parts, forming a small bag with a surface area of 20 mm x 20 mm. The bended mesh served as a sample holder and resistance heater. The sample temperature was monitored in dependency on the experimental heat treatment temperature by either a thermocouple type K (max. 1000°C), type S (max. 1450°C) or type B (max. 1700°C) with a diameter of 0.051 mm. The two wires of a thermocouple (type K/S/B) were directly welded into the middle of the upper mesh side to determine the mesh temperature based on the Seebeck effect. The control system was based on the LabView software (Version 8.6), and consisted of a PID controller that adjusted the power output to the required temperature.

The temperature distribution on the wire mesh was assumed to be uniform. However, on the mesh side near the electrodes, the temperature could be lower than in the middle as reported by Hoekstra et al. [47]. In order to ensure high reproducibility of char yield data, the sample was therefore placed centrally. The sample mass of 5 ± 1 mg for each experiment was selected based on the previous studies of Nola et al. [28] to achieve one monolayer of particles within a mesh bag. The fuel sample was distributed homogeneously in the mesh bag by using compressed air to remove particles of size < 0.042 mm. The wire mesh with the fuel sample was clamped between two electrodes. A two-stage rotary vane pump was used to remove air from the reactor before the experiment. The mesh was continuously swept by nitrogen at a defined flow rate to remove volatiles from the fuel during experiments.

3.3.2 Tubular furnace

A tubular reactor (TR), placed in a furnace (Entech, ETF3050/15S) was used for fixed-bed pyrolysis with a heating rate of $< 10\,\mathrm{K\ min^{-1}}$ and a temperature up to 1400°C. The furnace consisted of a stainless steel tube with an alumina tube fitted with electrical heating elements and gas supply. 5 mg of the virgin sample was loaded into the alumina boat placed in the furnace middle. The tubular reactor was purged with N_2. Once the preset temperature was reached, the sample was kept for about 10 min or 4 h in the furnace to ensure complete conversion. In the current investigation, the chars, prepared in the tubular reactor under the slow heating, were applied to study morphological transformations.

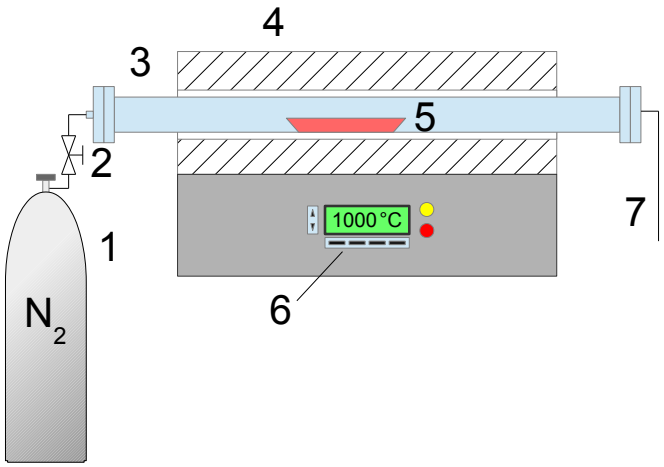

Figure 17: Schematic view of the tubular reactor at DTU: 1. Gas bottle (N_2); 2. Valve; 3. Ceramic tube; 4. Horizontal tubular furnace; 5. Quartz boat; 6. Electric heater and temperature controller; 7. Exhaust gas.

3.3.3 Single particle reactor

The single particle reactor (SPR) at DTU was designed for oxidation and pyrolysis studies on wood particles > 2 mm at temperatures up to 1500°C at high heating rates. Momeni et al. [48] applied the single particle reactor to study biomass combustion. The setup consists of the reactor, a burner with 94 injection nozzles, a gas supply system, gas analyzers and safety equipment as shown in Figure 18.

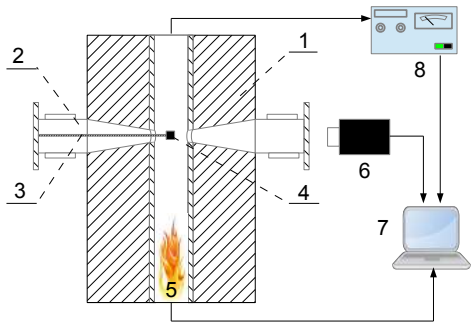

Figure 18: Schematic view of a single particle reactor at DTU: 1. Reactor corpus; 2. insertion ports with a water-cooled chamber; 3. particle holder; 4. sample particle; 5. 94 injection nozzles; 6. High-speed camera; 7. Computer; 8. Gas analyzers.

The reactor is an insulated ceramic tube with four insertion ports surrounded by water cooled chambers. Prior to an experiment, a fuel particle was placed precisely in the reactor center and held by a platinum wire, mounted on the ceramic tube, and protected from the hot environment by another ceramic tube, placed in an opposite insertion port. When the ceramic shield was removed, the particle experiences a preheated flow of gases generated by the hydrogen burner, and

it was rapidly heated in an oxidizing or reducing atmosphere. The transformation of a particle was recorded by a high speed camera (AVTS, F-033) that can take in average up to 65 images s^{-1}. The camera was controlled by AVT SmartView 1.11 and MatLab software. The gas flow rates were controlled by five mass flow controllers (Bronkhorst, EL-FLOW).

The SPR reactor was used to study the effect of particle size and intermediate heating rate (ca. 200 K s^{-1}) during pyrolysis on the char yield and char structural transformation. For the larger pinewood particles of 3-5 mm, the devolatilization time was determined.

3.3.4 Drop tube reactor

The Drop Tube Furnace (DTF) used in the present study is shown in Figure 19.

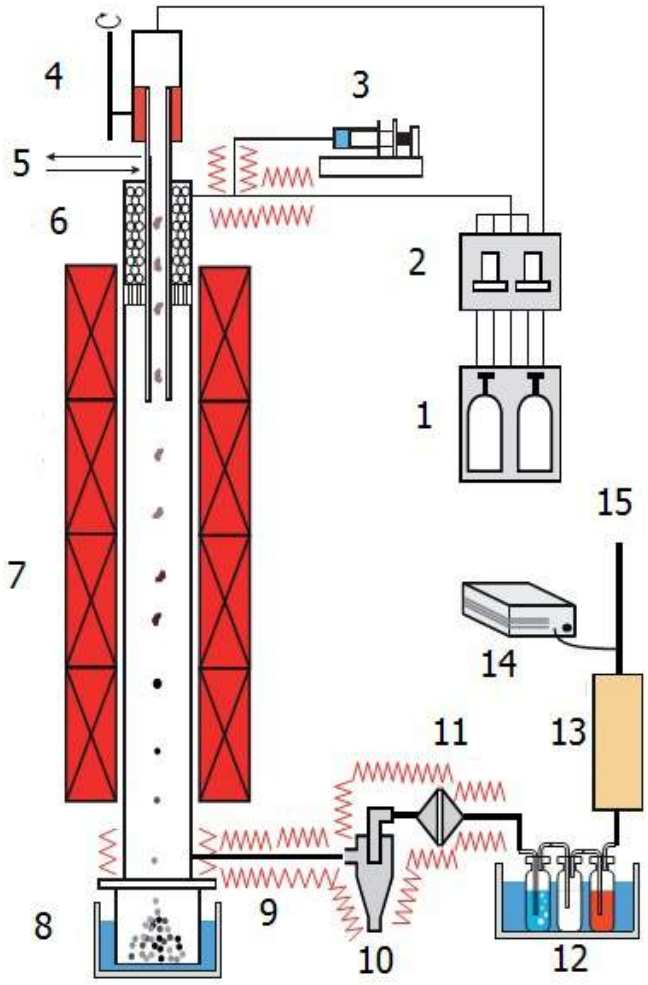

Figure 19: Schematic view of the Drop Tube Furnace at Luleå University of Technology: 1. Gas cylinders (O_2, N_2, CO_2, CO, H_2); 2. Mass flow controllers; 3. Syringe pump (water); 4. Biomass feeder (syringe type); 5. Cooling water; 6. Ceramic packed bed; 7. Tube furnace; 8. Char bin; 9. Heating tape (T = 200°C); 10. Cyclone; 11. Quartz filter; 12. Impinger bottles; 13. Activated Carbon filter; 14. MicroGC; 15. Exhaust.

The cylindrical reactor tube was made of alumina ceramic (grade C799) with an inner diam-

eter of 54 mm. The reactor tube was heated by tube furnace modules using SiC rods as heating elements (Elite Thermal Systems Ltd.) with a maximum temperature of 1500°C. Supply of primary gas was led through the biomass feeder, and secondary gas was led to the top of the reactor through a packed bed of ceramic balls that distributed the gas flow equally in the radial direction. Inlet gas flows of O_2, N_2, H_2, CO and CO_2 were controlled by mass flow controllers (EL-FLOW® Select, Bronkhorst High-Tech B.V.), while the flow rate of H_2O was controlled by a syringe pump (Legato 100, KD Scientific Inc.). A syringe pump type biomass feeder was used to supply biomass at low feeding rates [49]. The feeding probe was water-cooled at 20°C to ensure a high heating rate of the biomass when it entered the reactor. The Reynolds number of the gas flow inside the reactor was 60-100, dependent on the reaction temperature.

Biomass was rapidly heated and reacted while it fell down through the reactor. Reaction products were separated into coarse particles (mainly char and fly ashes), fine particles (mainly soot and precipitated ash vapor), and permanent gases. Soot particles passing the cyclone (cut size = 2.5 μm) were captured from the product gas flow by a grade QM-A quartz filter with a diameter of 50 mm (Whatman, GE Healthcare Life Science). The larger particles (e.g. char) could either fall down to a char bin or a stainless steel cyclone (URG-2000-30ENS-1, URG Corporation). After an activated carbon filter (VACU-GUARD 150, GE Healthcare Life Science), the gas composition was measured by a micro gas chromatograph (Model 490, Agilent Technologies). The μGC was equipped with two columns (CP-MolSieve 5 A for H_2, O_2, N_2, CH_4 and CO; and PoraPlot U for CO_2, C_2H_4, C_2H_6, C_2H_2, and C_3H_6/C_3H_8) and thermal conductivity detectors. The temperature of the char bin and product gas was controlled by heating controllers (HTC-5500, Hemi Heating AB) with thermo-tapes (S-type, Hemi Heating AB) and kept at 200°C to avoid tar condensation. The larger particles (0.85-1 mm) were pyrolyzed in a different alumina ceramic tube which was 3 mm long, and heated by 6 tube furnace modules.

3.3.5 Entrained-flow reactor

The entrained flow study was carried out with the Baby High Temperature Entrained Flow Reactor (BabiTER) at TU Munich. The layout of the reactor is shown in Figure 20 [50, 51]. The BabiTER can be operated at atmospheric pressure and at a maximal temperature of 1600°C. The particle residence time for the investigation in this work is below 1 s, calculated from the average gas residence time, and considering the effects of particle free fall velocity, velocity profile and biomass particle properties.

A defined gas mixture (2) is preheated (4) before entering the reaction tube (40 mm inner diameter, 1400 mm length, 99.7 % Al_2O_3). The reaction tube (5) is surrounded by three heating zones, each consisting of four $MoSi_2$ heating elements. A feeding system (3) is enclosed in a container and purged with nitrogen of 99.999 % high purity (1) to prevent air entering the reactor. It consists of two independently acting dosing systems which are placed on opposite sides. Each feeding system contains three vibrational chutes and one batch weighting unit for a constant and

uniform transport of the biomass materials into the reactor.

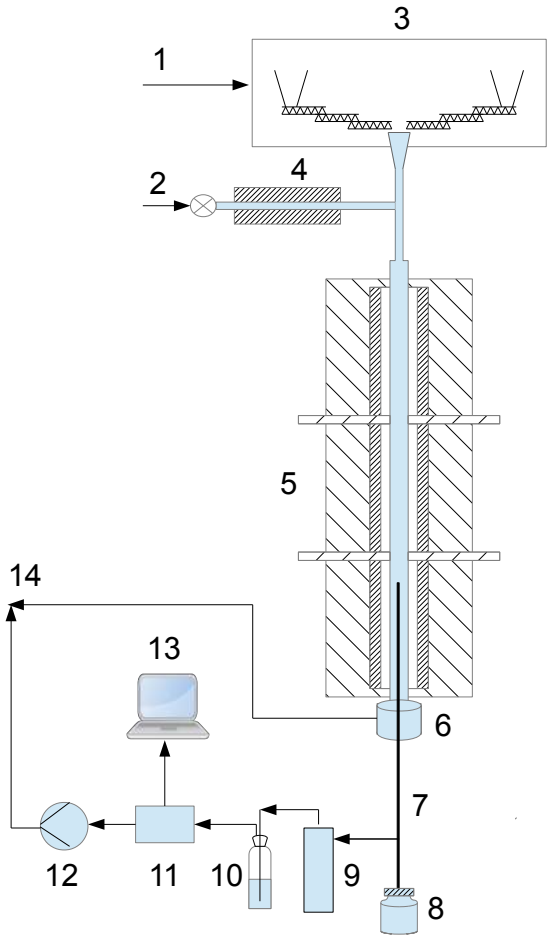

Figure 20: Schematic view of the entrained-flow reactor (BabiTER) at TU Munich [50, 51]: 1. Feeding gas (N_2) ; 2. Main gas (N_2); 3. Fuel feeding system; 4. Pre-heater; 5. Tube furnace; 6. Water quench; 7. Collection probe; 8. Solid residue char bin; 9. Metal filter; 10. Impinger bottle; 11. Gas analyzer; 12. Pump (Venturi); 13. Gas analysis/measurement controller; 14. Exhaust gas.

The mass flow of the pulverized biomass can be varied from 50 g h^{-1} to 1 kg h^{-1} and is controlled by a software connected to the balances. The pre-heated nitrogen is mixed with the biomass in the entry of the reaction tube. Char and gas samples in the reaction zone can be collected by a water cooled sampling probe (7), which is adjustable in height. The gas flow rate, sucked by the sampling probe, can be varied by a venturi nozzle, such that iso-kinetic sampling can be performed. Particles and gases, which are not collected with the sampling probe, are quenched by water (6). The collected char in the sampling probe is separated from the reaction gas on a char filter (9), and collected in a char bin (8). A part of the reaction gas is analyzed using a non-

dispersive infrared analysis (NDIR)/heat conductivity analyzer (13) for process control. In this work, the experiments were carried out with the entrained flow reactor at temperatures of 1000, 1250 and 1500°C. The BabiTER system is limited to use particles with a characteristic length $<$ 0.5 mm. A biomass feeding rate of 300 g h^{-1} was selected for the rice husk. At 1000 and 1250°C, the wheat straw was fed with 200 g h^{-1}, and at 1500°C with 100 g h^{-1} to ensure continuous biomass feeding. The sampling probe was kept at a constant height, enabling a residence time of about 1 s during all experiments.

3.4 Solid residue characterization

The char characterization was mostly carried out using SEM microscopy, whereas soot morphology and particle size were studied on TEM microscope. The compositional analysis of soot structure was carried out on TEM-EELS. The effect of silicon bearing compounds and organic matter on the char morphology was investigated using ^{29}Si solid state NMR spectroscopy, X-ray diffraction (XRD) and electron spin resonance spectroscopy (ESR). The particle size and shape of biomass char was characterized by 2D dynamic imaging device (CAMSIZER XT). The specific surface area (BET) of soot and char was investigated using N_2 adsorption. The elemental analysis of original biomass and chars was performed to determine O/C and H/C ratios. The analysis of char reactivity in oxygen and gasification environments was carried out in a thermogravimetric (TG) analyzer.

Elemental analysis. The elemental analysis was performed on two instruments of the same model (Eurovector, model EA3000). Acetanilide was used as a reference standard. The ash content was determined using a standard ash test at 550°C, according to procedure described in DIN EN 14775.

Ash compositional analysis. The ash compositional analysis was performed by an X-ray fluorescence instrument (Shimadzu, model EDX 800-HS) at TU Munich. Prior to the XRF analysis, char samples were pre-heated in oxygen at 5 K min^{-1} up to 550°C and kept at that temperature for 7 h. The generated ash (about 200 mg) was initially mixed and then pressed with a special wax (mixture ratio 1:5). The Cl and S content in the ash was analyzed by ICP-OES/IC at TU Wien. The ash sample was dissolved in ultrapure water at 120°C for 1 h, and then the solution was filtered and analyzed by ICP-OES/IC.

Particle size and shape. The particle size and shape of the original biomass and its char were characterized on a 2D dynamic imaging instrument (CAMSIZER XT, Retsch), designed for a particle size range of 3 μm to 3 mm. A particle shadow was captured by the CCD-basic and zoom cameras of the CAMSIZER XT. The zoom-camera was optimized to analyze smaller particles with a high resolution, whereas the basic-camera detected larger particles due to a large field of view. The projected area of a particle was analyzed by the CAMSIZER XT 6.3.10 software to

characterize its size and shape. Fine biomass particles tended to agglomerate which made it difficult to detect the true geometric dimensions of each individual particle. Therefore, the particle agglomerates were separated without destroying the primary particles by air pressure dispersion. For the particle size analysis, ca. 100 mg of sample was used. The particle size and shape measurements of char, collected from several drop tube pyrolysis experiments, were performed twice with the CAMSIZER XT for each operational condition to establish reproducible results.

The Martin minimal ($x_{Ma,min}$) and Feret maximal ($x_{Fe,max}$) diameters are suitable parameters to represent the biomass particle width and length in combustion. The Martin diameter is a chord length that divides the projected particle area into two equal halves [52], as shown in the supplemental material. The minimal Martin diameter ($x_{Ma,min}$) is determined from the smallest Martin diameter of the particle projection [53], and represents a particle width based on the assumption of a biomass particle to be thinner than its width in the diffusion process of a combustion modeling. The Feret diameter is the distance between two tangents placed perpendicular to the measurement direction [52], as shown in the supplemental material. The Feret maximal diameter is applied as the largest value of all measured Feret diameters of a particle [53], and the longest measurable diameter $x_{Fe,max}$ is the largest diameter to fulfill the assumption that the length of a particle has to be larger than its width. The results of the particle size analysis were represented as a frequency distribution over $x_{Ma,min}$, which is defined in equation 3:

$$q_3(x_{Ma,min}) = \frac{dQ_3(x_{Ma,min})}{x(x_{Ma,min})} \tag{3}$$

In this equation, Q_3 is the cumulative particle size distribution based on volume. The particle shape was characterized by sphericity (SPHT) and aspect ratio (b/l) in the present study. Sphericity is one of the most common ways to express the deviation of an 2D image shape from a sphere and is defined by equation 4:

$$SPHT = \frac{4 * \pi * A}{P^2} \tag{4}$$

In this equation, P is the measured circumference of a particle projection and A is the measured area of a particle projection. The particle is considered to be spherical when the value of sphericity is equal to 1 and non-spherical when it is smaller than 1. The aspect ratio AR is defined as the ratio of particle width (b=$x_{Ma,min}$) to the particle length (l=$x_{Fe,max}$).

$$AR = \frac{b}{l} \tag{5}$$

^{13}C and ^{29}Si solid state NMR spectroscopy. Solid-state NMR analysis was carried out on a Bruker Avance 400 NMR spectrometer (9.4 T) operating at Larmor frequencies of 400.13, 100.58 and 79.48 MHz for ^{1}H, ^{13}C and ^{29}Si, respectively. All experiments were conducted using a double resonance probe equipped with 4 mm (o.d.) rotors. Samples were analyzed as without any additional preparation at room temperature by single-pulse (SP) magic angle spinning (MAS) as well as cross polarization (CP) MAS [54] utilizing high-power ^{1}H two-pulse phase-modulated decoupling (TPPM) [55] during acquisition and employing a spinning rate of 9 kHz. The ^{13}C CP/MAS

spectra were recorded using a recycle delay of 8 s, a contact time of 1 ms, an acquisition time of 45.9 ms and 4096 scans, whereas the ^{13}C SP/MAS spectra were recorded using a recycle delay of 128 s, an acquisition time of 45.9 ms and 1080 scans. The ^{29}Si CP/MAS spectra were recorded using a recycle delay of 2 s, a contact time of 8 ms, an acquisition time of 42.6 ms and 8192 scans, while a recycle delay of 256 s, an acquisition time of 42.6 ms and 512 scans were utilized for recording the ^{29}Si SP/MAS spectra. All recycle delays and contact times were optimized on the original biomass of wheat straw (^{13}C) and protobind 1000 (^{29}Si) and then used for all samples in this study. The NMR spectra were referenced to TMS (0 ppm) using secondary reference compounds. All ^{13}C NMR spectra were referenced to the carbonyl resonance in an external sample of α-glycine at 176.5 ppm [56], and the ^{29}Si NMR spectra were referenced to an external sample of 3-(Trimethylsilyl)-1-propanesulfonic acid sodium salt at 1.6 ppm.

N_2 adsorption analysis. The specific surface area (SSA) of biomass chars was determined based on nitrogen adsorption at its boiling point (77 K). To remove surface contaminants, the samples were heated to 350°C in a dry N_2 flow prior to the measurement. The multipoint Brunauer-Emmett-Teller (BET) theory with seven points in the range of p/p_0 from 0.01 to 0.2 is applied on the BET instrument (Quantachrome iO2). BET equation was used to determine the specific surface area [57].

Thermogravimetric analysis. The reactivity of char and soot was determined using a TG instrument (Netzsch, STA 449 F1) by loading 3 mg of sample in an Al_2O_3 crucible and heating it from 35 to 1350°C in 5 % volume fraction O_2 (50 cm^3 min^{-1} of O_2 and 95 cm^3 min^{-1} of N_2 measured at 20°C and 101.3 kPa) and in 5 % volume fraction (50 cm^3 min^{-1} of CO_2 and 95 cm^3 min^{-1} of N_2 measured at 20°C and 101.3 kPa) at a constant heating rate of 10 K min^{-1}.

Electron spin resonance spectroscopy. Electron spin resonance (ESR) spectra were recorded on a Jeol JES-FR30 ESR spectrometer (JEOL Ltd., Tokyo, Japan). Samples were placed in a closed-bottom quartz capillary tube with a wall thickness of 0.75 mm and an outer diameter of 5 mm. The measurements were carried out at room temperature with a microwave power of 4 mW, and a modulation width of 0.1 mT, sweep width of 50 G, sweep time of 0.5 min, time constant of 0.3 s. The intensity of all signals was recorded relative to the intensity of a Mn (II)-marker (JEOL Ltd., Tokyo, Japan) attached to the cavity of the spectrometer. Since the area under the ESR adsorption curve is directly proportional to the number of paramagnetic centers contributing to the resonance, the spin concentration (spins g^{-1}) of a sample, $N_{s.spin}$, was calculated by comparing the double integrated areas of the sample signals, A_{sample}, and the Mn (II) internal marker signals as shown in equation 6 [58]:

$$N_{s.spin} = \frac{N_{marker} \cdot A_{sample}}{A_{marker}} \tag{6}$$

A solid sample of $CuSO_4{\cdot}5H_2O$ of known weight was used as a standard for calculating the number of spins in the Mn(II)-marker signals as shown in equation 7 [59]:

$$N_{marker} = \frac{n_{CuSO_4{\cdot}5H_2O} \cdot N_A \cdot A_{marker}}{A_{CuSO_4{\cdot}5H_2O}} \tag{7}$$

The calculation of a spin sample concentration ($c_{s.spin}$) is based on the ratio of a number of spins and a sample weight (m_s) using equation 8 [59]:

$$c_{s.spin} = \frac{N_{s.spins}}{m_s} \tag{8}$$

The ESR g-factor is determined in equation 9 [59]:

$$g = \frac{g_1 \cdot H}{H + H_1} \tag{9}$$

g_1-factor of a digital marker (1.981), H_1 and H are positions of the digital marker (H = 335.7 mT) and signal center (H = 337.1 mT). In equation 9, g_1-factor of a digital marker (1.981), H_1 and H are positions of the digital marker (H = 335.7 mT) and signal center (H = 337.1 mT).

Fitting of experimental ESR-spectra to simulated data was done using WinSim software, as described by Duling et al [60]. The WinSim software is based on the LMB and simplex optimization methods to fit an experimental ESR spectrum to a combination of simulated free radical ESR spectra. Each spectra was assumed to be isotropic, spin = 1/2 without contributions from hyperfine splittings. The simulation of spectra gave the relative amounts of radical derivatives as well as optimized values of line widths and g-factors. Optimizations all gave best fits to the experimental ESR spectra with a root mean square (RMS) > 0.85.

The ESR analysis of biomass char was conducted the next day after char generation, and compared with the results seven month later. The radical concentration showed negligible differences ($< 5\,\%$) over a period of seven month, and therefore being independent on the storage time.

FTIR Spectroscopy. The wheat straw soot samples were analyzed by a Thermo Nicolet 6700 FTIR spectrometer equipped with a Golden gate (diamond) ATR accessory and DTGS (KBr) detector. All transmission spectra were obtained in the 4000-600 cm^{-1} range by 100 scans at 4 cm^{-1} resolution. For background, 200 scans were acquired. A good contact between sample and ATR-crystal surface was ensured by the pressure device of the unit (up to 30000 psi) [61]. All samples were measured in triplicate.

X-ray diffraction. The crystalline constituents of the soot matter were characterized using a Bruker D8 AXS X-ray diffractometer with (Cu-Kα1, λ = 1.54056 Å and Cu-Kα2 radiation, λ = 1.54439 Å) operating in Bragg-Brentano (reflection) mode, using a secondary graphite monochromator, and a scintillation detector, in the range 5 to 80 degrees for 12.5 h. The sample was placed in a small cup rotated during data collection. The interlayer distance d_{002}, based on similarities

with the graphite structure, is calculated by Bragg's equation [62]:

$$d_{002} = \frac{\lambda}{2sin\theta_{(002)}} \tag{10}$$

θ is a Bragg angle. The stacking height (L_c) of the crystallites was estimated using the Scherrer's formula with the constant $K_{Scherrer}$ = 0.9 [63]:

$$L_c = \frac{0.9 \cdot \lambda}{B(2\theta)_{(002)} \cdot cos\theta_{(002)}} \tag{11}$$

B(2θ) is the sample broadening of the reflection, calculated in radians, at full width half maximum (FWHM). The lateral extension (L_a) was calculated using the Scherrer equation with the constant $K_{Scherrer}$ = 1.84 for the two-dimensional lattice reflections of the type (hk0) [63]:

$$L_a = \frac{1.84 \cdot \lambda}{B(2\theta) \cdot cos\theta} \tag{12}$$

The number of layers (N) is determined using L_c in equation 13 with the assumption that a carbon material consists of parallel layers [64]:

$$N = \frac{L_c + d_{002}}{d_{002}} \tag{13}$$

The collected XRD patterns were analyzed using Crystallographica Search-Match software (Version 3,1,0,0). The instrumental reflection broadening was subtracted from the experimental pattern by Winprep software.

SEM microscopy. SEM analysis of char was performed on a microscope (FEI Company, Inspect) with a tungsten filament under high vacuum in order to understand char structural and chemical properties. Prior to the analysis, char samples were coated with a thin layer of carbon (40 s, 5 mA) using a Cressington 208 Carbon Coater to avoid sample charging.

Soot pretreatment for the microscopy. Prior to the microscopy, soot samples were kept at 350°C for 4 h in a thermogravimetric instrument to reduce the amount of volatiles. However, the TG curves as shown in Appendix D (Figure 98) quantified the remaining volatiles yield to be less than 5 %. Samples were grounded in a mortar to ensure a homogeneous particle distribution and dry dispersed on a lacey carbon copper grid.

Transmission electron microscopy. Soot morphology and composition were studied using either a FEI Titan transmission electron microscope operated at 120 keV or a FEI Tecnai operated at 200 keV, both equipped with an Oxford Instruments X-Max SDD EDS detector.

Electron energy-loss spectroscopy (TEM-EELS). EELS analysis of soot samples was performed in the FEI Titan presented before, equipped with a Gatan GIF Tridiem spectrometer. For anisotropic materials like graphite and soot, the fine structure of the ionization edges is dependent on the orientation of the sample and the collection angle of the spectrometer. To compare

different samples, the so called magic-angle condition is used, which minimizes the influence of the anisotropic structure [65–69]. Magic-angle conditions were chosen by acquiring a spectrum of the C-K edge (about 285 eV) in parallel illumination under two different tilt angles of the sample. The right parameters are found as both spectra matches in shape and relative intensity. The EELS spectra are background subtracted and corrected for multiple scattering.

Particle size distribution analysis using TEM. The particle size of soot samples was estimated manually from TEM images using the ImageJ software. The clearly visible primary particles were selected for accurate analysis. The data were assessed to establish particle size distributions. For the size analysis, soot particles were assumed spherical. Particle size analysis was conducted on 50 particles at each operating condition. The geometric standard deviation was calculated as shown in equation 14 [70]:

$$\sigma_g = exp\left(\sqrt{\frac{\sum_{i=1}^{n} ln(\frac{A_i}{\mu_g})^2}{n}}\right) \tag{14}$$

In equation 14, μ_g is the geometric mean of a set of numbers A_i. The standard deviation was calculated for curvature, fiber length (see definition below) and separation distance of graphene layers.

Graphitic structure. The term graphitic structure was used to compare soot nanostructure with graphitic carbon in terms of graphene layer length, curvature and parallelism within the primary soot particles. The amorphous core of the soot particles was referred to the short-ranged structures. The curvature of a single graphene sheet is defined in equation 15:

$$Curvature = \frac{Length}{Fiber\ \ length} \tag{15}$$

The length is a straight line that connects both ends of a graphene sheet. The fiber length is a contour or arc length as shown in Figure 21. Both length and fiber length were estimated by Gatan Digital Micrograph software according to method of Müller et al. [71]. The part of the image with the more visible graphene layers was magnified to a size of 10 nm x 10 nm, and both length and fiber length were manually determined by the software ruler which draws a straight or contour line to connect both ends of a graphene sheet.

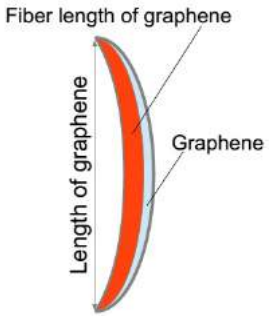

Figure 21: Graphene fiber length and length used for the curvature calculation.

References

[1] Kandiyoti R, Herod A, and Bartle K. *Solid Fuels and Heavy Hydrocarbon Liquids*. Elsevier, 2006.

[2] Hindmarsh CJ, Thomas KM, Wang WX, Cai HY, Guell AJ, and Kandiyoti R et al. A comparison of the pyrolysis of coal in wire-mesh and entrained-flow reactors. *Fuel*, 74(8):1185–90, 1995.

[3] Suuberg EM, Peters WA, and Howard JB. Product composition and kinetics of lignite pyrolysis. *Ind Eng Chem Process Des Dev*, 17(1):37–46, 1978.

[4] Hamilton LH, Ayling A, and Shiboaka MA. A new experimental device for pyrolysing coal particles under controlled conditions over a wide range of heating rates. *Fuel*, 58(12):873–6, 1979.

[5] Stangeby PC and Sears PL. Rapid pyrolysis and hydropyrolysis of Canadian coals. *Fuel*, 60(2):131–5, 1981.

[6] Niksa SJ, Heyd LE, Russel WB, and Saville DA. On the role of heating rate in rapid coal devolatilization. *Symp Int Combust*, 20(1):1445–53, 1985.

[7] Hajaligol MR, Howard JB, Longwell JP, and Peters WA. Product composition and kinetics for rapid pyrolysis of cellulose. *Ind Eng Chem Process Des Dev*, 21(3):457–65, 1982.

[8] Nunn TR, Howard JB, Longwell JP, and Peters WA. Product composition and kinetics in the rapid pyrolysis of sweet gum hardwood. *Ind Eng Chem Process Des Dev*, 24(3):836–44, 1985.

[9] Drummond ARF and Drummond IW. Pyrolysis of sugar cane bagasse in a wire-mesh reactor. *Ind Eng Chem Res*, 35(4):1263–8, 1996.

[10] Solomon PR, Serio MA, and Suuberg EM. Coal pyrolysis: experiments, kinetic rates and mechanisms. *Prog Energy Combust Sci*, 18(2):133–220, 1992.

[11] Prins AJ, Bastiaans RJM, van Oijen JA, de Goey LPH, Linden J, and Alden M et al. Visualization of Pyrolysis and Temperature Imaging in a Heated-Grid Reactor. *Energy Fuels*, 23(2):993–1006, 2009.

[12] Zolin A. Reactivity of solid fuels. PhD thesis, Technical University of Denmark, 2001.

[13] Ip LT, Baxter LL, Mackrory AJ, and Tree DR. Surface temperature and time-dependent measurements of black liquor droplet combustion. *AIChE J*, 54(7):1926–31, 2008.

[14] Lu H, Robert W, Peirce G, Ripa B, and Baxter LL. Comprehensive study of Biomass particle combustion. *Energy Fuels*, 22(4):2826–39, 2008.

[15] Lu K, Ip E, Scott J, Foster P, Vickers M, and Baxter LL. Effects of particle shape and size on devolatilization of biomass particle. *Fuel*, 89(5):1156–68, 2010.

[16] Lin L and Strand M. Investigation of the intrinsic CO_2 gasification kinetics of biomass char at medium to high temperatures. *Appl Energy*, 109:220–8, 2013.

[17] Simmons G and Sanchez M. High-temperature gasification kinetics of biomass pyrolysis. *J Anal Appl Pyrolysis*, 3(2):161–71, 1981.

[18] Blackham AU, Wells WF, Kramer SK, and Smoot LD. Reactivity and combustion of coal chars. *Symp Int Combust*, 20(1):1539–46, 1985.

[19] Hargrave G, Pourkashanian M, and Williams A. The combustion and gasification of coke and coal chars. *Symp Int Combust*, 1:221–30, 1988.

[20] Fraga AR, Gaines AF, and Kandiyoti R. Characterization of biomass pyrolysis tars produced in the relative absence of extraparticle secondary reactions. *Fuel*, 70(7):803–9, 1991.

[21] Hajaligol MR, Howard JB, and Peters W. An Experimental and Modeling Study of Pressure Effects on Tar Release by Rapid Pyrolysis of Cellulose Sheets in a Screen Heater. *Combust Flame*, 95(1-2):47–60, 1993.

[22] Zanzi R, Sjöström K, and Björnbom E. Rapid pyrolysis of agricultural residues at high temperature. *Biomass Bioenergy*, 23(5):357–66, 2002.

[23] Svenson J, Pettersson JBC, and Davidsson KO. Fast pyrolysis of the main components of birchwood. *Combust Sci Technol*, 176(5-6):977–90, 2004.

[24] Cetin E, Moghtaderi B, Gupta R, and Wall TF. Influence of pyrolysis conditions on the structure and gasification reactivity of biomass chars. *Fuel*, 83(16):2139–50, 2004.

[25] Guo J. Pyrolysis of wood powder and gasification of wood-derived char. PhD thesis, Eindhoven University of Technology, 2004.

[26] Zhang Y, Kajitani S, Ashizawa M, and Miura K. Peculiarities of Rapid Pyrolysis of Biomass Covering Medium- and High-Temperature Ranges. *Energy Fuels*, 20(6):2705–12, 2006.

[27] Dall'Ora M, Jensen PA, and Jensen AD. Suspension combustion of wood: Influence of pyrolysis conditions on char yield, morphology, and reactivity. *Energy Fuels*, 22(5):2955–62, 2008.

[28] Di Nola G, De Jong W, and Spliethoff H. The fate of main gaseous and nitrogen species during fast heating rate devolatilization of coal and secondary fuels using a heated wire mesh reactor. *Fuel Process Technol*, 90(3):388–95, 2009.

[29] Lu H. Experimental and Modeling Investigations of Biomass Particle Combustion. PhD thesis, Brigham Young University, 2006.

[30] Zhang Y, Kajitani S, Ashizawa M, and Oki Y. Tar destruction and coke formation during rapid pyrolysis and gasification of biomass in a drop-tube furnace. *Fuel*, 89(2):302–9, 2010.

[31] Sun S, Tian H, Zhao Y, Sun R, and Zhou H. Experimental and numerical study of biomass flash pyrolysis in an entrained flow reactor. *Bioresour Technol*, 101(10):3678–84, 2010.

[32] Sepman AV and de Goey LPH. Plate reactor as an analysis tool for rapid pyrolysis of biomass. *Biomass Bioenergy*, 35(7):2903–9, 2011.

[33] Umeki K, Kirtania K, Chen L, and Bhattacharya S. Fuel Particle Conversion of Pulverized Biomass during Pyrolysis in an Entrained Flow Reactor. *Ind Eng Chem Res*, 51(43):13973–9, 2012.

[34] Septien S, Valin S, Dupont C, Peyrot M, and Salvador S. Effect of particle size and temperature on woody biomass fast pyrolysis at high temperature (1000-1400°C). *Fuel*, 97:202–10, 2012.

[35] Zanzi R. Pyrolysis of biomass. PhD thesis, Royal Institute of Technology, 2001.

[36] Dall'Ora M. Reactivity and burnout of wood fuels. PhD thesis, Technical University of Denmark, 2011.

[37] Grønli MG. A theoretical and experimental study of the thermal degradation of biomass. PhD thesis, Norwegian University of Science and Technology, 1996.

[38] Septien Stringel S. High temperature gasification of millimetric wood particles between 800°C and 1400°C. PhD thesis, Institut National Polytechnique de Toulouse, 2011.

[39] Sluiter A, Hames B, Ruiz R, Scarlata C, Sluiter J, and Templeton D et al. Determination of Structural Carbohydrates and Lignin in Biomass. Golden (CO): National Renewable Energy Laboratory; 2011 July Report No. NREL/TP-510-42618. Contract No.: DE-AC36-08-GO28308.

[40] Willför S, Hemming J, and Leppänen AS. Analysis of extractives in different pulps - Method development, evaluation, and recommendations. Finland: Åbo Akademi University, Laboratory of Wood and Paper Chemistry; 2004-2009 Report No. B1 of the EU COST E41 action "Analytical tools with applications for wood and pulping chemistry".

[41] Hames B, Ruiz R, Scarlata C, Sluiter J, and Sluiter A. Preparation of Samples for Compositional Analysis. Golden (CO): National Renewable Energy Laboratory; 2011 June Report No. NREL/TP-510-42620. Contract No.: DE-AC36-99-GO10337.

[42] Chen Y, Stark NM, Tschabalala MA, Gao J, and Fan Y. Moisture performance of wood-plastic composites reinforced with extracted and delignified wood flour. *Proc ANTEC 2014 April 28-30th*.

[43] Horvath AL. Solubility of Structurally Complication Materials: I. Wood. *J Phys Chem Ref Data*, 35(1):77–92, 2006.

[44] Demirbas A. Methylation of wood fatty and resin acids for production of biodiesel. *Fuel*, 90(6):2273–9, 2011.

[45] Thammasouk K, Tandjo D, and Penner MH. Influence of Extractives on the Analysis of Herbaceous Biomass. *J Agric Food Chem*, 45(2):437–43, 1997.

[46] Tremel A and Spliethoff H. Gasification kinetics during entrained flow gasification - Part I; Devolatilisation and char deactivation. *Fuel*, 103:663–71, 2013.

[47] Hoekstra E, van Swaaij WPM, Kersten SRA, and Hogendoorn KJA. Fast pyrolysis in a novel wire mesh reactor: Design and initial results. *Chem Eng J*, 191:45–58, 2012.

[48] Momeni M, Yin C, Kær SK, Hansen TB, Jensen PA, and Glarborg P. Experimental Study on Effects of Particle Shape and Operating Conditions on Combustion Characteristics of Single Biomass Particles. *Energy Fuels*, 27(1):507–14, 2013.

[49] Göktepe B, Umeki K, and Gebart R. Does distance among biomass particles affect soot formation in entrained flow gasification process? *Fuel Process Technol*, 141(1):99–105, 2016.

[50] Tremel A, Haselsteiner T, Kunze C, and Spliethoff H. Experimental investigation of high temperature and high pressure coal gasification. *Appl Energy*, 92:279–85, 2012.

[51] Tremel A. Reaction Kinetics of Solid Fuels during Entrained Flow Gasification. PhD thesis, Technical University of Munich, 2012.

[52] Stiess M. *Mechanische Verfahrenstechnik 1 (in German)*. Springer, 1992.

[53] Merkus HG. *Particle Size Measurements*. Springer, 2009.

[54] Peersen OB, Wu X, Kustanovich I, and Smith SO. Variable-Amplitude Cross-Polarization MAS NMR. *J Magn Reson Ser A*, 104(3):334–9, 1993.

[55] Bennett AE, Rienstra CM, Auger M, Lakshmi KV, and Griffin RG. Heteronuclear decoupling in rotating solids. *J Chem Phy*, 103(16):6951–8, 1995.

[56] Potrzebowski MJ, Tekely P, and Dusausoy Y. Comment to ^{13}C NMR studies of α and γ polymorphs of glycine. *Solid State Nucl Magn Reson*, 11(3-4):253–7, 1998.

[57] Brunauer S, Emmett PH, and Teller E. Adsorption of Gases in Multimolecular Layers. *J Am Chem Soc*, 60(2):309–19, 1938.

[58] Yadav LDS. *Organic Spectroscopy*. Springer, 2005.

[59] Gerson F and Huber W. *Electron Spin Resonance Spectroscopy of Organic Radicals*. Wiley-VCH, 2003.

[60] Duling DR. Simulation of Multiple Isotropic Spin-Trap EPR Spectra. *J Magn Reson Ser B*, 104(2):105–10, 1993.

[61] Barsberg S, Thygesen LG, and Sanadi AR. Control of Lignin Solubility and Particle Formation Modulates its Antioxidant Efficiency in Lipid Medium: An In Situ Attenuated Total Reflectance FT-IR Study. *Environ Sci Technol*, 28(7):4539–44, 2014.

[62] Warren BE. X-ray study of the graphitization of carbon black. *Phys Rev*, 59:693–8, 1941.

[63] Stenebråten JF, Johnson WP, and McMullen J. Characterization of Goldstrike ore carbonaceous material. Part 2: Physical characteristics. *Miner Metall Process*, 17(1):7–15, 2000.

[64] Saikia BK, Boruah RK, and Gogoi PK. A X-ray diffraction analysis on graphene layers of Assam coal. *J Chem Sci*, 121(1):103–6, 2009.

[65] Leapman RD, Fejes PL, and Silcox J. Orientation dependence of core edges from anisotropic materials determined by inelastic scattering of fast electrons. *Phys Rev B*, 28:2361–73, 1983.

[66] Pettifer RF, Brouder C, Benfatto M, and Natoli CR. Magic-angle theorem in powder X-ray-absorption spectroscopy. *Phys Rev B Condens Matter*, 42(1):37–42, 1990.

[67] Daniels H, Brown A, Scott A, Nichells T, Rand B, and Brydson R. Experimental and theoretical evidence for the magic angle in transmission electron energy loss spectroscopy. *Ultramicroscopy*, 96(3-4):523–34, 2003.

[68] Schattscheider P, Hebert C, Franco H, and Jouffrey B. Anisotropic relativistic cross sections for inelastic electron scattering, and the magic angle. *Phys Rev B*, 72(4):1–8, 2005.

[69] Hebert C, Schattschneider P, Franco H, and Jouffrey B. ELNES at magic angle conditions. *Ultramicroscopy*, 106(11-12):1139–43, 2006.

[70] Finlay WH. *The Mechanics of Inhaled Pharmaceutical Aerosols. An Introduction*. Academic Press, 2001.

[71] Müller JO, Su DS, Wild U, and Schlögl R. Bulk and surface structural investigations of diesel engine soot and carbon black. *Phys Chem Chem Phys*, 9(30):4018–25, 2007.

4 Experimental investigations on biomass fast pyrolysis

4.1 Introduction

This chapter describes the results of the experimental investigation of fast pyrolysis of biomass (pinewood, beechwood, alfalfa straw, wheat straw, leached wheat straw, rice husk) and biomass major components (cellulose, hemicellulose, lignin) in a wire mesh reactor, a single particle reactor and a drop tube reactor. The aim of this study was to understand the influence of temperature (600-1400°C), intermediate and fast heating rates (10-10^4 K s^{-1}) and particle size (0.05-5 mm) on the char yield. Information on the soot yield and formation was subsequently obtained by pyrolyzing wood, straw and leached wheat straw in a drop tube reactor. This chapter closely resembles the papers entitled "Effect of fast pyrolysis conditions on biomass solid residues at high temperatures" and "Influence of fast pyrolysis conditions on yield and structural transformation of biomass char".

4.2 Effect of operational conditions on the pyrolysis in a wire mesh reactor

4.2.1 Fuels and operating parameters

Materials and procedure Wood (pinewood, beechwood) and herbaceous biomass (wheat straw, washed wheat straw, alfalfa straw, rice husk) were selected for the experimental work in a wire mesh reactor. The original biomass particles were sieved to fractions of 0.05-0.2, 0.25-0.355, 0.355-0.425, 0.425-0.6, 0.6-0.85, and 0.85-1 mm. The char yield was determined at temperatures of 600°C, 1000°C, 1250°C and 1400°C. The heating rate was varied from 10 to 3000 K s^{-1}. The effect of holding time was investigated by keeping biomass samples from 1 s to 4 s at temperatures of 600°C, 1000°C and 1250°C. The effect of larger particle size on the char yield and devolatilization time was studied in a single particle reactor. Pinewood cubes of 3 mm, 4 mm and 5 mm were prepared for the pyrolysis experiments at temperatures of 1190°C, 1350°C and 1450°C.

Char yield The influence of temperature, heating rate, particle size, holding time and biomass origin on the char yields were studied in the wire mesh reactor at TU Munich. Products resulting from the biomass pyrolysis included gases, tar, reaction water and solid char. The char yield (Y_s) was defined as the solid fraction of the reacted biomass, remaining on the mesh after an experiment on dry ash free basis (daf) excluding inorganic matter of original biomass, and it was calculated according to equation 16:

$$Y_s\,[daf, \%] = \frac{m_{mesh+char} - m_{mesh}}{(m_{mesh+biomass} - m_{mesh}) \cdot (1 - X_{water} - X_{ash})} \cdot 100 \qquad (16)$$

where X_{water} and X_{ash} is the mass fraction of moisture and fraction of ash in the original biomass. Characterization work was carried out on the combined char from several experiments. The volatile yield was determined by the difference between the total mass loss and the remaining solid fraction.

Elemental analysis In Figure 22, results of the elemental analysis of original biomasses and char, generated at different pyrolysis conditions are shown. It is observed that carbon contents in wood and herbaceous chars increase with the higher pyrolysis temperature, whereas oxygen and hydrogen contents decrease, due to the scission of weaker bonds and formation of aromatic structures favored by the higher temperature. The higher O/C ratios in the herbaceous chars compared to the beechwood can be observed under slow and fast heating at 600 and 1000°C.

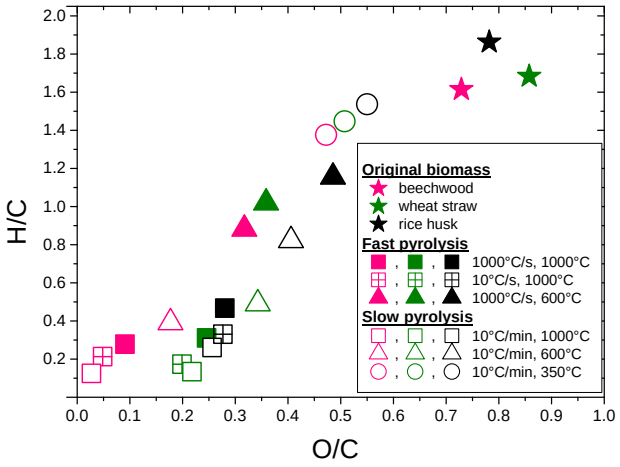

Figure 22: Elementary analysis of beechwood, wheat straw and rice husk original samples and chars from WMR (600°C; 1000 K s^{-1}, 1 s), (1000°C; 10 K s^{-1}, 1 s); (1000°C; 1000 K s^{-1}, 1 s), and tubular furnace (600 and 1000°C, 10 K min^{-1}, 10 min). The following colors were used in labels for: beechwood (pink), wheat straw (green) and rice husk (black).

Measurement uncertainty The error bars shown in Figures 23-38 and 26 and 39 represent standard deviation from the mean of the series of experiments at each condition in the WMR. The char yield data obtained for each condition was plotted as a representative average of at least five experiments. The experiments conducted at 600°C were repeated ten times due to a high uncertainty in the char yield measurement. The absolute extended uncertainty of the product yield was determined by Gaussian error propagation procedure [1], based on the equations shown in the Appendix A (Equations 63 and 64). The average standard measurement error in the present study was $\pm$ 5 wt. %, within a 90 % confidence interval for the WMR experiments. The inaccuracy in determining the char yield was mainly caused by weighting errors. The char yields obtained from both wire mesh reactors were practically the same ($<$ 1.5 %) as it was shown in Appendix A (Table 21).

The inaccuracy in determining char yield in a single particle reactor was also $\pm$ 5 wt. %, within a 90 % confidence interval. The inaccuracy in determining the char yield was mainly caused by weighting errors and compositional inhomogeneity of pinewood cubes. The pinewood log combined both sapwood and heartwood which could additionally affect devolatilization due to the differences in a distribution of organic compounds (cellulose, hemicellulose, lignin, extractives). In addition, some pinewood cubes contained high ash containing limbs.

4.2.2 Effect of temperature

Pyrolysis experiments in a N_2 flow were carried out in the wire mesh reactor. The volatile yield for a range of biomasses, sieved to 0.05-0.2 mm, with a heating rate of 1000 K s^{-1} and a holding time of 1 s was measured as a function of temperature. The holding time of 1 s was considered to be sufficient for the complete pyrolysis of particles < 0.2 mm, as reported by Werkelin et al. [2]. The char yields of pinewood, beechwood, wheat straw, alfalfa straw, leached wheat straw and rice husk are plotted versus the heat treatment temperature, on a dry and ash free basis excluding original biomass inorganic matter in Figure 23. Pinewood pyrolysis is characterized by a lower char yield in comparison to the other fuels due to the low ash content. The higher char yields of wheat straw and alfalfa straw relative to the char yields of wood, leached wheat straw and rice husk may be associated with the catalytic effect of alkali metals that affect polymerization / cross-linking.

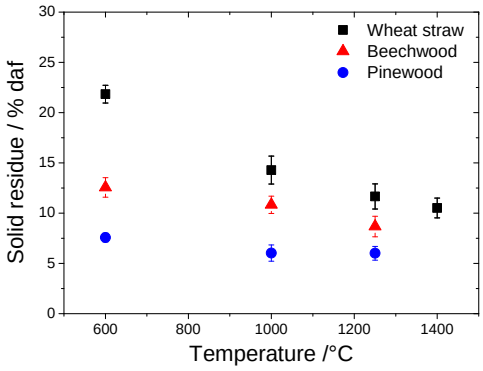

23(a): Pinewood, beechwood, wheat straw

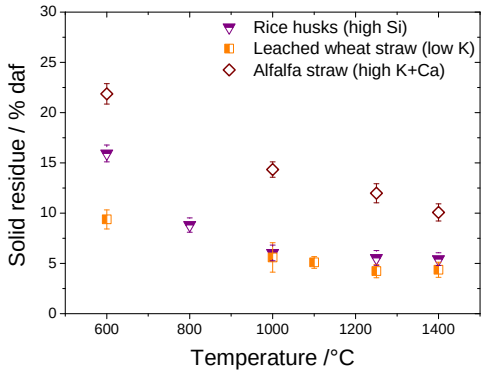

23(b): Alfalfa straw, leached wheat straw, rice husk

Figure 23: Influence of heat treatment temperature on the char yield of lignocellulosic materials, reacted in a N_2 stream in the WMR (heating rate: 1000 K s^{-1}, holding time: 1 s, particle size: 0.05-0.2 mm).

The reduced char yield for the leached wheat straw char in comparison to the untreated wheat straw is consistent with the hypothesis that K catalyzes the repolymerization and cross-linking reactions to char, as observed also by Jensen et al. [3] and Nik-Azar et al. [4]. The high level of potassium in the wheat straw and alfalfa straw may catalyze the conversion of bridges into char link, promoting faster devolatilization rates and suppressing tar formation [5], leading to the higher char yields. The lower char yield from pinewood pyrolysis in comparison to the beechwood may be related to the lower presence of K and Ca cations in the original pinewood. Interestingly, the char yield of pinewood, leached wheat straw and rice husk at temperatures above 1000°C is equally low (ca. 4 % daf). This indicates that any differences in major plant components (cellulose, hemicellulose and lignin) between straw and wood give rise to only small differences in the char yield, and in any case much smaller influence than potassium on the char formation.

The largest biomass compositional difference in this study is related to the large content of extractives and protein in the alfalfa straw, constituting up to 50 % of the total fuel carbohydrates.

The alfalfa straw has a char yield which is similar to wheat straw at T $>$ 600°C, again indicating that differences in the composition of organic matter is less important than the influence of potassium. Interestingly, the higher alkali amount in the original alfalfa straw (2.8 % of K and 1.3 % of Ca) than in the wheat straw (1.1 % of K and 0.24 % of Ca) seems to have no influence on the char yield. The effect of sodium on the decomposition cannot be clearly concluded based on its low presence in wood and herbaceous biomass, used in this study. The high Si content in the rice husk sample does not seem to affect the char yield, based on the similar char yields of rice husk (rich in Si) and leached wheat straw (low presence of Si).

4.2.3 Effect of heating rate

A wire mesh reactor can be operated over a wide ranges of heating rates and holding times. This work is carried out using a heat treatment temperature of 1000°C with a holding time of 1 s and heating rates from 10-3000 K s^{-1}. Pinewood, beechwood and wheat straw were sieved to obtain the particle size fraction of 0.05-0.2 mm. In Figure 24, the influence of heating rate is represented for pinewood, beechwood and wheat straw. In general, higher heating rates give greater mass losses for all three fuels. The most significant effect of heating rate is observed in the region between 10 and 600 K s^{-1}.

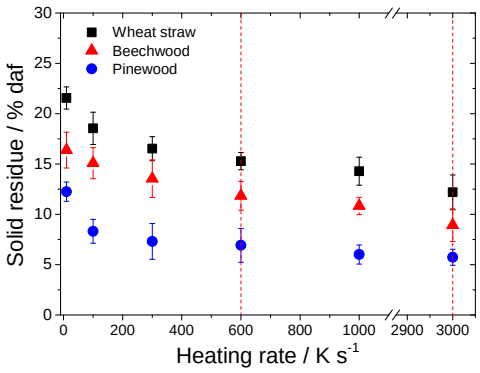

Figure 24: Influence of heating rate on the char yield of wheat straw, beechwood and pinewood, pyrolyzed in WMR (heat treatment temperature: 1000°C, holding time: 1 s) and shown as dots, and compared with the standard volatiles analysis at 900°C and shown as lines.

The tendency of a reduced influence of heating rate on the char yield above $>$ 600 K s^{-1} seems to be consistent for all applied fuels, although a smaller further drop in char yield is seen at a high heating rate of 3000 K s^{-1}. Zaror et al. [6] related the increased char yield at low heating rates to the longer residence times of volatiles in the particle, leading to predominance of secondary reactions with char, with tar cracking to form lighter compounds and char. Contrary to this, during fast heating a low molecular weight metaplast is formed due to the fast bond breaking, leading to an increased pressure inside the particle, fast volatiles evaporation, and a low char yield [7].

4.2.4 Effect of holding time

The effect of holding time in the WMR is studied for pinewood, wheat straw and leached wheat straw at 600 and 1000°C with a heating rate of 1000 K s^{-1} and particle size fractions of 0.05-0.2, 0.25-0.355, 0.355-0.425, 0.425-0.6, 0.6-0.85, and 0.85-1 mm as shown in Figure 25. At 600°C, particles of all biomasses with a mean diameter < 0.425 mm can be fully pyrolyzed within 2 s. The larger pinewood particles require a longer holding time. The char yield of smaller particles with 2 s holding time seems to become slightly lower than the char yield of larger particles with 4 s holding time. The particle fraction from 0.6 to 0.85 mm at 600°C exhibits a higher char yield than particles < 0.6 mm. The differences between pinewood particle size fractions 0.05-0.6 mm and 0.6-1 mm indicate the significance of extra- and/or intra-particle thermal resistances for larger particles.

Smaller particles are converted faster due to the larger heat fluxes, and because their temperature is more uniform (thermally thin), while the large particles have internal temperature gradients and thus a lower heat flux (W m^{-2}), leading to a slower pyrolysis. It was found for fast heating rates relevant for pulverized fuel combustion [8–11] that the assumption of thermally thin particles is no longer valid when the biomass particle size exceeds 0.2 mm. The pinewood particles between 0.05 and 0.85 mm are completely reacted within the first second of pyrolysis at 1000°C. For a complete pyrolysis of particles > 0.85 mm, 2 s holding time is required. Under the applied high heating rate (1000 K s^{-1}), the particles with a mean diameter < 0.425 mm may be considered as thermally thin, while the intra-particle heat conduction in larger particles plays an important role in the biomass char conversion (pyrolysis and char burnout), and must be accounted for in mathematical models at temperatures < 1000°C and at high heating rates. This observation is based on the almost negligible differences between char yields of particle size fractions in a range of 0.05 mm$<d_p<$0.425 mm.

The wheat straw at 600 and 1000°C and leached wheat straw at 600°C require 2 s for complete conversion. The demineralization of wheat straw decreases the required holding time for complete pyrolysis from 2 to 1 s at 1000°C. The leached wheat straw of size > 0.425 mm obtained a higher char yield at 600°C than untreated straw within 1 s. The present results show that at lower temperatures a high alkali content induces lower char yield, similarly to results of Saleh et al. [12]. Moreover, the holding time effect on the mass loss is not particularly dependent on the straw particle size. The pinewood particles tend to be more rod-like whereas wheat straw are more flake-like, based on the microscopic analysis, shown in Appendix B (Figure 77).

The flattened straw particles were probably kept aligned in the mesh pocket without any significant changes in the characteristic length over a wide range of apparent particle sizes. Thereby the required holding time for the complete pyrolysis at 600°C was shorter in comparison to the non-flattened pinewood particles, where the width may turn out to be a characteristic length. The characteristic length plays a predominant role in the fuel conversion at temperatures ≤ 1000°C with the non-sufficient holding time, so that more flattened particles yield less char. Particles of

larger thicknesses cause higher internal mass and heat transfer resistance resulting in thinner relative thickness of the char conversion region during pyrolysis. The present results show that the effect of holding time depends strongly on the heat treatment temperature.

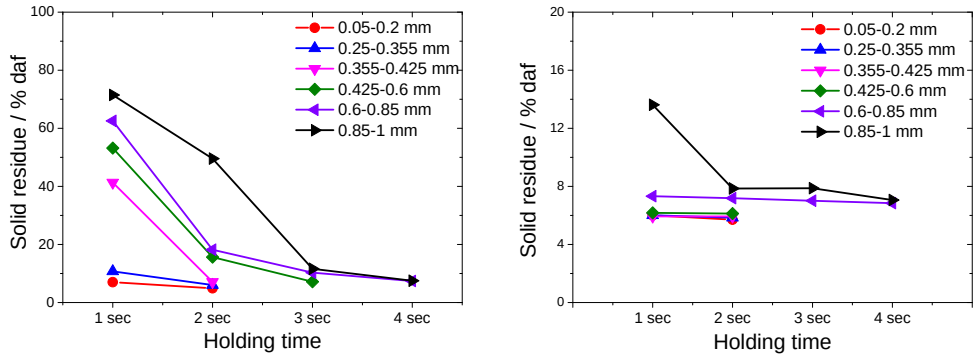

25(a): Pinewood, 600°C

25(b): Pinewood, 1000°C

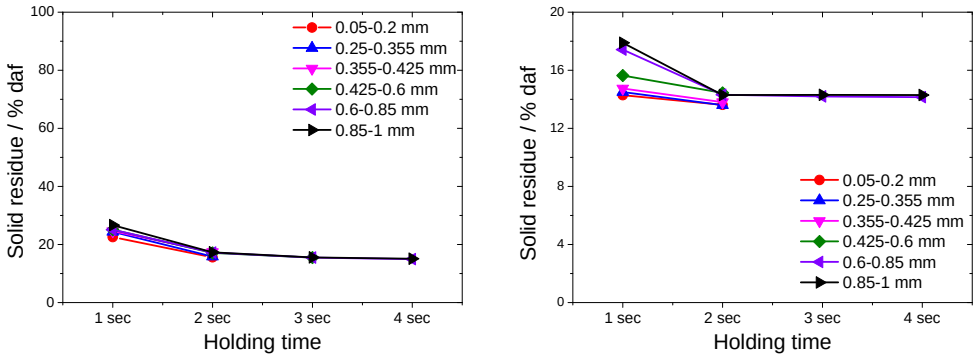

25(c): Wheat straw, 600°C

25(d): Wheat straw, 1000°C

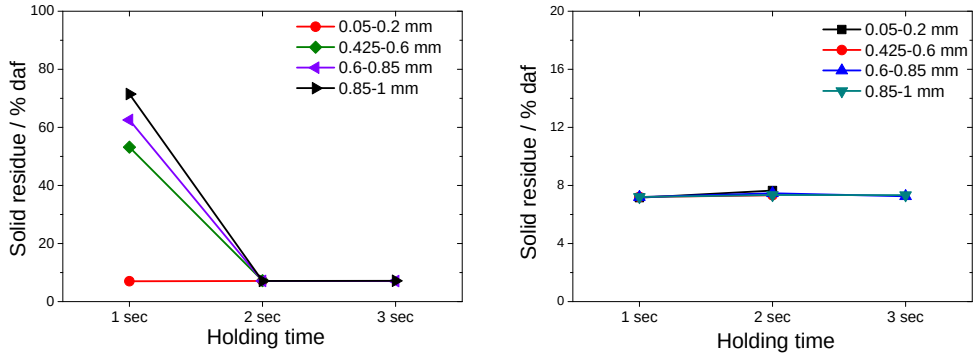

25(e): Leached wheat straw, 600°C

25(f): Leached wheat straw, 1000°C

Figure 25: Influence of holding time and particle size fraction on the pinewood, wheat straw and leached wheat straw char yield (heat treatment temperature: 600°C and 1000°C, heating rate: 1000 K s^{-1}).

The devolatilization time was also determined for cubes of 3 mm, 4 mm and 5 mm at temperatures of 1190°C, 1350°C and 1450°C by visualization with a high-speed camera of a particle in the single particle burner setup, according to investigations of Jepsen [13]. The particle was illuminated with a pocket lamp (2) as marked in Figure 26(a).

At a certain temperature, a soot cloud, surrounding the wood particle is observed indicating py-

rolysis. In the single-particle burner, soot formation occurs under the reducing condition. The oxygen level was kept very low during the experiments to eliminate char and soot oxidation. At the beginning of an experiment, a wood particle was placed in the center of the reactor. The devolatilization time is defined as the time from the soot cloud is seen until it extinguishes and char gasification begins. As the devolatilization time increases, the soot cloud, marked with the red ellipsoid (1), becomes more visible as shown in Figure 26(a).

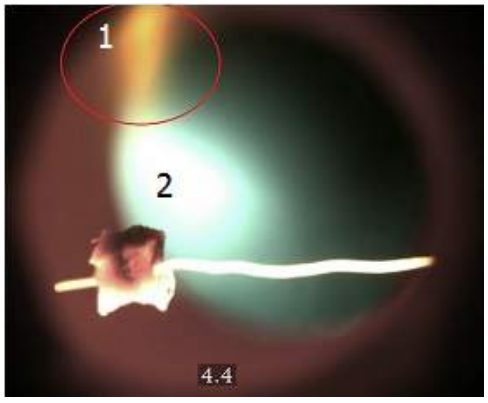

26(a): Flame surrounding a pinewood particle (4 mm), 1350 °C

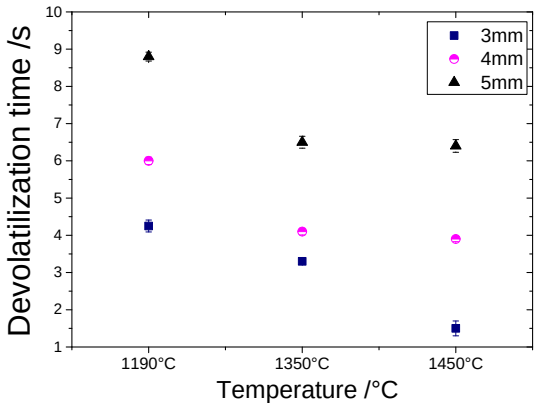

26(b): Devolatilization time of pinewood particles 3-5 mm

Figure 26: Influence of particle size and temperature on the devolatilization time in SPR with T = 1190°C (O_2 = 0.02, H_2 = 0.06, H_2O = 0.23, N_2 = 0.7) vol %, T = 1350°C (O_2 = 0.05, H_2 = 0.2, H_2O = 0.2, N_2 = 0.55) vol %, T = 1450°C (O_2 = 0.15, H_2 = 0.37, H_2O = 0.04, N_2 = 0.44) vol %; In Figure 24.1, the numbers mean: (a) a visible soot cloud, marked with the red ellipsoid (b) illumination of the particle with the pocket lamp.

In the pyrolysis experiments, the gas velocity was kept nearly constant to eliminate fluid dynamical effects on the results. In Figure 26(b), an increasing temperature is seen to reduce the time of devolatilization for different cube sizes. Interestingly, the devolatilization time of the 3 mm cube significantly reduces from 1350 to 1450°C, while it is nearly constant for the 4 mm and 5 mm cubes at these temperatures. This can be explained by the surface area/volume ratio of 3 mm particle equal to 2 mm^{-1}, while the 4 mm and 5 mm cubes indicate lower surface area to volume ratios equal to 1.5 mm^{-1} and 1.2 mm^{-1}. The heat up of these particles are thus more limited by the internal non-uniform heat transfer affecting devolatilization. In larger particles (4-5 mm) the internal heat transfer resistance are more pronounced than in smaller particles (0.05-1 mm). The devolatilization time of the 3 mm cube decreases from 4.5 to 1 s with the higher temperatures. The data for the 4 mm and 5 mm pinewood cubes shows smaller differences between conversion times of ca. 2.5 s at the temperature range of 1190-1450°C.

4.3 Effect of operational conditions on the pyrolysis in a drop tube reactor

4.3.1 Fuels and operating parameters

Materials and procedure Pinewood, beechwood, Danish wheat straw, leached Danish wheat straw and alfalfa straw were selected for the fast pyrolysis study. The fuels were milled on a Retsch rotor mill RZ200 and sieved to a particle size fraction of 0.2-0.4 mm. In addition, pinewood was milled and sieved to a larger particle size fraction of 0.85-1 mm. Carbon and hydrogen balances were prepared for the pinewood, beechwood, wheat straw and alfalfa straw. The product yields from leached wheat straw were limited to the char and soot determination. Ash compositional analysis of the wheat straw was not conducted in the present investigation.

Three temperatures (1000°C, 1250°C and 1400°C) were selected for the experimental work in the DTF. In the present study, the experiments were conducted by feeding ≈ 5 g of biomass at a rate of 0.2 g min^{-1}. Both primary (0.18 m^3 min^{-1} measured at 20°C and 101.3 kPa) and secondary (0.0048 m^3 min^{-1} measured at 20°C and 101.3 kPa) feed gases were N_2. The residence time of fuel particles was estimated to be about 1 s, taking into account density changes during pyrolysis [14].

Solid residue definition Three different solid residues were distinguished in the present study, namely char, soot and coke. Char and soot were collected in the char bin and on the filter in a temperature range of 1000 to 1400°C. Char yield of biomass pyrolyzed in the WMR is calculated on dry ash free basis (daf) excluding inorganic matter of original biomass and char in equation 17:

$$Y_s\,[daf,\%] = \frac{(m_{mesh+char} - m_{mesh}) \cdot (1 - Y_{ash})}{(m_{mesh+biomass} - m_{mesh}) \cdot (1 - X_{water} - X_{ash})} \cdot 100 \tag{17}$$

where X_{water} and X_{ash} is the mass fraction of moisture and fraction of ash in original biomass, and Y_{ash} is the mass fraction of inorganic matter in char. Char yield of biomass pyrolyzed in the DTF is calculated in equation 18:

$$Y_s\,[daf,\%] = \frac{m_{char} \cdot (1 - Y_{ash})}{m_{biomass} \cdot (1 - X_{water} - X_{ash})} \cdot 100 \tag{18}$$

The char yield of the Si-rich wheat straw and rice husk in the EFR including ash was quantified by using Si as a non-volatile tracer element, as proposed by Damø et al. [15], according to equation 19:

$$Y_s\,[db,\%] = \frac{c_{Si,fuel}}{c_{Si,char}} \cdot 100 \tag{19}$$

$c_{Si,fuel}$ is Si content in dry fuel, $c_{Si,char}$ is Si content in dry char.

Coke (< 5 % in a mass balance), the carbonaceous material deposited on the reactor walls, was quantified after each experiment by oxidation followed by measurement of the concentration of CO_2 by a micro gas chromatograph.

Measurement uncertainty For the DTF, the measurement error was calculated for each component of a mass balance (C_xH_y+vapor, gas, coke, soot). The absolute extended uncertainty of

the product yield was determined by a Gaussian error propagation procedure [1]. The average standard measurement error in the present study was ± 2 wt. %, within a 95 % confidence interval for the DTF experiments based on at least three replicates for each operating condition. Carbon and hydrogen balances for pinewood required at least seven experiments at 1250°C due to the high soot yield, and thereby challenges to collect all generated soot. The volatile measurements done with a micro gas chromatograph and soot loss in the DTF setup were major sources of an experimental error (< 15 %) as shown in the calculated carbon/hydrogen balances in chapter 4.3.2. Another source of error was the non-measured fractions of vapor, tars and larger hydrocarbons in the DTF. The investigations on the leached wheat straw were carried out after cleaning the drop tube reactor with the oxygen for several hours at 1400°C, limiting options for a product contamination. However, it was not excluded that the inorganic matter of previously used fuels i.e. black liquor could remain on the DTF tube walls.

Elemental analysis Figure 27 shows the composition of char from woody and herbaceous biomass contains differences in terms of H/C and O/C atomic ratios. During fast pyrolysis of wood and also of herbaceous biomass, but at a higher level, the H/C and O/C ratios decrease rapidly and become constant with the highly aromatic structures above 1000°C, indicating almost complete removal of hydrogen and oxygen containing functional groups. It was observed that the herbaceous chars have a higher H/C level than the wood chars. The char yield decrease of alfalfa straw and wheat straw between 1000 and 1400°C may be additionally related to further reduction of H/C and O/C ratios, in addition to the high-temperature ash reactions.

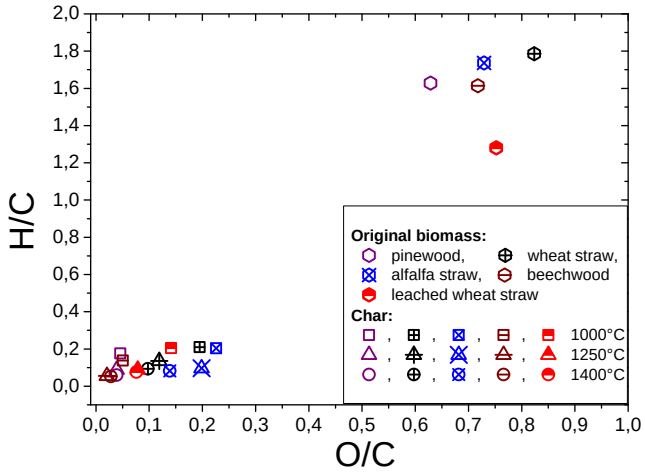

Figure 27: Elemental analysis of original biomasses and their chars, reacted in the DTF at 1000, 1250 and 1400°C.

4.3.2 Carbon and hydrogen balances

The mass balances of the DTF experiments with respect to measured solid residues (char, soot, coke) and major gaseous products (CO_2, H_2, CO, CH_4, C_3H_8, C_2H_4, C_2H_2) in dependency

on the pyrolysis temperature are shown in Figure 28. The amount of vapor, tars, and larger hydrocarbons was not measured in the present study, but estimated by difference from the mass balance. Carbon and hydrogen balances represent an average of at least two measurements. During fast pyrolysis, mainly gaseous products were formed, along with lower amounts of solid residues at higher temperatures.

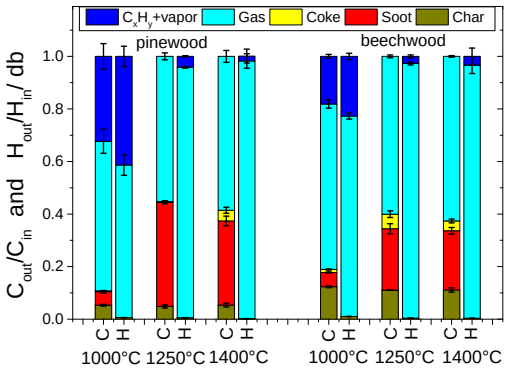

28(a): Pinewood and beechwood

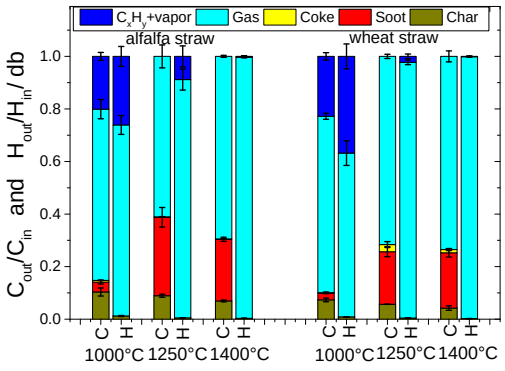

28(b): Alfalfa straw and wheat straw

Figure 28: Carbon and hydrogen distribution of (a) pinewood, beechwood and (b) alfalfa straw, straw straw at 1000, 1250 and 1400°C in the DTF.

At 1000°C, the yield of larger hydrocarbons and vapor was significantly larger than at higher temperatures. The carbon in wood and herbaceous biomasses was converted to gas, soot and char. Hydrogen was present mostly in gaseous products, tars, larger hydrocarbons and vapor at 1000°C. Almost all hydrogen ($> 90\,\%$) was found in the form of gaseous products above 1250°C for wood and herbaceous biomasses. Higher temperatures suppressed tar formation and enhanced hydrogen and oxygen release to gaseous products.

4.3.3 The solid product yield

Char yield The wire mesh reactor (WMR) results were obtained by Trubetskaya et al. [16]. In that study, the char yield (daf) was represented including inorganic matter in char relative to the biomass on dry and ash-free basis. In the present work, char yields of wood and herbaceous biomass in both reactors are shown on dry ash free basis (daf), excluding inorganic matter in char relative to original biomass (daf) in Figure 29. The biomass char yield at fast pyrolysis conditions depends strongly on the biomass origin, temperature and heating rate. Straw (herbaceous) samples showed higher char yields compared with wood and leached wheat straw due to the presence of alkali metals as known from the literature [3, 17–19].

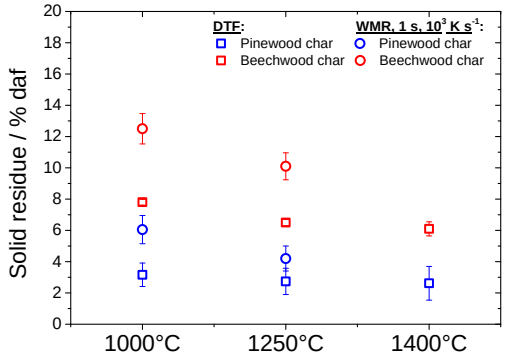

29(a): Pinewood and beechwood

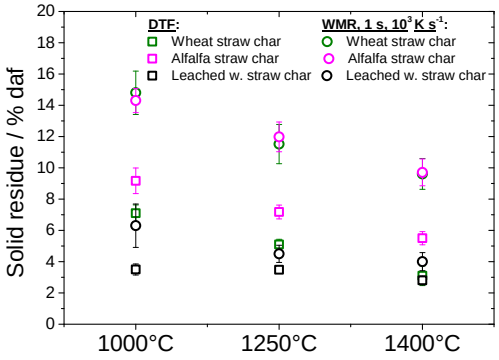

29(b): Alfalfa straw, wheat straw, leached wheat straw

Figure 29: Char yield comparison of (a) pinewood, beechwood and (b) alfalfa straw, wheat straw and leached wheat straw, reacted in the WMR (heating rate: 1000 K s^{-1}, particle size: 0.05-0.2 mm) [16] and DTF (0.2-0.4 mm) at 1000, 1250 and 1400°C.

As a general trend, the char yield of beechwood, wheat straw and alfalfa straw decreased with increasing temperature, indicating a dependency of the char yield on the heat treatment temperature. On the other hand, the char yield of pinewood and leached wheat straw decreased only slightly between 1000 and 1400°C, being lower than the char yield of other fuels at 1000°C. Interestingly, the char yield of herbaceous biomasses continued to decrease between 1250 and 1400°C, whereas the char yield of pinewood, beechwood and leached wheat straw remained almost unaltered.

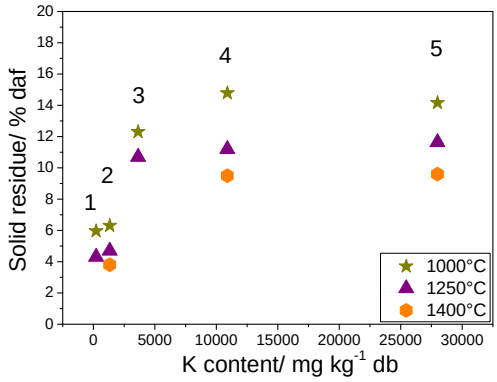

30(a): Char yield versus K element (WMR)

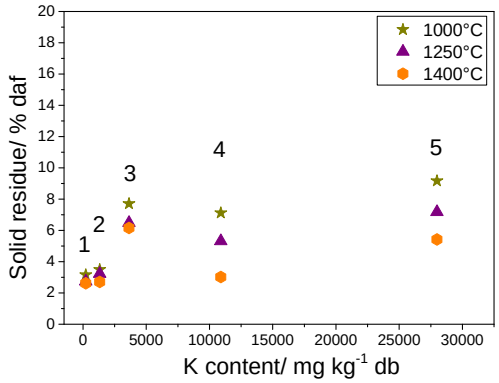

30(b): Char yield versus K element (DTF)

Figure 30: Char yield versus potassium content in the fuel obtained from pyrolysis of pinewood (1), leached wheat straw (2), beechwood (3), wheat straw (4) and alfalfa straw (5). (a) WMR at (heat treatment temperature: 1000, 1250 and 1400°C, heating rate: 1000 K s^{-1}, holding time: 1 s); (b) DTF.

A similar trend in terms of the continuously decreasing char yield by wheat straw (rich in K, Si) and alfalfa straw (rich in Ca, K) was attributed to high-temperature ash reactions, leading to the volatile ash release, and affecting an organic matter release. The results indicated that the influence of alkali on the char yield at high heat treatment temperatures is more pronounced at low

and intermediate heating rates than at fast heating rates in the DTF as shown in Figure 30. The char yields of pinewood and beechwood showed significant differences, possibly due to differences in lignin content, presence of temperature stable extractives, and alkali metal content (higher in beechwood).

As a general trend, the char yield of beechwood, wheat straw and alfalfa straw decreased with increasing temperature, indicating a dependency of the char yield on the heat treatment temperature. On the other hand, the char yield of pinewood and leached wheat straw decreased only slightly between 1000 and 1400°C, being lower than the char yield of other fuels at 1000°C. The continuous decrease in char yield from wheat straw (rich in K, Si) and alfalfa straw (rich in Ca, K) was attributed partly to high-temperature ash reactions, leading to the volatile ash release, and affecting the organic matter release. The results indicate that the influence of alkali on the char yield is more pronounced at low and intermediate heating rates than at fast heating rates in the DTF as shown in Figure 30.

The results showed that there is a clear difference between char yields in the WMR and DTF. The char yield in the DTF was 3-7 % wt. (daf) lower than that in the WMR, possibly due to the differences in heating rate and residence time. The pyrolysis in the WMR was carried out with a lower heating rate (1000 K s^{-1}) than in the DTF (10^4-10^5 K s^{-1}). When the holding time in the WMR was increased from 1 to 2 s, the char yield became slightly lower [16].

Soot yield Figure 31 shows the soot and char yields, each separated into organic matter and ash. The soot yield varied between different biomasses at similar operational conditions. The highest soot yield was observed during pinewood fast pyrolysis. The soot yield increased with temperature, reaching a peak value at 1250°C, and slightly decreased at higher temperatures, corresponding to the well-known soot yield curvature [20].

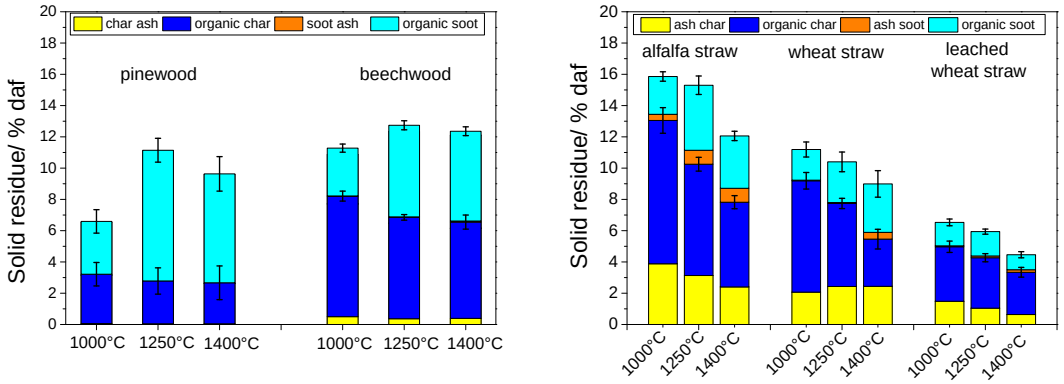

31(a): Pinewood and beechwood

31(b): Alfalfa straw, wheat straw, leached wheat straw

Figure 31: Soot and char yields of (a) pinewood, beechwood and (b) alfalfa straw, wheat straw and leached wheat straw, reacted at 1000-1400°C in the DTF (wt. % relative to the original biomass). The total yield of soot and char is separated in ash and organic matters. The error bars characterize the deviations between the total yields of the char and soot.

Figure 31 shows large differences in the soot yield of wood, leached wheat straw and herbaceous biomass. The fact that beechwood and leached wheat straw exhibit major differences in soot yield despite similar alkali (i.e. K^+) and holocellulose contents indicate that these parameters are of minor importance for the soot fraction. Instead, lignin and extractives in the original biomass possibly are important for the soot yield. The leaching of alkali from wheat straw resulted in a removal of lignin and other organic compounds as shown in Table 4, leading to the decreased formation of PAH precursors, and thereby to lower soot yields. Williams et al. [21] suggested that biomass with a high content of lignin may form larger soot fractions due to its ability to generate phenolic tars. A significant fraction of aromatic tars and soot originates from lignin pyrolysis, mainly composed of guaiacol and syringol-type units [22–24]. Ross et al. [25] stated that wood soot contains PAH material, promoted by the presence of acetylene at higher temperatures. The suggestion is consistent with the gas measurement results of the present study. The measured C_2H_2 concentration is up to 0.05 % volume fraction in inert nitrogen during fast pyrolysis of wood and herbaceous biomasses at 1000°C shown in Figure 32. With increasing temperature, the C_2H_2 yield decreased, whereas the soot yield increased. Moreover, C_2H_4 might affect the soot yield at high temperatures, facilitating PAH molecule growth [25]. The high concentration of resin acids in pinewood could increase the soot yield in addition to a stronger formation of PAH precursors [26, 27].

4.3.4 Volatile gas composition

The concentrations of H_2, CO, CO_2 and C_xH_y (CH_4, C_2H_2, C_2H_4) are shown in Figure 32. The gas composition changed significantly with increasing heat treatment temperature. Higher temperatures favor cracking of the volatile hydrocarbon products, increasing the yield of H_2 generated mainly from dehydrogenation. Soot formation could lead to increase in the yields of H_2 and CO between 1000 and 1250°C due to polymerization and dry reforming reactions, equations 20 and 21.

$$\text{Hydrocarbon polymerization}: \ \mathrm{C_nH_m} \rightarrow \left(\frac{\mathrm{m}}{2}\right)\mathrm{H_2} + \mathrm{nC_{soot}} \tag{20}$$

$$\text{Dry reforming}: \ \mathrm{C_nH_m} + \mathrm{nCO_2} \rightarrow \mathrm{2nCO} + \left(\frac{\mathrm{m}}{2}\right)\mathrm{H_2} \tag{21}$$

$$\text{Steam reforming}: \ \mathrm{C_nH_m} + \mathrm{nH_2O} \rightarrow \left(\mathrm{n} + \frac{\mathrm{m}}{2}\right)\mathrm{H_2} + \mathrm{nCO} \tag{22}$$

$$\text{Water gas shift}: \ \mathrm{CO} + \mathrm{H_2O} \leftrightarrow \mathrm{H_2} + \mathrm{CO_2} \tag{23}$$

The yield of CO_2 decreased and those of CO and H_2 increased for all biomass at temperatures above 1250°C due to dry (equation 21) and steam reforming (equation 22) and the water-gas shift reactions (equation 23).

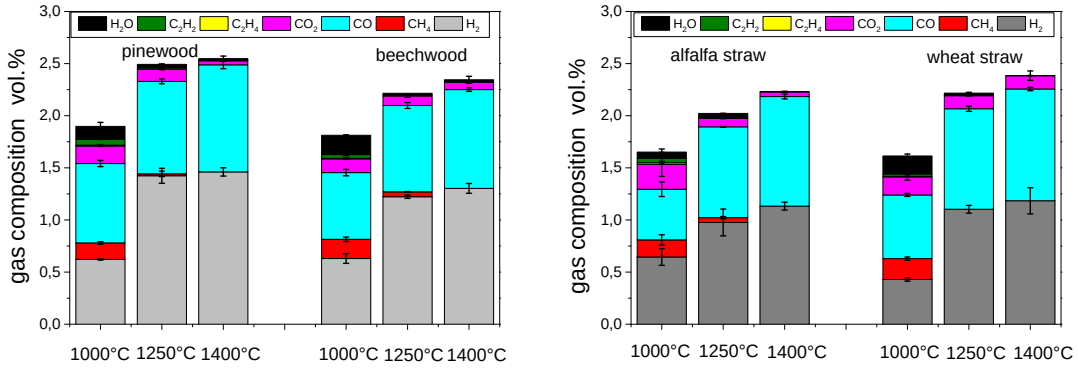

32(a): Pinewood and beechwood

32(b): Alfalfa straw and wheat straw

Figure 32: Gas composition of (a) pinewood, beechwood and (b) alfalfa straw, wheat straw from the DTF (% volume fraction), reacted at 1000 °C, 1250 °C and 1400 °C.

In the literature [28–31], the larger fractions of H_2 and CO and a lower fraction of CO_2 along with lower yields of char were related to self-gasification in a drop tube reactor. In order to evaluate a self-gasification effect on the char yield in the DTF, a uniform reaction particle model was used under assumption that the char gasification was influenced by both chemical kinetics and external mass transfer. The carbon consumption rate by gasificaition for a spherical char particle (0.07 mm) is proportional to the external area and calculate in equation 24:

$$\frac{dN_{char}}{dt} = -\frac{4 \cdot \pi \cdot R_0^2}{R \cdot T} \cdot k_g \cdot (p_b - p_s) \cdot \psi, \qquad k_g = \frac{Sh \cdot D_{CO_2}}{2 \cdot R_0} \tag{24}$$

where k_g is the mass transfer coefficient for small particles in the Stokes regime (Sh = 2), D_{CO_2} is the diffusion coefficient, determined according to Chapman-Enskog correlation [32], ψ is the stoichiometric coefficient (ψ = 1), p_b and p_s are the CO_2 pressures of the bulk and on the external char surface. The chemical reaction rate controlled by intrinsic kinetics (r_2) was determined as shown in equation 25 under the assumption (n=1):

$$\frac{dN_{char}}{dt} = k_s \cdot p_s^n \cdot N_{char}, \qquad N_{char} = \frac{\rho_c \cdot V}{M_c} \tag{25}$$

where N_{char} is the total number of moles of carbon in the particle, M_c is the molecular weight of carbon, ρ_c is the density of carbon, R_0 is the radius of a particle and k_s is the rate constant that was calculated from the k_0 and E_a parameters, which were taken from the linear regression of thermogravimetric data (in 5 % volume fraction CO_2) shown in chapter 6, assuming a first order reaction. The residence time, when self-gasification may occur, was calculated by difference of the estimated residence time in the DTF (1 s) and devolatilization time ($t_{devol} \approx 0.4$ s; d_{wood} = 0.32 mm; aspect ratio (cylinder-like); T_w = 1352°C; T_g = 1037°C) taken place from the pyrolysis experiments in the entrained-flow reactor of Lu et al. [33]. The effective reaction rate (r_{eff}) was calculated by combining equations 24 and 25. A percentage of the chemical kinetics control rate on the gasification (α) was calculated in equation 26:

$$\alpha = \frac{\frac{1}{r_2}}{\frac{1}{r_1} + \frac{1}{r_2}} \tag{26}$$

The fractional conversion (X_p) of the particle was calculated for the chemical kinetics controlled reaction in equation 27 under the assumption (n=1):

$$1 - X_p = exp(-k_s \cdot p_s^n \cdot t) \tag{27}$$

The results of calculations on self-gasification are shown in Table 5.

Table 5: Calculation on self-gasification of char ($x_{Ma,min}$ = 0.07 mm) based on parameters derived from thermogravimetric measurements in 5 % volume fraction CO_2 and operational parameters of DTF pyrolysis.

		Pinewood			Wheat straw		
Temperature	Unit	1000°C	1250°C	1400°C	1000°C	1250°C	1400°C
		Given parameters					
k_0	s^{-1}	$1{\cdot}10^6$	$3{\cdot}10^8$	$2{\cdot}10^8$	$7{\cdot}10^4$	$1{\cdot}10^4$	$1{\cdot}10^6$
E_a	kJ mol^{-1}	193	262	273	167	179	230
CO_2	% volume fraction	0.164	0.158	0.038	0.372	0.609	0.097
		Calculated parameters					
		$x_{Ma,min}$ = 0.07 mm					
r_{eff}	mol s^{-1}	$1{\cdot}10^{-9}$	$1{\cdot}10^{-9}$	$4{\cdot}10^{-10}$	$3{\cdot}10^{-9}$	$5{\cdot}10^{-9}$	$9{\cdot}10^{-10}$
N_{char}/r_{eff}	s	3.5	3.2	12.5	1.5	0.8	4.9
α	%	100	97	95	100	100	99
X_p		0	0.01	0	0	0	0

The calculations shown in Table 5 suggested that the self-gasification reaction is slow under the present conditions. The differences observed in the char yields between the WMR and DTF were mainly attributed to changes in heating rate and not self-gasification.

4.3.5 Alkali transformations of herbaceous biomasses

Char alkali The weight of each inorganic element retained in alfalfa and wheat straw char from DTF is shown in Figure 33, based on the original sample weight.

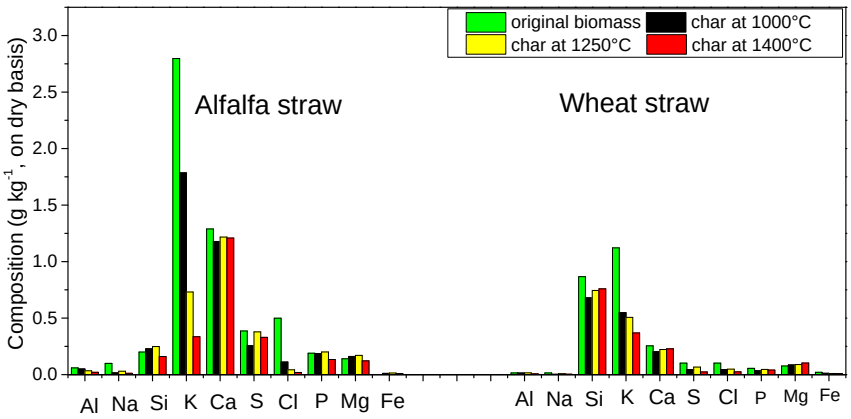

Figure 33: Ash elemental retention on the ash basis of original alfalfa and wheat straw and their chars (g kg^{-1} sample on dry basis), reacted at 1000, 1250 and 1400°C in the DTF.

The main difference between the composition of the two fuels was the ash content, which was higher (7.2 %) in alfalfa straw than in wheat straw (4.1 %). Wheat straw char contained predominantly Si, K and Ca elements, whereas the alfalfa straw char mostly consisted of Ca, K, S, Si, P and Mg. The original alfalfa straw was characterized by a high level of K and Ca, and therefore forming mainly K and Ca rich compounds in the char.

The inorganic composition of original wheat straw showed a large fraction of Si (seven times larger than in alfalfa straw), leading to the formation of silicates during devolatilization. Thermodynamic equilibrium calculations of gas and solid phases, performed with the Factsage software, indicated that under reducing conditions potassium in the alfalfa and wheat straw chars was most likely present as chlorides and silicates. In addition, potassium and calcium could be present as carbides in the alfalfa straw. In the wheat straw char, calcium was obtained as a silicate.

Soot inorganic content The beechwood and straw soot clusters contained both organic matter and minerals as shown in Figure 34. The mineral compounds in the soot arose from the condensation of inorganic species from the gas phase onto the soot. It appeared that the inorganic elements in alfalfa and wheat straw soot mainly consisted of K, Cl and S. The high levels of K and Cl in the soot matter was probably caused by the KCl release under fast heating in the DTF.

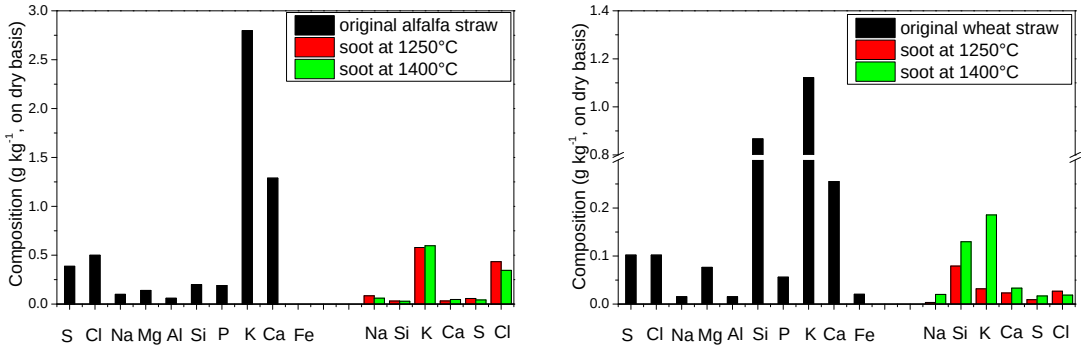

34(a): Alfalfa straw

34(b): Wheat straw

Figure 34: Ash compositional analysis of (a) alfalfa straw and (b) wheat straw inorganic matter incorporated with the soot particles obtained at 1250°C and 1400°C in the DTF and shown in g kg^{-1} on dry basis.

The potassium was found to be incorporated with both alfalfa and wheat straw soot samples. The K release from wheat straw at 1400°C was higher compared with that from Si lean alfalfa straw. The content of K and Cl elements in the wheat straw soot increased significantly in a temperature range of 1250-1400°C compared to the alfalfa straw soot where the K and Cl levels remained unaltered with the higher temperature. Knudsen et al. [34] experimentally determined that the release of K during combustion at high temperatures (900-1150°C) depends on the Si content of the biomass due to the incorporation of K into silicate structures. In the present study, the Si rich wheat straw probably released less K than the Si lean alfalfa straw. The lower Cl

content in the wheat straw could indicate that K was released in the form of KOH or to a minor extent in the form of KCl [35]. The high levels of K in the inorganic fraction of alfalfa straw soot were probably caused by the presence of Cl in the fuel that enhanced the release of K in fast pyrolysis [36]. Almost all Cl was probably released already at 500°C mostly in the form of HCl(g) and therefore the lower K release by evaporation of KCl(g) could be expected at higher temperatures [37]. Nearly all Cl and close to 20 % of the total potassium in alfalfa straw was released at high temperatures.

As it can be seen in Figures 33 and 34, a high level of sulfur was observed in both char samples. At fast pyrolysis conditions, up to 15 % of the total sulfur in alfalfa and wheat straw samples was released at 1250 and 1400°C. Knudsen et al. [36] reported that sulfur remained in the form of inorganic sulfides at pyrolysis conditions above 600°C if Ca and K are not fixed in silicates. The present results showed that no significant sulfur was released from alfalfa and wheat straw at high temperatures probably due to the incorporation with K and Ca. As it can be seen in Figure 34, a high level of sulfur (about 0.8 wt. %) was observed in both soot samples. The Factsage equilibrium calculation showed that sulfur was most likely released as H_2S gas, in agreement with literature results [38, 39]. Hydrogen sulfide could possibly react with soot active sites or with metals, as shown by Cal et al. [40]:

$$\mathrm{C} + \mathrm{H_2S} \rightarrow \mathrm{C\text{-}S} + \mathrm{H_2} \tag{28}$$

$$\mathrm{C\text{-}M} + \mathrm{H_2S} \rightarrow \mathrm{C\text{-}M\text{-}S} + \mathrm{H_2} \tag{29}$$

4.4 Effect of particle size on pinewood pyrolysis

4.4.1 Carbon and hydrogen balances

The mass balances of small (0.2-0.4 mm) and large (0.85-1 mm) pinewood particles are compared in Figure 35(a). The mass balances are shown with respect to measured solid and volatile products in dependency on the heat treatment temperature in the DTF. At 1000°C, the yield of larger hydrocarbons from pyrolysis of both particle size fractions was significantly larger than at higher temperatures. Hydrogen was present mostly in gaseous products, tars, larger hydrocarbons and vapor at 1000°C. Almost all hydrogen (> 90 %) was found in the form of gaseous products above 1250°C for both particle size fractions as shown in Figure 36.

The char yield of large particles was higher compared to smaller pinewood particles, and decreased from 8 to 5 % (daf) in a temperature range of 1000-1400°C. The larger particles almost reached the complete conversion in a temperature range of 1250-1400°C, whereas significantly longer residence time (> 1.5 s) is required for the complete devolatilization of pinewood at 1000°C based on the thermogravimetric analysis of char shown in Figure 36.

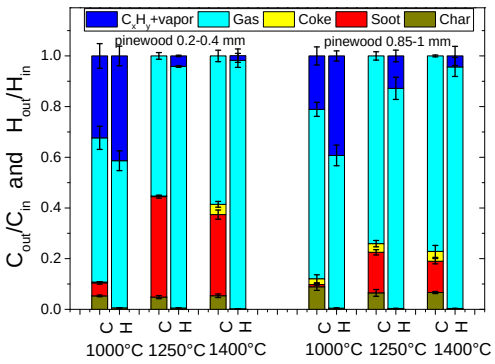

35(a): Carbon and hydrogen distribution

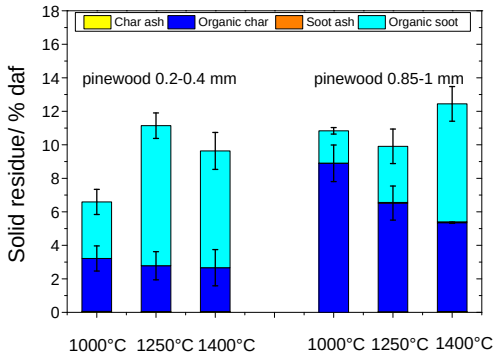

35(b): Soot and char yields (wt. % relative to the original biomass)

Figure 35: (a) Carbon and hydrogen distribution of 0.2-0.4 mm and 0.85-1 mm pinewood particles pyrolyzed at 1000°C, 1250°C and 1400°C in the DTF; (b) Influence of particle size on the pinewood soot and char yields shown as inorganic and organic fractions.

Higher temperatures suppressed tar formation and enhanced hydrogen and oxygen release to gaseous products for both particle size fractions. However, the tar formation from pyrolysis of larger wood particles was stronger, whereas the soot yield was twice lower compared to smaller particles. The lower soot yields were related to the less formed PAH precursors. Tar inside larger particles underwent secondary reactions due to the lower heat flux, leading to a slower pyrolysis and thereby higher char yields and less soot, corresponding to investigations of Miller and Bellan [41]. They reported that secondary reactions occurring in larger particles strongly decreased the tar release in pyrolysis. Figure 35(b) shows the increased soot formation at higher temperatures in pyrolysis of larger pinewood particles, probably due to the faster heat flux and less secondary reactions within the particles.

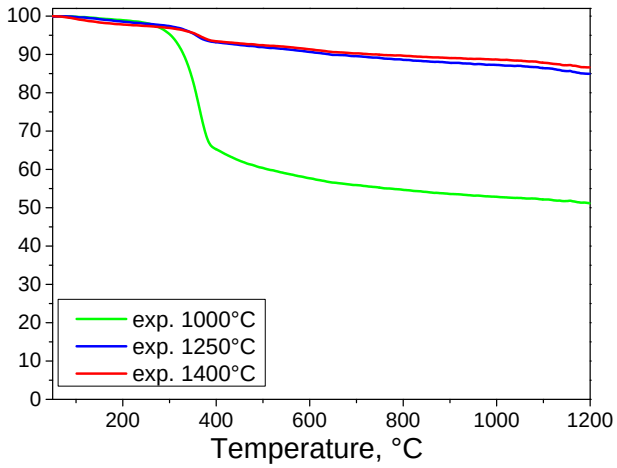

Figure 36: Thermogravimetric experiments (in N_2) on pinewood char generated during pyrolysis of larger particles (0.85-1 mm) in the DTF at 1000, 1250 and 1400°C.

4.4.2 Volatile gas composition

The gas compositions from pyrolysis of small and large pinewood particles are compared in Figure 37. The large wood particles formed less hydrogen. At 1000°C more CO_2 was released from pyrolysis of larger pinewood particles, whereas above 1250°C the differences in CO_2 yield became less dependent on a particle size. The differences in a gas yield in pyrolysis of smaller and larger pinewood particles were small.

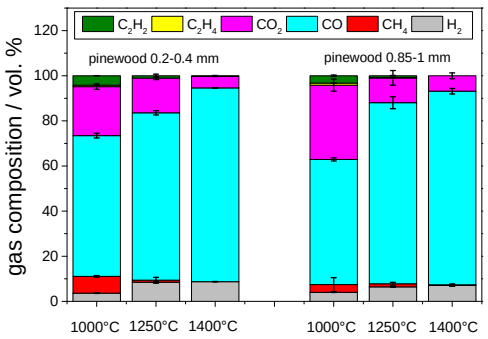

37(a): Gas composition (% volume fraction)

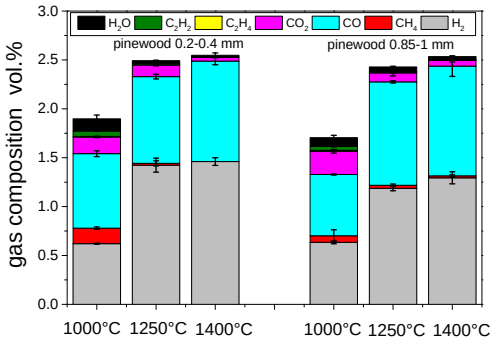

37(b): Gas composition (% volume fraction in nitrogen)

Figure 37: Gas composition in (% volume fraction) and (% volume fraction in nitrogen) of biomass samples from the DTF, reacted at 1000, 1250 and 1400°C.

The evaluation of a self-gasification effect on the char yield of smaller pinewood particles (0.2-0.4 mm) suggested that the reaction was controlled by the chemical kinetics, and therefore self-gasification did not influence the char yield of larger pinewood particles (0.85-1 mm) as illustrated in Figure 37.

4.4.3 The solid product yield

The effect of particle size (0.05-0.2, 0.25-0.355, 0.355-0.425, 0.425-0.6, 0.6-0.85, 0.85-1 mm) was studied using pinewood, wheat straw and leached wheat straw. The experiments were carried out at 1000°C and 1250°C with a heating rate of 1000 K s^{-1} and 2 s holding time. The experimental results obtained at 600°C clearly indicate that a holding time of 1 s was not enough to convert particles above 0.355 mm, and the results are shown in Appendix A. The char yields shown in Figure 38 and supported by the experimental investigations discussed in chapter 4.2.4 indicated that the pinewood, wheat straw and leached wheat straw particles were completely pyrolyzed.

The char yields are illustrated in Figure 38. By raising the temperature from 1000°C up to 1250°C, the char yield decreases for all particle sizes. The experimental data in this work shows a slight char yield growth when a particle size is increased from 0.6 mm to 1 mm at 1000°C and 1250°C, indicating a slower pyrolysis for the large particles which leads to an increased char yield. Yet, it seems that the particles size change from 0.05 to 1 mm of all biomasses with the 2 s holding

time has less influence on the char yield than the heat treatment temperature.

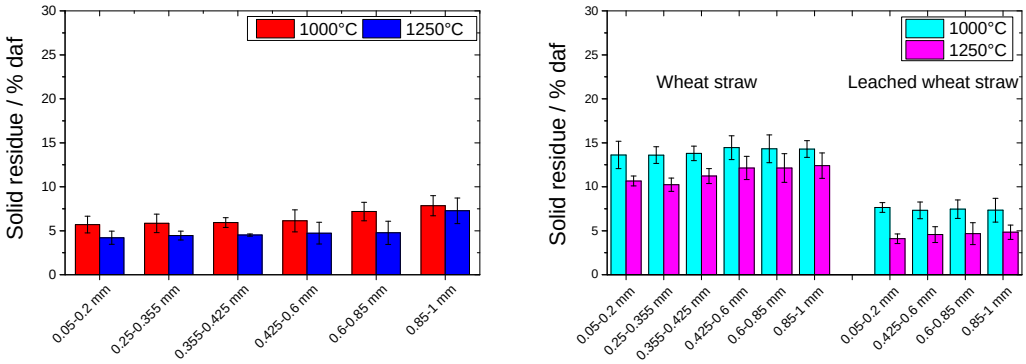

38(a): Pinewood

38(b): Wheat straw and leached wheat straw

Figure 38: Influence of particle size on the char yield of pinewood, wheat straw and leached wheat straw, pyrolyzed in WMR (heat treatment temperature: 1000°C and 1250°C, heating rate: 1000 K s^{-1}, holding time: 2 s, particle size: 0.05-1 mm). The char yield was calculated on daf basis excluding the mass fraction of water and inorganic matter of original biomass.

In Figure 38(b), the results of pinewood pyrolysis are compared with the results for wheat straw and leached wheat straw in order to understand the effect of biomass particle size in dependency on the biomass origin. The wheat straw and leached wheat straw show also a slightly increased char yield as the particle sizes increase from 0.05 mm to 1 mm at 1000°C and 1250°C. The char yield of pinewood at 1000°C and 1250°C is similar to that of leached wheat straw results.

Figure 39 shows the char yields obtained in the wire mesh reactor, drop tube reactor and single particle reactor for the of small (0.2-0.4 mm) and large (0.85-1 mm, 3-5 mm) pinewood particles.

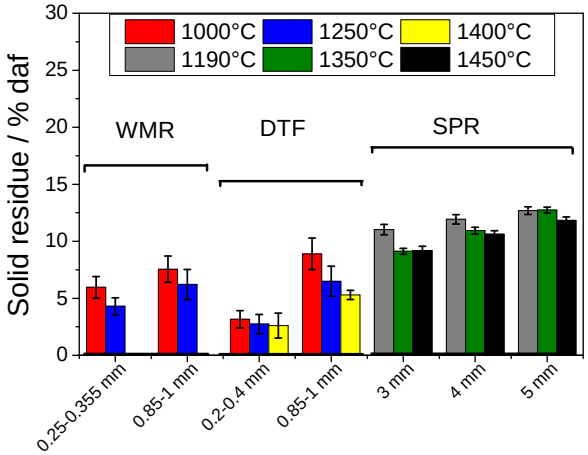

Figure 39: Influence of particle size on the char yield of pinewood in WMR (heat treatment temperature: 1000 and 1250°C, heating rate: 1000 K s^{-1}, holding time: 2 s, particle size: 0.25-0.355 mm and 0.85-1 mm); in DTF (heat treatment temperature: 1000, 1250, 1400°C, particle size: 0.2-0.4 mm and 0.85-1 mm) and in SPR (heat treatment temperature: 1190, 1350, 1450°C, particle size: 3-5 mm).

The results indicated that the larger pinewood particles (0.85-1 mm) required more than 1 s in the WMR and DTF at 1000°C for complete conversion, corresponding to results of Septien [42], where complete conversion of 0.8 mm beechwood particles was achieved within 2 s in the DTF. The differences between 0.05-0.355 mm and 0.5-1 mm particle size fractions indicated the significance of extra- and/or intra-particle thermal resistances for larger particles, leading to higher char yields. The 0.85-1 mm particles pyrolyzed in the WMR and DTF and 3 mm cube reacted in the SPR at temperatures 1350-1450°C showed negligible differences in a char yield, indicating less influence of high heating rate. However, 4 mm and 5 mm cubes obtained 2-3 % points more char than 3 mm cube and 0.85-1 mm pinewood pyrolyzed in the DTF, emphasizing the effect of particle size on the char yield at fast heating rates.

In addition, the results obtained in the SPR showed that the char yield of 3 mm pinewood cube decreased from ca. 7.3 to 6.0 % when the temperature was raised from 1190 to 1450°C. A similar tendency in terms of a decreasing char yield with higher temperatures was observed for the 4 and 5 mm pinewood particles. The results of 5 mm cube pyrolysis indicated no differences in a mass loss at 1190 and 1350°C, while at 1450°C the char yield decreased from 8.5 to 7.7 %. The char yield of the 5 mm pinewood particle was higher than for the 3 mm and 4 mm particles. The differences between the char yields at various temperatures in the SPR pyrolysis became less pronounced with increasing particle size.

4.5 Conclusion

The aim of the current investigation was to understand the effect of heat treatment temperature, heating rate, particle size, holding time and fuel origin on the product yields in fast pyrolysis. The experimental study was mainly performed in a wire mesh reactor and drop tube reactor. The wire mesh reactor was applied to understand the influence of operating conditions and differences in a biomass composition on the char yield. The experimental work in the drop tube reactor mainly addressed the effect of temperature, heating rate and particle size on the volatile and solid residue yields. The influence of > 3 mm wood particles on the char yield was studied in a single particle reactor.

The investigations in a wire mesh reactor showed that the largest effect of heating rate on the char yield is in the region between 10 K s^{-1} and 600 K s^{-1}. Above > 600 K s^{-1} the char yield seemed to become relatively insensitive to the heating rate increase. The heat treatment temperature and presence of potassium and possibly to a small extent by calcium affected the char yield stronger than the heating rates and differences in the plant cell composition. At the applied heating rates, up to 3000 K s^{-1}, the particle could be assumed to be thermally thin, when its size did not exceed 0.425 mm. The char yields of wheat straw and leached wheat straw were less affected by the holding time and particle size because the characteristic length for heat transport was determined by the particle thickness.

Char yields from the DTF were lower than those obtained in a wire mesh reactor. This

was attributed to the higher heating rates in the DTF. No self-gasification effect leading to lower char yields caused by the CO_2 and H_2O release during the pyrolysis process was observed in the present study. The straw samples showed a significant char yield decrease in the DTF when the temperature was increased from 1000 to 1400°C, whereas the char yields of pinewood ($\approx$ 3.5 %, daf) and beechwood ($\approx$ 7 %, daf) were almost constant at a very low level. It was observed that a low fuel alkali content, high temperatures, and fast heating rates lead to low biomass char yields. The results indicated that the influence of alkali on the char yield is more pronounced at low and intermediate heating rates than at fast heating rates in the DTF.

The measured soot yield of wood was 3-7 % higher compared to herbaceous biomass above 1250°C. The higher concentration of lignin and resin acids in the wood could lead to a stronger formation of PAH precursors and thus higher soot yields. The lower soot yields in pyrolysis of leached wheat straw compared to alfalfa straw and non-treated wheat straw were related to the removal of some lignin fraction (from 25.7 to 15.8 wt. %), and therefore decreased formation of PAH precursors. The leaching of wheat straw showed that lignin could play a dominating role on the soot yield. In addition, the higher soot yield in pyrolysis of wood compared with herbaceous biomass was to a minor extent related to the suppression of soot by the higher potassium content. High levels of K, Cl and S elements were found in the straw soot. The larger pinewood particles showed an increasing soot yield at high temperatures due to the lower conversion. A higher soot yield was obtained from smaller pinewood particles (0.2-0.4 mm) compared to larger particles (0.85-1 mm).

The larger pinewood particles ($>$ 0.85 mm) required more than 1 s holding time for the complete conversion at intermediate and fast heating rates. The influence of heating rate on the char yields was less pronounced for particle sizes from 0.85 to 4 mm obtained at temperatures $>$ 1250°C in the WMR, SPR and DTF, due to the predominance of internal heat transfer control within the large particles. In addition, the results of char yield comparison indicated a key role of heat treatment temperature and particle size on the char yield due to its increase with higher temperatures and larger particle sizes.

References

[1] Tremel A. Reaction Kinetics of Solid Fuels during Entrained Flow Gasification. PhD thesis, Technical University of Munich, 2012.

[2] Werkelin J and Hupa M. Release of ash-forming matter of woody biomass during fast pyrolysis in a wire mesh reactor. *Proc Impacts Fuel Qual Power Prod Envir; 2010 Aug. 30^{th}- Sep. 3^{rd}, Saariselkä, Finland.*

[3] Jensen A, Dam-Johansen K, Wojtowicz MA, and Serio MA. TG-FTIR Study of the Influence of Potassium Chloride on Wheat Straw Pyrolysis. *Energy Fuels*, 12(5):929–38, 1998.

[4] Nik-Azar M, Hajaligol MR, Sohrabi M, and Dabir B. Mineral matter effects in rapid pyrolysis of beechwood. *Fuel Process Technol*, 51(1-2):7–17, 1997.

[5] Niksa S. Predicting the rapid devolatilization of diverse forms of biomass with bio-Flashchain. *Proc Combust Inst*, 28(2):2727–33, 2000.

[6] Zaror CA, Hutchings IS, Pyle DL, Stiles HN, and Kandiyoti R. Secondary char formation in the catalytic pyrolysis of biomass. *Fuel*, 64(7):990–4, 1985.

[7] Solomon PR, Best PE, Yu ZZ, and Charpenay S. An Empirical Model for Coal Fluidity Based on a Macromolecular Network Pyrolysis Model. *Energy Fuels*, 6(2):143–54, 1992.

[8] Ma L, Jones JM, Pourkashanian M, and Williams A. Modelling the combustion of pulverized biomass in an industrial combustion test furnace. *Fuel*, 86(12-13):1959–65, 2007.

[9] Jimenez S, Remacha P, Ballesteros JC, Gimenez A, and Ballester J. Kinetics of devolatilization and oxidation of a pulverized biomass in an entrained flow reactor under realistic combustion conditions. *Combust Flame*, 152(4):588–603, 2008.

[10] Yang YB, Sharifi VN, Swithenbank J, Ma L, Darvell LI, and Jones JM et al. Combustion of a Single Particle of Biomass. *Energy Fuels*, 22(1):306–16, 2008.

[11] Gubba SR, Pourkashanian M, and Williams A. Influence of particle shape and internal thermal gradients of biomass particles on pulverized coal/biomass co-fired flames. *Fuel Process Technol*, 92(11):2185–95, 2011.

[12] Saleh SB, Hansen BB, Jensen PA, and Dam-Johansen K. Influence of Biomass Chemical Properties on Torrefaction Characteristics. *Energy Fuels*, 27(12):7541–8, 2013.

[13] Jepsen MS. *Pyrolysis of Large Biomass Particles in a Single Particle Combustion Reactor*. MSc thesis, DTU Chemical Engineering, Technical University of Denmark, 2014.

[14] Umeki K, Kirtania K, Chen L, and Bhattacharya S. Fuel Particle Conversion of Pulverized Biomass during Pyrolysis in an Entrained Flow Reactor. *Ind Eng Chem Res*, 51(43):13973–9, 2012.

[15] Damø AJ, Frandsen FJ, Jensen PA, Wu H, and Glarborg P. Residual Ash Formation during suspension-firing of biomass. Effects of Residence Time and Fuel Type. *Proc Impacts Fuel Qual; 2014 Oct 26^{th}-31^{rd}, Snowbird, UT, US*, pages 627–48.

[16] Trubetskaya A, Jensen PA, Jensen AD, Steibel M, Spliethoff H, and Glarborg P. Influence of fast pyrolysis conditions on yield and structural transformation of biomass char. *Fuel Process Technol*, 140:205–14, 2015.

[17] Jones JM, Darwell LI, Bridgeman TG, Pourkashanian M, and Williams A. An investigation of thermal and catalytic behaviour of potassium in biomass combustion. *Proc Combust Inst*, 31(2):1955–63, 2007.

[18] Wornat MJ, Hurt RH, Yang NYC, and Headley TJ. Structural and compositional transformations of biomass chars during combustion. *Combust Flame*, 100(1-2):131–43, 1995.

[19] Mermoud F, Salvador S, van de Steene L, and Glofier F. Influence of the pyrolysis heating rate on the steam gasification rate of large wood char particles. *Fuel*, 85(10-11):1473–82, 2006.

[20] Warnatz J, Maas U, and Dibble RW. *Combustion*. Springer, 1996.

[21] Williams A, Jones JM, Ma L, and Pourkashanian M. Pollutants from the combustion of solid biomass fuels. *Prog Energy Combust Sci*, 38(2):113–37, 2012.

[22] Evans RJ and Milne TA. Molecular characterization of the pyrolysis of biomass. *Energy Fuels*, 1(2):123–37, 1987.

[23] Dufour A, Weng J, Jia L, Tang X, Sirjean B, and Fournet R et al. Revealing the chemistry of biomass pyrolysis be means of tunable synchrotron photoionisation-mass spectrometry. *RSC Advances*, 3(14):4786–92, 2013.

[24] Daily JW, Jarvis MW, Gaston KR, James FW, Nimlos MR, and Donohoe BS et al. Elucidation of Biomass Pyrolysis Products Using a Laminar Entrained Flow Reactor and Char Particle Imaging. *Energy Fuels*, 25(1):324–36, 2011.

[25] Ross AB, Junyapoon S, Jones JM, Williams A, and Bartle KD. A study of different soots using pyrolysis-GC-MS and comparison with solvent extractable material. *J Anal Appl Pyrolysis*, 74(1-2):494–501, 2005.

[26] Rogge WF, Mazurek MA, Hildemann LM, Cass GR, and Simoneit BRT. Quantification of urban organic aerosols at a molecular level: identification, abundance and seasonal variation. *Atmos Environ A. General Topics*, 27(8):1309–30, 1993.

[27] Schauer JJ, Kleeman MJ, Cass GR, and Simoneit BRT. Measurement of Emissions from Air Pollution Sources. 2. C_1-C_{29} Organic Compounds from Fireplace Combustion of Wood. *Environ Sci Technol*, 35(9):1716–28, 2001.

[28] Menendez JA, Dominguez A, Fernandez Y, and Pis JJ. Evidence of Self-Gasification during the Microwave-Induced Pyrolysis of Coffee Hulls. *Energy Fuels*, 21(1):373–8, 2007.

[29] Huang YF, Kuan WH, Chiueh PT, and Lo SL. Pyrolysis of biomass by thermal analysis-mass spectrometry (TA-MS). *Bioresour Technol*, 102(3):3527–34, 2011.

[30] Sanchez-Silva L, Lopez-Gonzalez D, Villasanor J, Sanchez P, and Valverde JL. Thermogravimetric-mass spectrometric analysis of lignocellulosic and marine biomass pyrolysis. *Bioresour Technol*, 109:163–72, 2012.

[31] Qin K, Lin W, Jensen PA, and Jensen AD. High-temperature entrained flow gasification of biomass. *Fuel*, 93:589–600, 2012.

[32] Chapman S and Cowling TG. *The Mathematical Theory of Non-uniform Gases*. Cambridge University Press, 1970.

[33] Lu K, Ip E, Scott J, Foster P, Vickers M, and Baxter LL. Effects of particle shape and size on devolatilization of biomass particle. *Fuel*, 89(5):1156–68, 2010.

[34] Knudsen JN, Jensen PA, and Dam-Johansen K. Transformation and Release to the Gas Phase of Cl, K and S during Combustion of Annual Biomass. *Energy Fuels*, 18(5):1385–99, 2004.

[35] Dayton DC and Milne TA. *Laboratory Measurements of Alkali Metal Containing Vapors Released during Biomass Combustion. In: L Baxter and R. DeSollar (ed.), Application of Advanced Technologies to Ash-Related Problems in Boilers*. Plenum Press, 1996.

[36] Knudsen JN. Volatilization of Inorganic Matter during Combustion of Annual Biomass. PhD thesis, Technical University of Denmark, 2003.

[37] Van Lith SC, Alonso-Raminez V, Jensen PA, Frandsen FJ, and Glarborg P. Release to the Gas Phase of Inorganic Element during Wood Combustion. Part I: Development and Evaluation of Quantification Methods. *Energy Fuels*, 20(3):964–78, 2006.

[38] Puri BR. *Surface complexes on carbons. In: PL Walker (ed.), Chemistry and Physics of Carbon*. Marcel Dekker, 1970.

[39] Puri BR and Hazra RS. Carbon-sulfur surface complexes on charcoal. *Carbon*, 9(2):123–34, 1971.

[40] Cal MP, Strickler BW, Lizzio AA, and Gangwal SK. High temperature hydrogen sulfide adsorption on activated carbon - II. Effects of gas temperature, gas pressure and sorbent regeneration. *Carbon*, 38(13):1767–74, 2000.

[41] Miller RS and Bellan J. Tar Yield and Collection from the Pyrolysis of Large Biomass Particles. *Combust Sci Tech*, 127(1-6):97–118, 1997.

[42] Septien Stringel S. High temperature gasification of millimetric wood particles between 800°C and 1400°C. PhD thesis, Institut National Polytechnique de Toulouse, 2011.

5 Solid residue characterization and structural transformations

5.1 Introduction

In this chapter, the results of investigations on char morphology are presented. The yield of char and its property, including morphology and size depend strongly on composition of original biomass and pyrolysis conditions. The effects of heating rate and temperature on the morphological transformations at both slow ($< 10\,\mathrm{K\ s^{-1}}$), intermediate and fast pyrolysis environments ($> 100\,\mathrm{K\ s^{-1}}$) of the same feedstock have rarely been studied. The aim of this study was to understand the influence of operating parameters and biomass origin on the solid residue morphology using mainly a wire mesh reactor, a drop tube furnace, an entrained flow system and to a minor extent a tubular reactor and a single particle burner. The influence of extractives on the structural changes, on which available literature is not extensive, was also studied using char obtained from the drop tube reactor. The influence of ash composition, particularly of K, Ca and Si elements, on the char morphological changes under fast heating was investigated using samples of straw, leached straw and rice husk.

This chapter resembles the papers entitled "Effect of fast pyrolysis conditions on biomass solid residues at high temperatures", "Influence of fast pyrolysis conditions on yield and structural transformation of biomass char", "Comparison of high temperature chars of wheat straw and rice husk with respect to chemistry, morphology and reactivity" and "Characterization of free radicals by Electron Spin Resonance Spectroscopy in biochars from pyrolysis at high heating rates and at high temperatures".

5.2 Characterization of char

5.2.1 Char morphology at slow and intermediate heating rates

The char morphology and structural transformations from the fast pyrolysis of pinewood, wheat straw, alfalfa straw and rice husk in the wire mesh reactor at a temperature range of 350-1400°C were compared with data from fast pyrolysis at 1000°C and with a heating rate of $10\,\mathrm{K\ min^{-1}}$ in a tubular furnace. This comparison shows the effect of heating rate and heat treatment temperature on the char structural transformations during pyrolysis.

The current investigation shows softening of the solid char matrix already at 350°C at both low and high heating rates as it can be observed from SEM images in Appendix B (Figure 80). In contrast to results of Cetin et al. [1] who reported negligible morphological changes at low heating rates, the data in this study indicate softening of pinewood and wheat straw solid matter at 1000°C with a heating rate of $10\,\mathrm{K\ min^{-1}}$ as shown in Figure 40. However, the plasticization at high heating rates is stronger than at low heating rates, as can be seen by the microscopy observations in this study.

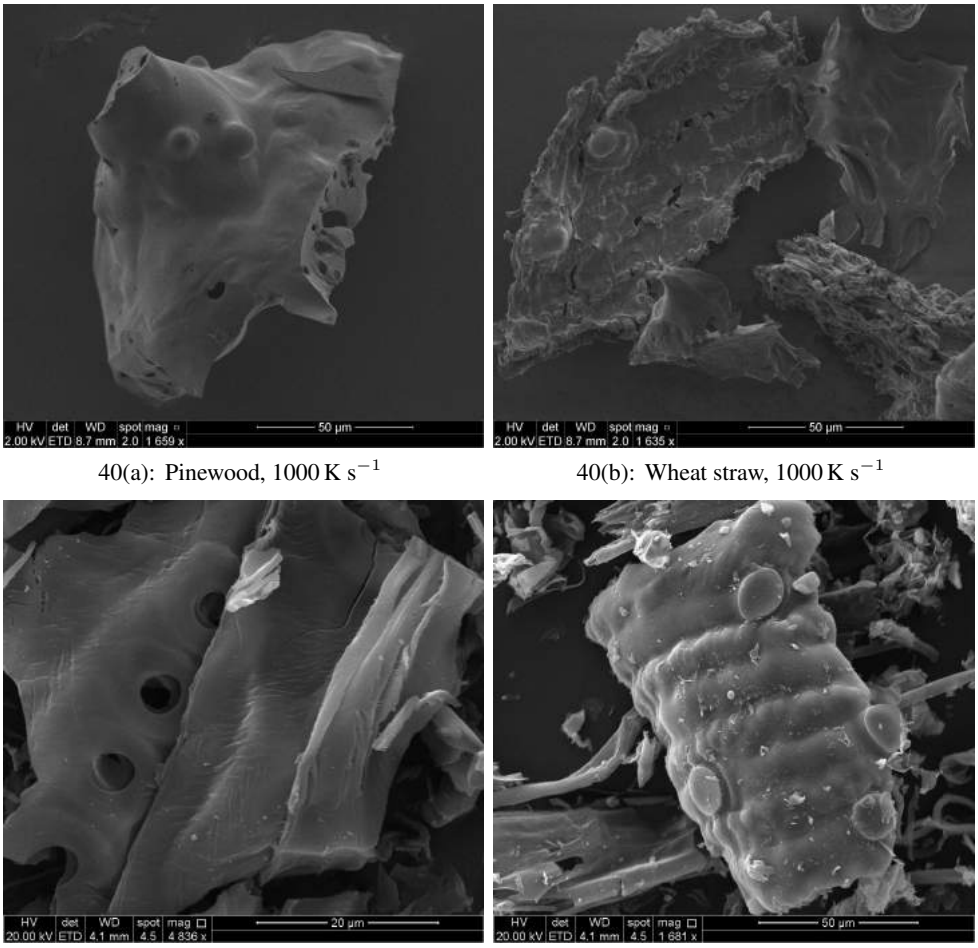

40(a): Pinewood, 1000 K s^{-1}

40(b): Wheat straw, 1000 K s^{-1}

40(c): Pinewood, 10 K min^{-1}

40(d): Wheat straw, 10 K min^{-1}

Figure 40: SEM images of pinewood and wheat straw, pyrolyzed (heat treatment temperature: 1000°C, heating rate: 1000 K s^{-1}, holding time: 1 s, particle size: 0.05-0.2 mm), and compared with particles (heat treatment temperature: 1000°C, heating rate: 10 K min^{-1}, holding time: 10 min, particle size: 0.05-0.2 mm).

The devolatilization and fluidity of biomass involve the same basic steps as in the devolatilization of coal, i.e. bond breaking, possible formation of a metaplast, evaporation of tar and release of light gases, followed by repolymerization finally forming a char. In low rank coals such as lignite, which have a high oxygen content, low temperature bond formation (mainly ethers) can take place as well, which to some extent may prevent formation of a metaplast [2–5]. The situation for biomass is complicated by the fact that it contains three distinctly different building blocks, i.e. cellulose, hemicellulose and lignin. The cellulose and hemicellulose are quite different from coal structures while the lignin has more resemblance with coal, containing aromatic moieties [4, 6]. However, both pure cellulose [7], with its relatively weak hemi-acetal bonds, and lignin [2, 8] are known to form a melt at high heating rates and there is no reason to believe that hemicelluloses will not do the same under similar conditions. DeGroot et al. [9] suggested that the decomposition of hemicelluloses contributes significantly to char formation and morphology due to the close

association of inorganic species with the hemicelluloses through ion exchange on glucuronic acid groups.

Moreover, the inorganic matter, that resides as minerals in coal, influences the pyrolysis behavior in a different way than in the case of biomass, where potassium and calcium play a role as active catalysts that may additionally affect the metaplast formation [8]. However, it is not well known to what extent the formation of a metaplast depends on the presence of alkali, and how this influence is changed with a heating rate.

Heating rates affect the melting and swelling behavior of both biomass and coal and thereby how the competing processes of tar formation (bond-breaking, cross-linking, internal mass transport) change with the temperature. The heating rates determine the temperature at which the reactions occur [10]. Under slower heating conditions, plasticization on the char surface is hindered by cross-linking prior to bridge-breaking. At high heating rates, biomass behaves similarly to the bituminous coals and undergoes significant bridge-breaking before it starts to cross-link and therefore becomes fluid.

Cetin et al. [1, 11] assigned the melting of fuel at high heating rates to a lack of cell structure, causing plastic transformation on the char surface. The results of this work illustrated by Figure 40 show that the differences in morphological transformations at 600°C and 1000°C are not significant for pinewood and wheat straw in terms of plasticization, probably because the primary pyrolysis reactions occur at temperatures < 600°C.

Moreover, alfalfa straw and rice husk underwent plastic deformation during fast pyrolysis in the wire mesh reactor, but less melting than pinewood, indicating an effect of ash on the char morphology as shown in Figure 41. The alfalfa straw char at 1250°C shows an increase in macropores. It loses its structural distinctions and maintains a very fragile and thin walled layer consisting of several molten fused particles. The high levels of K and Ca in the alfalfa straw may cause less severe plasticization, similarly to the wheat straw, by catalyzing the conversion of bridges into char links, and therefore increasing polymerization / cross-linking and reducing char fluidity.

The preserved rice husk char shape is probably mainly related to the high content of Si that hinders char polymerization / cross-linking . At high temperatures, a stable shell of rice husk char is formed, probably due to the softening of amorphous SiO_2 at about 700°C, and when it is rapidly cooled, the silica melt solidifies without crystallization [12]. The formation of glassy structures in the rice husk may be caused by the presence of potassium that could decrease the melting temperature of SiO_2 [13], leading to a stronger char transformation at 1400°C in comparison to chars, prepared at 1000 and 1250°C as shown in Appendix B (Figure 78).

The morphological changes of biomass during pyrolysis may be a result of the degradation of different plant components that affect the metaplast formation. Hemicellulose degradation is known to occur over a relatively broad range of temperatures, and it forms more char than cellulose [14]. The results of this study on the hemicellulose correspond to the investigations of Sharma et al. [15] at 350°C under slow heating, where molten clusters of a pectin char were formed with

the closed vesicles and open pores.

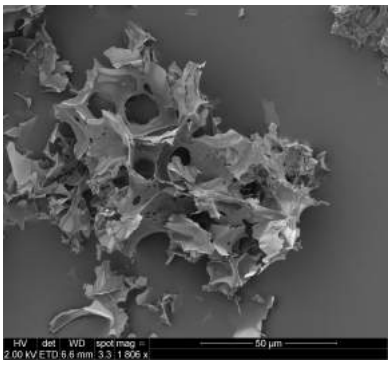

41(a): Alfalfa straw char

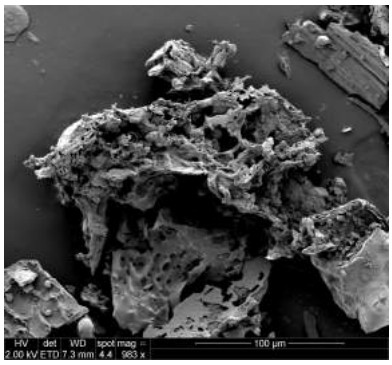

41(b): Rice husk char

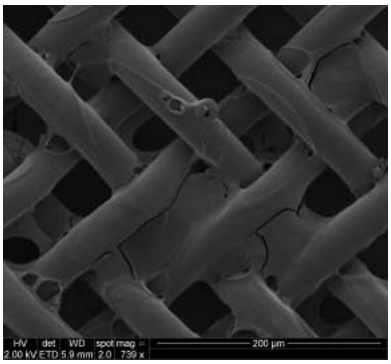

41(c): Cellulose char

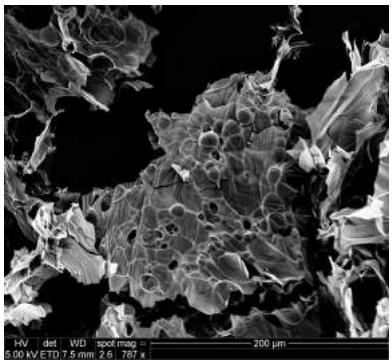

41(d): Xylan char

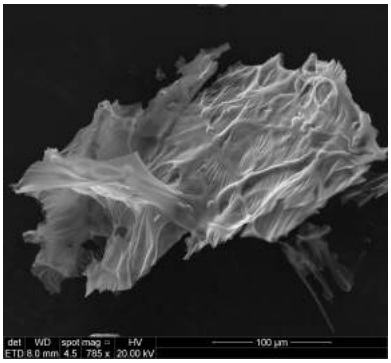

41(e): Lignin (softwood) char

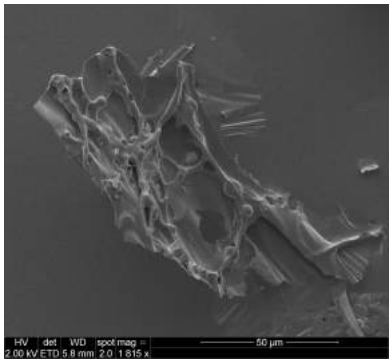

41(f): Lignin (straw) char

Figure 41: SEM images of alfalfa straw char (heat treatment temperature: 1250°C, heating rate: 1000 K s^{-1}, particle size: 0.05-0.2 mm) and rice husk char (heat treatment temperature: 1400°C, heating rate: 1000 K s^{-1}, particle size: 0.05-0.2 mm); cellulose, xylan from beechwood and ORGANOSOLV lignin from softwood and from wheat straw (heat treatment temperature: 1000°C, heating rate: 1000 K s^{-1}, particle size: 0.05-0.1 mm), pyrolyzed in WMR.

The cellulose char, prepared at a peak temperature of 1000°C, was available on the mesh only in a very small quantity. Figure 41 suggests that the hemicellulose char solidifies after the fast pyrolysis, and forms a glassy amorphous structure, similarly to the cellulose, which was probably even stronger plasticized. Lignin tends to be less volatile than cellulose and hemicellulose, leading to the formation of higher char yields [16].

Figure 41 also shows the foamed softwood and hardwood lignin types at 1000°C with the formation of elongated vesicles on a smooth surface. The current investigation indicates an intensive swelling and foaming of lignin at 350°C as it is shown in Appendix B (Figure 81). The optical differences between softwood and wheat straw are nearly negligible. In this study it is believed that under fast heating the formation of metaplast is mostly affected by the bond-breaking and cross-linking of organic components present in lignin that is less volatile than holocelluses. The stronger plasticized chars of pinewood and beechwood contain higher fractions of lignin ($>$ 30 %) than herbaceous chars with (20-26 %). The high presence of inorganic matter in herbaceous biomass may also affect the metaplast formation, resulting in a less plasticized char.

Interestingly, Jepsen [17] also reported in his pyrolysis experiments with larger pinewood particles that the surfaces of 3 mm and 5 mm particles were plasticized with the formation of elongated pores in the cutting direction of the original pinewood during pyrolysis as shown in Figure 42(a).

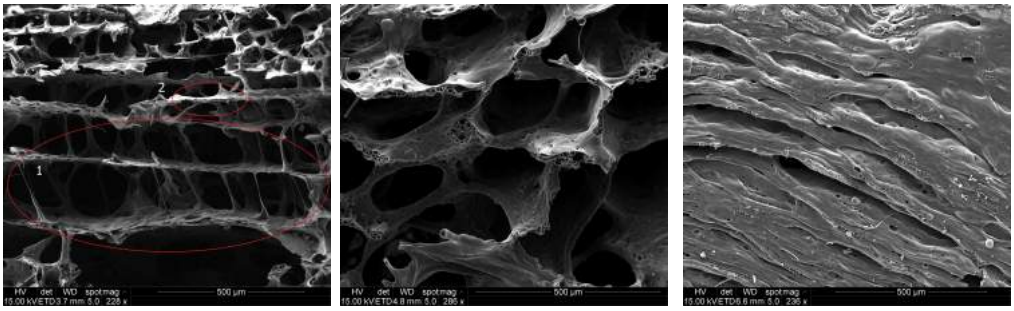

42(a): 5 mm (1350°C; center) 42(b): 3 mm (1190°C; center) 42(c): 3 mm (1190°C; surface)

Figure 42: SEM images of a pinewood particle (heat treatment temperature: 1350°C, particle size: 5 mm); (heat treatment temperature: 1190°C and 1350°C, particle size: 3 mm) in center and on the outer surface, pyrolyzed in the SPR.

This indicates that even for large particles fast heating rates at the surface may lead to local formation of a metaplast. Metaplast formation was not observed inside the particles, presumably due to lower heating rates as shown in Figures 42(b) and 42(c).

5.2.2 Char morphology at fast heating rates in the DTF

Figure 43 shows SEM images of wood and herbaceous char, pyrolyzed at 1000°C and 1400°C in the DTF reactor. For the structural investigations smaller (0.2-0.4 mm) and larger (0.85-1 mm) original biomass particles were used. The morphology of char obtained at intermediate and fast heating rates ($>$ 10 K s^{-1}) in the WMR as shown in Figure 40 and fast heating rates in the DTF lost all features of the parental structure. In contrast to the WMR results where pinewood char was molten and formless, the pinewood char particles became spherical and porous with large inner cavities, formed from the simultaneous release of a large volatiles fraction. The pinewood particles have undergone stronger melting during fast pyrolysis and formed smooth and near-

spherical structures. Surprisingly, beechwood char particles were only slightly molten on the outer surface and kept the shape and size characteristics of the parental fuel, contrary to the results of Dall'Ora et al. [18].

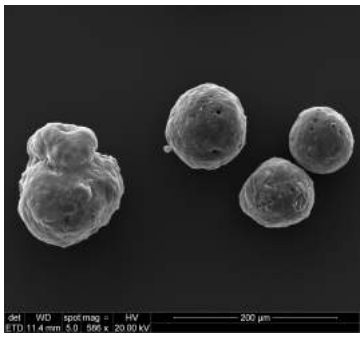

43(a): Pinewood char, (1000°C, 0.2-0.4 mm)

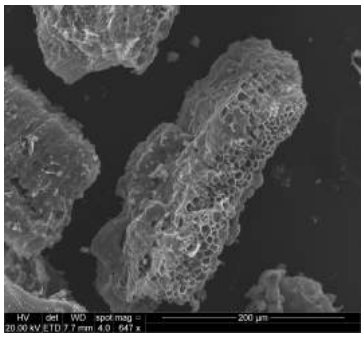

43(b): Beechwood char, (1000°C, 0.2-0.4 mm)

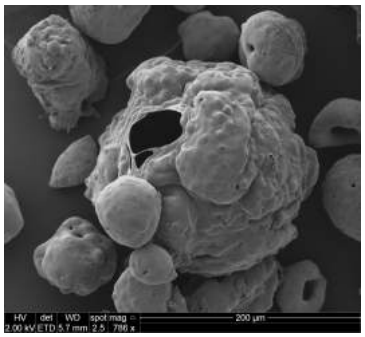

43(c): Pinewood char ext.-free, (1000°C, 0.2-0.4 mm)

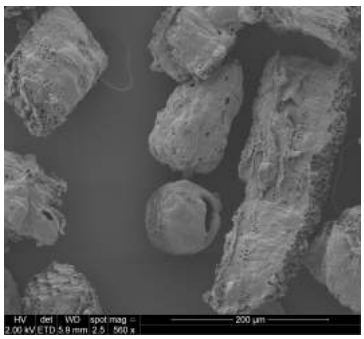

43(d): Beechwood char ext.-free, (1000°C, 0.2-0.4 mm)

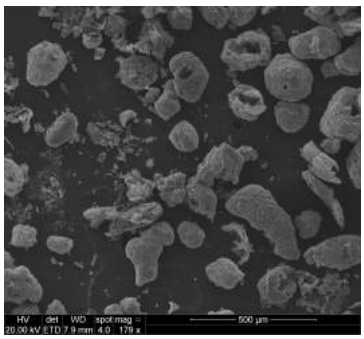

43(e): Alfalfa straw char, (1400°C, 0.2-0.4 mm)

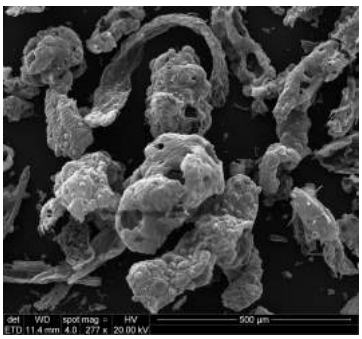

43(f): Wheat straw char, (1400°C, 0.2-0.4 mm)

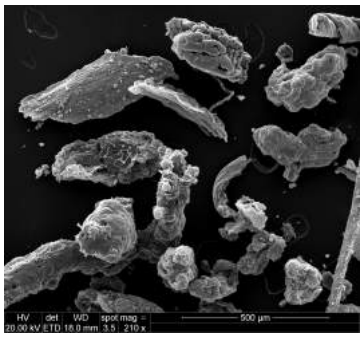

43(g): Leached wheat straw char, (1400°C, 0.2-0.4 mm)

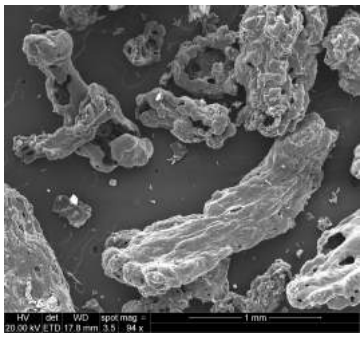

43(h): Pinewood char, (1000°C, 0.85-1 mm)

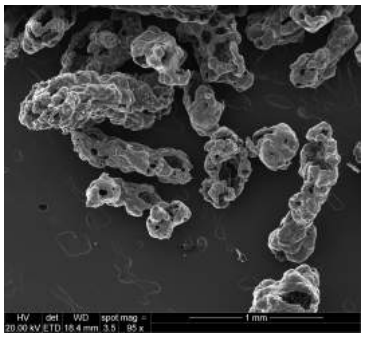

43(i): Pinewood char, (1400°C, 0.85-1 mm)

Figure 43: (a)-(d). SEM images of biomass pinewood and beechwood chars, reacted at 1000°C and compared with the pinewood and beechwood after extraction with acetone, reacted at 1000°C and with a original biomass size of 0.2-0.4 mm in the drop tube reactor, and (e)-(g). Alfalfa, wheat straw and leached wheat straw chars, reacted at 1400°C and with a original biomass size of 0.2-0.4 mm; (h)-(i). SEM images of pinewood char prepared at 1000°C and 1400°C with a original pinewood size of 0.85-1 mm in the drop tube reactor. SEM images of alfalfa straw, wheat straw, leached wheat straw and larger pinewood char particles were taken under a lower magnification due to a significantly larger size of particles.

This observation is possibly caused by the presence of beechwood at a stage of being con-

verted from the water-conducting sapwood to the heartwood [19]. In the angiosperm species, air-filled vessels in the sapwood are sealed off by the intrusive growth of the parenchyma cells, preventing fungal growth in the vessel lumens [20]. These inclusions or tyloses shown in Figure 44(b) are formed when the wood parenchyma cells press bubbles of photoplasm through the pits into a vessel that is filled with the large quantity of phenolic compounds, lignin, and aromatic substances shown in Figure 44(a). Tyloses developed in response to pruning from both axial parenchyma cells and ray parenchyma cells [21]. In wild plants, tyloses and phenolics are formed as defense reactions against pathogens and for physical and chemical isolation of wounds [22].

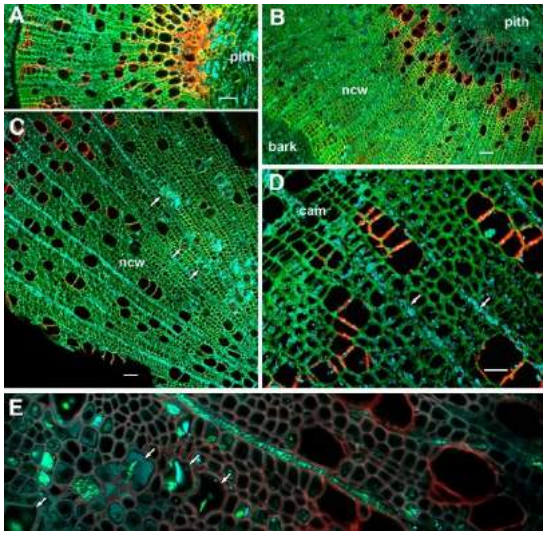

44(a): Non-conductive wood with phenolics (blue-green) [22]

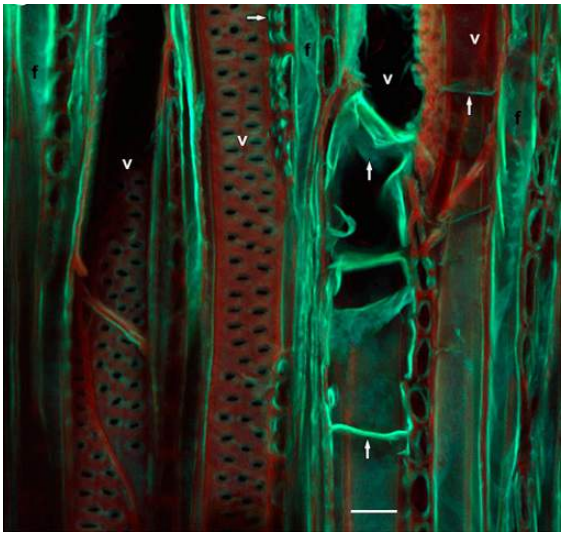

44(b): Tyloses (vertical arrows) and lignified walls (red) [22]

Figure 44: (a) Confocal microscopy showing conductive vessels (red walls) and non-conductive wood with phenolics (green or blue); (b) Tyloses (vertical arrows) and lignified walls (red) [22].

The formed phenolic compounds polymerize in insoluble forms, for example in a non-lignin related bio-polymer suberin that makes the wood particle more stable at high heat treatment temperatures [23, 24].

Alfalfa straw and wheat straw have underwent plasticization, but less melting than pinewood, indicating an effect of inorganic matter and higher oxygen content on the char morphology. In herbaceous biomass, which have a high oxygen content, low temperature bond formation (mainly ethers) can take place, preventing formation of a metaplast, and therefore leading to less plasticization [2–5]. The high levels of K and Ca in the herbaceous biomasses could cause less severe plasticization, by catalyzing the conversion of bridges into char links, and therefore increasing polymerization / cross-linking and reducing char fluidity. The alfalfa and wheat straw char obtained two types of a particle shape (elongated cylindrical and near-spherical). This is related to the initial length of the particle, whereas shorter biomass particles become more spherical during pyrolysis. The transformation of herbaceous char shapes was probably affected by the presence of potassium and calcium silicates, remaining in the char. The high Ca content in the alfalfa straw

could give an additional mechanical stability to the char, preserving the particle shape and size of the original fuel. Figure 43(g) shows the char structure of leached wheat straw at 1400°C. In the present study, the wheat straw and leached straw were of a similar form with a molten surface. Also, no differences in a char morphology of non-treated and leached wheat straw was observed at lower heating rates (600-1000 K s^{-1}) in the wire mesh reactor as shown in Appendix B (Figures 79 and 80).

Both non-treated straw and leached wheat straw chars obtained different shapes from near-spherical to cylindrical. The cylindrical form of non-treated and leached wheat straw was probably influenced by the formation of silicates which give an additional mechanical stability to the char as it was suggested for the alfalfa straw, containing high amounts of calcium. ESEM-EDS (environmental SEM microscopy) investigations indicated that single regions of the wheat straw char obtained high contents of potassium and calcium silicates. Silicate rich regions, resulting in a char solidification are shown in Figure 45(a), whereas other parts of wheat straw char obtained potassium rich regions as illustrated in Figure 45(b). In addition, on the wheat straw char surface, the ongoing soot formation was observed.

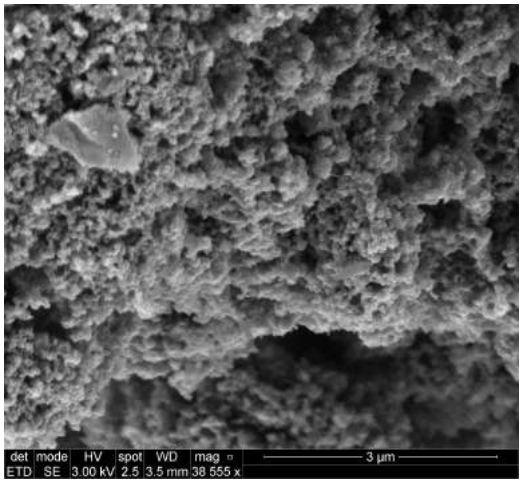

45(a): Silicate rich region of wheat straw char

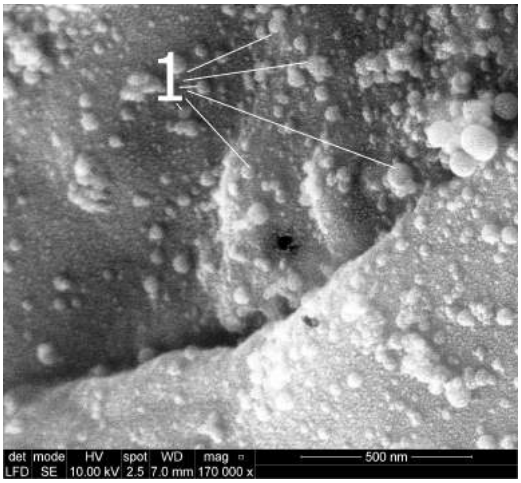

45(b): K rich regions of wheat straw char

Figure 45: ESEM images of wheat straw char, reacted at 1250°C in the DTF; (1) is for the soot particles on the char surface. (a) silicate rich region of wheat straw char and (b) K rich regions of wheat straw char.

The nearly similar levels of K and Ca in the char of non-treated and extracted wood showed that the extraction process did not have an effect on biomass ash content as shown in Table 3. In the present study, the effect of extractives on the char structural transformations was studied by removing resin, fatty acids, waxes, and phytosterols from the pinewood and beechwood by acetone extraction. Figure 43 shows the char structures of pinewood and beechwood. The pinewood char after the extraction indicated slightly stronger swelling and enhanced sticking of smaller particles to the surface of larger particles at 1000°C. The beechwood char without extractives did not show any morphological differences compared to non-treated beechwood chars. The extractives could slightly affect the char fluidity.

The morphology of 0.85-1 mm pinewood particles prepared at 1000 and 1400°C was compared in Figures 43(h) and 43(i). SEM image of pinewood char prepared at 1000°C showed a slightly molten surface probably due to the incomplete conversion, keeping the particle size similar to the original pinewood particle. The pinewood char underwent severe plasticization at 1400°C, indicating metaplast formation. In addition, the pinewood particle decreased in size, and formed molten rigid structures with large cavities due to the rapid volatiles release. Large pinewood particles obtained mainly a cylindrical and to a minor extent near-spherical shapes in fast pyrolysis.

5.2.3 Particle size and shape characterization

The particle size and shape of the original biomass and its char were analyzed by CAMSIZER XT instrument.

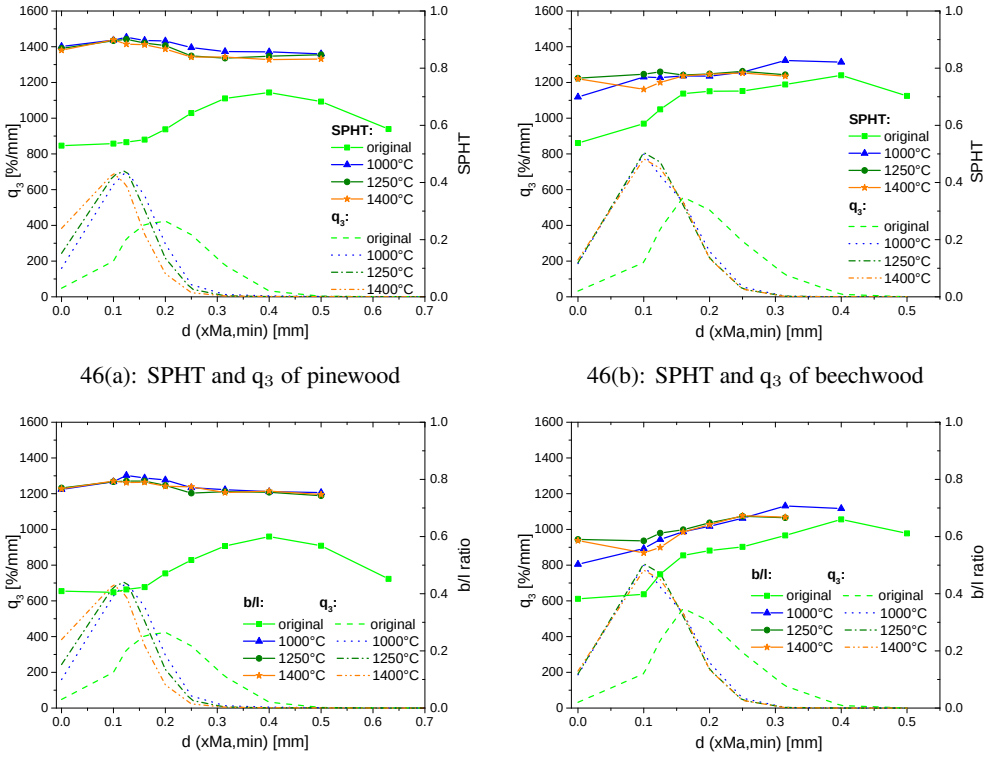

46(a): SPHT and q_3 of pinewood

46(b): SPHT and q_3 of beechwood

46(c): b/l ratio and q_3 of pinewood

46(d): b/l ratio and q_3 of beechwood

Figure 46: Particle frequency distribution based on volume (q_3), sphericity (SPHT) and width/length ratio (b/l) of original pinewood, beechwood and their chars, reacted at 1000, 1250 and 1400°C.

Prior to the 2D dynamic imaging analysis, the original fuel was sieved to the particle size fraction of 0.2-0.4 mm. As shown in Figures 46 and 47, the results of the particle characterization study indicate nearly 50 % decrease of the characteristic length of pinewood, beechwood and wheat straw during pyrolysis in comparison to the original fuel. The changes in particle size between 1000 and 1400°C are almost negligible. The particle size of alfalfa straw char remained similar to the original fuel at pyrolysis temperatures of 1000-1400°C. This may be attributed to

formation of calcium carbonates and silicates (as shown by the Factsage simulation), which form a very stable inorganic matter shell, hindering particle shrinkage. The particle shape of biomass was characterized using sphericity (SPHT) and width/length ratio (b/l) parameters. The pinewood char particles showed a near-spherical shape (SPHT = 0.8-0.9; b/l = 0.7-0.8). The beechwood and herbaceous chars obtained cylindrical or rectangular shapes (SPHT = 0.5-0.8; b/l ratios = 0.4-0.7). The results of particles > 0.4 mm in terms of shape description were considered as non-representative due to the low presence of particles in this fraction. It seems that at the heating rates in the DTF a biomass particle transforms to one particular shape that stays unchanged with the increasing temperature from 1000°C.

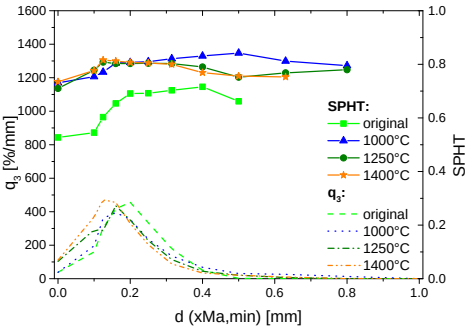

47(a): SPHT and q_3 of alfalfa straw

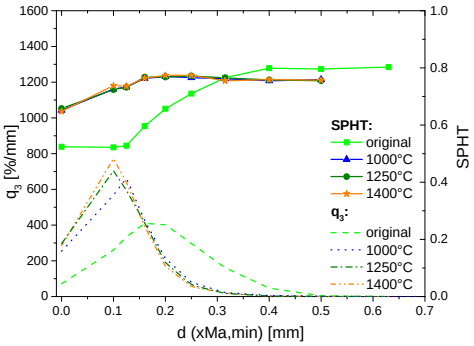

47(b): SPHT and q_3 of wheat straw

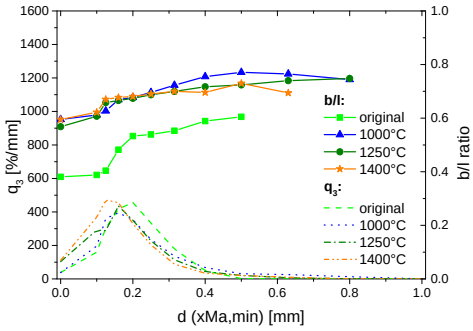

47(c): b/l ratio and q_3 of alfalfa straw

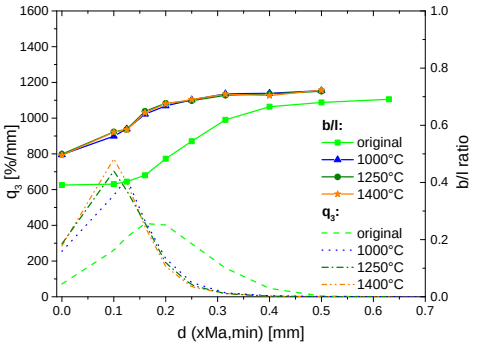

47(d): b/l ratio and q_3 of wheat straw

Figure 47: Particle frequency distribution based on volume (q_3), sphericity (SPHT) and width/length ratio (b/l) of original alfalfa straw, wheat straw and their chars, reacted at 1000, 1250 and 1400°C.

5.2.4 N_2 adsorption measurements

The specific surface areas (SSA) of wheat straw and rice husk chars, measured by the N_2 adsorption, are shown in Table 6. It can be observed that the pinewood chars had a higher surface area than the beechwood and wheat straw at the same operational conditions. The surface area of wood and herbaceous chars was recalculated as surface area (dry ash free basis) using equation 30, and SSA (dry ash free basis) values are shown in Table 6.

$$SSA_{daf} = \frac{SSA}{1 - X_{ash} - X_{H_2O}} \tag{30}$$

In this equation, X_{ash} and X_{H_2O} are the inorganic matter and moisture fractions.

Table 6: BET surface area (SSA) of pinewood, beechwood, wheat straw and rice husk chars, determined by N_2 adsorption. Due to the volatile matter presence in lignocellulosic chars generated at 1000°C, the N_2 adsorption was not conducted.

Soot	**1250°C**	**1400°C**	**1250°C**	**1400°C**
	$m^2\ g^{-1}$, as received		$m^2\ g^{-1}$, daf	
Pinewood	331.2	329.6	360	358
Beechwood	336	326.4	382	375
Wheat straw	197	167	318	293
Rice husk	94.9	53.9	527	533

Since the ash has a lower surface area compared to char, and rice husk has a higher ash content compared to pinewood, beechwood and wheat straw, the surface area of rice husk became smaller. The surface area on ash free basis of pinewood, beechwood, wheat straw and rice husk was almost constant for chars prepared at 1250 and 1400°C, indicating no significant changes with increasing temperature.

5.3 Structural char differences of wheat straw and rice husk

5.3.1 Introduction

Little is known about the structural transformation of pulverized biomass during high heating rate and high temperature pyrolysis. The majority of investigations on the fuel potential of agricultural waste is focused on wheat straw and rice husk chars, pyrolyzed under slow heating rate (1-50 K min^{-1}) and long holding time (1-4 h) [25–30]. Guerrero et al. [31] reported no major morphological changes of rice husk under fast heating, and ascribed this observation to a high thermal resistance of rice husk ash, containing mostly silica compounds. Pottmaier et al. [30] concluded that rice husk is less reactive than wheat straw, prepared at temperatures (300-1300°C) under slow and fast heating, and related differences in reactivity to the higher contents of lignin and silica in the rice husk. The investigation of Freitas et al. [28] on slowly pyrolyzed rice husk at high temperatures (1000-1400°C) and long holding time (1-2 h) indicated an increased formation of crystalline silica carbides at the expense of amorphous silica oxides with increasing temperature. Nehdi et al. [32] stated that silica oxides in rice husk can remain in amorphous form at combustion temperatures of up to 900°C if the combustion time is less than one hour, whereas crystalline silica oxides are produced at 1000°C with combustion time greater than 5 min.

5.3.2 Ash analysis

The ash composition of the original rice husk and its chars was analyzed by X-ray fluorescence (XRF), Inductively Coupled Plasma Optical Emission Spectroscopy (ICP-OES) and Ion Chromatography (IC) and shown in Figure 48. The chars were collected from the fast pyrolysis

at 1000, 1250 and 1500°C, and the analysis showed a high concentration of silicon oxides along with smaller amounts of potassium, aluminium, iron, sodium and magnesium. The wheat straw char at all applied heat treatment temperatures contained potassium and calcium along with a high concentration of silicon, leading to the formation of silicates [33].

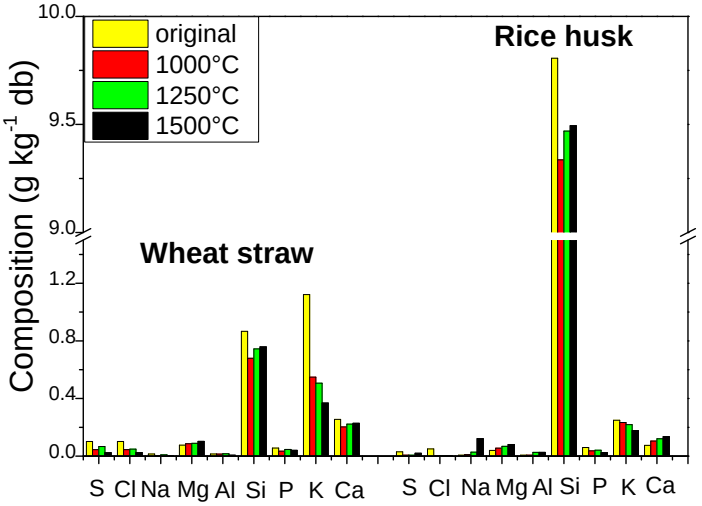

Figure 48: Ash compositional analysis of rice husk and wheat straw, pyrolyzed in the BabiTER reactor at 1000, 1250 and 1500°C. The ash composition of both lignocellulosic materials and their chars is shown in g kg^{-1} on dry basis.

Figure 48 shows that close to 70 % potassium in the wheat straw has been released in a temperature range of 1000-1500°C, and the residual potassium at 1500°C retained in the silicate matrix. Equilibrium calculations were conducted for the major inorganic components in the wheat straw (K, Si and Ca) as shown in Appendix A (Figure 76) using the Factsage software. These calculations indicated that potassium silicates (K_2SiO_3 and $K_2Si_2O_5$, melting temperature < 900°C [34]) and calcium silicate ($Ca_3Si_2O_7$, melting temperature < 1450°C [35]) should be present in the wheat straw chars.

5.3.3 X-ray diffraction

The structural characteristics of the biomass chars, formed during the fast pyrolysis in the BabiTER reactor, have been examined by X-ray diffraction (XRD) in terms of carbon and ash transformations. The X-ray diffractograms for the wheat straw and rice husk chars, prepared at 1000-1500°C, are shown in Figure 49. In the original rice husk, silicon oxides are present in an amorphous form bonded with monosaccharides [27], corresponding to the diffuse peak with its maximum at about $2\Theta = 21.8°$. The XRD peak at 21.8°, measured for the original rice husk, remained at the same position for the chars with increasing heat treatment temperature in the present study.

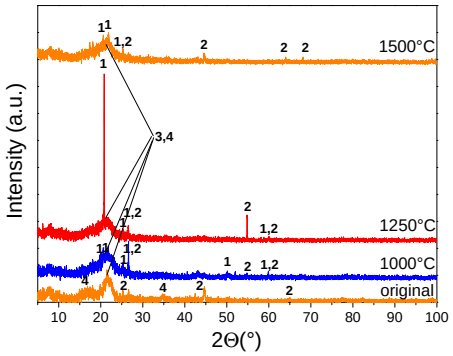

49(a): Rice husk

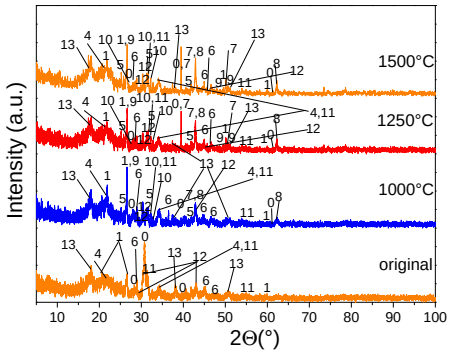

49(b): Wheat straw

Figure 49: XRD measurements of original wheat straw and rice husk and chars. The XRD patterns were assigned to: 0 - KCl, 1 - SiO_2 (tridymite, cristobalite, quartz), 2 - Mullite, 3 - Amourphous silica, 4 - Turbostratic structure, 5 - K_2CO_3, 6 - $CaCO_3$, 7 - $CaSO_4$, 8 - MgO, 9 - $Ca_3(PO_4)_2$, 10 - KOH, 11 - CaO, 12 - K_2SO_4, 13 - $Ca(OH)_2$ [36].

The weak sharp and narrow reflections from crystalline silicon oxides as compared to the broad band of amorphous silicon oxides ($2\Theta = 21.8°$) indicate only partial crystallization at high heating conditions. Comparing the reflections from crystalline silicates in the rice husk ash oxidized for 24 h reported by Hamdan et al. [37] and in glass-ceramics investigated by Jing et al. [38], the reflections from crystalline silicates in the rice husk chars are significantly weaker in the present study. The XRD results indicate that the rice husk chars exhibit mainly amorphous silicates structure with a few weak reflections from crystalline silicates. The XRD analysis did not show any SiC peaks between 1000 and 1500°C as it was previously observed under slow heating and at heat treatment temperatures below 1000°C by Sharma et al. [39].

In comparison to the rice husk, the XRD analysis of wheat straw char between 1000 and 1500°C showed a wide range of inorganic components, mostly present as oxides (SiO_2, CaO, MgO) as illustrated in Figure 49(b). In addition to the oxides, potassium and calcium elements form carbonates and sulfates. The potassium retained in the ash was proposed to appear as hydroxide [40] and to a minor extent as chloride due to the low concentration of chlorine [41]. With the exception of $Ca_3(PO_4)_2$ and $CaSO_4$ identified here, all other compounds identified in this study have been previously detected in ash samples by Wu et al. [40]. The peaks at about 23°, 34.4° and 42.5° in the wheat straw char indicated a decrease in cellulose crystallinity and formation of a turbostratic structure [42–44]. The peak at 23° in the rice husk char was hypothesized to overlap with the broad peak of amorphous silicon oxides at 21.8°.

5.3.4 ^{29}Si solid-state NMR analysis

The effect of heat treatment temperature on the organic matter transformation in the rice husk and wheat straw fast pyrolysis was monitored using ^{13}C CP/MAS and ^{13}C SP/MAS NMR spectroscopy. In the ^{13}C CP/MAS experiments the resonances of the carbons in immobile regions

of the samples were enhanced by polarization transfer from the highly abundant ^{1}H nuclei via hetero-nuclear dipolar coupling. All carbon sites were observed quantitatively by the ^{13}C SP/MAS NMR measurements. In Figure 50, the ^{13}C CP/MAS and ^{13}C SP/MAS NMR spectra of rice husk and wheat straw and chars produced at different heat treatment temperatures are displayed, and an assignment of resonances is shown in Appendix B (Table 23) using literature data [45–49].

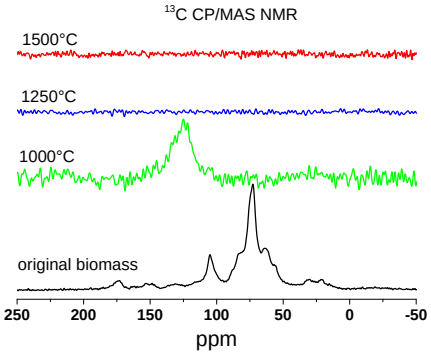

50(a): Rice husk ^{13}C CP/MAS NMR

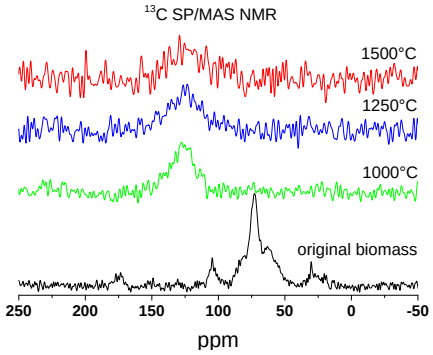

50(b): Rice husk ^{13}C SP/MAS NMR

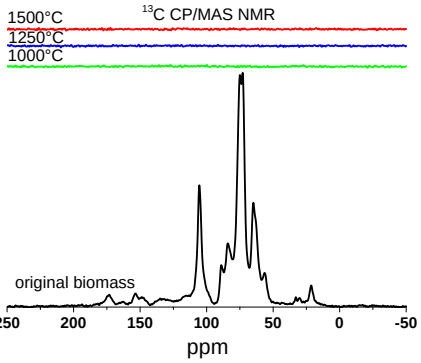

50(c): Wheat straw ^{13}C CP/MAS NMR

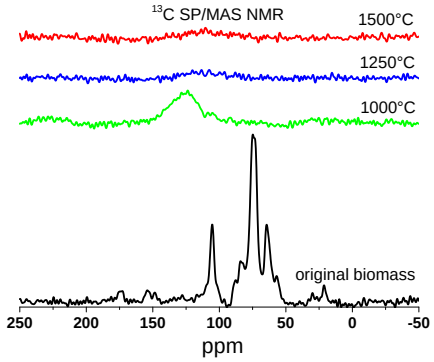

50(d): Wheat straw ^{13}C SP/MAS NMR

Figure 50: ^{13}C CP/MAS and ^{13}C SP/MAS spectra of rice husk and wheat straw and their chars generated at 1000, 1250 and 1500°C.

Comparing the spectra of the original biomass to the spectra of the chars at 1000°C showed that the polysaccharides were the most abundant components in the original biomass, whereas the spectra of chars are characterized by a broad resonance centered at 125 ppm originating from aromatics. Above 1000°C it was observed that no resonances were present in the CP/MAS spectra and that the S/N-ratio in the SP/MAS spectra were reduced. These spectra indicate the aromatization of the lignocellulosic material and formation of graphene-like structures [28]. The reasons for the lack of resonances in the CP/MAS spectra of the pyrolyzed samples are the lower content of hydrogen as shown in Appendix B (Figure 25) and a higher content of paramagnetic species (e.g. radicals) in the sample.

SP/MAS and CP/MAS spectra were also recorded, but the ^{29}Si CP/MAS only resulted in observable resonances for the original biomass, which is in agreement with the results of Freitas et al. [28]. The higher heat treatment temperatures led to the low hydrogen content of chars which

made unlikely occurrence of silanol groups at fast pyrolysis conditions. In Figure 51, the spectra of rice husk chars, prepared at 1000-1500°C in the entrained flow reactor are presented.

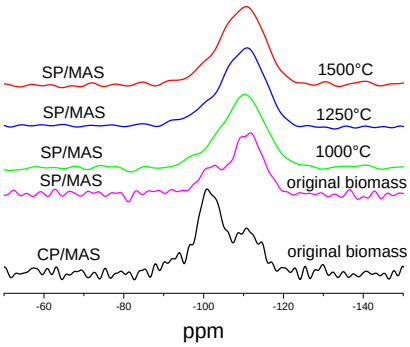

51(a): ^{29}Si CP/MAS and SP/MAS NMR

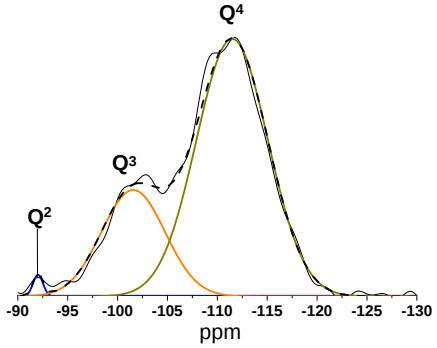

51(b): SP/MAS spectrum fitting with Gaussian function for original rice husk

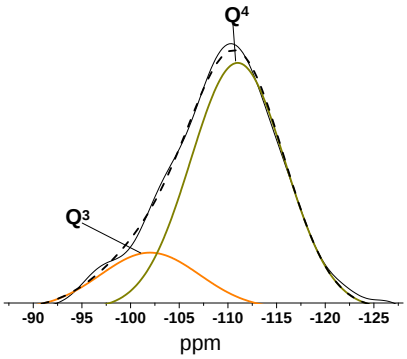

51(c): SP/MAS spectra fitting with Gaussian function for rice husk char prepared at 1000°C

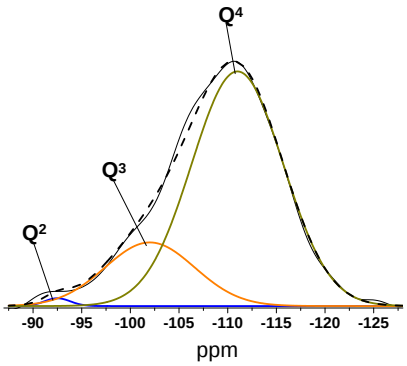

51(d): SP/MAS spectrum fitting with Gaussian function for rice husk char prepared 1500°C

Figure 51: (a) ^{29}Si CP/MAS and SP/MAS NMR spectra of original rice husk; ^{29}Si SP/MAS NMR spectra of rice husk chars at 1000, 1250 and 1500°C; (b) results of the ^{29}Si SP/MAS NMR data fitting with Gaussian function for original rice husk; chars prepared at (c) 1000°C and (d) 1500°C.

By comparison of the SP/MAS and the CP/MAS spectra of the original biomass the Si sites situated close to hydrogen are identified as these are enhanced by CP. Another factor influencing CP/MAS spectra is related to the presence of paramagnetic species which reduce the efficiency of the polarization transfer, leading to no resonances present in the CP/MAS spectra of chars generated at 1250 and 1500°C. The resonances in the SP/MAS spectra can be characterized by a broad intense resonance at -111 ppm assigned to Q^4 sites and less intense shoulders at -102 ppm and at -92 ppm assigned to the Q^3 and Q^2 sites, respectively, as shown in Figure 51 [50, 51]. In Table 7, the mean chemical shift and line width are displayed.

Table 7: Fitted parameters for the ^{29}Si NMR lines in the spectrum of original rice husk and its chars, prepared at 1000-1500°C, which show the peak position and full width at half maximum, as it was proposed in the literature [28, 52–55].

Silicon species	**Mean iso. chem. shift (ppm)**	**Full width at half maximum (Hz)**			
		Raw sample	Char (1000°C)	Char (1250°C)	Char (1500°C)
Q^4, [$Si(OSi)_4$]	-111	731	930	994	994
Q^3, [$(OH)\cdot Si(OSi)_3$	-102	604	874	962	963
Q^2, [$(OH)_2\cdot Si(OSi)_2$	-92	96	-	217	219

Deconvolution of the spectra by Gaussian functions (least-squares fitting of spectra) resulted in Gaussian curves from which the full width at half maximum was obtained as shown in Figures 51(b)-51(d). A center of the full width at half maximum was selected according to constraints of Bertermann et al. [56]. The same type of data fitting was used to analyze the ^{29}Si SP/MAS NMR spectra. The results of fitting with Gaussian function indicated that the silicon oxides were mainly present in the rice husk chars in the amorphous form due to the width of the resonances originating from the Q^4 sites, which is in line with earlier studies on rice husk ashes of Hamdan et al. [37] and Lippmaa et al. [57]. They assigned the dominating relative area of Q^4 site of rice husk ash to an "ill-ordered" amorphous silicates structure found in highly dispersed form. It seemed that no significant changes appeared in the ^{29}Si NMR spectra and thereby in the rice husk silicate structure at fast heating conditions. The increasing heat treatment temperature caused the relative amount of Q^3 species of original rice husk to decrease and Q^4 sites of original rice husk to increase, leading to a denser network with less surface sites and smaller reactivity towards oxygen [51]. The site oxygen reactivity in the silicon network follows the trend $Q^1 > Q^2 > Q^3 > Q^4$ [58]. In Q^2 and Q^3 sites, the presence of non-bridging oxygen atoms made these silicon species more reactive than Q^4 sites due to the easier rearrangement of silicon network in chars. The Q^2 and Q^3 sites, due to the peak broadening, indicated an increase in the width from 96 Hz to 219 Hz and from 604 Hz to 963 Hz at 1500°C as shown in Table 7. The relative areas of Q^2, Q^3 and Q^4 sites of chars obtained at 1000, 1250 and 1500°C remain nearly similar as shown in Table 8.

Table 8: Calculated relative amounts of Q^2, Q^3 and Q^4 (%) based on the Gaussian fitting of ^{29}Si SP/MAS NMR spectra.

Temperature	**Q^2 (%)**	**Q^3 (%)**	**Q^4 (%)**
raw biomass	0.9	26.6	72.5
1000°C	-	19.5	80.5
1250°C	1.1	22.9	76
1500°C	0.7	20.9	78.4

The results indicated that the original rice husk and their chars are composed mainly of Q^4 sites (72-80 %) and to a minor extent of Q^3 sites (21-27 %) along with small amounts (< 1.2 %)

of Q^2 sites. In the present study, a lower relative area of Q^4 sites than in investigations of Nair et al. [51], except for RHA-12Q sample oxidized for 12 h, was related to the differences in a rice husk preparation. In their study, the rice husk was oxidized at 500, 700 and 900°C in a fixed bed furnace from 15 min to 24 h, and the rice husk ash was collected immediately or after it was naturally cooled down inside the oven, whereas in the present study the rice husk char was immediately cooled down after fast pyrolysis in a temperature range of 1000-1500°C. The fast quenching of rice husk chars in the entrained flow reactor favored the formation of amorphous silicates which is similar to the structure of silica glasses prepared at cooling rates of 1 kK s^{-1} to 1 MK s^{-1} [12, 59–61].

The presence of broad resonances and lack of narrow resonances in the ^{29}Si SP/MAS NMR spectra indicates a glassy/disordered structure of the silica glasses[62], in line with earlier studies on rice husk ashes [51]. A crystalline phase in the rice husk ashes was formed at 1100°C after 12 h oxidation, which was characterized by two intense narrow peaks with a maximum at -110 ppm (FWHH $\approx$ 79.5 Hz) and -112 ppm (FWHH $\approx$ 278 Hz) assigned to cristobalite and tridymite phases. In the present study, the line width of Q^3 site was almost three times broader than the narrow peak of crystalline silicates reported by Nair et al. [51], and exhibited a resonance broadness which is similar to non-crystalline silica glasses (i.e. non-crystalline opals) [63]. The peak with a maximum at -112 ppm, which characterizes the crystallization of cristobalite, was not detected for rice husk chars prepared in a temperature range of 1000-1500°C. Thus, no comparison of the peak with a maximum at -112 ppm reported by Nair et al. [51] was made in the present investigation. This shows that silica remained mainly amorphous at fast pyrolysis conditions with the low content of a crystalline phase. However, the comparison of Q^4 sites indicated that the broadness of the peak at -111 ppm in the literature remains similar to the line width of Q^4 site in the present study which is equal to 2186 Hz at 1000°C and 2384 Hz at 1250°C and 1500°C.

For the chars of wheat straw resonances in the ^{13}C CP/MAS spectra were only observed for the original biomass, whereas resonances were observed from both the original biomass and the char at 1000°C in the ^{13}C SP/MAS spectra. The decreased experimental sensitivity was related to the presence of paramagnetics in the carbonaceous bulk as it was proposed by Bardet et al. [29]. Due to the lower content of Si, no resonances were observed in the ^{29}Si MAS NMR spectra of the wheat straw samples as shown in Figures 50(c)-50(d).

5.3.5 Electron spin resonance spectroscopy analysis

The effect of free radicals at their decay (termination stage) at fast heating rates and at high temperatures (above 1000°C) on the biomass char yield has not been discussed previously. A room-temperature electron spin resonance spectroscopy study was conducted on original wood and herbaceous biomass and their chars, prepared in an entrained-flow reactor. The radical concentrations in the chars from the decay stage range up to a maximum between $7{\cdot}10^{16}$ and $5{\cdot}10^{17}$ spins g^{-1}.

The formation of free radicals is believed in this study to be initiated by primary pyrolysis reactions, where the organic compounds are cracked to small unstable radical fragments. These radicals react with more stable low-molecular weight PAH such as naphthalene that may grow into larger high-molecular PAHs structures, containing delocalized unpaired carbon-centered π-electrons with an additional presence of aliphatic radicals. Due to the homolytic cleavage of β-aryl-ether bonds of lignin, the highly reactive and unstable free radicals are initially obtained that may react through rearrangement, electron abstraction or interactions between radicals, to form stable products as described in the literature [64–66].

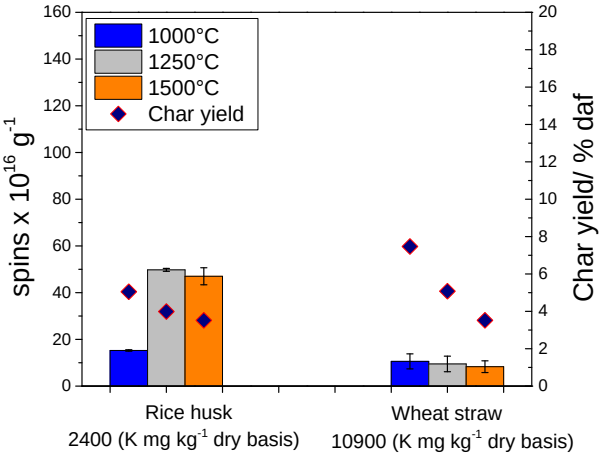

Figure 52: Char yields (blue-red diamonds) and ESR concentration (spins x 10^{16} g^{-1}): (a) pinewood, beechwood, rice husk, leached wheat straw and wheat straw chars prepared in the wire mesh reactor (heat treatment temperature: 1000°C, heating rate: 1000 K s^{-1}, holding time: 1 s) and shown as green stars; (b) wheat straw and rice husk chars prepared in the entrained flow reactor (heat treatment temperatures: 1000, 1250 and 1500°C) versus potassium content in the original lignocellulosic materials.

The high levels of carbon-centered radicals, which were detected in the chars from the decay stage, were proposed to supply hydrogen to inhibit repolymerization / cross-linking [64], and decrease the wood char yield. At high heating rates in the EFR due to a strong bridge-breaking in biomass, leading to the significant tar release, the catalyzed reaction by potassium likely has a minor influence on the char yield. In the present study, the wood and leached wheat straw chars, generated in the entrained flow reactor, have no remaining free radicals, indicating the recombination of radicals and formation of complex polyaromatic structures as shown in Figure 52. The free radicals remained in the wheat straw and rice husk chars from the decay stage of pyrolysis in the entrained flow reactor.

The high potassium content in the wheat straw affected catalytically the radical concentration in the char matrix. Sancier et al. [67] discussed the mechanism of potassium effect on the radical concentration in catalytic coal gasification. The high potassium levels accelerate the formation of reactive aliphatic radicals (g = 2.0030). The formation of potassium-carbon bonds, such as in the potassium rich wheat straw, can weaken carbon-carbon bonds in aromatic rings and thereby

facilitate bond breaking at high temperatures. This leads to formation of aliphatic radicals which react further to produce stable polyaromatic compounds through polymerization / cross-linking reactions at an early stage of the pyrolysis [68–71]. At temperatures of 1000-1500°C close to 70 % potassium in the wheat straw has been released (Figure 48), and the remaining potassium was probably bonded to the wheat straw char in phenolate groups or intercalated in graphene layers [72], reducing the mobility of potassium in the char matrix. The higher radical concentrations in the wheat chars from the decay stage of pyrolysis in the entrained flow reactor compared to the wood chars may be related to the decreased mobility of potassium in the char matrix, leading to the less efficient catalytic effects of potassium on the bond-breaking and radical re-attachments.

The increased radical concentrations in the rice husk chars, generated in the entrained flow reactor, were caused by the formation of carbon-centered radicals. The rice husk contains high concentrations of silicon that is present as silicon oxides with small amounts of alkalis and other trace elements. Lanning [73] concluded that silicon occurs in rice husk in a hydrated amorphous form (opal or silica gel), located mainly in the outer epidermis and filling the inner channels in the spiral structure of the epidermal cells. In addition, Liu et al. [74] and Sharma et al. [75] proposed that the silica in the rice husk is combined with carbohydrates. In the present study, the ash compositional analysis showed that the elemental silicon content in the rice husk chars generated in the entrained flow reactor remained unchanged (Figure 48). The radicals formed at rapid heating rates were proposed to be trapped upon fast cooling in a glassy char structure composed of an amorphous silica phase (glass transition temperature $\approx$ 730°C) [12]. Trapping of organic radicals in amorphous silicon has been reported by Friebele et al. [76], who detected methyl radicals in a heat-treated synthetic silicon fused in a hydrogen-oxygen flame.

5.3.6 Particle size and shape characterization

The particle size and shape of the original rice husk and wheat straw and chars prepared at 1000-1500°C were analyzed with a 2D dynamic imaging device (CAMSIZER XT, Retsch) and SEM microscopy. The SEM microscopy results showed that rice husk chars contained large cavities inside the particle as shown in Figure 53(b), whereas the outer part of the char exhibited a glassy shell consisting of rigid silica beads as shown in Figure 53(c). Krishnarao et al. [27] observed smooth outer surface and a large number of small grains on the char after oxidation of rice husk at 700°C for 3 h. They obtained only amorphous silicates and residual carbon in the white rice husk ash based on the XRD pattern. Overall, in the rice husk chars mainly amorphous silica and polyaromatic structures were detected in the present study. The XRD peak at about 23° in the rice husk chars indicated formation of a turbostratic structure [42–44]. In addition, EDS analysis confirmed that the rice husk chars contained mainly carbon and silicon as described in Appendix B (Table 24).

The amorphous silicates dispersed throughout the organic matrix caused heterogeneous softening of rice husk char at high pyrolysis temperatures due to the molecular disorder of the structure

as shown in Figure 53(b). The shape of the rice husk chars remained preserved even at higher temperatures, due to the low softening temperature of amorphous silicon oxides ($\approx$ 730°C) [12] and rapid cooling of chars. The wheat straw chars obtained different shapes from near-spherical to cylindrical as shown in Figures 53(e)-53(f). However, the wheat straw char particles were mainly cylindrically-shaped as shown in Figure 53(f).

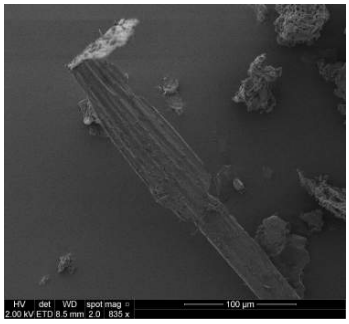

53(a): Original rice husk

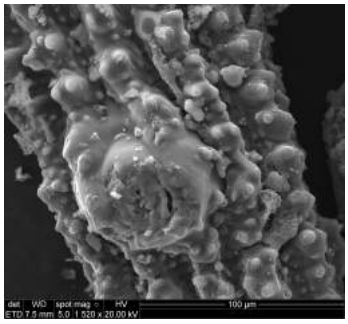

53(b): Outer surface of rice husk char 1500°C

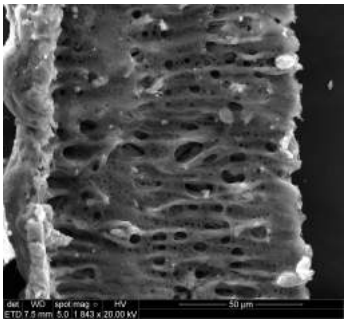

53(c): Inner surface of rice husk char 1500°C

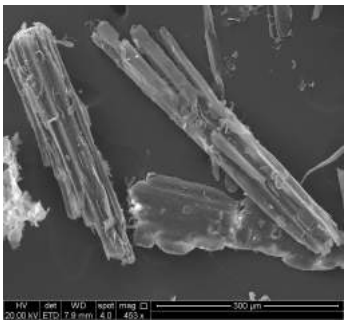

53(d): Original wheat straw

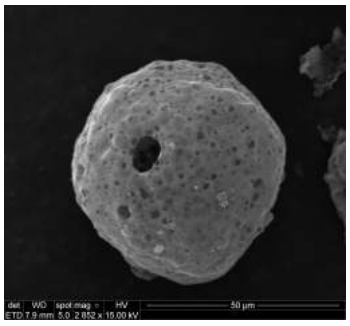

53(e): Wheat straw char at 1250°C

53(f): Wheat straw char at 1250°C

Figure 53: SEM images of wheat straw char at 1250°C and rice husks char at 1500°C, pyrolyzed in the BabiTER reactor.

Figure 54 shows the particle frequency distribution based on volume (q_3) as a function of the characteristic length ($x_{Ma,min}$) of the original rice husk and wheat straw and their chars. The rice husk char kept the particle size of the original lignocellulosic material in a temperature range of 1000-1500°C. The particle size of wheat straw chars, however, was significantly reduced compared to the raw lignocellulosic material. The difference between the two biomass materials was due to the lower content of silicates in the wheat straw.

Regarding the shape, the main difference between the two herbaceous chars was that the rice husk char formed particles of a rectangular shape (SPHT $\approx$ 0.8) while the wheat straw char particles were mainly cylindrically-shaped and to a minor extent near-spherical (SPHT $\approx$ 0.5-0.8) as shown in Figure 54.

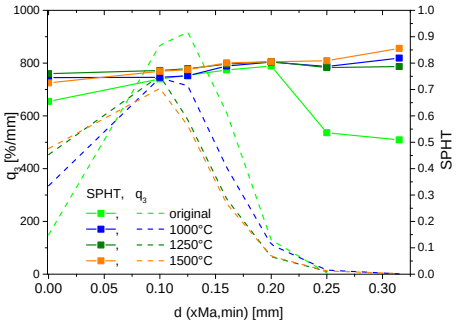

54(a): q_3 and SPHT (rice husk, 0.09-0.18 mm)

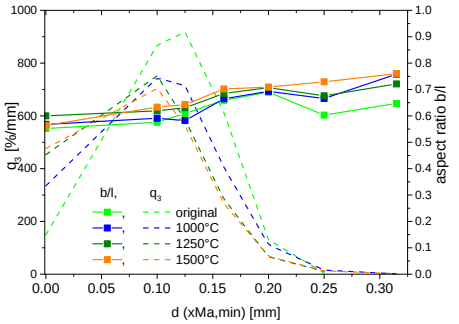

54(b): q_3 and b/l (rice husk, 0.09-0.18 mm)

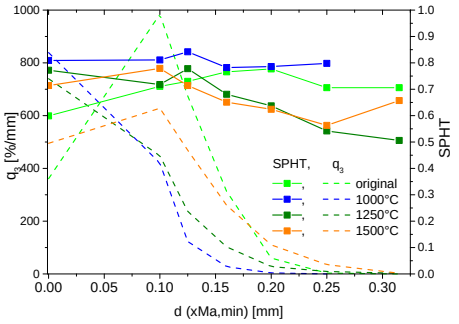

54(c): q_3 and SPHT (wheat straw, 0.09-0.18 mm)

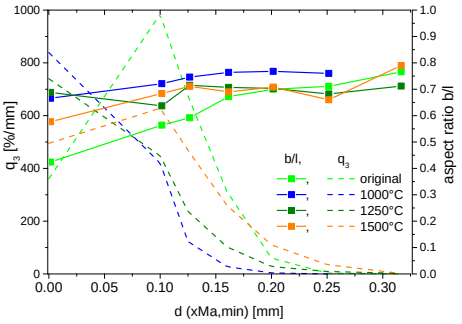

54(d): q_3 and b/l (wheat straw, 0.09-0.18 mm)

Figure 54: Particle frequency distribution based on volume (q_3), sphericity (SPHT) and width to length ratio (b/l) of original wheat straw, rice husk and their chars, pyrolyzed in the BabiTER reactor at 1000, 1250 and 1500°C. The original wheat straw and rice husk after the milling were sieved to fraction 0.09-0.18 mm. Sphericity and width to length ratio are shown as straight lines and q_3 is shown with a dashed line.

The formation of near-spherical wheat straw chars containing cavities was affected by the presence of low-temperature melting potassium silicates. The cylindrically-shaped wheat straw particle formed a smooth surface without any pores, keeping the char structure similar to the original wheat straw particle due to the formation of high-temperature melting calcium silicates. The morphological differences between wheat straw char particles were related to the inorganic compounds allocation in the wheat straw as it was observed by Knudsen [41]. Pseudostem has a very high calcium content [77], whereas the wheat straw leaves contain high amounts of silicon and potassium [78, 79]. Furthermore, the distribution of plant cell constituents in the biomass was also proposed to affect the formation of near-spherical char particles. The biomass char particles undergo softening and melting under fast heating [1]. At higher temperatures, the char plasticization occurs due to the formation of liquid metaplast. Depolymerization with subsequent repolymerization and cross-linking lead to char formation [4]. The differences in cross-linking propensity influence the fluidity of char significantly. The formation of metaplast depends on the complex interaction of all plant cell compounds (holocelluloses, lignin and extractives). Hansen et al. [80] reported that the stems of wheat straw contain more lignin and xylan compared to leaves. Trubetskaya et al. [81] suggested that at fast heating rates the formation of metaplast is mostly affected by

the bond-breaking and cross-linking of organic components present in lignin that are less volatile than holocelluloses. In the present study, the extent of plasticization of the char particles derived from wheat straw leaves was greater than that of char particles derived from straw stems. In addition, the b l^{-1} ratio of rice husk and wheat straw chars decreased from 0.8 to 0.6 with decreasing particle size, indicating that both char particles exhibited a more elongated shape.

5.4 Conclusion

Scanning electron microscopy on the chars indicated structural transformations of lignocellulosic materials during both slow (10 K min^{-1}) and intermediate and fast pyrolysis ($>$ 100 K s^{-1}). At high heating rates in the WMR and DTF reactors, the char underwent strong deformation with clear signs of melting and development of macropores at all applied temperatures. The ability of char to melt in the WMR followed the order wood $>$ wheat straw, alfalfa straw $>$ rice husk, and was related to the formation of metaplast where lignin contributes probably more than holocelluloses due to its lower volatility. The investigations in the DTF showed a similar tendency to melt, except beechwood, which probably contained the high-temperature stable extractives (suburin, tannin) preventing char from the structural transformation. A slightly stronger melting of pinewood char after extraction could indicate extractives influence on the char morphology.

The 2D imaging analysis of wood and herbaceous chars showed that the pyrolysis process caused the characteristic length of all biomass particles to decrease by a factor of two, while the pinewood char obtained the most spherical shape. The beechwood and herbaceous char particles retained a cylindrical shape. The particle shape of rice husk remained preserved at high heat treatment temperatures as observed by the 2D dynamic imaging analysis and SEM microscopy. The particle size of wheat straw char was significantly more reduced compared to rice husk char. The wheat straw chars obtained different shapes from near-spherical to cylindrical. However, the wheat straw char particles were mainly cylindrically-shaped. The morphological differences between wheat straw char particles were mainly related to the inorganic compounds allocation in the wheat straw. The major factors affecting the biomass morphology were addressed to the alkali content. An essential catalytic effect of K and to a minor extent Ca on the fuel structural changes was hypothesized, probably owing to a stronger cross-linking of herbaceous chars, leading to the less fluidity.

The non-treated and leached wheat straw particles obtained a similar cylindrical shape at fast heating rates. No morphological differences between leached wheat straw and non-treated straw was also observed at lower heating rates in the wire mesh reactor. SEM images revealed a molten surface of both char samples without any significant differences. ESEM-EDS spot analysis indicated that potassium is dispersed throughout the char along with solidified silicate rich regions, leading to an additional stability of herbaceous char. Equilibrium calculations using Factsage software indicated that wheat straw chars might contain potassium and calcium silicates. The high Ca content in the alfalfa straw could also help to preserve the particle size of the original fuel.

By ^{29}Si MAS NMR of both original rice husk and their chars broad resonances similar to what was observed in silica glasses were obtained. This demonstrates that the major part of the silicates were present in a disordered/amorphous state. No significant changes appeared in the ^{29}Si NMR spectra for Q^2, Q^3 and Q^4 branches of rice husk chars, meaning almost negligible differences in the char Si bearing compounds in a temperature range of 1000-1500°C in fast pyrolysis. The resonances in ^{29}Si CP/MAS NMR spectra of original wheat straw and its chars were not observed due to the low amount of silicates, high content of paramagnetics or an increased electrical conductivity of chars in fast pyrolysis. However, equilibrium calculations using Factsage software indicated that wheat straw chars contain potassium and calcium silicates. The presence of silicates in the rice husk and wheat straw was proposed to affect the obtained char morphology. The particle shape of rice husk remained preserved at high heat treatment temperatures as observed by the 2D dynamic imaging analysis and SEM microscopy. The lower silicates content and high levels of alkali in the wheat straw caused variations in char particle shapes from cylindrical to near-spherical. The lack of long-range order in XRD analysis and the broad resonances in ^{29}Si solid-state NMR confirmed that silicates in rice husk chars were present in a glass-amorphous form, leading to the formation of a glassy char shell due to the softening of the amorphous silicon oxides. The results of the present study indicated a key role of Si bearing compounds on the char mechanical integrity.

The investigations on larger pinewood particles in the SPR showed that fast heating rates may lead to local formation of metaplast on the outer parts of the particle. Metaplast formation was not observed inside 3-5 mm cubes, presumably due to lower heating rates. In contrast, high heating rates led to metaplast formation inside the 0.85-1 mm pinewood particles pyrolyzed in the DTF. The pinewood particles decreased in size, and formed molten rigid structures with large cavities due to the rapid volatile release. SEM microscopy investigations indicated that 0.85-1 mm pinewood particles obtained mainly a cylindrical and to a minor extent near-spherical shapes in fast pyrolysis.

Despite the high heterogeneity of biomass composition, metaplast formation depends mainly on the heating rate and less on the organic compositional differences. The results of the present study indicated a key role of silicates on the char mechanical integrity of herbaceous biomass. More investigations are required to understand the exact role of alkali on the char morphology in fast pyrolysis.

References

[1] Cetin E, Moghtaderi B, Gupta R, and Wall TF. Influence of pyrolysis conditions on the structure and gasification reactivity of biomass chars. *Fuel*, 83(16):2139–50, 2004.

[2] Chen Y, Charpenay S, Jensen A, Serio MA, and Wojtowicz MA. Modeling biomass pyrolysis kinetics and mechanisms. *ACS Div of Fuel Chem*, 213:96–100, 1997.

[3] Solomon PR, Best PE, Yu ZZ, and Charpenay S. An Empirical Model for Coal Fluidity Based on a Macromolecular Network Pyrolysis Model. *Energy Fuels*, 6(2):143–54, 1992.

[4] Solomon PR, Hamblen DG, Serio MA, and Yu ZZ. A characterization method and model for predicting coal conversion behaviour. *Fuel*, 72(4):469–88, 1993.

[5] Serio MA, Charpenay S, Bassilakis R, and Solomon PR. Measurement and modeling of lignin pyrolysis. *Biomass Bioenergy*, 7(1-6):107–24, 1994.

[6] Bassilakis R, Carangelo RM, and Wojtowicz MA. TG-FTIR analysis of biomass pyrolysis. *Fuel*, 80(12):1765–86, 2001.

[7] Dauenhauer PJ, Colby JL, Balonek CM, Suszynski WJ, and Schmidt LD. Reactive boiling of cellulose for integrated catalysis through an intermediate liquid. *Green Chem*, 11(10):1555–61, 2009.

[8] Niksa S. Predicting the rapid devolatilization of diverse forms of biomass with bio-Flashchain. *Proc Combust Inst*, 28(2):2727–33, 2000.

[9] DeGroot WF and Shafizadeh F. The influence of exchangeable cations on the carbonization of biomass. *J Anal Appl Pyrolysis*, 6(3):217–32, 1984.

[10] Solomon PR, Hamblen DG, Carangelo RM, Serio MA, and Deshpande GV. General Model of Coal Devolatilization. *Biomass Bioenergy*, 2(4):405–22, 1988.

[11] Cetin E, Moghtaderi B, Gupta R, and Wall TF. Biomass gasification kinetics: influences of pressure and char structure. *Combust Sci Technol*, 177(4):765–91, 2005.

[12] Hedler A, Klaumünzer SL, and Wesch W. Amorphous silicon exhibits a glass transition. *Nat Mater*, 3(11):804–9, 2004.

[13] Bharadwaj A, Wang Y, Sridhar S, and Arunachalam VS. Pyrolysis of rice husk. *Current Sci*, 87(7):981–6, 2004.

[14] Sharma RK, Wooten JB, Baliga VL, Lin X, Chan WG, and Hajaligol MR. Characterisation of chars from pyrolysis of lignin. *Fuel*, 83(11-12):1469–82, 2004.

[15] Sharma RK, Wooten JB, Baliga VL, and Hajaligol MR. Characterization of chars from biomass-derived materials: pectin chars. *Fuel*, 80(12):1825–36, 2001.

[16] Orfao JJM, Antunes FJA, and Figueiredo JL. Pyrolysis kinetics of lignocellulosic materials - three independent reactions model. *Fuel*, 78(3):349–58, 1999.

[17] Jepsen MS. *Pyrolysis of Large Biomass Particles in a Single Particle Combustion Reactor*. MSc thesis, DTU Chemical Engineering Department, Technical University of Denmark, 2014.

[18] Dall'Ora M, Jensen PA, and Jensen AD. Suspension combustion of wood: Influence of pyrolysis conditions on char yield, morphology, and reactivity. *Energy Fuels*, 22(5):2955–62, 2008.

[19] Mauseth JD. *Botany: an introduction to plant biology*. Jones and Barlett Publishers, 2003.

[20] Myburg AA and Sederoff RR. *Xylem Structure and Function*. Embryonic Encyclopedia of Life Science. Nature Publishing Group: Macmillan, 1999.

[21] Zhao XH, Liu LY, Nan LJ, Wang H, and Li H. Development of Tyloses in the Xylem Vessels of Meili Grapevine and Their Effect on Water Transportation. *Russ J Plant Physiol*, 61(2):194–203, 2014.

[22] Kitin P, Voelker SL, Meinzer FC, Beeckman H, Strauss SH, and Lachenbruch B. Tyloses and Phenolic Deposits in Xylem Vessels Impede Water Transport in Low-Lignin Transgenic Poplars: A Study by Cryo-Fluorescence Microscopy. *Plant Physiol*, 154(2):887–98, 2010.

[23] Pearce RB and Holloway PJ. Suberin in the sapwood of oak (Quercus robur L.): its composition from a compartmentalization barrier and its occurrence in tyloses in undecayed wood. *Physiol Plant Path*, 24(1):71–81, 1984.

[24] Pouzoulet J, Pivovaroff AL, Santiego LS, and Rolshausen PE. Can vessel dimension explain tolerance toward fungal vascular wilt diseases in woody plants? Lessons from Dutch elm disease and esca disease in grapevine. *Front Plant Sci*, 253(5):1–11, 2014.

[25] Real C, Alcala MD, and Criado JM. Preparation of silica from rice husks. *J Am Ceram Soc*, 79(8):2012–6, 1996.

[26] Cassiday JR, Beaman DR, Black CK, Weimer AW, and Susnitzky DW. Carbothermal nitridation synthesis of α-Si_3N_4 powder from pyrolysed rice hulls. *J Mater Sci*, 31:6005–13, 1996.

[27] Krishnarao RV and Godkhindi MM. Distribution of Silica in Rice Husk and its Effect on the Formation of Silicon Carbide. *Ceram Int*, 18(4):243–9, 1992.

[28] Freitas JCC, Emmerich FG, and Bonagamba TJ. High-Resolution Solid-State NMR Study of the Occurance and Thermal Transformations of Silicon-Containing Species in Biomass Materials. *Chem Mater*, 12(3):711–8, 2000.

[29] Bardet M, Hediger S, Gerbaud G, Gambarelli S, Jacquot JF, and Foray MF et al. Investigation with ^{13}C NMR, EPR and magnetic susceptibility measurements of char residues obtained by pyrolysis of biomass. *Fuel*, 86(12-13):1966–76, 2007.

[30] Pottmaier D, Costa M, Farrow T, Oliveira AAM, Alarcon O, and Snape C. Comparison of Rice Husk and Wheat Straw: From Slow and Fast Pyrolysis to Char Combustion. *Energy Fuels*, 27(11):7115–25, 2013.

[31] Guerrero M, Pilar-Ruiz M, Millera A, Alzueta MU, and Bilbao R. Characterization of Biomass Chars Formed under Different Devolatilization Conditions: Differences between Rice Husk and Eucalyptus. *Energy Fuels*, 22(2):1275–84, 2008.

[32] Nehdi M, Duquette J, and Damatty AE. Performance of rice husk ash produced using a new technology as a mineral admixture in concrete. *Cem Concr Res*, 33(8):1203–10, 2003.

[33] Knudsen JN, Jensen PA, and Dam-Johansen K. Tranformation and Release to the Gas Phase of Cl, K and S during Combustion of Annual Biomass. *Energy Fuels*, 18(5):1385–99, 2004.

[34] Kracek FC, Bowen NL, and Morey GW. Equilibrium relations and factors influencing their determination in the system K_2SiO_3-SiO_2. *J Phys Chem*, 41(9):1183–93, 1937.

[35] Seil GE. Orthosilicates of the alkaline earths with special reference to their uses in the refractory field. *J Am Ceram Soc*, 24(1):1–19, 1941.

[36] Etiegni L and Campbell AG. Physical and Chemical Characteristics of Wood Ash. *Bioresour Technol*, 37(2):173–8, 1991.

[37] Hamdan H, Muhid MNM, Endud E, Listiorini E, and Ramli Z. Si-29 MAS NMR, XRD and FESEM studies of rice husk silica for the synthesis of zeolites. *J Non-Cryst Solids*, 211(1):126–31, 1997.

[38] Jing L, Yu-Zhao M, Zhi-Wei L, and An-Xian L. Preparation of transparent glass-ceramics with high crystallinity. *Chin J Nonferrous Metals*, 21(6):1450–6, 2011.

[39] Sharma MK, Williams WS, and Zangvil A. Formation and Structure of Silicon Carbide Whiskers from Rice Hulls. *J Am Ceram Soc*, 67(11):715–20, 1984.

[40] Wu H, Bashir MS, Jensen PA, Sander B, and Glarborg P. Impact of coal fly ash addition on ash transformation and deposition in a full-scale wood suspension-firing boiler. *Fuel*, 113:632–43, 2013.

[41] Knudsen JN. Volatilization of Inorganic Matter during Combustion of Annual Biomass. PhD thesis, Technical University of Denmark, 2004.

[42] Keiluweit M, Nico RS, Johnson MG, and Kleber M. Dynamic Molecular Structure of Plant Biomass-Derived Black Carbon (Biochar). *Environ Sci Technol*, 44(4):1247–53, 2010.

[43] Poletto M, Pistor V, and Zattera AJ. *Chapter 2. Structural Characteristics and Thermal Properties of Native Cellulose. In: T van de Ven and L Godbout (ed.), Cellulose - Fundamental Aspects*. Intech, 2013.

[44] Kumar A, Negi YS, Choudhary V, and Bhardwaj NK. Characterization of Cellulose Nanocrystals Produced by Acid-Hydrolysis from Sugarcane Bagasse as Agro-Waste. *J Mater Phys Chem*, 2(1):1–8, 2014.

[45] Webster EA, Chudek JA, and Hopkins DW. Carbon transformations during decomposition of different components of plant leaves in soil. *Soil Biol Biochem*, 32(3):301–14, 2000.

[46] Bardet M, Maron S, Foray MF, Berger M, and Guillermo A. Investigation of gamma-Irradiated Vegetable Seeds with High-Resolution Solid-State ^{13}C NMR. *Radiat Res*, 161(4):458–63, 2004.

[47] Xu F, Sun JX, Sun R, Fowler P, and Baird M. Comparative study of organosolv lignins from wheat straw. *Ind Crops Products*, 23(2):180–93, 2006.

[48] Bardet M, Gerbaud G, Giffard M, Doan C, Hediger S, and Pape LL. ^{13}C high-resolution solid-state NMR for structural elucidation of archaeological woods. *Prog Nucl Magn Reson Spectrosc*, 55(3):199–214, 2009.

[49] Reid DG, Bonnet SL, Kemp G, and van der Westhuizen JH. Analysis of commercial proanthocyanidins. Part 4: Solid state ^{13}C NMR as a tool for in situ analysis of proanthocyanidin tannins, in heartwood and bark of quebracho and acacia, and related species. *Photochem*, 94:243–8, 2013.

[50] Lippmaa E, Maegi M, Samoson A, Engelhardt G, and Grimmer AR. Structural studies of silicates by solid-state high-resolution silicon-29 NMR. *J Am Chem Soc*, 102(15):4889–93, 1980.

[51] Nair DG, Fraaij A, Klaassen AAK, and Kentgens APM. A structural investigation relating to the pozzolanic activity of rice husk ashes. *Cem Concr Res*, 38(6):861–9, 2008.

[52] Abreu RF and Schneider J. Structure and Hydration Kinetics of Silica Particles in Rice Husk Ash Studied by ^{29}Si High-Resolution Nuclear Magnetic Resonance. *J Am Ceram Soc*, 88(6):1514–20, 2005.

[53] Prasetyoko D, Ramli Z, Endud S, Hamdan H, and Sulikowski B. Conversion of rice husk ash to zeolite beta. *Waste Manage*, 26(10):1173–9, 2006.

[54] Davidovits J. Application of Ca-based geopolymer with blast furnace slag, a review. *2^{nd} International Slag Valorisation Symposium*, pages 33–49, 2011.

[55] Palomo A, Krivenko P, Garcia-Lodeiro I, Kavalerova E, Maltseva O, and Fernandez-Jimenez A. A review on alkaline activation: new analytical perspectives. *Mater de Construccion*, 64(315):1–24, 2014.

[56] Bertermann R and Tacke R. Solid-State ^{29}Si VACP/MAS NMR Studies of Silicon-Accumulating Plants: Structural Characterization of Biosilica Deposits. *Z Naturforsch*, 55b:459–61, 2000.

[57] Lippmaa ET, Samoson AV, Brei VV, and Gorlov II. Investigation of the surface-structure of high-dispersed silica by the methods of high-resolution Si-29 and H-1-NMR in solid state. *Doklady Akademii Nauk SSSR*, 259(2):403–8, 1981.

[58] Bunker BC. Molecular mechanisms for corrosion of silica and silicate glasses. *J Non-Cryst Solids*, 179:300–8, 1994.

[59] Webb S. Silicate melts: relaxation, rheology, and the glass transition. *Rev Geophys*, 35(2):191–218, 1997.

[60] Debenedetti PG and Stillinger FH. Supercooled liquids and the glass transition. *Nature*, 410(6825):259–67, 2001.

[61] Birnie DP and Dyar MD. Cooling Rate Calculations for Silicate Glasses. *Proc 16^{th} Lunar and Planetary Sci Conf, Part 2, J Geophys Research*, 91(B4):D509–13, 1986.

[62] Stebbins JF. Identification of multiple structural species in silicate glasses by ^{29}Si NMR. *Nature*, 330(6147):465–7, 1987.

[63] Graetsch H, Mosset A, and Gies H. XRD and ^{29}Si MAS-NMR study on some non-crystalline silica minerals. *J Non-Cryst Solids*, 119(2):173–80, 1990.

[64] Blanchard CM and Gray MR. Free radical chain reactions of bitumen residue. *Preprints of Papers ACS Div Fuel Chem*, 42:137–41, 1997.

[65] Afifi AI, Hindermann JP, Chornet E, and Overrend RP. The cleavage of the aryl-o-CH_3 bond using anisole as a model-compound. *Fuel*, 68(4):498–504, 1989.

[66] Feng JW, Zheng S, and Maciel GE. EPR Investigations of Charring and Char/Air Interaction of Cellulose, Pectin, and Tobacco. *Energy Fuels*, 18(2):560–8, 2004.

[67] Wood BJ, Sancier KM, Sheridan DR, Chan BL, and Wise H. The mechanism of catalytic gasification of coal char. Morgantown (WV): US Department of Energy; 1981 December Report No. DE82-009461. Contract No.: DE-AC21-80-MC14593.

[68] Gilman JW, Lomakin S, Kashiwagi T, Vanderhart DL, and Nagy V. Characterization of Flame-retarded Polymer Combustion Chars by Solid-State ^{13}C and ^{29}Si NMR and EPR. *Fire Mater*, 22(2):61–7, 1998.

[69] Sancier KM. Effects of Catalysts and CO_2 Gasification on the ESR of Carbon Black II. *Preprints of Papers ACS, Div Fuel Chem*, 28(5):62–70, 1983.

[70] Butt DAE. Formation of phenols from the low-temperature fast pyrolysis of radiata pine (Pinus radiata) - Part I. Influence of molecular oxygen. *J Anal Appl Pyrolysis*, 76(1-2):38–47, 2006.

[71] Marsh H. The effects of impregnation of coal by alkali salts upon carbonization properties. *Fuel Process Technol*, 2(1):61–75, 1979.

[72] Wen YW. Mechanisms of Alkali Metal Catalysis in the Gasification of Coal, Char, or Graphite. *Cat Rev Sci Eng*, 22(1):1–28, 1980.

[73] Lanning FC. Silicon in Rice. *J Agric Food Chem*, 11(5):435–7, 1963.

[74] Liu SL and Ho CH. Study in the Nature of Silicon in Rice Hull. I. Solubility of the Silicon Part. *J Chin Chem Soc*, 6(2):141–53, 1960.

[75] Sharma RK, Wooten JB, Baliga VL, Lin X, Chan G, and Hajaligol MR. Characterization of Char from the Pyrolysis of Tobacco. *J Agric Food Chem*, 50(4):771–83, 2002.

[76] Friebele EJ, Griscom DL, and Rau K. Observation of the methyl radical CH_3; in irradiated, high-purity synthetic fused silica. *J Non-Cryst Solids*, 57(1):167–75, 1983.

[77] Nurfeta A, Tolera A, Eik LO, and Sundstøl F. Feeding value of enset (Ensete ventricosum), Desmodium intortum hay and untreated or urea and calcium oxide treated wheat straw for sheep. *J Anim Physiol Anim Nutr*, 93(1):94–104, 2008.

[78] Atik C and Ates S. Mass balance of silica in straw from the perspective of silica reduction in straw pulp. *Bioresources*, 7(3):3274–82, 2012.

[79] Ikeda S, Yamashita Y, and Kreft I. Mineral composition of buckwheat by-products and its processing characteristics to konjak preparation. *Fagopyrum*, 16:89–94, 1999.

[80] Hansen MAT, Hidayat BJ, Mogensen KK, Jeppesen MD, Jørgensen B, and Johansen KS et al. Enzyme affinity to cell types in wheat straw (Triticum aestivum L.) before and after hydrothermal pretreatment. *Biotech Biofuels*, 6(1):1–15, 2013.

[81] Trubetskaya A, Jensen PA, Jensen JD, Steibel M, Spliethoff H, and Glarborg P. Influence of fast pyrolysis conditions on yield and structural transformation of biomass chars. *Fuel Process Tech*, 140:205–14, 2015.

6 A comparison of char and soot reactivity determined from thermogravimetric experiments

6.1 Introduction

In this chapter, the results of the investigations on char and soot reactivity are presented. Little is known about influence of biomass organic and inorganic composition on the soot formation and reactivity. In the present study, the reactivities of soot and char were investigated by thermogravimetric (TG) analysis in oxygen and CO_2 gasification. The woody and herbaceous biomass chars were collected from a tubular reactor, wire mesh reactor, drop tube reactor and entrained flow reactor to study the effect of heating rate on the char reactivity. Soot samples were obtained only in drop tube investigations. The aim of this study was to investigate the effects of soot nanostructure, inorganic matter, surface area and particle size on the reactivity of pinewood, beechwood and wheat straw soot samples. In addition, the objective was to understand the influence of alkali and silicates on the reactivity of woody and herbaceous biomass. The present results provide simple means for determining a fuel reactivity ranking that could be applied to full scale suspension fired plants. The knowledge about soot reactivity could help to obtain new solutions for the problems with fouling and corrosion in power plants due to close interaction of soot particles with alkali. This chapter resembles the results of paper entitled "Effects of Several Types of Biomass Fuels on the Yield, Nanostructure and Reactivity of Soot from Fast Pyrolysis at High Temperatures".

6.2 Reaction kinetics of solid residues

The reactivity of char and soot in 5 % volume fraction O_2 or CO_2 (50 cm^3 min^{-1} of O_2 or CO_2 and 95 cm^3 min^{-1} of N_2 measured at 20°C and 101.3 kPa) was determined using a thermogravimetric instrument (Netzsch, STA 449 F1) by loading 3 mg of sample in an Al_2O_3 crucible and heating from 35 to 1350°C in O_2 and from 35 to 1450°C in CO_2 at a constant heating rate of 10 K min^{-1}. The initial sample mass and heating rate used in the TG experiments were selected to minimize possible mass transfer limitations that may occur by O_2 / CO_2 gasification concentration gradients through the TG crucible down to the particle bed, through the particle bed, and inside of soot particle agglomerates [1, 2]. The results of Abian et al. [3] showed that less than 3.5 mg of soot samples should be applied to avoid mass transfer limitations using a heating rate of 10 K min^{-1} in 10 % volume fraction CO_2 gasification. The kinetic parameters of soot and char samples were derived by the integral method presented by Coats and Redfern [4]. Through integral transformation and mathematical approximation, the linear equation was expressed in the form:

$$ln\left(-\frac{ln(1-X)}{T^2}\right) = ln\left(\frac{A \cdot R}{\kappa \cdot E_a}\right) - \frac{E_a}{R \cdot T} \tag{31}$$

In equation 31, κ is the heating rate and R is the gas constant. A plot of ln(-ln(1-X) T^{-2}) versus T^{-1} gives a straight line whose slope and intercept determine the values of the activation energy

(E_a) and pre-exponential factor (A). The results of Qin et al. [5] showed that a first order reaction model in both soot mass and gasification agent can describe the experimental results well.

The reactivities of wood and wheat straw soot samples were compared using reaction rates calculated from the derived kinetic parameters (A and E_a) at a fixed oxidation / gasification temperature of 600°C and 1100°C. The reaction rates of char samples were calculated at a fixed oxidation temperature of 400°C and at a fixed CO_2 gasification temperature of 900°C.

6.3 Reactivity of char

6.3.1 Materials and methods

Pinewood, beechwood, Danish wheat straw, leached Danish wheat straw and rice husk were used in this work to represent softwood, hardwood and agricultural residues. Woody and herbaceous biomass were selected to investigate the effect of differences in inorganic composition (K and Si elements) and organic matter (cellulose, hemicellulose, lignin) on the char reactivity. For the soot reactivity investigations a smaller range of fuels was selected that includes pinewood, beechwood and wheat straw. Graphite (Sigma-Aldrich, purity $> 99.99\,\%$, particle size $< 45\,\mu$m) was used to investigate the effect of structural differences on the char and soot reactivity in oxidation and CO_2 gasification. The effect of heating rate on the char reactivity was investigated using char prepared in a tubular reactor (slow heating rates), a wire mesh reactor (intermediate / fast heating rates) and a drop tube reactor (Luleå University of Technology).

The effect of silicon oxides on the char reactivity was investigated using beechwood doped with 5 % and 30 % SiO_2 (Sigma-Aldrich, purity $> 99.5\,\%$, particle size 5-15 nm). The leaching procedure of wheat straw was described previously in Chapter 3. The silicates effect on the oxygen reactivity was investigated using wheat straw and rice husk chars, prepared in the entrained flow reactor (BabiTER, TU Munich).

6.3.2 Reactivity of char prepared at low and intermediate heating rates

The reactivity of chars of non-pyrolyzed beechwood, wheat straw and rice husk, obtained at slow (tubular reactor) and intermediate and fast heating (wire mesh reactor) rates respectively and at temperatures of 1000°C and 1400°C were compared in the present study. Moreover, the effect of varying holding time at a fixed heat treatment temperature (1000°C) in the tubular furnace from 10 min to 4 h was investigated. The reactivity of char samples was examined for O_2 and CO_2 gasification (5 % reactive gas and 95 % N_2) using the STA instrument with a heating rate of 10 K min^{-1}.

In Figure 55, the oxidation of the beechwood and wheat straw chars took place between 400 and 500°C and gasification between 700 and 900°C. The maximum reaction rate of rice husk chars was shifted to temperatures about 100°C higher than for the other biomasses (in O_2 between 500 and 600°C; in CO_2 between 900 and 1450°C). The reactivities of chars under slow and rapid

heating and various holding times were essentially the same in oxidation and gasification, due to the structure formation of a similar polyaromatic type for woody and herbaceous chars after the devolatilization stage was completed so that the small differences in reactivity between biomasses were mostly caused by the inorganic matter. The low oxidation and gasification rates of rice husk chars after high temperature pyrolysis might be influenced by the low alkali presence (1.1 wt. %) in original rice husk compared to original beechwood (0.8 wt. %) and wheat straw (1.9 wt. %).

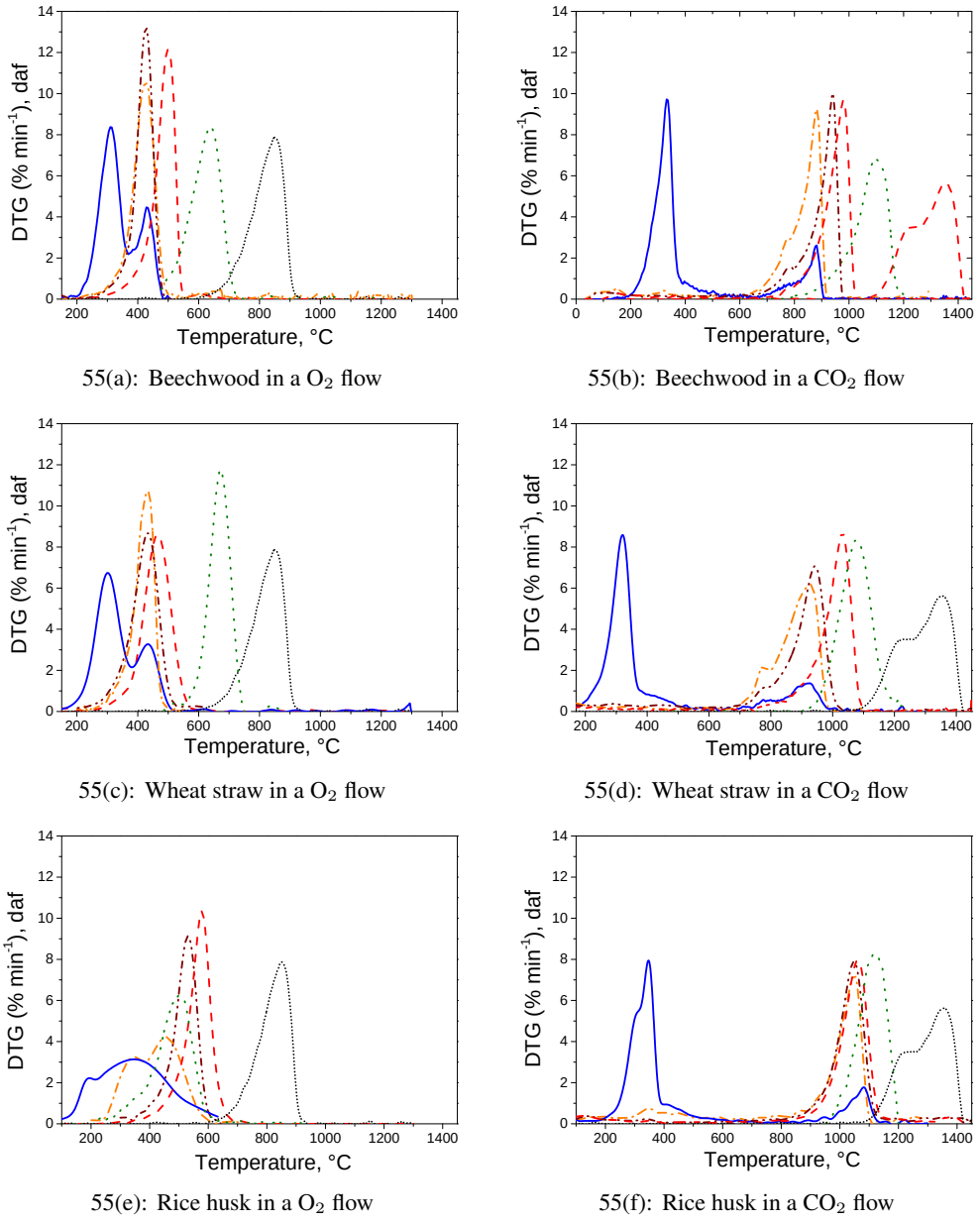

55(a): Beechwood in a O_2 flow

55(b): Beechwood in a CO_2 flow

55(c): Wheat straw in a O_2 flow

55(d): Wheat straw in a CO_2 flow

55(e): Rice husk in a O_2 flow

55(f): Rice husk in a CO_2 flow

Figure 55: Differential thermogravimetric analysis (DTG), obtained in a O_2 and CO_2 flows for original samples ——, char (WMR, 1000°C, 1000 K s^{-1}, 1 s) – · – · –, char (furnace, 1000°C, 10 min) – · · – · · –, (1000°C, 4 h) – – –, char (furnace, 1400°C, 10 min) – – –, graphite •••••.

In the present study, all biomass chars were several times more reactive at all applied conditions than the commercial graphite. The calculated reaction rate of beechwood and wheat straw

decreased from $2{\cdot}10^{-3}$ to $6{\cdot}10^{-6}\,s^{-1}$ and from $2{\cdot}10^{-3}$ to $3{\cdot}10^{-7}\,s^{-1}$ in oxidation with the increased temperature and prolongated residence time as shown in Table 9. In gasification the reaction rate of wheat straw was significantly influenced by the heat treatment temperature due to the reaction rate decrease from $4{\cdot}10^{-3}$ to $7{\cdot}10^{-5}\,s^{-1}$. Beechwood and wheat straw deactivated in oxidation and gasification to a different order of magnitude. The lower inorganic matter content in beechwood led to less char deactivation and higher char reactivity compared to other fuels. The reaction rates of rice husk chars were only slightly affected by the heat treatment temperature and holding time in oxidation and gasification, due to the low alkali content in the original fuel.

Table 9: Kinetic parameters for O_2 and CO_2 reactivity of original beechwood, wheat straw, rice husk and their chars, pyrolyzed in a WMR (1000°C, 1000 K s^{-1}, 1 s) and TR (1000°C or 1400°C, 10 K min^{-1}, 10 min or 4 h).

Sample	Temperature	Holding time	E_a	A	r_A at 400°C	E_a	A	r_A at 900°C
	°C		kJ mol^{-1}	s^{-1}	s^{-1}	kJ mol^{-1}	s^{-1}	s^{-1}
			O_2			CO_2		
				Beechwood				
	raw		115	$2{\cdot}10^{6}$	$2{\cdot}10^{-3}$	197	$4{\cdot}10^{6}$	$8{\cdot}10^{-3}$
WMR	1000	1 s	92	$3{\cdot}10^{4}$	$2{\cdot}10^{-3}$	190	$2{\cdot}10^{6}$	$7{\cdot}10^{-3}$
TR	1000	10 min	93	$3{\cdot}10^{4}$	$2{\cdot}10^{-3}$	209	$5{\cdot}10^{6}$	$2{\cdot}10^{-3}$
TR	1000	4 h	138	$3{\cdot}10^{5}$	$6{\cdot}10^{-6}$	227	$1{\cdot}10^{7}$	$1{\cdot}10^{-3}$
TR	1400	10 min	87	$3{\cdot}10^{3}$	$5{\cdot}10^{-4}$	221	$7{\cdot}10^{5}$	$1{\cdot}10^{-4}$
				Wheat straw				
	raw		76	$1{\cdot}10^{3}$	$2{\cdot}10^{-3}$	208	$6{\cdot}10^{6}$	$4{\cdot}10^{-3}$
WMR	1000	1 s	69	437	$2{\cdot}10^{-3}$	207	$6{\cdot}10^{6}$	$3{\cdot}10^{-3}$
TR	1000	10 min	63	117	$1{\cdot}10^{-3}$	209	$3{\cdot}10^{6}$	$2{\cdot}10^{-3}$
TR	1000	4 h	94	$1{\cdot}10^{4}$	$6{\cdot}10^{-4}$	211	$10{\cdot}10^{5}$	$4{\cdot}10^{-4}$
TR	1400	10 min	195	$3{\cdot}10^{10}$	$3{\cdot}10^{-7}$	315	$8{\cdot}10^{9}$	$7{\cdot}10^{-5}$
				Rice husk				
	raw		51	10	$1{\cdot}10^{-3}$	260	$3.8{\cdot}10^{7}$	$1{\cdot}10^{-4}$
WMR	1000	1 s	81	$10{\cdot}10^{3}$	$5{\cdot}10^{-3}$	246	$2{\cdot}10^{7}$	$2{\cdot}10^{-4}$
TR	1000	10 min	91	$3{\cdot}10^{3}$	$5{\cdot}10^{-4}$	224	$2{\cdot}10^{6}$	$2{\cdot}10^{-4}$
TR	1000	4 h	94	$2{\cdot}10^{3}$	$8{\cdot}10^{-5}$	216	$8{\cdot}10^{5}$	$2{\cdot}10^{-4}$
TR	1400	10 min	63	42	$2{\cdot}10^{-4}$	223	$1{\cdot}10^{6}$	$1{\cdot}10^{-4}$
				graphite				
	pure		195	$5{\cdot}10^{6}$	$4{\cdot}10^{-9}$	276	$3{\cdot}10^{6}$	$1{\cdot}10^{-6}$

The results of the present study at slow and intermediate heating rates showed that the heat treatment temperature, residence time and inorganic matter differences (mainly potassium) affected the reactivity in oxidation and CO_2 gasification more than the pyrolysis heating rate. The biomass chars prepared at 1000 K s^{-1} and 10 K min^{-1} were more reactive and less deactivated than chars prepared at 1400°C and 1000°C with the residence time of 4 h.

6.3.3 Reactivity of char prepared at fast heating rates

Figure 56 shows differential mass loss curves (DTG) for the 5 % volume fraction O_2 oxidation and 5 % volume fraction CO_2 gasification of char samples, prepared in a temperature range of

1000-1400°C in a drop tube reactor. The oxidation and gasification of the beechwood, wheat straw and leached wheat straw chars took place at nearly the same temperature range from 350 to 550°C and from 700 to 1050°C, whereas the maximum reaction rate of pinewood char was shifted to temperatures about 100°C higher than for the other biomasses in both oxidation and CO_2 gasification. A general observation, valid for all fuels, is that char reactivity decreases as heat treatment temperature increases due to thermal deactivation.

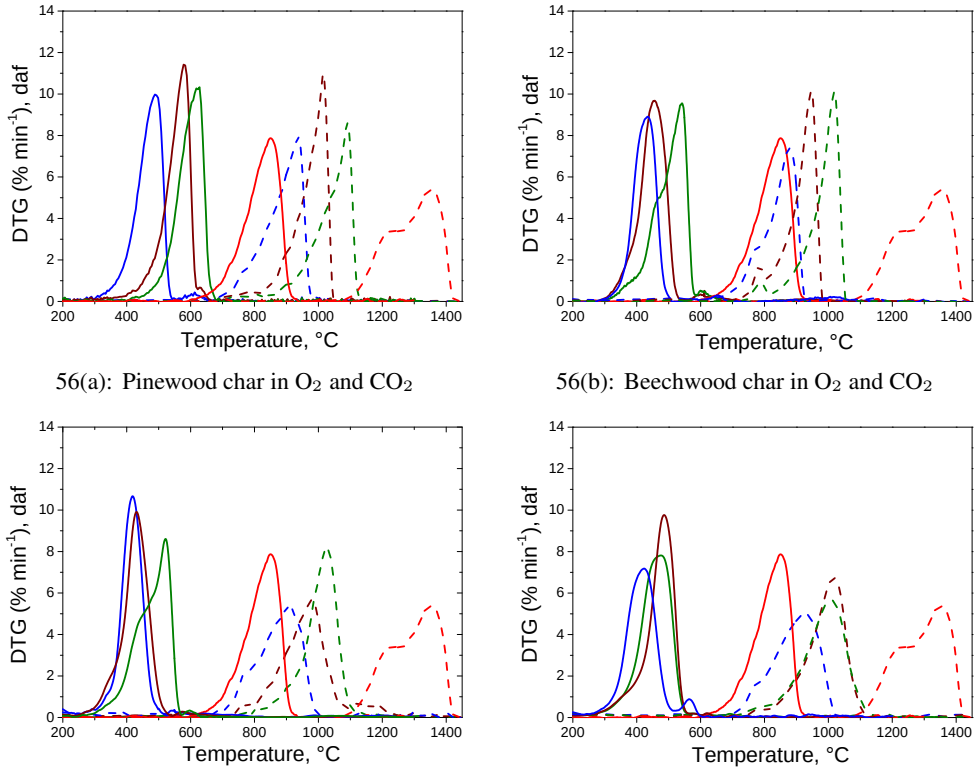

56(a): Pinewood char in O_2 and CO_2

56(b): Beechwood char in O_2 and CO_2

56(c): Straw char in O_2 and CO_2

56(d): Leached straw char in O_2 and CO_2

Figure 56: Differential thermogravimetric analysis (DTG) of pinewood, beechwood, wheat straw, leached straw chars, obtained in (5 % volume fraction O_2 + 95 % volume fraction N_2) flow at 1000°C ——; 1250°C ——; 1400°C ——; graphite ——; in (5 % volume fraction CO_2 + 95 % volume fraction N_2) flow: at 1000°C - - -; 1250°C - - -; 1400°C - - -; graphite - - -.

The DTG signal of chars prepared at 1000 and 1250°C is shown as a single broad peak in both O_2 and CO_2 gasification. In oxidation, the beechwood and wheat straw chars prepared at 1400°C show two peaks with the high temperature peaks at 450 and 520°C, respectively. At high heat treatment temperatures, there is probably a transition region where more reactive phase disappears, while the less reactive phase is formed as observed by Zolin et al. [6]. In this transition, the char reactivity is reduced and the activation energy is increased due to the char deactivation. In order for graphitization to occur, carbon crystallites with the sufficient mobility are required to align and coalesce. The carbon crystallite mobility is enhanced in the presence of hydrogen in the char, leading to char plasticity when heated, whereas high oxygen content in a char leads

to the development of highly cross-linked structures, which hinder crystallite mobility and thus graphitization [7].

The wheat straw char contains more oxygen (7-14 %) than wood char (3-5 %) and leached wheat straw char (6-11 %). The wheat straw char is therefore probably more cross-linked, and thus more reactive compared to other chars. The more cross-linked or disordered wheat straw char contains a higher proportion of edge carbons, which are more reactive [8]. However, due to the nearly similar oxygen content of pinewood and beechwood, the char cross-linking had probably less influence on the transition phase formation of beechwood char prepared at 1400°C in fast pyrolysis. It suggests that the char organic structure affected less the char reactivity due to the presence of a near similar polyaromatic fraction in woody and herbaceous chars. The formation of highly ordered graphitic structure in a char requires longer residence time and higher temperatures compared to the operating parameters applied in the present study. Beechwood, leached wheat straw and non-treated wheat straw had a medium to high content of potassium which catalyze the char conversion in both O_2 and CO_2 gasification.

At high temperatures, a larger part of the potassium can either evaporate or may undergo reactions in the char which decrease its catalytic activity [9]. The broad DTG peak might be related to both regions where potassium is still able to catalyze the reaction and regions where it is catalytically inactive. The potassium content contributed to high reactivities of beechwood, leached wheat straw and wheat straw chars in oxidation and CO_2 gasification. Table 10 shows that the pinewood was less reactive by a factor > 10 than other chars at heat treatment temperatures of 1000-1400°C, probably due to the lower potassium content, leading to the stronger deactivation. The reaction rates of pinewood chars were closer to the rates of commercial graphite due to the less active sites. In beechwood, leached wheat straw and non-treated wheat straw, the catalytic active potassium was probably intercalated and well dispersed in the char matrix [1].

Jensen et al. [10] showed that in pyrolysis of Danish wheat straw between 700 and 800°C, 20 % of the total potassium was incorporated into silicate structure. It was suggested that potassium silicates were formed by reaction of silicate with gaseous KCl. Wornat et al. [7] suggested that significant amounts of potassium and calcium in biomass chars were associated with oxygen functionalities because of high potassium, calcium and oxygen found dispersed in the char matrix. The elemental potassium is bonded to oxygen groups in the char matrix, which include phenolate compounds. The increased reactivity of K^+ rich char might be caused by the intercalation of potassium into the graphene layers of polyaromatic char structures [11]. This intercalation increases the interlayer distance of graphene sheets, leading to the turbostratic structure, and therefore to the higher char reactivity as observed by Liati et al. [12]. The catalytic activities of potassium salts followed the order KOH $\approx$ K_2CO_3 $\approx$ KNO_3 $>$ K_2SO_4 $>$ KCl, whereas potassium hydroxide is a key component in the activation of all salts [13]. A semi-empirical molecular orbital calculation on potassium phenolates (C-O-K) for gasification reactions of graphite was performed by Chen and Yang [14]. The calculations showed that the attachment of C-O-K to zigzag faces of graphite led to higher catalytic activity than the attachment of C-O-K to the armchair faces, leading to the

activity loss.

The maximum reaction rate of pinewood char was about 60°C higher than that of leached wheat straw char at all applied heat treatment temperatures (HTT), which could indicate the effect of higher potassium content remaining in leached wheat straw char or compositional differences of fuels, leading to a different degree of cross-linking. The higher remaining oxygen content in leached wheat straw char (6-12 %) compared to oxygen level in pinewood char (4-5 %) could explain a stronger cross-linking of leached wheat straw char as oxygen immobilizes layer-planes and hinders a crystallite growth in leached wheat straw char thus retaining a higher reactivity.

Table 10: Kinetic parameters for O_2 and CO_2 reactivity of pinewood, beechwood, wheat straw char and leached wheat straw char, pyrolyzed at 1000, 1250 and 1400°C in the drop tube reactor.

Temperature	E_a	A	r_A at 400°C	E_a	A	r_A at 900°C
°C	kJ mol^{-1}	s^{-1}	s^{-1}	kJ mol^{-1}	s^{-1}	s^{-1}
		O_2			CO_2	
			Pinewood			
1000	107	$9{\cdot}10^{4}$	$5{\cdot}10^{-4}$	193	$1{\cdot}10^{6}$	$3{\cdot}10^{-3}$
1250	135	$9{\cdot}10^{5}$	$3{\cdot}10^{-5}$	262	$3{\cdot}10^{8}$	$6{\cdot}10^{-4}$
1400	155	$6{\cdot}10^{6}$	$6{\cdot}10^{-6}$	273	$2{\cdot}10^{8}$	$1{\cdot}10^{-4}$
			Beechwood			
1000	132	$3{\cdot}10^{7}$	$1{\cdot}10^{-3}$	199	$5{\cdot}10^{6}$	$7{\cdot}10^{-3}$
1250	104	$1{\cdot}10^{5}$	$8{\cdot}10^{-4}$	239	$1{\cdot}10^{8}$	$3{\cdot}10^{-3}$
1400	97	$9{\cdot}10^{3}$	$3{\cdot}10^{-4}$	258	$2{\cdot}10^{8}$	$5{\cdot}10^{-4}$
			Wheat straw			
1000	92	$2{\cdot}10^{4}$	$2{\cdot}10^{-3}$	167	$7{\cdot}10^{4}$	$3{\cdot}10^{-3}$
1250	91	$2{\cdot}10^{4}$	$1{\cdot}10^{-3}$	179	$7{\cdot}10^{4}$	$7{\cdot}10^{-4}$
1400	92	$6{\cdot}10^{3}$	$4{\cdot}10^{-4}$	230	$5{\cdot}10^{6}$	$3{\cdot}10^{-4}$
			Leached wheat straw			
1000	91	$2{\cdot}10^{4}$	$2{\cdot}10^{-3}$	212	$1{\cdot}10^{6}$	$4{\cdot}10^{-4}$
1250	102	$4{\cdot}10^{4}$	$5{\cdot}10^{-4}$	221	$1{\cdot}10^{7}$	$2{\cdot}10^{-3}$
1400	110	$2{\cdot}10^{5}$	$5{\cdot}10^{-4}$	222	$3{\cdot}10^{6}$	$4{\cdot}10^{-4}$
			graphite			
pure	195	$5{\cdot}10^{6}$	$4{\cdot}10^{-9}$	276	$3{\cdot}10^{6}$	$1{\cdot}10^{-6}$

However, the differences in rate constants of non-treated straw and leached wheat straw chars were small, corresponding to observations of Jensen et al. [15]. This shows that the removed fraction of potassium does not affect the char reactivity. The differences in reactivity of pinewood and other biomass samples with the higher potassium content might be caused by the organically bonded potassium to the char matrix or potassium silicates. This indicates a key role of potassium on the reactivity of woody and herbaceous chars.

6.3.4 Silicates effect on the char reactivity at fast heating rates

The reactivity of rice husk and wheat straw chars towards oxygen was investigated in a TG instrument to understand the effect of heat treatment temperature and lignocellulosic material type. The wheat straw and rice husk chars, prepared at 1000, 1250 and 1500°C, were oxidized with a

heating rate of 10 K min^{-1} up to 1350°C. The derivatives of the mass loss signals of the char in 5 % volume fraction O_2 are shown as a function of temperature in Figure 57.

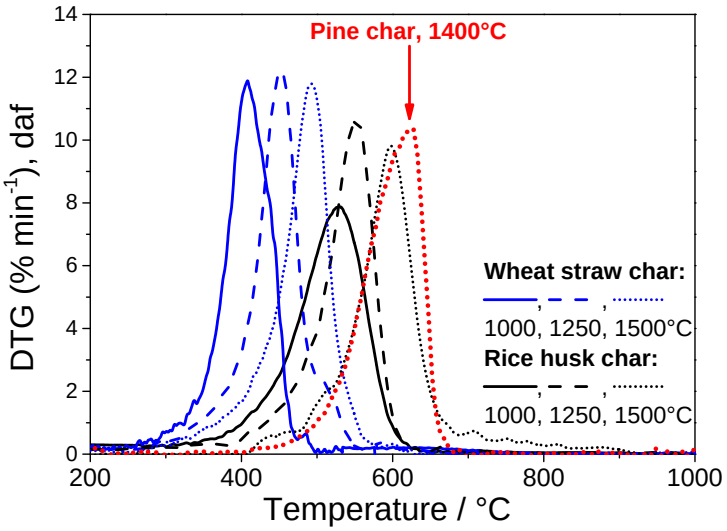

Figure 57: Differential thermogravimetric analysis (DTG curves) in 5 % volume fraction O_2 of rice husk and wheat straw chars as a function of heat treatment temperature, pyrolyzed in BabiTER reactor at 1000, 1250 and 1500°C and oxidized in a TG instrument, and compared with the DTG curve of pinewood char prepared at 1400°C in the drop tube reactor.

The maximum conversion rate of the wheat straw chars took place between 400 and 550°C, whereas the maximum conversion rate of rice husk chars was shifted to approximately 100°C higher temperatures. This shows that the wheat straw chars were significantly more reactive than the rice husk chars. The main reason for the difference in reactivity was the higher level of alkali metals in the wheat straw chars compared to rice husk, which catalyzes the oxidation reaction. The Arrhenius parameters for char oxidation derived from the TG experiments are shown in Table 11. At an average temperature of 400°C, the rate constant for wheat straw char oxidation decreased from $2{\cdot}10^{-3}$ to $5{\cdot}10^{-4}$ s^{-1} as the heat treatment temperature increased from 1000 to 1500°C. For rice husk, the rate constant decreased correspondingly from $3{\cdot}10^{-4}$ to $1{\cdot}10^{-5}$ s^{-1}. The reactivities of rice husk chars were compared with that of pinewood char generated in the drop tube reactor at 1400°C as reported by Trubetskaya et al. [16]. The reactivities of pinewood and rice husk chars were similar, indicating less influence of silicon oxides on the char reactivity. Furthermore, both chars were deactivated at high heat treatment temperatures due to thermal annealing forming more ordered polyaromatic structures with graphene-like layers, leading to char deactivation, in agreement with the results of Pottmaier et al. [17].

Table 11: Kinetic parameters for O_2 reactivity of wheat straw and rice husk chars, pyrolyzed in BabiTER (1000, 1250 and 1500°C) and original rice husk oxidized in a TG instrument.

Temperature of char formation	E_a	A	r_A at 400°C
°C	kJ mol^{-1}	s^{-1}	s^{-1}
Wheat straw			
original	76	$1{\cdot}10^{3}$	$2{\cdot}10^{-3}$
1000	99	$1{\cdot}10^{5}$	$2{\cdot}10^{-3}$
1250	95	$2{\cdot}10^{4}$	$9{\cdot}10^{-4}$
1500	96	$1{\cdot}10^{4}$	$5{\cdot}10^{-4}$
Rice husk			
original	51	10	$1{\cdot}10^{-3}$
1000	74	$2{\cdot}10^{2}$	$3{\cdot}10^{-4}$
1250	138	$2{\cdot}10^{6}$	$5{\cdot}10^{-5}$
1500	138	$5{\cdot}10^{5}$	$1{\cdot}10^{-5}$
graphite			
pure	195	$5{\cdot}10^{6}$	$4{\cdot}10^{-9}$

6.3.5 Conclusion

The influence of inorganic matter (K and Si) and original biomass compositional differences on the char reactivity in oxidation and CO_2 gasification was investigated. The woody and herbaceous biomass chars were pyrolyzed at heat treatment temperatures in a range of 1000-1500°C and at heating rates of 10-10^4 K s^{-1}. The char reactivity in oxidation and CO_2 gasification decreased as heat treatment temperature increased due to the char deactivation and thereby less reactive and less available sites. The results of the present study showed that the heat treatment temperature, residence time and inorganic matter differences affected the reactivity in oxidation and CO_2 gasification more than the pyrolysis heating rate.

The reactivities of pinewood and rice husk chars were similar in oxidation, indicating less influence of silicon oxides on the char reactivity, whereas the alkali rich wheat straw chars were more reactive than pinewood chars generated in a temperature range of 1000-1400°C in the drop tube reactor and rice husk chars prepared at temperatures of 1000-1500°C in the entrained flow reactor. The formation of the molten amorphous silicon oxides shell on the rice husk char originating from the low softening temperature of amorphous silicon oxides did not decrease the apparent reactivity. The reactivity of rice husk chars decreased only slightly at high heat treatment temperatures due to the carbon annealing.

When produced at the same pyrolysis conditions, beechwood, leached and non-treated wheat straw chars were more reactive in oxidation than pinewood and rice husk chars at all applied operating conditions. This observation was related to the differences in potassium content. The reactivities of non-treated and leached wheat straw chars were similar. The differences in reaction rates of non-treated and leached wheat straw chars at 1250 and 1400°C were small in CO_2 gasification. This indicates that the major part of potassium in the non-treated straw either evaporated or was incorporated into non-catalytic species such as potassium silicates. However, a small

part of the potassium retained its catalytic effect in both straw samples leading to a quite similar reactivity, which was still higher than the reactivity for pinewood. The importance of potassium on the char reactivity was additionally supported by the higher activation energies calculated for leached wheat straw char compared to that of non-treated wheat straw in both oxidation and CO_2 gasification. However, the maximum reaction rate of pinewood took place at 60°C higher than that of leached wheat straw due to the lower degree of cross-linking in the pinewood and higher potassium content remaining in the leached wheat straw. The results of the present study indicated a key role of potassium on the char reactivity.

6.4 Reactivity of soot

6.4.1 Materials and methods

Pinewood, beechwood and Danish wheat straw were chosen for the fast pyrolysis study in a drop tube reactor. Fuel selection was based on the differences in the ash composition and plant cell compounds (cellulose, hemicellulose, lignin, extractives). The wood samples are low in ash, with slightly higher potassium and calcium contents in beechwood than in pinewood. Danish wheat straw is rich in silicon and alkali (K, Ca, Na).

Biomass soot samples collected during fast pyrolysis at 1250 and 1400°C were further investigated under O_2 and CO_2 gasification conditions in a thermogravimetric analyzer. Reactivities of wood and straw soot were compared using reaction rates calculated from the derived kinetic parameters. Ash analysis was carried out by X-ray fluorescence instrument only on the wheat straw soot to determine the composition of inorganic matter incorporated in the soot particle. Equilibrium calculations using the Factsage program and Fourier transform infrared spectroscopy (FTIR) analysis were performed to characterize water-soluble potassium compounds found in the wheat straw soot.

Reaction rates of non-treated beechwood and wheat straw soot were compared with leached samples to investigate the effect of potassium on soot reactivity. Soot samples were leached in deionized water by continuous stirring at room temperature for 30 min, followed by drying at 30°C in an oven desiccator. Graphite (Sigma-Aldrich, purity > 99.99 %, particle size $< 45\,\mu$m) reactivity was compared with soot reactivity in O_2 and CO_2 gasification. To study the catalytic effect of potassium, KNO_3 (Sigma-Aldrich, purity > 99.999 %) was diluted in deionized water and added to 50 mg graphite to obtain 20 wt. % or 30 wt. % potassium. Samples were dried at 30°C in an oven desiccator for 12 h. Prior to gasification in 5 % volume fraction CO_2, graphite impregnated with 20 wt. % and 30 wt. % KNO_3 was kept at 500°C for 4 h in N_2 using the thermogravimetric instrument to degas the basal plane of the graphite and to calcine the sample to release NO_2.

The generated soot samples were further characterized using X-ray diffraction (XRD) and electron energy-loss spectroscopy (EELS) to investigate the structural differences in organic (crystal, polycrystalline, and amorphous) and inorganic composition. The particle size and nanostructure of woody and herbaceous soot samples were analyzed by transmission electron microscopy

(TEM).

6.4.2 Reactivity

Figure 58 shows differential mass loss curves (DTG) for the 5 % volume fraction O_2 and 5 % volume fraction CO_2 gasification of soot samples. The DTG curves show a single broad peak in both O_2 oxidation and CO_2 gasification, indicating a heterogeneous soot mixture with respect to the composition and particle size as suggested by Russell et al. [18].

The oxidation of beechwood and wheat straw soot at both preparation temperatures took place at nearly the same temperature range from 350 to 550°C, whereas the maximum reaction rate of pinewood soot was shifted to temperatures about 100°C higher than for the other biomasses (in O_2 between 450 and 700°C). The pinewood soot was clearly less reactive in comparison to beechwood and wheat straw soot. The pinewood soot reactivities at 1250 and 1400°C in the CO_2 atmosphere were nearly similar to graphite with the peak temperature at 1350°C.

The relative importance of external diffusion on the overall soot oxidation / gasification in the TG experiments was evaluated by comparing of the observed maximal reaction rate (r_{max}, % min^{-1}) with the calculated diffusion rate (r_{diff}, % min^{-1}) of O_2/CO_2 and shown in Table 12.

Table 12: The diffusion rate was calculated at the relevant peak temperature of the TG experiment in 5 % volume fraction O_2 and 5 % volume fraction CO_2, and compared with the reaction rate (r_{max}) measured by the thermogravimetric instrument and shown in Figure 58 as the first derivative (DTG) at the maximal temperature.

Fuel	**1250°C**	**1400°C**	**1250°C**	**1400°C**	**1250°C**	**1400°C**	**1250°C**	**1400°C**
	Peak temperature*		D_{AB}		r_{diff}		r_{max}/r_{diff}	
	°C		$m^2\ s^{-1}$		% min^{-1}			
				O_2 atmosphere				
Pinewood	1330	1290	$2.8{\cdot}10^{-4}$	$2.5{\cdot}10^{-4}$	22	19	0.23	0.27
Beechwood	1200	1050	$2.4{\cdot}10^{-4}$	$2{\cdot}10^{-4}$	25	21	0.33	0.28
Wheat straw	970	900	$1.8{\cdot}10^{-4}$	$1.6{\cdot}10^{-4}$	28	15	0.4	0.58
				CO_2 atmosphere				
Pinewood	650	600	$1.4{\cdot}10^{-4}$	$1.3{\cdot}10^{-4}$	27	34	0.37	0.35
Beechwood	500	480	$1{\cdot}10^{-4}$	$9.8{\cdot}10^{-5}$	34	37	0.29	0.27
Wheat straw	450	450	$9.2{\cdot}10^{-5}$	$9.2{\cdot}10^{-5}$	32	35	0.27	0.29

*Relevant peak temperature of the thermogravimetric experiment

The influence of convective flow on the mass transfer inside the crucible was assumed to be negligible, and so mass transport occurs by molecular diffusion only. Soot samples were assumed to be non-porous. The mass transfer of product gases on the reaction was neglected, and the temperature within the soot layer was assumed uniform. Furthermore, it was assumed that the soot particles were distributed equally in the TG crucible. The maximal reaction rate (r_{max}) measured by the thermogravimetric instrument is shown as the first derivative (DTG) at the maximal temperature in Figure 58.

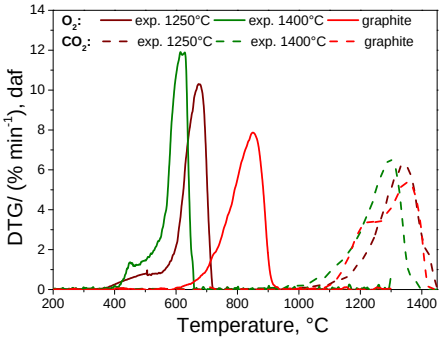

58(a): Pinewood soot in O_2 and CO_2

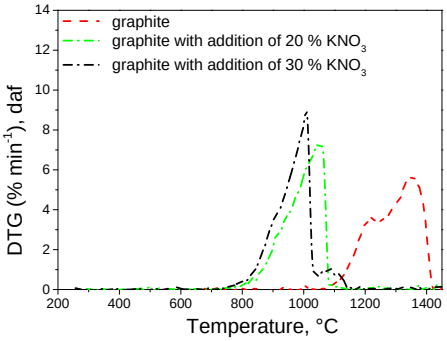

58(b): Graphite with added KNO_3 in CO_2

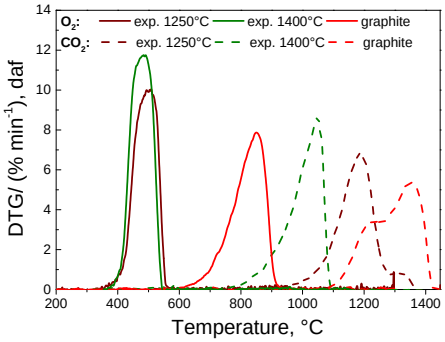

58(c): Beechwood soot in O_2 and CO_2

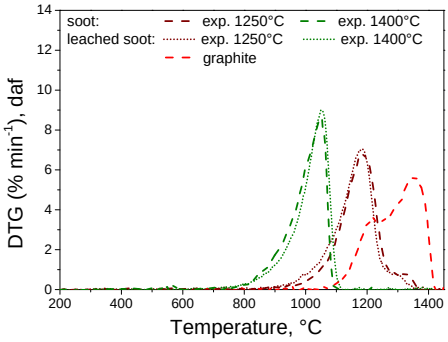

58(d): Leached beechwood soot in CO_2

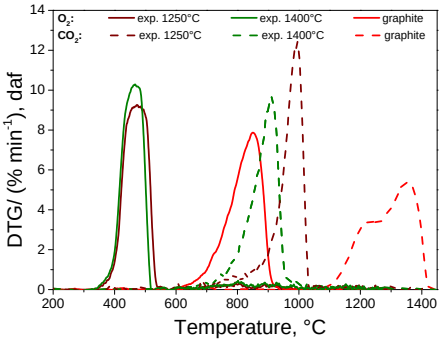

58(e): Wheat straw soot in O_2 and CO_2

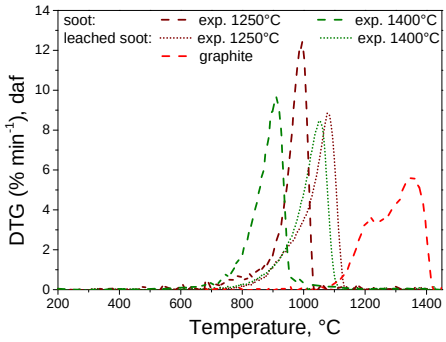

58(f): Leached straw soot in CO_2

Figure 58: (a),(c),(e) DTG curves of pinewood, beechwood, wheat straw soot samples and graphite in (5 % volume fraction O_2 + 95 % volume fraction N_2) at 1250°C ▬; 1400°C ▬; graphite ▬ and in (5 % volume fraction CO_2 + 95 % volume fraction N_2) at 1250°C - - -; 1400°C - - -; graphite - - -; (b),(d),(f) 20 wt. % KNO_3 -·-·-; and 30 wt. % KNO_3 -··-··-; added to graphite - - -; wheat straw and leached beechwood soot samples prepared at 1250°C ••••• and at 1400°C ••••• in the DTF and leached in deionized water. The reactivity of leached soot samples was measured in (5 % volume fraction CO_2 + 95 % volume fraction N_2).

The mass transfer (r_{diff}) of O_2 / CO_2 transfer to the surface of the soot particle bed was estimated in Table 12. The mass transfer (% min^{-1}) of O_2 / CO_2 transfer to the surface of the soot particle bed was estimated as shown in equation 32:

$$r_{diff} = \frac{A_{cr} \cdot D_{AB} \cdot 60 \cdot M_c \cdot C_B}{L_{cr} \cdot m_{TG,s}} \cdot 100 \tag{32}$$

In equation 32, M_c is molar carbon weight, L_{cr} and A_{cr} are height and area of a thermogravimetric

crucible, $m_{TG,s}$ is the initial sample weight. The diffusion coefficient (D_{AB}) was obtained from correlation of Chapman and Enskog [19]. C_B is the bulk concentration of O_2 / CO_2 in the inlet gas (N_2) and calculated in equation 33:

$$C_B = \frac{P \cdot y_{bulk}}{R \cdot T} \tag{33}$$

In equation 33, y_{bulk} is the mole fraction of the reacting gas in the bulk (O_2 or CO_2), and P is the total pressure.

The calculated r_{max}/r_{diff} ratio showed that the oxidation / gasification reaction in the TG analysis was mainly influenced by chemical kinetic limitations, and to a minor extent controlled by the external diffusion. It is interesting to observe that for both O_2 and CO_2, the maximal reaction rate was shifted to lower temperatures with increasing soot formation temperature, confirming previous results of Qin et al. [5] and Septien et al. [20], and contrary to the usual observation that the reactivity of carbonaceous materials decreases with increasing heat treatment temperature [5]. The reason for the increased reactivity observed in the TG experiments with increasing heat treatment temperature in the drop tube reactor will be discussed below.

The differences in the alkali content and nanostructure of woody and herbaceous soot samples are expected to influence the soot reactivity [12, 14, 21–24]. The impact of alkali metals on the soot reactivity appears to be related to the differences in potassium content among woody and herbaceous biomass. The elemental potassium, bonded to the soot matrix in phenolate groups or intercalated in graphene layers, determines the catalytic gasification rate [25, 26]. Chen and Yang [14] suggested that the alkali metal formed by reaction of K_2CO_3 with graphite might form C-O-K groups on the surface and thereby enhance the reactivity of the carbon substrate. In the present study, the catalytic effect of potassium on the soot reactivity was investigated by impregnating graphite with KNO_3. Graphite with added 20 wt. % and 30 wt. % KNO_3 was subjected to pretreatment in the TG analysis in N_2 for 4 h to promote the dispersion of potassium throughout the graphite [27, 28] and later to gasification in 5 % volume fraction CO_2. Figure 58(b) shows a shift of the maximal reaction rate to lower temperatures from 1350°C to 1050°C and 980°C. This shows that the potassium impregnation increased the reactivity of a graphite powder during CO_2 gasification.

The catalytic effect of alkali on soot reactivity was also investigated by removal of water-soluble potassium compounds from wheat straw and beechwood soot. The inorganic matter content of the wheat straw soot prepared at 1250 and 1400°C after leaching decreased from 12 to 4 % and from 21 to 7 % according to thermogravimetric experiments in 5 % volume fraction O_2. The ash content of beechwood soot after leaching remained unchanged. Figure 58(d) shows that the maximal reaction rate of leached wheat straw soot prepared at 1250 and 1400°C shifted to higher temperatures, from 980 to 1070°C and from 900 to 1050°C, showing that the removal of potassium leads to a lower reactivity of the soot. The estimated activation energies of wheat straw soot prepared at these temperatures increased from 183 to 208 kJ mol^{-1} after leaching and from 187 to 194 kJ mol^{-1} as shown in Table 13. In contrast, the changes in activation energy of beechwood

soot were small. Leaching of the beechwood did not alter its reactivity as shown by the identical peak temperatures for each soot sample preparation temperature (980°C for soot prepared at 1400°C and 1050°C for soot prepared at 1250°C). Potassium remaining in wheat straw soot and beechwood after the leaching was probably bonded to the soot matrix in oxygen-containing surface groups (i.e. carboxylic acids, phenolate) or by the intercalation in graphene layers [29, 30]. This led to a higher reactivity of leached soot in CO_2 gasification compared to the potassium lean pinewood soot where the activation energies remained higher ($\approx$ 275 kJ mol^{-1}). These results strongly suggest that potassium has a dominating influence on the soot reactivity.

Table 13: Kinetic parameters for O_2 and CO_2 reactivity of pinewood, beechwood, wheat straw, leached wheat straw, leached beechwood soot samples, pyrolyzed at 1250 and 1400°C in the drop tube reactor, and graphite and impregnated graphite with 20 wt. % and 30 wt. % KNO_3.

Temperature	E_a	A	r_{max} at 600°C	E_a	A	r_{max} at 1100°C
°C	kJ mol^{-1}	s^{-1}	s^{-1}	kJ mol^{-1}	s^{-1}	s^{-1}
		O_2			CO_2	
Pinewood soot						
1250	250	$4{\cdot}10^{11}$	$4.5{\cdot}10^{-4}$	270	$1{\cdot}10^{6}$	$7{\cdot}10^{-5}$
1400	252	$6{\cdot}10^{11}$	$4.9{\cdot}10^{-4}$	275	$6{\cdot}10^{6}$	$2{\cdot}10^{-4}$
Beechwood soot						
1250	155	$1{\cdot}10^{8}$	$7{\cdot}10^{-2}$	235	$5{\cdot}10^{5}$	$6{\cdot}10^{-4}$
1400	154	$1{\cdot}10^{8}$	$7{\cdot}10^{-2}$	195	$2{\cdot}10^{5}$	$7{\cdot}10^{-3}$
Wheat straw soot						
1250	145	$5{\cdot}10^{7}$	0.1	183	$1{\cdot}10^{5}$	0.01
1400	147	$1{\cdot}10^{8}$	0.15	187	$5.6{\cdot}10^{5}$	0.04
Leached beechwood soot						
1250				239	$2.3{\cdot}10^{5}$	$8{\cdot}10^{-4}$
1400				199	$2.3{\cdot}10^{5}$	$6{\cdot}10^{-3}$
Leached wheat straw soot						
1250				208	$3{\cdot}10^{5}$	$4{\cdot}10^{-3}$
1400				194	$1{\cdot}10^{5}$	$5{\cdot}10^{-3}$
Graphite						
pure	195	$5{\cdot}10^{6}$	$4{\cdot}10^{-9}$	276	$3{\cdot}10^{6}$	$1{\cdot}10^{-6}$
20 % KNO_3				236	$1{\cdot}10^{7}$	0.01
30 % KNO_3				240	$4{\cdot}10^{7}$	0.02

6.4.3 X-ray diffraction of soot

As seen in Figure 59, the XRD analysis of soot indicated formation of turbostratic patterns correlated to the graphite structure. The broad reflections at 25° and 43.6° show the development of a crystalline phase, where if axis "c" is perpendicular to and axes "a" and "b" lie on the plane layer, the crystalline reflection will be of type 001 and the two-dimensional reflection will be of the index type "hk0". The reflection at 25° was assigned to the parallel graphene layers, which are spaced at a well-defined inter-planar distance d_{002}, corresponding to 002 reflection of graphite.

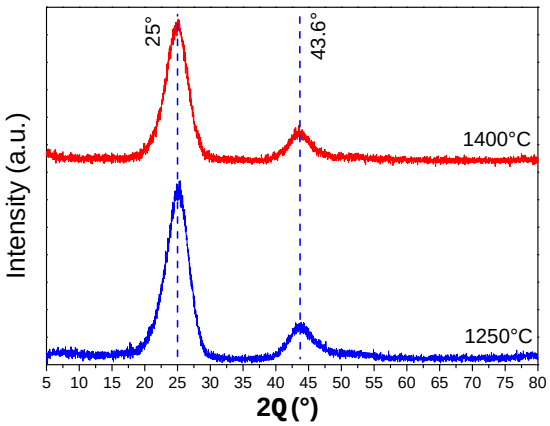

59(a): Pinewood soot

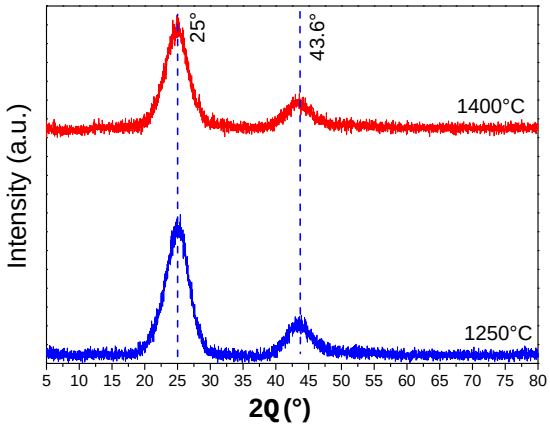

59(b): Beechwood soot

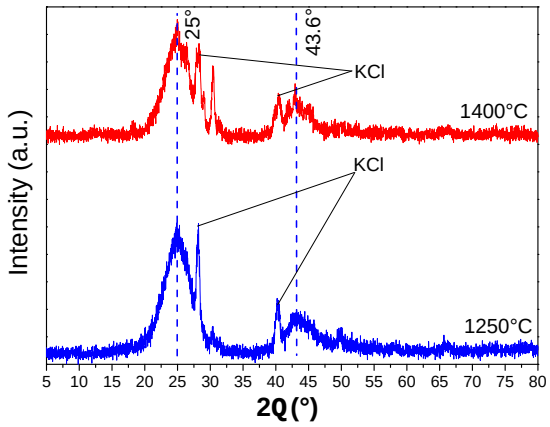

59(c): Wheat straw soot

Figure 59: XRD analysis of pinewood, beechwood and wheat straw soot samples (1250 and 1400°C) in the drop tube reactor.

The polyaromatic structures might be aligned in a similar manner as graphene layers. The reflection at 43.6° represented two-dimensional reflections, which arise from the ordering of carbon atoms inside the graphite layers, which take independently all reflections in space [31]. A

broadening of both reflections was attributed to the effect of the small crystalline size as quantified in Table 14 [32].

The average extension of graphene layers (L_a) and their thickness (L_c) were calculated for soot, prepared at 1250 and 1400°C, and shown in Table 14. The L_c and L_a values indicated no significant influence of temperature and biomass origin on the soot carbon structure. The average extension of graphene stacks (L_a) in the biomass soot was quantitatively similar to that of low-rank coal char (37.6 Å of naphthalene origin) with 4-10 graphene layers (N) [33, 34] and different from the graphite structure ($L_a > 100$ Å) [35]. The interlayer distance (d_{002}) was calculated for all soot samples (3.56 Å) by equation 10, which was higher than that of graphite (3.34 Å) [31]. However, the interlayer distance was comparable with the value typically found for carbon black interlayer distance (3.4-3.6 Å) [36, 37]. The lateral height (or grain size) was comparable for all six measured samples.

Table 14: Crystallite dimensions ($L_{c,002}$, $L_{a,100}$), determined from XRD measurements.

	$L_{c,002}$, Å		**$L_{a,100}$, Å**		**N layers**	
Soot	**1250°C**	**1400°C**	**1250°C**	**1400°C**	**1250°C**	**1400°C**
Pinewood	18.5	19.8	37.5	37.6	6	7
Beechwood	18	19.2	33	34	6	6
Wheat straw	13.3	13.4	33	36	5	5

The present results show that soot from woody and herbaceous fuels could be described as distorted graphite structures with a low graphitic stacking of parallel graphene layers, probably embedded in amorphous carbon. The XRD analysis did not show any significant differences between woody and herbaceous soot samples in terms of graphitization. The additional reflections, detected by the XRD measurements of wheat straw soot, represented the inorganic matter such as KCl.

6.4.4 Soot yield and inorganic matter effect

Figure 60(a) illustrates that the soot yields from pinewood pyrolysis at 1250 and 1400°C were the highest (8.3 % and 6.9 wt. % daf), whereas the wheat straw soot yields were the lowest (2.7 and 3.3 wt. % daf). Trubetskaya et al. [16] showed that the higher concentration of lignin and resin acids in woody samples may lead to a larger formation of PAH precursors and thus higher soot yields.

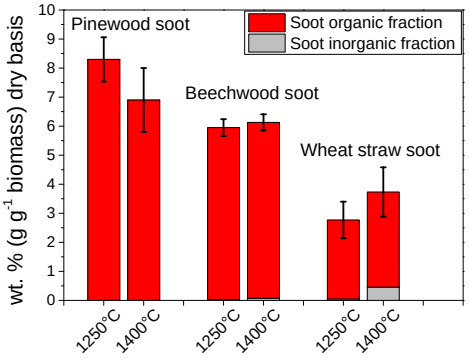

60(a): Organic and inorganic fractions

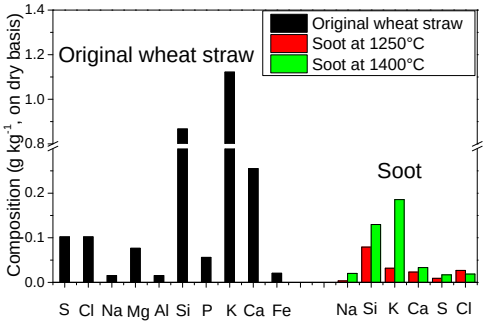

60(b): Ash analysis of original wheat straw and its soot (1250 and 1400°C)

Figure 60: (a) The total yield of soot is separated in inorganic and organic fractions of pinewood, beechwood and wheat straw (1250 and 1400°C) shown in wt. % relative to the original biomass (g g^{-1} on dry basis); (b) Ash compositional analysis of wheat straw soot (1250 and 1400°C) which is shown in g kg^{-1} on dry basis.

The soot matter from pinewood, beechwood and wheat straw consists of organic and inorganic fractions (Appendix D, Tables 26-27). The inorganic content of soot was determined by thermogravimetric analysis in 5 % volume fraction O_2. The ash composition analysis of wheat straw soot and original biomass was performed by an X-ray fluorescence instrument. The wheat straw soot showed an increasing inorganic fraction when the heat treatment temperature increased from 1250 to 1400°C, whereas the inorganic matter of the wood soot samples remained small at a level of 0.03 wt. %. Knudsen et al. [38] experimentally showed that at high temperatures, KCl sublimation and potassium silicates reactions are dominant during devolatilization, depending on the availability of Si, Cl, Ca and Mg in the original fuel. The lower Cl content in the wood might indicate that potassium was released in the form of KOH or to a minor extent in the form of KCl [39]. The high Cl content in the original wheat straw enhances the release of potassium, leading to the higher release of inorganic matter with the increasing temperature [40].

The ash compositional analysis was carried out only on the wheat straw soot, due to the high availability of this sample. The ash analysis indicated significant levels of K, Cl, S and Si, which in addition was supported by the transmission electron microscopy results. As seen in Figure 60(b), a low content of sulfur (up to about 0.02 wt. %) was observed in both straw soot samples. Thermodynamic equilibrium calculations using the Factsage program, with input parameters as listed in Appendix A (Table 22), show that sulfur was most likely released as H_2S during biomass pyrolysis, in agreement with experimental results from Puri et al. [41, 42].

The water-soluble alkali found in wheat straw soot can be related to the formation of KCl, KOH, $KHCO_3$ and K_2CO_3 salts. Equilibrium calculations and X-ray diffraction reflections in this study suggest an incorporation of water-soluble KCl in the wheat straw soot. Figure 60(b) shows that the soot matter prepared at 1400°C contained a higher K fraction than soot prepared 1250°C. However, the K fraction which reacted / deposited with the wheat straw soot at 1400°C

was significantly larger than the fractions of S and Cl.

Figure 61 shows the IR spectra of wheat straw soot, and the assigned species to each IR band.

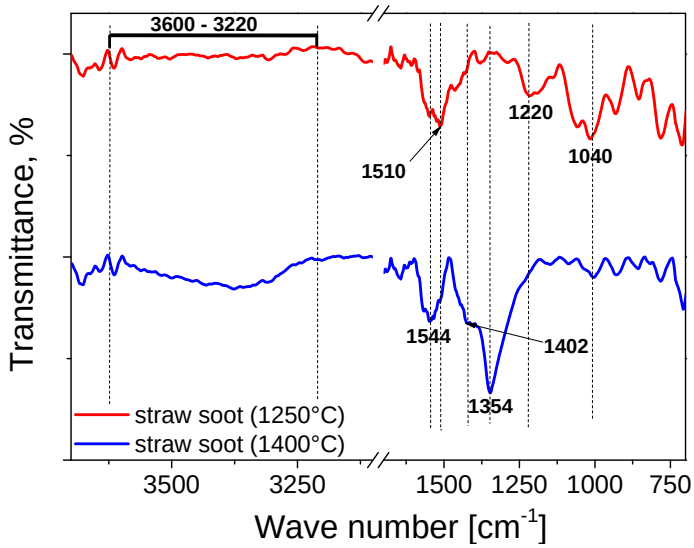

Figure 61: Experimental IR spectra of wheat straw soot prepared (1250 and 1400°C). The IR spectra was assigned to: 3600-3200 cm^{-1} - hydroxyl group [43, 44], 1550-1500 cm^{-1} - chelating bidentate carbonate [45], 1402 cm^{-1} - ionic carbonate [45], 1354 cm^{-1} - chelating bidentate carbonate [45], 1220 cm^{-1} - bicarbonate [46] and 1040 cm^{-1} - organic carbonate bond to K^+ [47, 48].

The IR measurements indicated that potassium was mostly deposited on the wheat straw soot surface as potassium carbonate and potassium bicarbonate. Due to the high content of potassium in wheat straw soot, the band at 1220 cm^{-1} was related to formation of potassium bicarbonate. The band completely disappears at the higher heat treatment temperature of soot. The 1354, 1402 and 1550-1500 cm^{-1} bands [45] were found in both wheat soot samples prepared at 1250 and 1400°C, and were associated with the formation of potassium carbonate. Chen and Yang [14] suggested that potassium can be anchored in the phenolate (C-O-K) groups to the carbon surface of soot samples. Potassium could also evaporate from wheat straw as potassium hydroxide, deposit on soot surface and react with the carbonaceous material according to equation 34:

$$KOH + \text{soot-OH} \leftrightarrow \text{soot-OK} + H_2O \tag{34}$$

Mul et al. [21] ascribed the 1118 cm^{-1} and 1300 cm^{-1} bands to the potassium phenolate. In the present study, the 1040 cm^{-1} band may be associated with the vibrations of complex organic-like carbonate species bonded to the K^+ ion (C-O-K) [47, 48]. Moreover, the measured IR signal is proportional to the number of groups in the path of IR light. In the present study, the concentration of potassium bonded to the soot matrix in the oxygen-containing surface groups was probably low, leading to the low IR signal. Ibrahim et al. [49] attributed the 1532 cm^{-1} and 1348 cm^{-1} bands to the asymmetric and symmetric stretching of carboxyl group bonded to the K^+ ion. However, these bands were not detected in the present study, probably indicating a low content of carboxyl surface groups bonded to potassium in the wheat straw soot.

Wen [27] suggested the formation of the potassium-carbon complexes or intercalates (lamellar compounds). Soot samples with a structure closer to graphite could more easily intercalate potassium due to the high electronegativity of graphite [50]. The oxygen lean beechwood soot with the more graphitic structure compared to pinewood soot may intercalate potassium similarly to graphite as discussed in later sections.

6.4.5 Particle size analysis

TEM investigations were carried out to examine the primary particle size characteristics of the soot samples prepared at 1250 and 1400°C. The size distribution of the primary soot particles was plotted as a fraction of the number of particles in each size range as shown in Figure 62. The calculated geometric mean diameters varied from 30.8 nm up to 77.7 nm, and were similar to the values reported for biomass smoke (30-50 nm) in other studies [51, 52]. The primary particle size range gives an interesting insight to the soot formation process, which seems to be influenced by the operating conditions and biomass origin. Ross et al. [53] hypothesized that the amount of volatiles, which is high for woody biomass, is a major factor influencing the soot yield and particle size. It was observed that the mean diameter of soot samples prepared at 1250°C was larger, while the particle size distribution was less uniform compared to soot samples prepared at 1400°C. Higher heat treatment temperatures led to a narrower particle size distribution for both the woody and herbaceous biomass soot.

Specifically, the mean diameter of pinewood soot particles prepared at 1250°C was almost twice as large as that of soot prepared at 1400°C. The pinewood soot produced at 1250°C resulted in the broadest particle size distribution from 27 to 263 nm compared to beechwood soot from 33.2 to 102 nm and wheat straw soot from 11.5 to 165.4 nm. The high potassium content in wheat straw may have inhibited coagulation of soot particles, leading to the smaller particle size of 30.8 nm compared to other soot samples. The larger mean diameter of pinewood soot particles was also confirmed by the specific surface area measurements using N_2 adsorption as shown in Table 15. The beechwood and wheat straw soot particles attained a larger surface area (56.3-92.3 $m^2\ g^{-1}$) than the pinewood soot (37.9-38.4 $m^2\ g^{-1}$).

Table 15: BET surface area (SSA) of pinewood, beechwood and wheat straw soot samples, determined by N_2 adsorption $m^2\ g^{-1}$.

Soot	**1250°C**	**1400°C**
	$m^2\ g^{-1}$	
Pinewood	37.9	38.4
Beechwood	56.3	74.3
Wheat straw	70	92.3

The surface areas of pinewood soot particles generated at 1250°C and 1400°C were similar, while the mean particle size determined by TEM microscopy decreased from 77.7 to 47.8 nm.

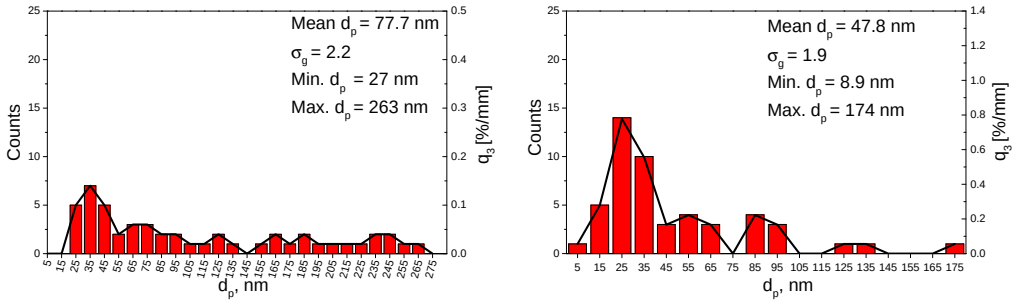

62(a): Pinewood soot (1250°C)

62(b): Pinewood soot (1400°C)

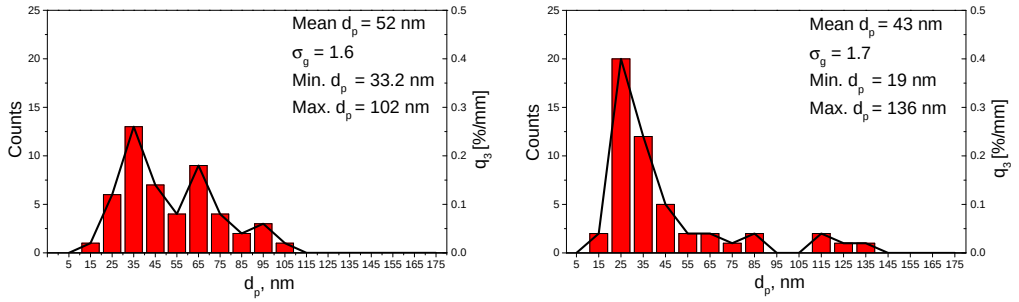

62(c): Beechwood soot (1250°C)

62(d): Beechwood soot (1400°C)

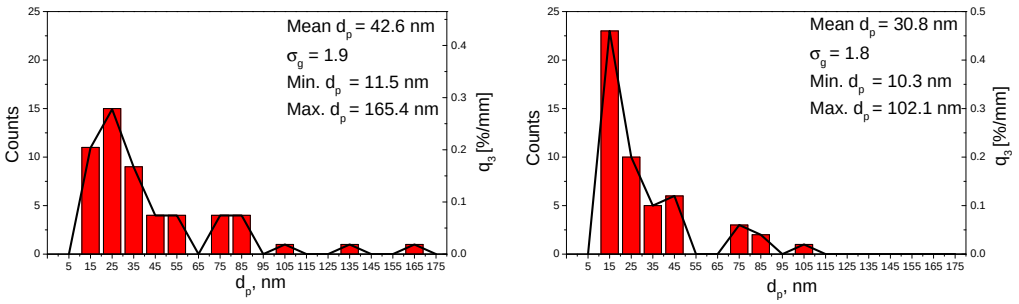

62(e): Wheat straw soot (1250°C)

62(f): Wheat straw soot (1400°C)

Figure 62: Particle size distributions of pinewood, beechwood and wheat straw soot samples (1250 and 1400°C). The particle size analysis was performed by the TEM. The mean diameter with the standard deviation, minimal and maximal diameters are illustrated. On the left y-axis, the number of particles in the fraction is shown , whereas on the right y-axis, the particle frequency distribution, based on volume (q_3) is illustrated in % mm^{-1}. The analysis was performed on 50 particles in each sample.

The surface area determined by N_2 adsorption might not only reflect the surface area of individual particles, but also be influenced by the type of agglomerate. TEM characterization gives information about individual particles.

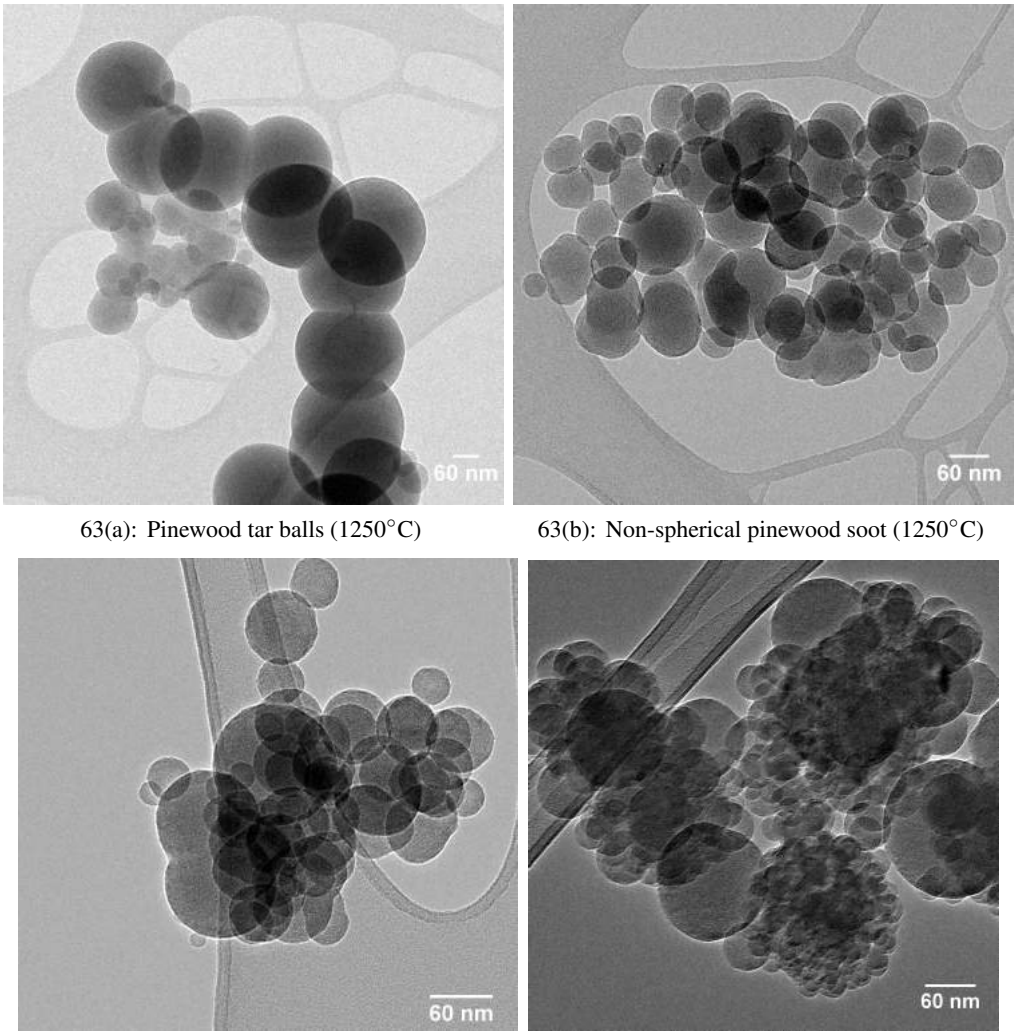

63(a): Pinewood tar balls (1250°C)

63(b): Non-spherical pinewood soot (1250°C)

63(c): Beechwood soot (1400°C)

63(d): Wheat straw soot (1400°C)

Figure 63: TEM images of particle agglomerates of pinewood, beechwood and wheat straw soot samples (1250 and 1400°C). (a) Pinewood tar balls (1250°C) (b) Non-spherical pinewood soot (1250°C) (c) Beechwood soot (1400°C) (d) Wheat straw (1400°C).

The larger particles with a diameter from 100 to 263 nm appear to be tar balls tar balls as reported by Posfai et al. [54, 55]. Pinewood produced at 1250°C formed chain-like structures of tar balls, whereas wheat straw soot particulate formed large agglomerates consisting of smaller particles dispersed on the tar ball surface as shown in Figure 63. Posfai et al. [54, 55] suggested the formation of tar balls from low volatile organic compounds, such as lignin pyrolysis products under smoldering conditions. Wiinikka et al. [24] observed similar larger soot particles (100-300 nm) at high temperatures in pinewood pressurized gasification. Arora et al. [56] reported that under smoldering conditions, the nature of lignocellulosic materials (wood, cow dung, mustard stalks) influenced the formation of tar balls, leading to various particle size distributions. The formation of larger particles at 1250°C may be related to a higher concentration of PAH components, which contribute to the growth of the soot particles. At higher temperatures, cracking of the PAH components would be promoted, limiting their contribution to the growth.

6.4.6 Surface structure

The nanostructure of the soot, prepared at 1250 and 1400°C, was studied by TEM as shown in Figure 64. The woody and herbaceous soot appeared as agglomerates. The nanostructure of the soot particles was well-ordered. The primary soot particles exhibited a core-shell structure, with both single and multiple cores as shown in Figure 64.

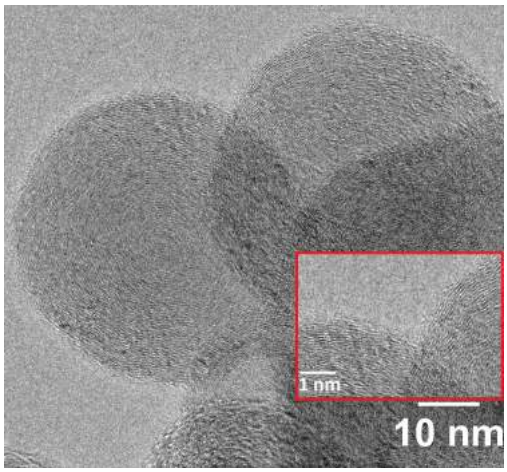

64(a): Pinewood soot (1250°C)

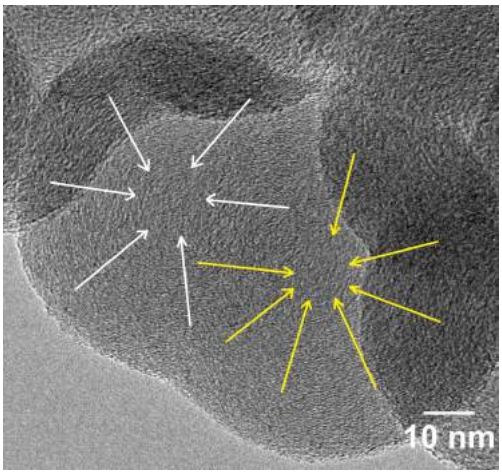

64(b): Multi-cores of pinewood soot (1250°C)

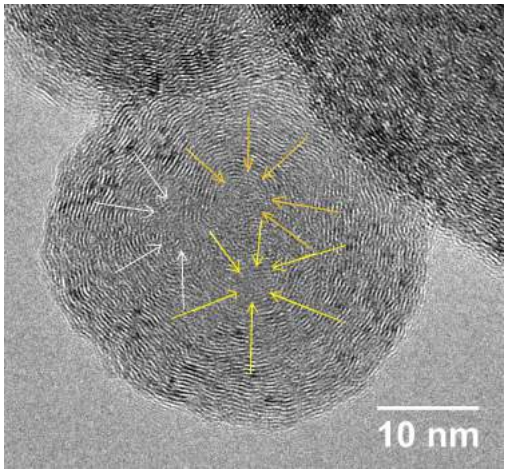

64(c): Beechwood soot (1400°C)

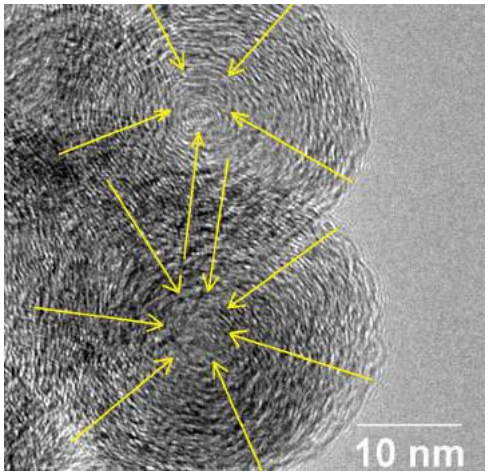

64(d): Wheat straw soot (1250°C)

Figure 64: TEM images of soot generated from (a)-(b) pinewood (1250°C), (c) beechwood (1400°C) and (d) wheat straw (1250°C). In Figure (a) the distance between graphene layers is enlarged using the red rectangle. In Figures (b)-(d) the arrows show the multiple cores of soot particles.

The primary particles in pinewood soot produced at 1250°C consisted of a mixture of single and multi-core structures, but at higher temperatures they contained mainly single cores, similar to the wheat straw soot prepared at 1250 and 1400°C. The primary particles in beechwood soot also possessed a mixture of single and multiple cores. Compared to the pinewood soot produced at 1250°C, the beechwood soot particles were located closer to each other due to the particle coalescence at an earlier stage. Liati et al.[12] related the multi-core structure to an early phase

of soot formation by nuclei coalescence and further development as a single particle. The multi-core structure of pinewood soot produced at 1250°C reflects formation by coalescence of several smaller particles, with this process governed by the particle concentration, as suggested by Lee et al. [57]. Due to the highest soot yield at 1250°C and the ability of pinewood to generate more soot compared to beechwood and wheat straw, the primary soot particles probably coalesced with other soot particles forming multi-core structures. Both fine and large primary soot particles consisted of monolayers of graphene sheets, which grow circumferentially from the particle core. The shell of small particles provided a clear fringe contrast from the stacking of the graphene layers, which is less obvious for larger particles due to their thickness in Figure 21. This limitation also applied to the core of larger particles, which characterization was not possible. Still, the shell nanostructure of smaller and larger particles seems to be similar as shown in Figure 64 and in Appendix D (Figures 93 and 94).

Figure 64 shows that the particle cores consist mainly of randomly orientated and curved graphene layers. Su et al. [58] investigated the reactivity of soot formed in the exhaust from diesel engine with respect to oxidation, and described a soot core as a highly reactive area of a soot particle due to the defects on the surface being functionalized with volatile groups. They hypothesized that the defective non-6-membered rings may produce highly localized olefinic electronic structures in the soot core that are prone to oxidation.

All soot samples exhibited a well-ordered graphitic structure. The graphene segments of the samples were mainly placed parallel to each other, and were relatively straight with the smaller curvature of an average particle size (flat graphene ≈1 [59]) as shown in Table 16.

Table 16: Summary of soot characteristics (cure, curvature, separation distance) prepared from pinewood, beechwood and wheat straw pyrolysis at 1250 and 1400°C. Standard deviation was calculated for curvature and separation distance.

Soot	**1250°C**				**1400°C**			
	Fiber length	Curvature[2]	d_{sep}[1,2]	Core[3,4]	Fiber length	Curvature[2]	d_{sep}[1,2]	Core[3,4]
	nm		nm		nm		nm	
Pinewood	2±0.8	0.88±0.02	0.33±0.01	mostly m	2.2±0.9	0.88±0.02	0.34±0.02	m & s
Beechwood	3.1±1.1	0.88±0.02	0.35±0.02	m & s	3.2±1.2	0.88±0.02	0.35±0.02	m & s
Wheat straw	2.7±0.9	0.85±0.05	0.35±0.02	s	2.6±1	0.86±0.05	0.35±0.02	s

[1] Separation distance

[2] Calculation of mean curvature and d_{sep} of graphene layers measured only on crystallites

[3,4] *s* - single core and *m* - multiple cores

Table 16 summarizes the characteristics of different soot samples with regards to single or/and multiple cores, curvature and separation distance of graphene layers. The mean separation distance of woody and herbaceous soot graphene segments was measured to be < 0.35 nm, which is similar to the layer distance determined by X-ray diffraction.

6.4.7 TEM-EELS Measurements

The carbon core-loss edge (C-K edge) at about 285 eV was recorded under magic-angle conditions to reduce the possible influence of anisotropy of the sample [60, 61]. Figure 65 shows the EELS spectra of graphite tilted in two different directions, verifying magic-angle conditions. The spectra were collected in diffraction mode. Due to limitation of the selected area diffraction aperture, agglomerates of typical 1-7 soot particles of different sizes were probed, with a total of 15-20 agglomerates per soot sample prepared at 1400°C.

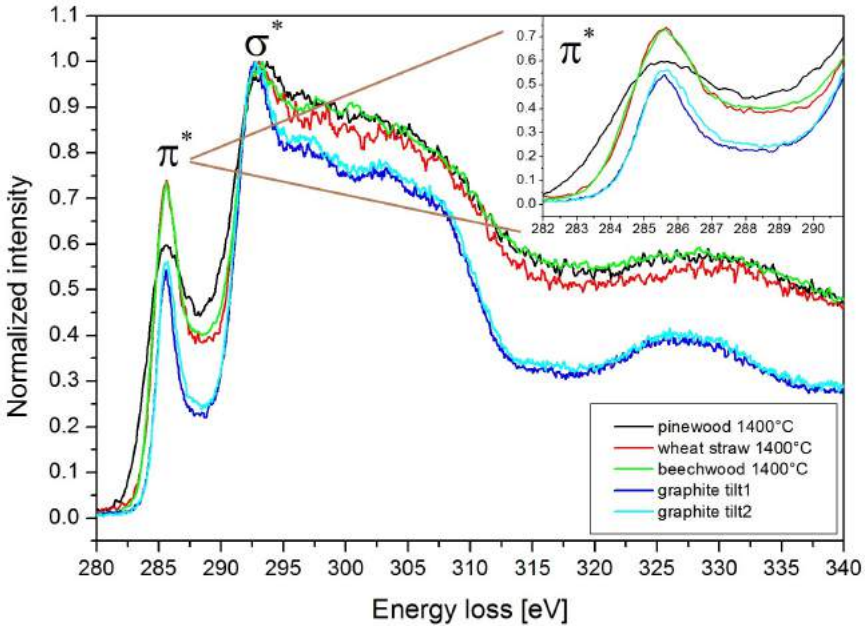

Figure 65: TEM-EELS averaged spectra of pinewood, beechwood and wheat straw soot samples (1400°C) which are shown by black, green and red lines. TEM-EELS spectra of graphite is shown by cyan and blue lines. The graphite was tilted in two different directions to verify magic-angle conditions. Maxima of 1 s-π* and 1 s-σ* transitions were illustrated by π* and σ* symbols.

The C-K edge showed mainly two distinct maxima, one at about 285 eV of 1 s-π* transitions, which was attributed to C=C bonds (sp^2 hybridization), and a second at about 292 eV of 1 s-σ* transitions, attributed to C-C bonds (sp^3 hybridization) as shown in Figure 65. To quantify the amount of sp^2/sp^3 hybridized carbon and to compare the samples, the two peaks were fitted by individual Gaussian peaks. The ratio of the area under the Gaussian curves, $r = A_{G,\pi*} / A_{G,\sigma*}$, gave an indication about the sp^2/sp^3 ratio in the probed volume (Appendix D, Figure 95). A defect-free clean graphite should give a ratio of about 0.33. From the manual fitting of these two peaks of the measured graphite a ratio of about 0.24 was calculated. This could be due to defects or amorphous carbon contamination, which reduced the amount of sp^2 hybridized carbon and increased the amount of sp^3 carbon. From the fit (Appendix D, Figure 95) it was obvious that these two peaks did fully resemble the spectra in this energy region. Additional intensity was required between 287 and 289 eV, presumably due to non-carbon-carbon bonding [59, 62–65].

The ratio for all three soot samples was higher than for pure graphite, 0.28-0.36 [66]. As graphite is the material with the highest sp^2/sp^3 ratio, this indicate that fewer sp^3 carbon-carbon bonds were present in soot. This is in agreement with the visible nanostructure, indicating defective graphene flakes, which were probably terminated by for example C-H bonds. The present EELS data suggest a structure closer to graphite for wheat straw and beechwood soot than for pinewood soot. The spectra of individual agglomerates within one sample showed no significant differences. No obvious particle size dependence of the spectra was observed.

An O-K edge was present in the EELS spectra of several wheat straw soot agglomerates. No oxygen edge was detected for pinewood and beechwood soot. Additionally, beechwood and wheat straw soot showed two additional peaks at about 298 eV and 300.5 eV for several agglomerates, which were assigned to the K-$L_{2,3}$ edge of potassium. In wheat straw soot both, the oxygen and potassium edge were detected for the same agglomerates.

6.4.8 Discussion

The thermogravimetric experiments demonstrated significant differences in the reactivity of pinewood, beechwood and wheat straw soot towards O_2 and CO_2. The reaction rate measured by TG instrument was mainly limited by chemical kinetics, while the importance of diffusion limitations, calculated under the assumption of reaction taking place on the outer surface of non-porous soot particles in Table 12 was small. The oxidation of the beechwood and wheat straw soot prepared at 1250 and 1400°C took place at nearly the same temperature range, whereas the maximum reaction rate of pinewood soot was shifted to higher temperatures, indicating a lower reactivity. Woody and herbaceous soot samples prepared at 1250°C were less reactive than soot produced at 1400°C at both oxidation and CO_2 gasification conditions.

The reactivity of soot samples can be affected by the differences in alkali content, particle size and soot nanostructure. Liati et al. [12] reported that soot nanostructure may affect the oxidation reactivity. Low separation distances (close to that of graphite) and high periodicity lead to lower oxidation of soot, while the more bent graphene layers might enhance the reactivity. The EELS analysis showed that the nanostructure of beechwood and wheat straw soot was more similar to graphite compared to the nanostructure of pinewood soot. Thus, based on structure alone it might be expected that pinewood soot should be reactive than the soot from beechwood and straw. However, it was observed that the low-ash containing pinewood soot prepared at 1250 and 1400°C was 143 and 571 times less reactive than the alkali rich wheat straw soot in CO_2 gasification. Significantly smaller differences in CO_2 reactivity were observed for the beechwood soot prepared at 1250 and 1400°C compared to pinewood soot (8 and 35 times), respectively. The particle size of wheat straw soot at 1250°C was two times smaller than pinewood soot, whereas the reaction rate of wheat straw soot was 143 times higher than pinewood soot as shown in Table 13. This indicates that neither soot structure nor particle size had a stronger influence on the observed differences in soot reactivity. In addition, the differences in nanostructure of pinewood, beechwood and wheat

straw soot were small compared to that of soot prepared by pyrolysis of acetylene and benzene, where the formation conditions have significantly more influence on the soot nanostructure [67].

The results show that it is the presence of potassium in beechwood and wheat straw soot which mainly affects the reactivity during CO_2 gasification. Based on the TEM EELS, XRD and FTIR analysis results and equilibrium calculations with Factsage it was concluded that the potassium species were incorporated in the wheat straw soot particles mostly as KOH, KCl, $KHCO_3$ and K_2CO_3 and to a minor extent bonded in the soot matrix to the oxygen-containing surface groups. In beechwood soot, potassium was likely intercalated in the graphene layers because the oxygen content was below the detection limit of the TEM EELS and elemental analysis. The removal of water-soluble potassium from wheat straw soot by leaching led to a lower reactivity in CO_2 gasification at 1250 and 1400°C (by factors of 2.5 and 8, respectively). Furthermore, the activation energy of leached wheat straw soot was higher than that of non-treated wheat straw soot samples, indicating loss of catalytic activity by potassium removal. The leaching of beechwood soot did not, however, influence its reactivity. The potassium content of beechwood soot was lower than for wheat straw soot, and the major part was likely bonded to sites from which it was difficult to wash out (e.g. intercalated or in phenolates etc). Even after leaching, the reactivity of straw and beechwood soot was higher than that of pinewood soot. For example, the rate constants of leached wheat straw prepared at 1250 and 1400°C were 57 and 25 times higher than pinewood soot which has a very low potassium content and shown in Table 13. This indicates that potassium has a dominant role on the soot reactivity and that both potassium deposited on the surface particles and potassium incorporated into the soot matrix can influence the reactivity. In addition, the reaction rates (0.01 and 0.02 s^{-1}) of potassium impregnated graphite with 20 % and 30 % KNO_3 and the reaction rates (0.01 and 0.04 s^{-1}) of wheat straw soot prepared at 1250 and 1400°C were of the same order of magnitude in CO_2 gasification, indicating the reactivity increase by graphite impregnation with potassium.

The observation made by Qin et al. [5] and Septien et el. [20] in terms of the increasing soot reactivity with increased heat treatment temperatures was confirmed in the present study. The reaction rate of pinewood, beechwood and wheat straw soot generated at 1400°C was 4, 12 and 3 times higher than the reactivity of soot prepared at 1250°C. The specific surface area of pinewood soot prepared at 1400°C was significantly larger (by 1.6, 1.2 and 1.4 times) than that of soot generated at 1250°C. The results showed that the reaction rates of woody and herbaceous biomass soot at both temperatures increased faster than the soot surface area increased. This shows that another more dominating factor, i.e., the potassium content, affects the differences in reactivity in O_2 and CO_2 gasification.

6.4.9 Conclusion

Fast pyrolysis of pinewood, beechwood and wheat straw was conducted in a drop tube reactor to study the effect of biomass type on the yield, nanostructure and reactivity of soot at high tem-

peratures. The soot yields from pinewood pyrolysis at 1250 and 1400°C were the highest (8.4 % and 6.7 wt. % daf), whereas the wheat straw soot yields were the lowest (2.5 and 2.7 wt. % daf).

The major difference in the soot morphology was related to the formation of irregular-shaped pinewood soot particles with mostly multiple cores, whereas beechwood and wheat straw soot samples were mainly single core structures at both investigated temperatures. Minor differences in particle size were also observed. Larger soot particles were formed by pyrolysis of pinewood at 1250°C as compared to soot generated at 1400°C and beechwood and wheat straw soot prepared at both temperatures. The particle size distribution of pinewood soot generated at 1250°C was significantly broader (from 27 to 263 nm), compared to other soot samples. The differences in nanostructure of wood and wheat straw soot were small, except for presence of single and multiple cores.

The thermogravimetric analysis results showed that the soot reactivity towards O_2 and CO_2 depends mainly on the potassium content in the original fuel and on the heat treatment temperature and less on the soot nanostructure. For fuels with a high potassium content, there will be higher potassium release to the gas phase in the temperature range from 1250 to 1400°C, and so more potassium incorporates in the soot particles. The temperature (1250 or 1400°C) at which soot was formed therefore affects strongly the soot reactivity in CO_2 gasification and to a minor extent at oxidation conditions. The pinewood soot was less reactive than beechwood and wheat straw soot generated under similar operating conditions due to the low potassium content of the original pinewood, despite the pinewood soot having a less graphitic structure. The potassium was present both as water-soluble alkali and incorporated with the oxygen containing surface groups in the soot matrix and both contributed to the higher reactivity of beechwood and wheat straw soot in CO_2 gasification.

6.5 Conclusion on soot and char reactivity

Biomass fast pyrolysis experiments were performed in a bench scale atmospheric pressure drop tube reactor with the aim to investigate the effects of operating parameters and biomass types on reactivity of char and soot with respect to oxidation and CO_2 gasification using thermogravimetric analysis. The experimental study was focused on the influence of alkali, particle size and nanostructure, heat treatment temperature, heating rate, residence time on the char and soot reactivity. Wood and herbaceous biomass were used as fuels.

The heat treatment temperature and potassium content affected the char reactivity with respect to oxidation and CO_2 gasification stronger than the heating rates and differences in the plant cell wall compounds. Based on the similar reactivity of pinewood (low ash-containing fuel) and rice husk (Si rich fuel) in oxidation it was concluded that the reactivities of woody and herbaceous char samples were mainly influenced by the potassium content and not by silicium. Significant differences in morphology of pinewood char (near-spherical particles) and rice husk char (preserved shape of original fuel) affected the reactivity less than the differences in alkali content of

original fuels. The importance of potassium on the char reactivity was additionally supported by the higher activation energies calculated for pinewood and leached wheat straw char compared to that of non-treated wheat straw in both oxidation and CO_2 gasification.

Similar to results of char reactivity, woody and herbaceous soot generated at 1250 and 1400°C showed that its reactivity with respect mainly to CO_2 gasification and to a minor extent in oxidation depends mainly on potassium content. Opposite to large differences in morphology of woody and herbaceous chars, the differences in nanostructure of pinewood, beechwood and wheat straw soot were small, except for the presence of single and multiple cores and formation of larger pinewood soot particles at 1250°C than at higher temperatures and soot particles from beechwood and wheat straw generated at both temperatures. Due to the similar nanostructure of woody and herbaceous biomass, the potassium content of soot samples and the heat treatment temperature in high heating rate pyrolysis affected the reactivity significantly more than the soot nanostructure and particle size. The pinewood char generated at 1250°C was 9 times more reactive than pinewood soot prepared at the same operating conditions, whereas with the increasing temperature the pinewood char was 2 times less reactive than soot due to the carbon deactivation. The wheat straw soot prepared at 1250 and 1400°C was 14 and 133 times more reactive than the wheat straw char. The results showed that close to 70 % of potassium was released in wheat straw pyrolysis in a temperature range of 1000-1500°C, leading to the incorporation of potassium with wheat straw soot samples, and thus to the higher soot reactivity in CO_2 gasification.

References

[1] Zolin A. Reactivity of solid fuels. PhD thesis, Technical University of Denmark, 2001.

[2] Septien Stringel S. High temperature gasification of millimetric wood particles between 800°C and 1400°C. PhD thesis, RAPSODEE (Ecole des Mines d'Albi-Carmaux), 2011.

[3] Abian M, Jensen AD, Glarborg P, and Alzueta MU. Soot Reactivity in Conventional Combustion and Oxy-fuel Combustion Environments. *Energy Fuels*, 26(8):5337–44, 2012.

[4] Coats AW and Redfern JP. Kinetic parameters from thermogravimetric data. *Nature*, 201:68–9, 1964.

[5] Qin K, Lin W, Fster S, Jensen PA, Wu H, and Jensen AD. Characterization of Residual Particulates from Biomass Entrained Flow Gasification. *Energy Fuels*, 27(1):262–70, 2013.

[6] Zolin A, Jensen AD, Jensen PA, and Dam-Johansen K. Experimental study of char thermal deactivation. *Fuel*, 81(8):1065–75, 2002.

[7] Wornat MJ, Hurt RH, Yang NYC, and Headley TJ. Structural and Compositional Transformations of Biomass Chars during Combustion. *Combust Flame*, 100(1-2):131–43, 1995.

[8] Laine NR, Vastola FJ, and Walker PL. The importance of active surface area in the carbon-oxygen reaction. *J Phys Chem*, 67(10):2030–4, 1963.

[9] Jensen AD, Dam-Johansen K, Wojtowicz MA, and Serio MA. TG-FTIR Study of the Influence of Potassium Chloride on Wheat Straw Pyrolysis. *Energy Fuels*, 12(5):929–38, 1998.

[10] Jensen PA, Frandsen FJ, Dam-Johansen K, and Sander B. Experimental investigation of the transformation and release to gas phase of potassium and chlorine during straw pyrolysis. *Energy Fuels*, 14(6):1280–5, 2000.

[11] Purewal J, Keith JB, Ahn CC, Brown CM, Tyagi M, and Fultz B. Hydrogen diffusion in potassium intercalated graphite studied by quasielastic neutron scattering. *J Chem Phys*, 137(22):1–11, 2012.

[12] Liati A, Eggenschwiler PD, Schreiber D, Zelenay V, and Ammann M. Variations in diesel soot reactivity along the exhaust after-treatment system, based on the morphology and nanostructure of primary soot particles. *Combust Flame*, 160(3):671–81, 2013.

[13] Hüttinger KJ and Minges R. The influence of the catalyst precursor anion in catalysis of water vapour gasification of carbon by potassium. 2. Catalytic activity as influenced by activation and deactivation reactions. *Fuel*, 65(8):1122–8, 1986.

[14] Chen SG and Yang RT. The Active Surface in Alkali-Catalyzed Carbon Gasification: Phenolate (C-O-M) Groups vs Clusters (Particles). *J Catal*, 141(1):102–13, 1993.

[15] Jensen PA, Sander B, and Dam-Johansen K. Removal of K and Cl by leaching of straw char. *Biomass Bioenergy*, 20(6):447–57, 2001.

[16] Trubetskaya A, Jensen PA, Jensen JD, Llamas Garcia AD, Umeki K, and Glarborg P. Effect of fast pyrolysis conditions on biomass solid residues at high temperatures. *Fuel Process Technol*, 143:118–29, 2016.

[17] Pottmaier D, Costa M, Farrow T, Oliveira AAM, Alarcon O, and Snape C. Comparison of Rice Husk and Wheat Straw: From Slow and Fast Pyrolysis to Char Combustion. *Energy Fuels*, 27(11):7115–25, 2013.

[18] Russell NV, Beeley TJ, Man CK, Gibbins JR, and Williamson J. Development of TG measurements of intrinsic char combustion reactivity for industrial and research purposes. *Fuel Process Technol*, 57(2):113–30, 1998.

[19] Poling BE, Prausnitz JM, and O'Connell J. *The properties of Gases and Liquids*. McGRAW-HILL, 2000.

[20] Septien S, Valin S, Dupont C, Peyrot M, and Salvador S. Effect of particle size and temperature on woody biomass fast pyrolysis at high temperature (1000-1400 °C). *Fuel*, 97:202–10, 2012.

[21] Mul G, Kapteijn F, and Moulijn JA. Drift analysis of surface oxygen complexes on soot formed by metal oxides. *ACS Div Fuel Chem*, 41(1):230–4, 1996.

[22] Hirschon AS, Du Y, Wu HJ, Wilson RB, and Malhotra R. Effect of Doping Fullerene Soots with Metals on the Conversion of Methane into Higher Hydrocarbons. *Res Chem Intermed*, 23(7):675–82, 1997.

[23] Müller JO. Investigations on Environmental Carbons. PhD thesis, Technical University of Berlin, 2012.

[24] Wiinikka H, Weiland F, Pettersson E, Öhrman O, and Carlsson P. Characterisation of submicron particles produced during oxygen blown entrained flow gasification of biomass. *Combust Flame*, 161(7):1923–34, 2014.

[25] Meijer R, Weeda M, Kapteijn F, and Moulijn JA. Catalyst loss and retention during alkali-catalysed carbon gasification in CO_2. *Carbon*, 29(7):929–41, 1991.

[26] Moulijn JA and Kapteijn F. Towards a unified theory of reactions of carbon with oxygen-containing molecules. *Carbon*, 33(8):1155–65, 1995.

[27] Wen YW. Mechanisms of Alkali Metal Catalysis in the Gasification of Coal, Char, or Graphite. *Cat Rev Sci Eng*, 22(1):1–28, 1980.

[28] McKee DW. Gasification of graphite in carbon dioxide and water vapor - the catalytic effects of alkali metal salts. *Carbon*, 20(1):59–66, 1982.

[29] Decesari S, Facchini MC, Matta E, Mircea M, Fuzzi S, and Chughtai AR et al. Water soluble organic compounds formed by oxidation of soot. *Atmos Environ*, 36(11):1827–32, 2002.

[30] Takahama S, Liu S, and Russell LM. Coatings and clusters of carboxylic acids in carbon-containing atmospheric particles from spectromicroscopy and their implications for cloud-nucleating and optical properties. *J Geophys Research*, 115(D1):1–21, 2010.

[31] Warren BE. X-ray study of the graphitization of carbon black. *Phys Rev*, 59:693–8, 1941.

[32] Bi H, Kou KC, Ostrikov K, and Zhang JQ. Graphitization of nanocrystalline carbon microcoils synthesized by catalytic chemical vapor deposition. *J Appl Phys*, 104(3):1–6, 2008.

[33] Blayden HE, Gibson J, and Riley HL. An X-Ray Study of the Structure of Coals and Cokes. *Proc British Coal Util Res Assoc*, pages 176–231, 1944.

[34] Roberts MJ, Everson RC, Neomagus NWJP, van Niekerk D, Mathews JP, and Branken DJ. Influence of maceral composition on the structure, properties and behaviour of chars derived from South African coals. *Fuel*, 142:9–20, 2015.

[35] Belenkov EA. Formation of Graphite Structure in Carbon Crystallites. *Inorg Mater*, 37(9):928–34, 2001.

[36] Marsh PA, Voet A, Mullens TJ, and Price LD. *Electron microscopy of interplanar spacing in carbon blacks. Proc Meeting ACS Div of Rubber Chem; 1969 October 14^{th}-17^{th}, Buffalo, NY, US, 470-80.*

[37] Bockhorn H, D'Anna A, Sarofim AF, and Wang H. *Combustion Generated Fine Carbonaceous Particles*. KIT Sci Publ, 2009.

[38] Knudsen JN, Jensen PA, and Dam-Johansen K. Transformation and Release to the Gas Phase of Cl, K and S during Combustion of Annual Biomass. *Energy Fuels*, 18(5):1385–99, 2004.

[39] Dayton DC and Milne TA. *Laboratory Measurements of Alkali Metal Containing Vapors Released during Biomass Combustion. In: L Baxter and R DeSollar (ed.), Application of Advanced Technologies to Ash-Related Problems in Boilers*. Plenum Press, 1996.

[40] Knudsen JN. Volatilization of Inorganic Matter during Combustion of Annual Biomass. PhD thesis, Technical University of Denmark, 2003.

[41] Puri BR. Surface complexes on carbons. *Chem Phys Carbon*, 6:191–282, 1970.

[42] Puri BR and Hazra RS. Carbon-sulfur surface complexes on charcoal. *Carbon*, 9:123–34, 1971.

[43] Guenzler H and Boeck H. *IR-Spektroskopie. Eine Einführung*. Verlag Chemie and Physik, 1983.

[44] Reddy BVR, Chakrapani C, Babu CS, Rao KS, Agarwal K, and Prasad M. FT-IR, TG, XRD and SEM Studies of Activated Carbons Prepared from Agricultural Waste. *Asian J Chem*, 22(3):1822–8, 2010.

[45] Zhang Z, Zhang Y, Su Q, Wang Z, Li Q, and Gao X. Determination of Intermediates and Mechanism for Soot Combustion with NO_x/O_2 on Potassium-Supported Mg-Al Hydrotalcite Mixed Oxides by In Situ FTIR. *Environ Sci Technol*, 44(21):8254–8, 2010.

[46] Philipp R, Omata K, Aoki A, and Fujimoto K. On the active site of MgO/CaO mixed oxide for oxidative coupling of methane. *J Catal*, 134:422–33, 1992.

[47] Legutko P, Jakubel T, Kaspera W, Stelmachowski P, Sojka Z, and Kotarba A. Soot oxidation over K-doped manganese and iron spinels - How potassium precursor nature and doping level change the catalyst activity. *Catal Commun*, 43:34–7, 2014.

[48] Gu B, Schmitt J, Chen Z, Liang L, and McCathy JF. Adsorption and Desorption of Natural Organic Matter on Iron Oxide: Mechanisms and Models. *Environ Sci Technol*, 28(1):38–46, 1994.

[49] Ibrahim M, Nada A, and Kamal DE. Density functional theory and FTIR spectroscopic study of carboxyl group. *Indian J Pure Appl Phys*, 43(12):911–7, 2005.

[50] Akuzawa N, Yoshioka J, Ozaki C, Tokuda M, Ohkura K, and Soneda Y. Preparation and characterization of sodium-graphite intercalation compounds. *Mol Cryst Liq Cryst*, 388(1):1–7, 2002.

[51] Chakrabarty RK, Moosmüller H, Garro MA, Arnott WP, Walker J, and Susott RA et al. Emissions from the laboratory combustion of wildland fuels: Particle morphology and size. *J Geophys Research*, 111(D7):1–16, 2006.

[52] Sachdeva K and Attri AK. Morphological characterization of carbonaceous aggregates in soot and free fall aerosol samples. *Atmos Environ*, 42(5):1025–34, 2008.

[53] Ross AB, Junyapoon S, Jones JM, Williams A, and Bartle KD. A study of different soots using pyrolysis-GC-MS and comparison with solvent extractable material. *J Anal Appl Pyrolysis*, 74:494–501, 2005.

[54] Posfai M, Simonics R, Hobbs PV, and Buseck PR. Individual aerosol particles from biomass burning in Southern Africa: 1. Composition and size distributions of carbonaceous particles. *J Geophys Res Atmos*, 108(D13):1–20, 2003.

[55] Posfai M, Gelencser A, Simonics R, Li J, Hobbs PV, and Buseck PR. Atmospheric tar balls: Particles from biomass and biofuel burning. *J Geophys Res*, 109(D6):1–9, 2003.

[56] Arora P and Jain S. Morphological characteristics of particles emitted from combustion of different fuels in improved and traditional cookstoves. *J Aerosol Sci*, 82:13–23, 2015.

[57] Lee KO, Cole R, Sekar R, Kang J, Bae C, and Zhu J. Detailed Characterization of Morphology and Dimensions of Diesel Particulates via Thermophoretic Sampling. *Sae Tech Papers*, pages 1–10, 2001.

[58] Su DS, Müller JO, Jentoft RE, Rothe D, Jacob E, and Schlögl R. Fullerene-like Soot from EURO-IV Diesel Engine: Consequences for Catalytic Automotive Pollution Control. *Topics in Catal*, 30(31):241–5, 2004.

[59] Müller JO, Su DS, Wild U, and Schlögl R. Bulk and surface structural investigations of diesel engine soot and carbon black. *Phys Chem Chem Phys*, 9:4018–25, 2007.

[60] Loretto MH. *Electron beam analysis of materials*. Chapman & Hall, 1994.

[61] Daniels H, Brown A, Scott A, Nichells T, Rand B, and Brydson R. Experimental and theoretical evidence for the magic angle in transmission electron energy loss spectroscopy. *Ultramicroscopy*, 96(3-4):523–34, 2003.

[62] Papworth AJ, Kiely CJ, Burden AP, Silva SRP, and Amaratunga GAJ. Electron-energy-loss spectroscopy characterization of the sp^2 bonding fraction within carbon thin films. *Phys Rev B*, 62:628–31, 2000.

[63] Brauns A, Huggins FE, Shah N, Chen Y, Wirick S, and Mun SB. Advantages of soft X-ray absorption over TEM-EELS for solid carbon studies - a comparative study on diesel soot with EELS and NEXAFS. *Carbon*, 43(1):117–24, 2005.

[64] Mackovic M. Characterization of soot particles from diesel engines and tin dioxide particles milled in stirred media mills. PhD thesis. University of Erlangen-Nürnberg, 2012.

[65] Cohen-Ofri I, Popovitz-Biro R, and Weiner S. Structural characterization of modern and fossilized charcoal produced in natural fires as determined by using electron energy loss spectroscopy. *Chem Eur J*, 13(8):2306–10, 2007.

[66] Berndt F, Kleebe HJ, and Ziegler G. Evidence for Structural Changes of Amorphous Carbon Coatings on Silicon Carbide During Tribological Tests. *J Am Ceram Soc*, 82(11):3161–6, 1999.

[67] Vander Wal RL and Tomasek AJ. Soot nanostructure: dependence upon synthesis conditions. *Combust Flame*, 136(1-2):129–40, 2004.

7 Fast pyrolysis model

7.1 Introduction

In this chapter, a 1D model for fast pyrolysis of biomass is presented and simulation results are discussed. In spite of numerous studies existing on biomass devolatilization mechanisms, there is no generally accepted model that can predict the reaction rate and provide information about final conversion and product yields over a wide range of operating conditions. The aim of this study was to develop a simple model for the char yield prediction at conditions relevant to suspension firing. The representation of biomass particle shape in fast pyrolysis will be discussed. The model has been used to obtain pyrolysis kinetics for non-isothermal particles considering the intra-particle heat transport limitations as well as the catalytic effect of potassium on the product yields. The model describes the char yields of both woody and herbaceous biomass particles. The model was validated against the experimentally determined char yields at high heating rates $>$ 200 K s^{-1} obtained by a wire mesh reactor, a single particle burner and a drop tube reactor.

7.2 Model development

In the present work a model for devolatilization of non-isothermal cylindrical biomass particles is described. The model includes both chemical kinetics, external and internal heat transfer. A single biomass particle enters a pre-heated gas flow and heats up by the heat transfer from surroundings through convection and radiation in the single particle reactor and drop tube reactor, or by conductive heat transfer from the mesh to biomass particles in the wire mesh reactor. The model is based on the assumptions:

1. Fuel particle is cylindrical
2. Model is one-dimensional and thermal gradients within the particle are considered to be only in the radial direction
3. Particle is considered to be non-shrinking during pyrolysis
4. Drying is included, but the moisture content of all fuels in this work was low ($<$ 5 wt. %)
5. Internal and external mass transfer is fast [1], and is therefore not considered
6. Only the reactor walls contribute to the radiative external heat transfer, whereas the flame around the particle due to ignition of volatiles is neglected
7. Heat transfer to the fuel particles from the surroundings occur through convection and radiation
8. Heat transfer within a biomass particle is due to conduction
9. Potassium has the highest influence on the char yield compared to other ash elements
10. Variations in plant cell wall composition (cellulose, hemicellulose, lignin, extractives) are relatively small and have less influence on the biomass char yield than variations in the

potassium content

The last two assumptions were based on previous experimental results obtained in a wire mesh reactor and a drop tube reactor [2, 3]. The proposed model includes only primary pyrolysis reactions, i.e. not cracking of tar. The schematic view of the proposed kinetic model is shown in Figure 66.

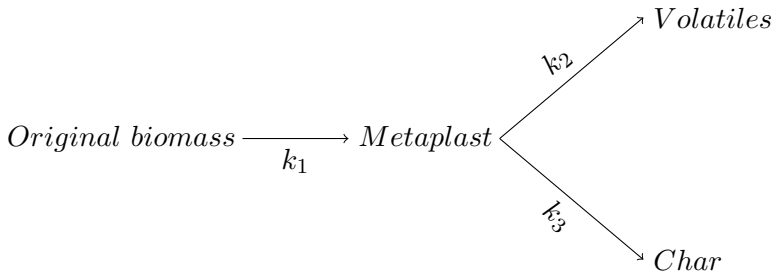

Figure 66: Three reaction model of biomass pyrolysis [4–6].

The non-shrinking particle is converted to an intermediate liquid compound (so called metaplast) which reacts further to form volatiles and char. Only the formation of metaplast is assumed to influence devolatilization whereas the split between products is determined by the heating rate and alkali content. The pyrolysis reactions are assumed to be irreversible first order with an Arrhenius type of rate expression. One fixed set of kinetic parameters (activation energy and pre-exponential factor for each of the three reactions) for a generic biomass was obtained by fitting the model to the char yields obtained in the wire mesh and entrained flow reactors. The catalytic effect of potassium on the char yield was included by decreasing the activation energy required for the reaction from metaplast to char (E_3), thereby leading to higher char yields.

The system of equations is converged into one objective function by forming the sum of squares of the residuals, and then minimizing the sum of the squares function using the fitting function fmincon in Matlab. The system is satisfied, when the sum of the squares function is minimized. The model was solved with the initial conditions:

$\rho_b(r, 0) = 1$

$\rho_M(r, 0) = 0$

$\rho_c(r, 0) = 0$

The local radial concentrations of biomass, metaplast and char are calculated from:

$$\frac{d\rho_b}{dt} = -k_1 \cdot \rho_b \tag{35}$$

$$\frac{d\rho_M}{dt} = k_1 \cdot \rho_b - k_2 \cdot \rho_M - k_3(\omega_K) \cdot \rho_M \tag{36}$$

$$\frac{d\rho_c}{dt} = k_3(\omega_K) \cdot \rho_M \tag{37}$$

$$k_i = A_i \cdot exp\left(-\frac{E_{a,i}}{R \cdot T}\right) \tag{38}$$

$$E_{a,3,max} = \Omega_K(\omega_K) \cdot E_{a,i} \tag{39}$$

$$\Omega_K(\omega_K) = 1 - K_1 \cdot \left(1 - exp\left(-\frac{\omega_K}{K_2}\right)^2\right) \tag{40}$$

ρ_b: Biomass density

ρ_M: Metaplast density

ρ_c: Char density

K_1, K_2: Constants which determine the activation energy of the char formation reaction as a function of the biomass potassium content.

ω_K: Potassium concentration in the raw biomass (mg kg^{-1})

The parameters were also defined in nomenclature. The factor for the adjustment of potassium content (Ω_K) becomes $\Omega_K(\omega_K$ = 0)=1 and the activation energy $E_{a,3}$ is equal to the maximal activation energy $E_{a,3,max}$ when there is no potassium in the sample. Ω_K approaches the minimal value and the activation energy $E_{a,3}$ is equal to the minimal activation energy $E_{a,3,min}$ when the biomass contains high amounts of potassium. K_1 parameter is a constant that describes a range of activation energy, and K_2 parameter is a constant for the exponential adjustment of the potassium content (ω_K in mg kg^{-1}). Various expressions of Ω_K to describe the influence of potassium content were tested during the optimization over the char yield, and equation 40 was found to work the best.

The results of the fitting using MatLab showed that the kinetic parameters (A_i and $E_{a,i}$) for the metaplast formation and volatiles release are similar. The char yields were calculated in the model by keeping the kinetic parameters (k_1 and k_2) of other reaction constants.

7.2.1 Heat transfer equations

The heat transport into the particle is described by the intra-particular heat flux through a cylindrical fuel particle driven by the external heat transport from the surroundings, and described

by Fourier's law under non-steady-state:

$$c_{p,s} \cdot \frac{dT_p}{dt} = \frac{1}{\rho_s} \cdot \frac{1}{r^n} \cdot \frac{\partial}{\partial r}\left(r^n \lambda_{eff} \frac{\partial T_p}{\partial r}\right) + \sum_{j=1}^{3} r_{pyr,j} \cdot (-\Delta H_{reac,j}) + r_{H_2O} \cdot (-\Delta H_{vap}) \tag{41}$$

$$r_{pyr,j} = -A_{pyr,j} \cdot exp\left(-\frac{E_{pyr,j}}{RT}\right) \cdot \left(\frac{\rho_b}{\rho_{b,0}}\right)^m \tag{42}$$

$$r_{H_2O} = -A_{H_2O} \cdot T_p^{1/2} \cdot exp\left(-\frac{E_{H_2O}}{RT}\right) \cdot \left(\frac{\rho_w}{\rho_{b,0}}\right)^m \tag{43}$$

In equation 41, λ_{eff} is the effective thermal conductivity of a fuel particle, and m is the reaction order of the biomass in equation 42. The parameters ρ_s and $c_{p,s}$ are the particle density and specific heat capacity of the solid phase (non-converted biomass, metaplast and char). In equations 42 and 43, $\rho_{b,0}$ is the initial biomass particle density. The overall reaction enthalpy includes the heat of reaction ($\Delta H_{reac,j}$) multiplied with the pyrolysis reaction rate ($r_{pyr,j}$) for each reaction (metaplast (j=1), char (j=2) and volatiles (j=3)). The reactions from metaplast to gas or char are competitive. In this study, the formation of metaplast was set as thermally neutral [7, 8], gas formation to be endothermic, and char formation to be exothermic [9, 10]. This approach result in the dependence of overall heat of reaction on the char yield [11], which is consistent with experimental results [12, 13]. In the present model, the overall reaction enthalpy changes with the char yield, similar to the modeling approach of Haseli et al. [11]. The presence of potassium in fuels has a catalytic effect on pyrolysis reactions favouring the formation of char, and therefore, the overall endothermic heat of pyrolysis decreases with the increasing char yield, and eventually shifts to an exothermic process, similar to results of Rath et al. [13] and Mack et al. [12]. The exothermal and endothermal heat of reactions ($\Delta H_{reac,2}$ = -255000 J kg^{-1}; $\Delta H_{reac,3}$ = 20000 J kg^{-1}) were proposed by Koufopanos et al. [9].

The rates of mass loss during drying and devolatilization were described by equations 35-37 [14]. A first order reaction model (m=1) was chosen to describe the experimental results [15]. In the model, the heat of vaporization was assumed to be ΔH_{vap} = 2440000 J kg^{-1} [16, 17]. The initial condition is given by the ambient temperature:

$$T_p(r, 0) = T_{amb} \tag{44}$$

The boundary conditions specify that the heat flux at the particle center is zero (due to symmetry) as shown in equation 45 and that heat transferred to the particle surface by convection and radiation is conducted into the particle as shown in equation 46 or given by the temperature of the mesh in equation 47:

$$\lambda_{eff} \left.\frac{dT_p}{dr}\right|_{r=0} = 0 \tag{45}$$

$$\lambda_{eff} \left.\frac{dT_p}{dr}\right|_{r=R_p} = h \cdot (T_g - T_p|_{r=R_p}) + \epsilon \cdot \sigma \cdot (T_w^4 - T_p^4|_{r=R_p}) \quad drop\ tube\ reactor \tag{46}$$

$$T_p|_{r=R_p} = T_{mesh}(t) \quad wire\ mesh\ reactor \tag{47}$$

In equation 46, T_w is the temperature of a radiating wall and h is the convective heat transfer coefficient between the gas and fuel particle. T_{mesh} in equation 47 is the mesh temperature in the wire mesh reactor. When the biomass sample is heated up in the wire mesh reactor, it is assumed that the particle surface temperature follows temperature of the mesh. The locally varying effective thermal conductivity (λ_{eff}) inside the particle is approximated by equation 48 [18, 19]:

$$\lambda_{eff} = \xi \cdot \lambda_g + \lambda_b \cdot \psi \cdot (1-\xi) + \lambda_c \cdot (1-\psi) \cdot (1-\xi) + \lambda_r \cdot (1-\xi) \tag{48}$$

$$\lambda_r = \frac{4 \cdot \xi}{(1-\xi)} \cdot \epsilon \cdot \sigma \cdot d_{pore} \cdot T_p^3 \tag{49}$$

$$\rho_{c,0} = \frac{\rho_{b,0} \cdot Y_c}{f_{sh,min}} \tag{50}$$

$$\psi = \frac{\rho_b + \rho_M}{\rho_b + \rho_M + \rho_{c,0}} \tag{51}$$

In equation 49, λ_r is thermal conductivity induced by radiation through pores, correlated from previous investigations [18, 19], λ_g, λ_b and λ_c are thermal conductivities of gas, unconverted biomass and char, ξ is the void fraction occupied by the gas phase and ψ is the biomass fraction of a solid phase which varies 0 to 1, when a biomass particle is not reacted. In equation 51, the thermal conductivity of metaplast is assumed to be equal to the thermal conductivity of original biomass. The convective heat transfer coefficient between gas and fuel particles in the drop tube reactor is described in equation 52:

$$h = \frac{Nu \cdot \lambda_g}{d_p} \tag{52}$$

The particle Reynolds, Prandtl and Nusselt numbers are defined in equations 53-55 [**?**]:

$$Re = \frac{d_p \cdot (v_p - v_g) \cdot \rho_g}{\mu_g} \tag{53}$$

$$Pr = \frac{c_{p,g} \cdot \mu_g}{\lambda_g} \tag{54}$$

$$Nu = 0.3 + \frac{0.62 \cdot Re^{1/2} \cdot Pr^{1/3}}{(1 + (\frac{0.4}{Pr})^{2/3})^{1/4}} \cdot \left(1 + \left(\frac{Re}{282000}\right)^{5/8}\right)^{4/5} \quad RePr > 0.2 \tag{55}$$

The terminal velocity of a biomass particle is calculated from correlations for the Stokes regime, steady separated and unsteady separated flows in equations 56-58 [20]:

$$v_p = \frac{d_p^2 \cdot g \cdot (\rho_s - \rho_g)}{18 \cdot \mu_g} \qquad Re < 2 \tag{56}$$

$$v_p = 0.153 \left[\frac{(\rho_s - \rho_g) \cdot d_p^{1.6} \cdot g}{\mu_g^{0.6} \cdot \rho_g^{0.4}}\right]^{0.714} \qquad 2 < Re < 400 \tag{57}$$

$$v_p = 1.74 \cdot \sqrt{\frac{d_p \cdot (\rho_s - \rho_g) \cdot g}{\rho_g}} \qquad 400 < Re < 200000 \tag{58}$$

The terminal velocity of small fuel particles was calculated by Stokes law in equation 56. In the transition flow, the terminal velocity of intermediate fuel particles is calculated in equation 57. The heat transfer between gas and large fuel particles takes place in the turbulent flow regime and is calculated from equation 58 [21].

7.2.2 Method of lines

Most of the pyrolysis models [5, 18, 22–25] involve solution schemes based on the method of lines (finite difference method) to solve the heat transfer equations. The numerical solution of a partial differential equation is often complicated and unstable [25]. The main advantage of the method of lines is that the spatial and temporal accuracy are decoupled, and can be considered separately, which is useful in several space dimensions [26]. Another advantage of the method of lines is its simplicity and the possibility to easily obtain high-order approximations for the achievement of high-order accuracy of the spacial discretization [27].

The method of lines is based on the discretization of partial differential equations (PDEs), and further conversion of the partial differential equations into a set of ordinary differential equations (ODEs) [28]. The core idea of the finite-difference method is to replace continuous derivatives with so-called difference equations that involve only the discrete values associated with positions on the mesh using Taylor series expansions [29]. The mesh is a set of locations where the discrete solution is computed. Nodes are usually associated with each cell thus producing a mesh of points. The distance between any two nodes is the mesh spacing. The governing equation 41 for the heat transfer in the fuel particle is discretized using a central difference scheme:

$$c_{p,s,i} \cdot \frac{dT_i}{dt} = \left(\frac{\lambda_{eff,i}}{\rho_{s,i}} \cdot \left(\frac{T_{i-1} - 2 \cdot T_i + T_{i+1}}{\Delta r^2} + \frac{n}{r_i} \cdot \frac{T_{i+1} - T_{i-1}}{2 \cdot \Delta r} \right) \right) + \sum_{j=1}^{3} r_{pyr,i,j} \cdot (-\Delta H_{reac,i,j}) + r_{H_2O,i} \cdot (-\Delta H_{vap,i}) \tag{59}$$

In the present model, the ode15s method was chosen as an ODE solver. The ode15s function based on the Backward Differentiation Formula (BDF) is recommended for the solution of stiff problems [30]. The number of mesh points was set to 101.

7.2.3 Biomass particle properties

Biomass samples were analyzed with a 2D dynamic imaging instrument by using different size measures (width and length). In the present model, the diameters $x_{Ma,min}$ and $x_{Fe,max}$ were chosen to represent the biomass particle's width and length. Diameter $x_{Fe,max}$ is the largest diameter to fulfill the assumption that the length of a particle has to be larger than its width. Diameter $x_{Ma,min}$ is an area bisector representing the shortest distance to the particle's opposite edges.

In the present work, a biomass particle was described as an infinite cylinder, corresponding to n=1 in equation 41 with a particle size equal to R_p/2, where R_p is represented by $x_{Ma,min}$. The thermo-physical parameters used in the devolatilization model are listed in Table 17.

Table 17: Thermophysical properties used in the devolatilization model and geometrical parameters of the drop tube reactor.

Symbol	Unit	Description	Expression	
ϵ		Emissivity	0.85	[31]
σ	J·(s·m^2·K^4)$^{-1}$	Stefan-Boltzmann	5.67·10^{-8}	[31]
ξ		Void fraction	1- $\frac{(\rho_b+\rho_M+\rho_{c,0})}{1500}$	[24]
$\rho_{b,0}$	kg·m^{-3}	Raw biomass density	650 (wood) and 700 (straw)	[32, 33]
ρ_g	kg·m^{-3}	Gas density (N_2)	362.65·T$_g^{-1}$	[34]
d_{pore}	m	Pore diameter	3.2·10^{-6}	[31]
$d_{pore,c}$	m	Char pore diameter	2·10^{-4}	[35]
$c_{p,b}$	J·(kg·K)$^{-1}$	Raw biomass specific heat capacity	1500+T$_p$	[19]
$c_{p,c}$	J·(kg·K)$^{-1}$	Char specific heat capacity	420+2.09·T$_p$+6.85·T$_p^2$	[19]
$c_{p,g}$	J·(kg·K)$^{-1}$	Gas specific heat capacity	770+0.629·T$_g$+1.91·10^{-4}·T_g^2	[18]
λ_g	W·(m·K)$^{-1}$	Gas thermal conductivity	0.026	[36]
λ_b	W·(m·K)$^{-1}$	Raw biomass thermal conductivity	0.35	[19]
λ_c	W·(m·K)$^{-1}$	Char thermal conductivity	0.1	[19]
μ_g	Pa·s	Gas phase dynamic viscosity	4.847·10^{-7}·T$_g^{0.64487}$	[24]
$\Delta H_{reac,1}$	J·kg^{-1}	Heat of reaction from biomass to metaplast	0	[7, 8]
$-\Delta H_{reac,2}$	J·kg^{-1}	Heat of reaction from metaplast to char	-255000	[9]
$\Delta H_{reac,3}$	J·kg^{-1}	Heat of reaction from metaplast to gas	20000	[9]
ΔH_{vap}	J kg^{-1}	Heat of vaporization	2440000	[17]
A_{H_2O}	s^{-1}K$^{-0.5}$	Pre-exponential factor	5.1·10^{10}	[24]
E_{H_2O}	J mol^{-1}	Activation energy	88000	[24]
L	m	Drop tube reactor's length	2.3	
D_r	m	Drop tube reactor's diameter	0.054	

7.2.4 Overview of performed experiments

The fitting was performed for pinewood particle sizes of 0.2 and 1 mm. The devolatilization time and char yield of 3,4 and 5 mm pinewood particles in a temperature range of 1350 to 1450°C were determined in the single particle reactor. The main characteristics of the conducted experiments are summarized in Table 18:

Table 18: Overview of the conducted experiments in the WMR, DTF and SPR.

Setup	Particle size	Heating rate	Final Temperature	Reference
	mm	K s^{-1}	°C	
Wire mesh reactor	0.2 & 1	10-10^3	350-1400	[2]
Drop tube reactor	0.2 & 1	calculated by model	1000-1400	[3]
Single particle reactor	3, 4, 5	calculated by model	1350 & 1450	[37]

7.3 Results

7.3.1 Kinetic parameters

The results of the fitting of the rate constants, including the influence of potassium are shown in Table 19.

Table 19: The best fit values of the kinetic parameters. In the model, the constants K_1 = 0.068 and K_2 = 4500 (mg kg^{-1}) were fitted.

Metaplast		Volatiles		Char	
$E_{a,1}$	A_1	$E_{a,2}$	A_2	$E_{a,3}$	A_3
J mol^{-1}	s^{-1}	J mol^{-1}	s^{-1}	J mol^{-1}	s^{-1}
228000	$3.2{\cdot}10^8$	174100	$3.6{\cdot}10^{12}$	$132500{\cdot}\Omega_K$	$5.6{\cdot}10^8$

Figure 67 illustrates that the char yield increases with increasing potassium content in the lignocellulosic material and decreases with the higher heating rate. The activation energy of the char forming reaction decreases with increasing potassium content, and thus, the influence of potassium becomes smaller at higher heating rates. In Figure 67(b), the model estimates the char yield which increases from 2.6 % to 32.5 % when the heating rates decrease from 10^4 to 2 K s^{-1}.

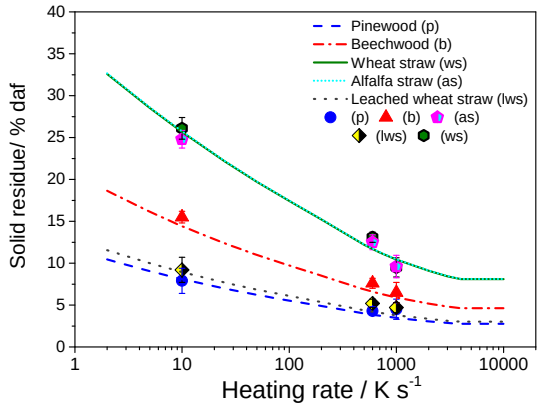

67(a): Heating rate effect on the char yield

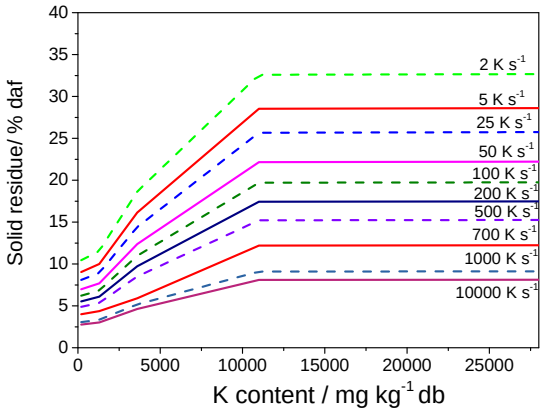

67(b): Char yields versus potassium content in the fuel

Figure 67: (a) Comparison of simulated and experimental data for the influence of heating rate on the char yield of pinewood, beechwood, wheat straw, leached wheat straw and alfalfa straw in the wire mesh reactor, and (b) Simulated char yields versus potassium content in the original fuel (heat treatment temperature: 1400°C, holding time: 1 s, particle size: 0.2 mm).

The estimated biomass particle mass as a function of mean particle temperature is shown in Figure 68. The effect of alkali, particle size and heating rate on the mass loss during pyrolysis was

investigated. The mass loss of smaller particles is shown only at 1400°C in the wire-mesh reactor, since pyrolysis is completed at temperatures below 800°C. The simulation results show that char yields from pyrolysis of wood and leached wheat straw in the drop tube reactor were similar in a temperature range of 1000-1400°C, whereas the char yield of wheat and alfalfa straw decreased slightly from 10.3 to 7.6 % by weight. The present results show that the model accurately estimates the char yield for smaller (0.2 mm) biomass particles.

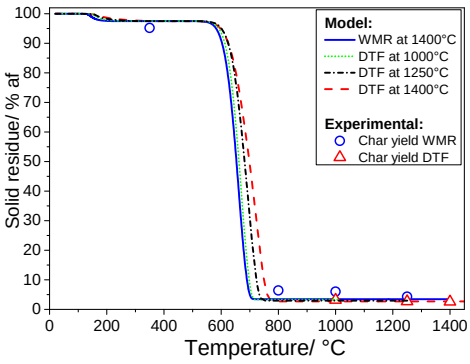

68(a): Pinewood 0.2 mm

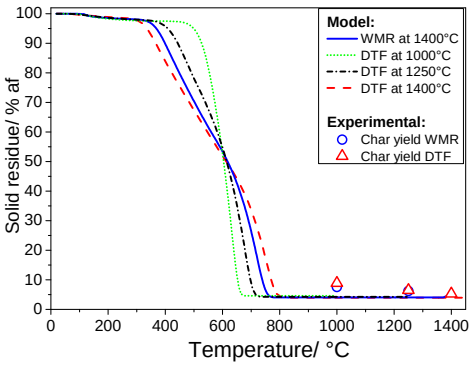

68(b): Pinewood 1 mm

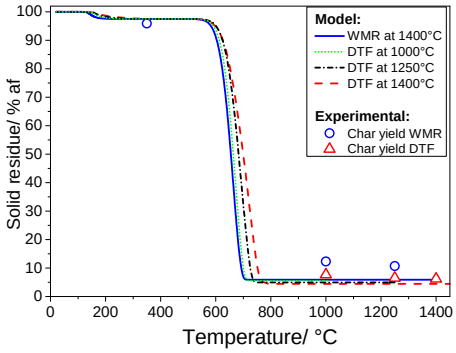

68(c): Beechwood 0.2 mm

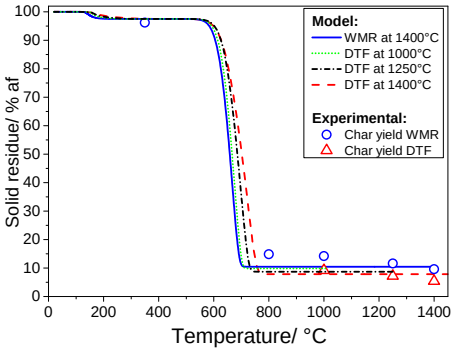

68(d): Alfalfa straw 0.2 mm

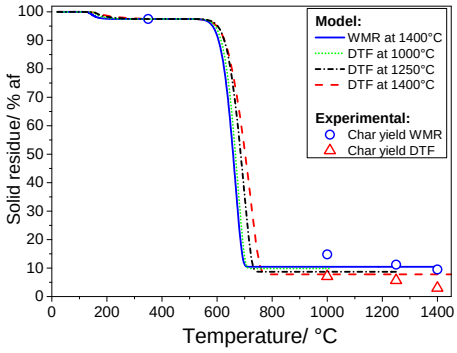

68(e): Wheat straw 0.2 mm

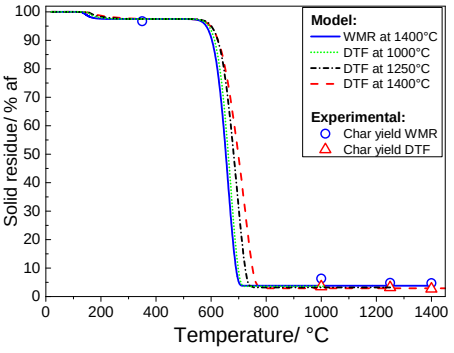

68(f): Leached wheat straw 0.2 mm

Figure 68: Simulated mass loss over the mean temperature (% af) of pinewood, beechwood, wheat straw, alfalfa straw, leached wheat straw cylindrical particle at 1000, 1250 and 1400°C in the DTF and at 1400°C in the WMR, and comparison with the char yields determined experimentally in the wire mesh reactor at (heat treatment temperature: 350, 800, 1000, 1250 and 1400°C; heating rate: 1000 K s^{-1}; holding time: 1 s) and drop tube reactor at 1000, 1250 and 1400°C as determined by Trubetskaya et al. [2, 3].

The char yield from pyrolysis of 1 mm pinewood particles is also estimated well and is about 3 % points lower than the experimentally determined char yields in the drop tube reactor. The experimental data obtained in the wire mesh reactor are in agreement with the mass loss estimated by the model. The lower WMR heating rate caused the reaction to take place at lower temperatures because of the longer time to reach a certain temperature compared to pinewood particles pyrolyzed in the drop tube reactor.

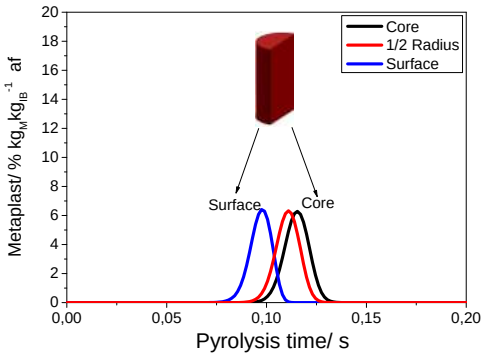

69(a): Pinewood 0.2 mm, DTF

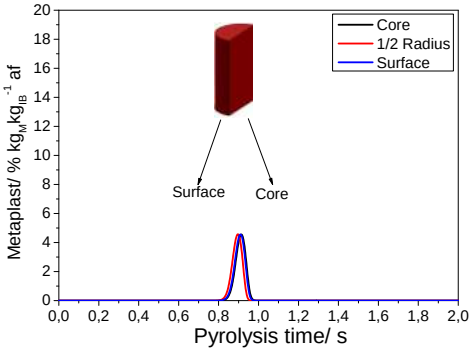

69(b): Pinewood 0.2 mm, WMR (10^3 K s^{-1})

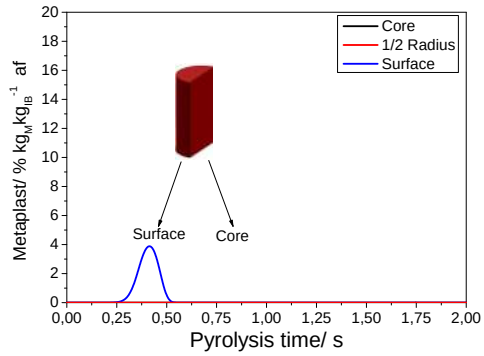

69(c): Pinewood 3 mm, DTF

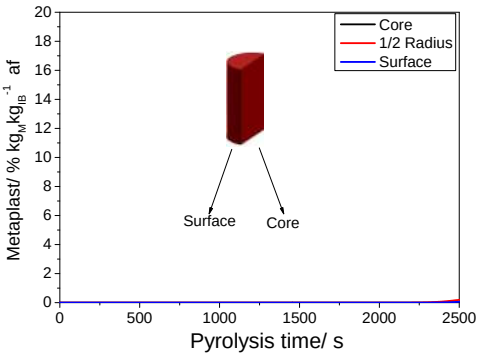

69(d): Pinewood 3 mm, 10 K min^{-1}

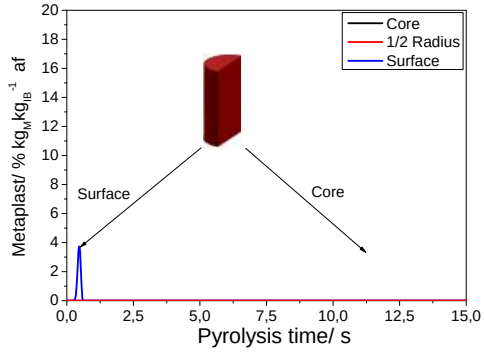

69(e): Pinewood 10 mm, DTF

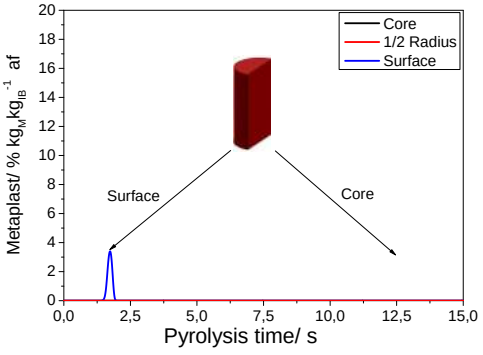

69(f): Pinewood 10 mm, WMR (10^3 K s^{-1})

Figure 69: Simulated metaplast formation (% af) from pyrolysis of 0.2, 3 and 10 mm pinewood particles at slow heating rate in the thermogravimetric instrument (10 K min^{-1}), at intermediate heating rate (10^3 K s^{-1}) in the wire mesh reactor and at high heating rates in the drop tube reactor. The metaplast formation (kg$_M$ kg$_{IB}^{-1}$) is showed over the pyrolysis time.

Figure 69 illustrates the mass fraction of metaplast formed at the particle surface, middle and

center as a function of time. The simulation results show that both the heating rate and particle size influence the metaplast formation. In general, high heating rates promote the formation of metaplast. Due to negligible temperature gradients, high heating rates cause small particles first to become fluid and form a molten sphere, and later lead to the char solidification as mentioned previously [2, 38, 39]. For large particles significant formation of metaplast at high heating rates is only observed at the surface.

This means that the particle surface melts during pyrolysis, whereas the interior retains the structure of original biomass particle [2]. The rate of metaplast formation was slower than formation of volatiles and char at lower temperatures. Thus, metaplast was formed faster than consumed at higher temperatures. At low heating rates, the particle was nearly isothermal, indicating only small differences in the metaplast formation as function of position in the particle. Thus, the relatively lower heating rate of the core increased the time for the three reactions, leading to lower metaplast yields.

7.3.2 Biomass shape representation

Figure 70 illustrates the mass loss of 0.2, 1 and 5 mm pinewood particles. The devolatilization time decreased with the higher heating rate in the drop tube reactor compared to the pyrolysis in the wire mesh reactor. The heating rate in the wire mesh reactor was setup to 1000 K s^{-1}.

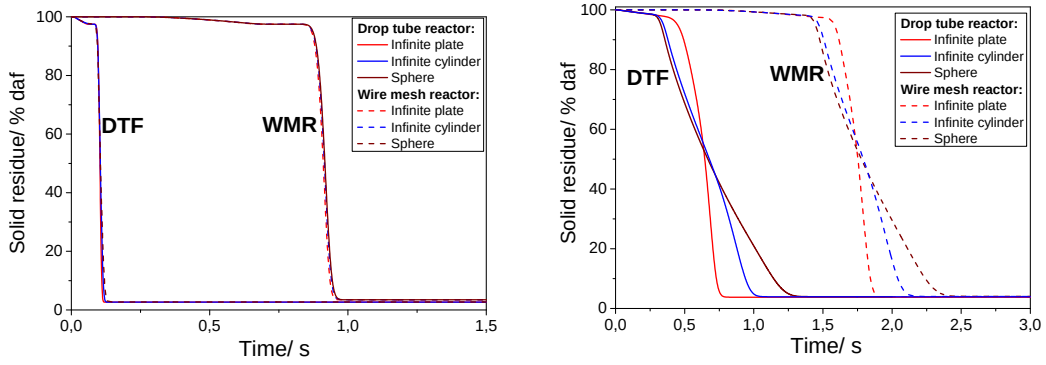

70(a): Pinewood 0.2 mm

70(b): Pinewood 1 mm

Figure 70: Mass loss histories of pinewood particles (0.2 and 1 mm) with the similar volume to surface ratio and different characteristic lengths which were calculated based on equations 60-62 in spherical (n=2), cylindrical (n=1) and plate-like (n=0) geometries at the final temperature of 1400°C during pyrolysis in the wire mesh and drop tube reactors.

In the drop tube reactor, the heating rate was calculated by the model using dimensions and operating parameters of the reactor shown in Table 17. A biomass particle was represented as plate, cylinder and sphere in spherical (n=2), cylindrical (n=1), plate-like (n=0) coordinates under

the assumption of similar volume to surface ratio using a different characteristic length:

$$d_p = x_{Ma,min} \quad (cylinder) \tag{60}$$

$$d_p = \frac{1}{2} \cdot x_{Ma,min} \quad (plate) \tag{61}$$

$$d_p = \frac{3}{2} \cdot x_{Ma,min} \quad (sphere) \tag{62}$$

The representation of the 0.2 mm particles with the similar volume to surface ratio using different characteristics lengths does not give large deviations with respect to char yield and devolatilization time among the three particle geometries as shown in Figure 70(a). The influence of particle shape became more pronounced with the increasing particle size, based on the larger internal temperature gradients in 1 mm pinewood particle as shown in Figure 70(b). The relative influence of heating rate on devolatilization time of 1 mm pinewood was less compared to the heating rate influence on pyrolysis of smaller particles. This is because of the predominance of internal heat transfer control within the large particles.

7.3.3 Particle size effect on devolatilization time

Figure 71 compares the time required for complete devolatilization of 3, 4 and 5 mm pinewood particles in the single particle reactor to the results estimated by the model for the particles from 0.01 to 10 mm. In the model, the complete devolatilization time is defined as the time when 95 % of the volatile matter in original pinewood particle was released.

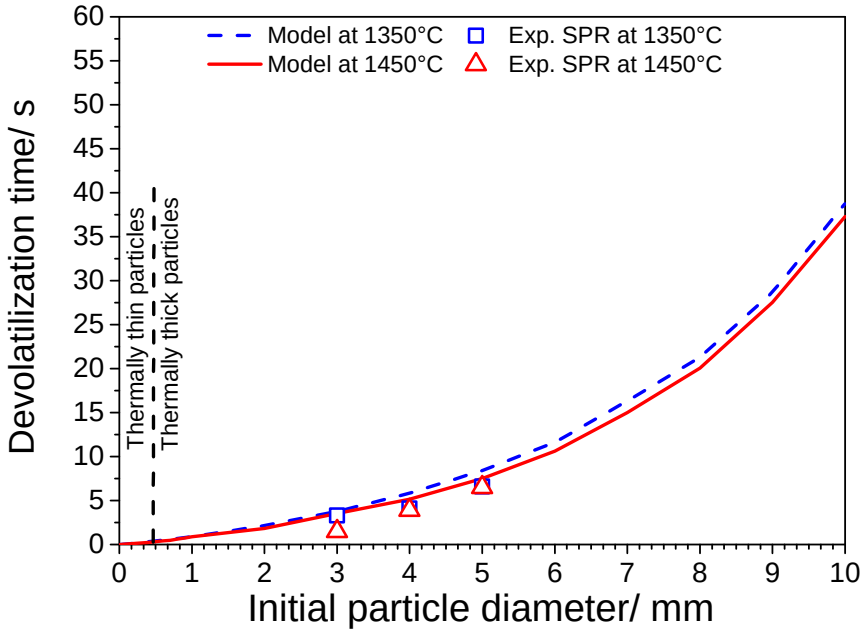

Figure 71: Simulated devolatilization time of non-shrinking pinewood particles (from 0.01 mm to 10 mm) at 1000, 1250 and 1400°C, and compared with the experimental results obtained in the SPR for 3, 4 and 5 mm particles at 1350 and 1450°C. Experimental data was taken from the investigations of Jepsen [37]. The black dashed line separates the thermally thin regime ($Bi < 0.5$) from the thermally thick ($Bi > 0.5$).

Figure 71 shows that under fast heating the particles with a mean diameter < 0.25 mm may be considered as thermally thin based on the modeling results with 0.1 s deviation, while the intra-particle heat conduction in larger particles plays a key role in the biomass devolatilization. The diameter of 3, 4 and 5 mm pinewood cubes was recalculated in a corresponding cylindrical diameter under assumption of a similar volume to surface ratio (3, 4 and 5 mm). A comparison of experimental and estimated devolatilization times showed that the model estimates the devolatilization time of pinewood particles well. In addition, the results showed that the 1 mm pinewood particles require more than 1 s in the WMR and DTF for complete conversion. The estimated devolatilization time by the model showed a similar trend for the experiments in the drop tube reactor.

7.4 Discussion

The present pyrolysis model estimates the char yield at high temperatures (up to 1500°C) and high heating rates $> 200\,\mathrm{K\ s^{-1}}$. In the model, an intermediate liquid (so called metaplast) is formed from the decomposition of biomass which reacts further to char and gas. It is assumed that the kinetics for metaplast formation does not depend on the biomass type. The further reaction of metaplast to char and gas is influenced by the fuel potassium content that determines the kinetic of char formation reaction.

The simulation results showed that at lower heating rates lower concentrations of metaplast were formed. At low heating rates, the particle temperature was nearly uniform over the particle diameter, and thus only smaller differences in the metaplast formation were observed. At high heating rates such as in the wire mesh and drop tube reactors, lower mass fractions of metaplast were formed in the particle core compared to the particle surface due to the lower heating rate of the core compared to at the surface. At high heating rates the formation of metaplast is initially fast compared to the reactions from metaplast to char and gas, and so a high concentration of metaplast is obtained before it reacts further to gas and char. Under conditions with a high fraction of metaplast the particle may become molten (either locally or the whole particle), thereby leading to structural changes of the particle as supported by experimental data [2].

The char yield was experimentally shown to increase with the potassium content in the original biomass [2, 3], and this effect was implemented in the model by changing the activation energy for the char formation reaction as a function of the potassium content. The simulation results showed that the effect of potassium on the char formation became stronger with decreasing heating rate which corresponds to the experimental observations from the wire mesh and drop tube reactors.

The particle size has a more significant influence on the metaplast formation and reaction to char and gas in the drop tube reactor ($10^{-4}\,\mathrm{K\ s^{-1}}$) compared to pyrolysis in the wire mesh reactor ($10\,\mathrm{K\ s^{-1}}$). The larger internal temperature gradients led to slower pyrolysis of 3 and 10 mm pinewood particles compared to 0.2 mm particles. For large particles the formation of metaplast mainly takes place at the particle surface at high heating rates, whereas at the interior, the lower

heating rates result in high metaplast concentrations. At low heating rates, the particle temperature of both small and large particles were nearly isothermal, leading to smaller local differences in the metaplast formation. The differences in local mass fractions of metaplast became larger with the increasing particle size and heating rates because of the predominance of internal heat transfer control within the large particles.

Miller and Bellan [6] hypothesized that the tar inside larger particles may undergo secondary reactions, leading to higher char yields. They reported that secondary reactions occurring in larger particles strongly decreased the tar release and increased char formation in pyrolysis. This effect was not included in the model and could be the reason why the model slightly underpredicts the char yield for large particles.

7.5 Conclusion

A non-isothermal non-shrinking particle model has been developed to describe biomass pyrolysis at different heating rates, high temperatures (up to 1500°C) and for different biomass particle sizes. The model estimates the yields of volatiles and char. The model relies on the kinetic scheme previously introduced by Broido and Shafizadeh, applied in fast pyrolysis of cellulose through the formation of an intermediate liquid (so called metaplast) which reacts further to char and gas. The influence of fuel potassium content on the pyrolysis process was implemented in the model by its influence on the char formation kinetics.

Cylindrical representation of a biomass particle shape was chosen to be the most suitable for the pyrolysis model. The evolution of devolatilization time required for the complete pyrolysis showed that the particles with a mean diameter < 0.25 mm may be considered as thermally thin even at high heating rates of 10^3-10^4 K s^{-1}. The estimated results by the 1D model are in agreement with the experimental work, and emphasize a key role of intra-particle heat conduction in biomass particles > 0.25 mm.

The influence of potassium on the char yield was implemented in the model by reduction in the activation energy of char formation with increasing potassium content, and fitted to the experimental results obtained in wire mesh and drop tube reactors. A stronger catalytic effect of potassium on the char yield at low and intermediate heating rates compared to pyrolysis at high heating rates was observed. The model showed that the heating rate and potassium content affected significantly the char yield in agreement with experimental data obtained in the wire mesh and drop tube reactors. Thus, the model including these two parameters is in an acceptable agreement with the experimentally measured char yield. The proposed kinetic model for fast biomass pyrolysis is relatively simple and estimates reasonably accurately the char yield of biomass particles < 10 mm using one set of kinetic parameters valid for both wood and herbaceous biomass.

Nomenclature

AR	Aspect ratio
A_i	Pre-exponential factor (s^{-1})
A_p	Particle area (m^2)
c_p	Specific heat capacity (J (kg K)$^{-1}$)
D_r	Reactor's diameter (m)
d_p	Particle diameter (m)
d_{pore}	Particle pore diameter (m)
E_i	Activation energy (J mol^{-1})
g	Gravity (m s^{-2})
ΔH_{vap}	Heat of vaporization (J kg^{-1})
h	Convective heat transfer coefficient (W ($m^{-2}K^{-1}$))
K_1, K_2	Constants which determine the activation energy of the char formation reaction as a function of the biomass potassium content
k_i	Reaction rate constant (s^{-1})
L	Reactor's length (m)
m	Reaction order
n	Dimensionality factor
R	Gas constant (J (K mol)$^{-1}$)
r	Particle radius (m)
r	Reaction rate (kg kg^{-1} s^{-1})
R_p	Particle radius at a specific point inside (m)
T	Temperature (°C)
t	Time (s)
V_p	Particle volume (m^3)
v_p	Slip velocity between gas and particle (m s^{-1})
X	Conversion
$x_{Fe,max}$	Feret maximal diameter (m)
$x_{Ma,min}$	Martin minimal diameter (m)
Y	Fraction

Dimensionless numbers

Bi	Biot number
Nu	Nusselt number
Pr	Prandlt number
Re	Reynolds number

Greek symbols

α_p	Particle thermal diffusivity (m^2 s^{-1})
ϵ	Emissivity
κ	Heating rate (K s^{-1})
λ	Thermal conductivity (W $m^{-1}K^{-1}$)
μ_g	Gas phase viscosity (Pa s)
Ω_K	Factor for the adjustment of potassium content influence on the activation energy ($E_{a,3}$)
ω_K	K^+ concentration (mg kg^{-1})
ψ	Biomass fraction of a solid phase
ρ	Density (kg m^{-3})
σ	Stefan-Boltzmann constant (J (s m^2 K^4)$^{-1}$)

τ	Holding time (s)	M	metaplast
ξ	Void fraction occupied by the gas phase	$mesh$	wire mesh
Subscripts		p	particle
0	initial	pyr	pyrolysis
b	biomass	r	radiative
c	char	s	solid phase
g	gas	$total$	overall
H_2O	water	w	wall

References

[1] Umeki K and Biswas AK. Simplification of devolatilization models for thermally-thick particles: Differences between wood logs and pellets. *Chem Eng J*, 274:181–91, 2015.

[2] Trubetskaya A, PA Jensen, Jensen AD, Steibel M, Spliethoff H, and Glarborg P. Influence of fast pyrolysis conditions on yield and structural transformation of biomass char. *Fuel Process Technol*, 140:205–14, 2015.

[3] Trubetskaya A, Jensen PA, Jensen JD, Llamas Garcia AD, Umeki K, and Glarborg P. Effect of fast pyrolysis conditions on biomass solid residues at high temperatures. *Fuel Process Technol*, 143:118–29, 2016.

[4] Shafizadeh F. Introduction to Pyrolysis of Biomass. *J Anal Appl Pyrolysis*, 3(4):283–305, 1982.

[5] Koufopanos CA, Maschio G, and Lucchesi A. Kinetic Modelling of the Pyrolysis of Biomass and Biomass Components. *Can J Chem Ing*, 67(1):75–84, 1989.

[6] Miller RS and Bellan J. Tar Yield and Collection from the Pyrolysis of Large Biomass Particles. *Combust Sci Tech*, 127(1-6):97–118, 1997.

[7] Arseneau DF. Competitive Reactions in the Thermal Decomposition of Cellulose. *Can J Chem*, 49(4):632–8, 1971.

[8] Mok WSL and Antal MJ. Effects of pressure on biomass pyrolysis. I Cellulose pyrolysis products. *Thermochimica Acta*, 68:155–64, 1983.

[9] Koufopanos CA, Papayannakos N, Maschio G, and Lucchesi A. Modelling of the Pyrolysis of Biomass Particles. Studies on Kinetics, Thermal and Heat Transfer Effects. *Can J Chem Ing*, 69(4):907–15, 1991.

[10] Haseli Y, van Oijen JA, and de Goey LPH. Modeling biomass particle pyrolysis with temperature-dependent heat of reactions. *J Anal Appl Pyrolysis*, 90(2):140–54, 2011.

[11] Haseli Y, van Oijen JA, and de Goey LPH. Numerical study of the conversion time of single pyrolyzing biomass particles at high heating conditions. *Chem Eng J*, 169:299–312, 2011.

[12] Mack CH and Donaldson DJ. Effects of Bases on the pyrolysis of Cotton Cellulose. *Textile Research J*, 37(12):1063–71, 1967.

[13] Rath J, Wolfinger MG, Steiner G, Krammer G, Barontini F, and Cozzani V. Heat of wood pyrolysis. *Fuel*, 82:81–91, 2003.

[14] Gubba SR, Ma L, Pourkashanian M, and Williams A. Influence of particle shape and internal thermal gradients of biomass particles on pulverized coal/biomass co-fired flames. *Fuel Process Technol*, 92(11):2185–95, 2011.

[15] Qin K, Lin W, Jensen PA, and Jensen AD. High-temperature entrained flow gasification of biomass. *Fuel*, 93:589–600, 2012.

[16] Ragland KW, Boerger JC, and Baker AJ. A model of chunkwood combustion. *Forest Prod J*, 38:27–32, 1988.

[17] Borman GL and Ragland KW. *Combustion engineering*. McGraw Hill Book Company, 1998.

[18] Bellais M. Modelling of the pyrolysis of large wood particles. PhD thesis, KTH Royal Institute of Technology, 2007.

[19] Grønli MG. A Theoretical and Experimental Study of the Thermal Degradation of Biomass. PhD thesis, Norwegian University of Science and Technology, 1996.

[20] Clement KH, Fangel P, Jensen AD, and Thomsen K. *Kemiske enhedsoperationer*. Polyteknisk Forlag, 2004.

[21] Wu Y. *Impinging Streams. Fundamentals, Properties and Applications*. Chemical Industry Press, 2007.

[22] Alves SS and Figueiredo JL. A model for pyrolysis of wet wood. *Chem Eng Sci*, 44(12):2861–9, 1989.

[23] Janse AMC, Westerhout RWJ, and Prins W. Modelling of flash pyrolysis of a single wood particle. *Chem Eng Proc*, 39(3):239–52, 2000.

[24] Bryden KM and Hagge MJ. Modeling the combined impact of moisture and char shrinkage on the pyrolysis of a biomass particle. *Fuel*, 82(13):1633–44, 2003.

[25] Fan LS, Miyanami K, Chen TY, and Walawender WP. A mathematical model for pyrolysis of a solid particle: Effects of the Lewis number. *Can J Chem Eng*, 55(1):47–53, 1977.

[26] LeVeque RJ. *Numerical Methods for Conservation Laws. Lectures in Mathematics*. ETH Zürich, 1990.

[27] Blazek J. *Chapter 3. Principles of Solution of the Governing Equations. In: Computational Fluid Dynamics. Principles and Applications (2nd edition)*. Elsevier, 2005.

[28] Ames WF. *Numerical Methods for Partial Differential Equations*. Academic Press, 1992.

[29] Prakash N and Karunanithi T. Advances in Modeling and Simulation of Biomass Pyrolysis. *Asian J Sci Research*, 2(1):1–27, 2009.

[30] Celaya EA, Aguirrezabala JJA, and Chatzipantelidis P. Implementation of an Adaptive BDF2 Formula and Comparison with the MATLAB ode15s. *Proc Comp Sci*, 29:1014–26, 2014.

[31] Lu H, Robert W, Peirce G, Ripa B, and Baxter LL. Comprehensive Study of Biomass Particle Combustion. *Energy Fuels*, 22(4):2826–39, 2008.

[32] Jensen PA, Sander B, and Dam-Johansen K. Pretreatment of Straw for Power Production. *Biomass Bioenergy*, 20(6):431–46, 2001.

[33] Miller RS and Bellan J. Numerical Simulation of Vortex Pyrolysis Reactors for Condensable Tar Production from Biomass. *Energy Fuels*, 12(1):25–40, 1998.

[34] Perry R. *Perry's chemical engineers' handbook*. McGraw Hill Book Company, 2007.

[35] Di Blasi C and Russo G. Modeling of Transport Phenomena and Kinetics of Biomass Pyrolysis. *Adv Thermochem Biomass Conv*, pages 906–21, 1994.

[36] Di Blasi C. Modelling the Fast Pyrolysis of Cellulosic Particles in Fluid-Bed Reactors. *Chem Eng Sci*, 55(24):5999–6013, 2000.

[37] Jepsen MS. Pyrolysis of Large Biomass Particles in a Single Particle Combustion Reactor. MSc thesis, DTU Chemical Engineering, Technical University of Denmark, 2014.

[38] Cetin E, Moghtaderi B, Gupta R, and Wall TF. Influence of pyrolysis conditions on the structure and gasification reactivity of biomass chars. *Fuel*, 83:2139–50, 2004.

[39] Dall'Ora M, Jensen PA, and Jensen AD. Suspension combustion of wood: Influence of pyrolysis conditions on char yield, morphology, and reactivity. *Energy Fuels*, 22:2955–62, 2008.

8 Conclusion

Biomass fast pyrolysis was investigated in a laboratory-scale wire mesh reactor and bench scale atmospheric pressure drop tube and entrained flow reactors. The effect of operating parameters and biomass types on product yields, solid residue morphology and reactivity using thermogravimetric analyzer was investigated. A wide range of operating parameters including the heat treatment temperature (350-1500°C), heating rate (10-10^4 K s^{-1}), residence time (1-4 s), particle size (0.05-5 mm) was selected relevant to the operating conditions in suspension biomass combustion. Wood (pinewood, beechwood) and herbaceous biomass (wheat straw, alfalfa straw, leached wheat straw, rice husk), which are typical forestry and agricultural wastes, were used as fuels.

The results showed that char yields of woody and herbaceous biomass from the drop tube reactor were lower than those obtained in the wire mesh reactor. The straw samples showed a significant char yield decrease in the drop tube reactor (≈ 4 % points lower) when the temperature was increased from 1000 to 1400°C, whereas the char yields of pinewood (≈ 3.5 wt. %, daf) and beechwood (≈ 7 wt. %, daf) were almost constant at a very low level. It was observed that a low fuel alkali content, high temperatures, and fast heating rates lead to low biomass char yields. The char yield decreased significantly between 10 and 600 K s^{-1}, but continued to decrease with increasing heating rate, and was lowest for the drop tube / entrained flow reactors with estimated heating rate of $> 10^4$ K s^{-1}. The heat treatment temperature and potassium content affected the char yield stronger than the heating rates and differences in the plant cell wall compounds between 600 and 3000 K s^{-1}. The heat treatment temperature affected more the herbaceous biomass char yield compared with wood. The differences in the char yield for particle size fractions in the range of 0.05 mm $< d_p <$ 0.425 mm were negligible, leading to the conclusion that the biomass particle can be assumed isothermal, when its size did not exceed 0.425 mm. The char yields of wheat straw and leached wheat straw were less affected by the holding time and particle size because the characteristic length for heat transport was determined by the particle thickness. The larger pinewood particles ($d_p > 0.85$ mm) required more than 1 s holding time for the complete conversion at intermediate and fast heating rates. The influence of heating rate on the char yields was less pronounced for particle sizes (from 0.85 to 4 mm) obtained at temperatures > 1250°C in the drop tube reactor, single particle reactor and drop tube reactor, due to the predominance of internal heat transfer control within the large particles.

Potassium compared to all other ash elements in the fuels had the highest influence on the char yield. However, the effect of potassium on the char yield was stronger at low and intermediate heating rates where potassium catalyzed the repolymerization and cross-linking reactions, leading to higher char yields. Moreover, the catalytic effect of potassium on the fuel structural changes was hypothesized to be due to a stronger cross-linking of herbaceous chars, leading to less fluidity, and therefore less spherical char particles. Silicon compounds abundant in herbaceous biomass had a negligible influence on the char yield, based on the similar char yields of rice husk (rich in Si), leached wheat straw (medium in Si) and pinewood (low in Si). However, a very high content of

silicon oxides in biomass ($> 50\,\%$ of the overall biomass inorganic matter) significantly affected the char morphology, as observed for rice husk. For this fuel, the high content of low-temperature melting amorphous silicon oxides led to the formation of a glassy shell on rice husk chars at 1000-1500°C. Similar reactivities of low ash-containing pinewood and silicon oxides rich rice husk showed that silica has less influence on the char reactivity. The ability of char to melt in fast pyrolysis followed the order pinewood $>$ beechwood, straw $>$ rice husk, and was related to the formation of metaplast. Different particle shapes of beechwood and leached wheat straw chars produced in the drop tube reactor which have similar potassium content suggested a stronger influence of the major biomass cell wall compounds and silicates on the char morphology than alkali metals.

In this study, potassium lean pinewood (0.06 wt. %) produced the highest soot yield (9 and 7 wt. %) at 1250 and 1400°C, whereas leached wheat straw with the higher potassium content (0.3 wt. %) generated the lowest soot yield (2 and 1 wt. %). Soot yields of wheat and alfalfa straw at both temperatures were 5 % points lower than wood soot yields and 3 % points higher than leached wheat straw soot yield, indicating that potassium plays a minor role on the soot formation. The leaching of alkali from wheat straw additionally resulted in a removal of lignin, possibly leading to the decreased formation of polycyclic aromatic hydrocarbon precursors, and thereby to lower soot yields. The higher soot yield of wood compared with herbaceous biomass was to a minor extent related to the suppression of soot formation by the higher potassium content. K^+ ions probably promote ionization of soot particles, and thus inhibit their coagulation in pyrolysis. Primary soot particles were characterized by HRTEM microscopy and electron energy-loss spectroscopy (EELS) to obtain information about particle size distribution, nanostructure and soot composition. Pinewood soot particles generated at 1250°C were significantly larger (77.7 nm) than soot particles produced in pinewood (47.8 nm) pyrolysis at 1400°C, beechwood (43 nm) and wheat straw (30.8 nm) devolatilization at both temperatures. The larger pinewood soot particles were related to the formation of tar balls known from smoldering combustion.

The influence of soot nanostructure, inorganic matter content and particle size on the reactivity in O_2 and CO_2 gasification was investigated. The thermogravimetric analysis showed that the maximal reaction rate of pinewood soot was shifted to temperatures about 100°C higher than for the other samples with respect to both oxidation and CO_2 gasification, indicating its lower reactivity. It appeared that soot samples produced at 1400°C were more reactive than soot generated at 1250°C. The beechwood and wheat straw soot samples were more graphitic than pinewood soot based on the EELS analysis. In contrast to expectations of graphitic structures to react slower than amorphous samples, beechwood and wheat straw soot were 35 and 571 times more reactive than pinewood soot prepared at 1400°C. The presence of potassium in wheat straw soot mainly as water-soluble KCl, KOH, $KHCO_3$ and K_2CO_3 and to a minor extent bonded to the soot matrix in oxygen-containing surface groups (e.g. carboxyl, phenolate) or intercalated in soot graphene layers led to a higher reactivity in CO_2 gasification compared to low-alkali containing pinewood soot. The major difference in nanostructure of pinewood, beechwood and wheat straw soot was

in the formation of multi and single core particles. Pinewood soot particles generated at 1250°C were mainly multi core structures compared to pinewood soot generated at 1400°C, combining both single and multi core particles. Beechwood and wheat straw soot samples had multi and single core particles at both temperatures. The length, separation distance and curvature of graphene layers affected the soot reactivity less than potassium.

Moreover, the reactivity of char was investigated in O_2 and CO_2 gasification. The results of this study showed that the heat treatment temperature, residence time and inorganic matter differences affected the reactivity more than the pyrolysis heating rate. The reaction rates were the same order of magnitude for the woody and herbaceous biomass pyrolyzed at 1000 K s^{-1} and 10 K min^{-1} in both oxidation and CO_2 gasification. The differences in reaction rates of non-treated and leached wheat straw chars at 1250 and 1400°C were small in CO_2 gasification. This indicates that the major part of potassium in the non-treated straw either evaporated or was incorporated into non-catalytic species such as potassium silicates. However, a small part of the potassium retained its catalytic effect in both straw samples leading to a quite similar reactivity, which was still higher than the reactivity for pinewood.

A non-isothermal model has been developed to describe biomass pyrolysis at fast heating rate (600-10^4 K s^{-1}), high temperatures (up to 1500°C) and valid for different biomass particle sizes (up to 10 mm). The model was developed to estimate the yields of volatile gas and char. The model includes both chemical kinetics, external and internal heat transfer, assuming that mass transfer is fast. The decomposition kinetics was coupled to the fuel properties and the external heat transfer environment. The kinetics of the fast pyrolysis was described through the Broido-Shafizadeh scheme for the uniform biomass particle. The model relies on the concept applied in fast pyrolysis of cellulose through the formation of an intermediate liquid (so called metaplast) which reacts further to form char and gas. The fast pyrolysis reactions were assumed to be irreversible first order with an Arrhenius type of rate expression. One fixed set of kinetic parameters (activation energy and pre-exponential factor for each of the three reactions) valid for woody and herbaceous biomass was estimated by fitting to the experimental data. The averaged char and gas yields were fitted to the experimental pyrolysis data by keeping the kinetic parameters of metaplast to volatile matter reaction and activation energies of original biomass to metaplast constant. The potassium influence on the char yield was implemented in the model based on the experimental results with respect to the stronger catalytic effect of potassium on the char yield at low and intermediate heating rates. The catalytic effect of potassium on the char yield was included through the decrease of activation energy by potassium ions, leading to higher char yields. The proposed kinetic model for the fast biomass pyrolysis is relatively simple and predicts reasonably the char yield of woody and herbaceous biomass particles < 10 mm, which are relevant for suspension fired combustion.

9 Suggestions for future work

In the present work, a relation between alkali and char morphology was not established. The investigations on leached wheat straw and beechwood with a similar potassium content suggested that alkali may have less influence on the char morphology than the distribution of the three major biomass constituents and silicates. In order to be able to understand the effect of alkali on the char yield, a wider range of experiments on a heated stage microscope is suggested. The surface investigations at different heating rates and by addition of potassium, calcium and sodium to wood and herbaceous fuels and plant cell wall compounds (cellulose, hemicellulose, lignin, extractives) may provide a new relation between fuel morphology and alkali metals. Moreover, the ability of char to melt under fast pyrolysis showed that low ash containing beechwood underwent less deformation than wheat and alfalfa straw samples, indicating the importance of biomass organic structure. It was hypothesized that lignin contributes probably more than holocelluloses to the metaplast formation. The experimental work at intermediate and high heating rates on the major plant cell wall compounds and fuels with the different distribution of the biomass constituents is needed. The yields and composition of volatile (gas, tar) and solid (soot, char) products may provide a new relation between the major biomass constituents affecting the metaplast formation.

The differences in yield of soot generated at high temperatures were related to the differences in lignin and extractives composition of original biomass and to a minor extent alkali metals. In order to understand how the differences in plant cell wall compounds affected the soot yield, it would be of great advantage to investigate the effect of ash free lignin on the soot formation at high heating rates. The alkali influence on the soot yield could be investigated using fuels with a similar organic composition containing a different potassium amount. The precise description of biochemical composition of leached wheat straw is needed to evaluate accurately the competitive influence of the major biomass constituents and alkali metals. The formation of tar balls at fast heating rates was not explained. The morphological changes of soot at a given heat treatment temperature depends on the distribution of the major biomass constituents and alkali metals, and thereby a correlation between a particle size of soot and biomass organic / inorganic composition is needed. The proposed correlation can be based on the extensive experimental work. Knowledge about differences in the composition and morphology of smaller and larger soot particles is needed. This can be characterized by transmission electron microscopy (TEM), Fourier transform infrared spectroscopy (FTIR), X-ray photoelectron (XPS) and Raman spectroscopies.

Finally, the model used in this work would benefit from validity in both slow and fast pyrolysis. The implementation of secondary reactions taking place in gas phase could improve the model accuracy. A wider range of experimental data can be included in the model to improve the optimization tool for the prediction of reaction kinetics. Soot and tar formation can be included in the model to predict the tar and soot yields during fast pyrolysis. Another approach to model the biomass devolatilization is suggested by introducing the distributed activation energy model to improve the product yield prediction. However, the complexity of the model may cause the com-

putational issues. The char reaction kinetics at high temperatures used in the model was estimated by the measured kinetics at low temperatures ($< 1000°C$), and therefore may contain certain errors in the prediction. If the kinetics of char and soot can be determined at high temperatures, the accuracy of solid residue reaction rate in the model could be increased.

A Appendix

A.1 Comparison of biomass char yield in WMR and DTF in ar and daf basis

Table 20: Comparison of pinewood, beechwood, wheat straw and alfalfa straw in wt. % on as received or dry ash free basis.

Fuel	Temperature, °C	Char yield, wt. %			
		Wire mesh reactor		Drop tube reactor	
basis		ar	daf	ar	daf
Pinewood	1000	6.5	6	3.2	3.2
	1250	4.7	4.3	2.8	2.7
	1400	-	-	2.7	2.6
Beechwood	1000	13.8	12.3	8.2	7.7
	1250	12.1	10.7	6.9	6.5
	1400	-	-	6.6	6.2
Alfalfa straw	1000	20.3	14.2	13.1	9.2
	1250	18.1	11.6	10.3	7.2
	1400	15.6	9.6	7.8	5.4
Wheat straw	1000	18.9	14.8	9.2	7.1
	1250	17.4	11.2	7.7	5.7
	1400	16	9.5	5.5	3
Leached wheat straw	1000	9	6.3	5	3.5
	1250	6.6	4.7	4.3	3.2
	1400	5.5	3.8	3.3	2.7

A.2 Wire mesh reactor

A.2.1 Effect of ash on the char yield

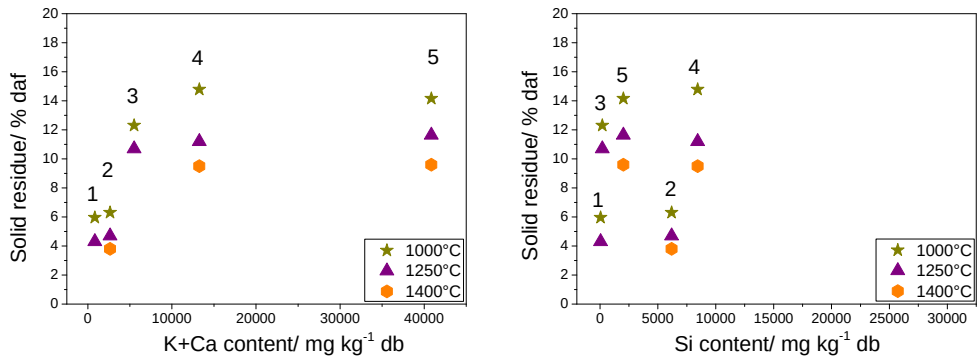

72(a): Effect of K and Ca on char yield

72(b): Effect of Si on char yield

Figure 72: Char yield of pinewood (1), leached wheat straw (2), beechwood (3), wheat straw (4) and alfalfa straw (5) (a) versus potassium and calcium content in the fuel, and (b) silicon content in the fuel, pyrolyzed in the WMR at (heat treatment temperature: 1000, 1250 and 1400°C, heating rate: 1000 K s^{-1}, holding time: 1 s, particle size: 0.05-0.2 mm).

A.2.2 Effect of particle size

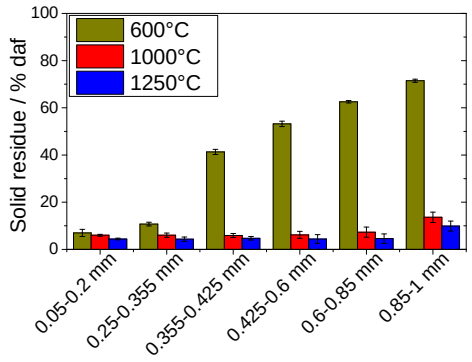

73(a): Pinewood

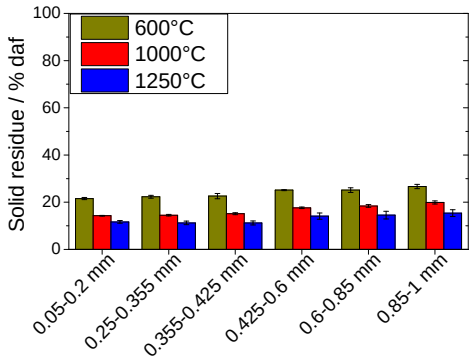

73(b): Wheat straw

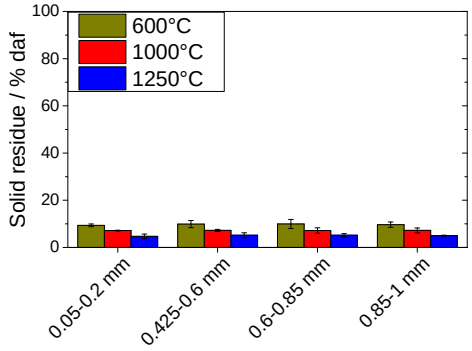

73(c): Leached wheat straw

Figure 73: Influence of a particle size on the pinewood, wheat straw and leached straw char yield (heat treatment temperature: 600, 1000 and 1250°C, heating rate: 1000 K s^{-1}, holding time: 1 s).

A.3 Drop tube reactor

A.3.1 Measurements inaccuracy

$$y = f(x_1, x_2, ..., x_m) \qquad u(y) = \sqrt{\sum_{k=1}^{m} \frac{\partial G}{\partial x_k} \cdot u^2(x_k)}, \qquad y = y \pm u(y) \tag{63}$$

where y and x_k were the output and input quantity, and u is the uncertainty of each quantity. The confidence interval was defined in equation 64:

$$y - \sigma \cdot u(y) \leq y \leq y + \sigma \cdot u(y) \tag{64}$$

with σ·u(y) was the extended uncertainty.

Table 21: Uncertainty calculation (confidence interval = 90 %; critical value = 1.645) for the pinewood char yield (particle size: 50-200 μm; heat treatment temperature: 1000°C) on the original WMR and redesigned setup for the section about heat treatment temperature and heating rate effects on the char yield.

Heating rate, K s^{-1}	**Original WMR**			**Redesigned WMR**		
Heating rate, K s^{-1}	**Mean char yield, % daf**	**STDEV**	**90 % CI for y**	**Mean char yield, % daf**	**STDEV**	**90 % CI for y**
10	12.3	1	1.6	13.5	2.3	3.7
100	8.3	1.2	1.9	8.5	1.1	1.8
300	7.3	1.2	1.9	7.6	1.4	2.3
600	6.9	1.7	2.8	7.4	1.9	3.1
1000	6	1	1.6	6.5	1.5	2.5
3000	5.7	0.8	1.3	5.6	0.5	0.9
Temperature, °C	**Mean char yield, % daf**	**STDEV**	**90 % CI for y**	**Mean char yield, % daf**	**STDEV**	**90 % CI for y**
600	7.6	0.4	0.7	8.1	0.8	1.3
1000	6	1	1.6	6.5	1.5	2.5
1250	6	0.7	1.1	5.9	1.7	2.8

A.4 Van Krevelen plot of wheat straw and rice husk reacted in BabiTER reactor

The H/C and O/C ratios of wheat straw and rice husk decrease rapidly and become constant with the formation of polyaromatic structures above 1250°C, indicating almost complete removal of hydrogen and oxygen-containing functional groups in the fast pyrolysis. The O/C ratio in the original rice husk and its chars is higher than in wheat straw at all heat treatment temperatures.

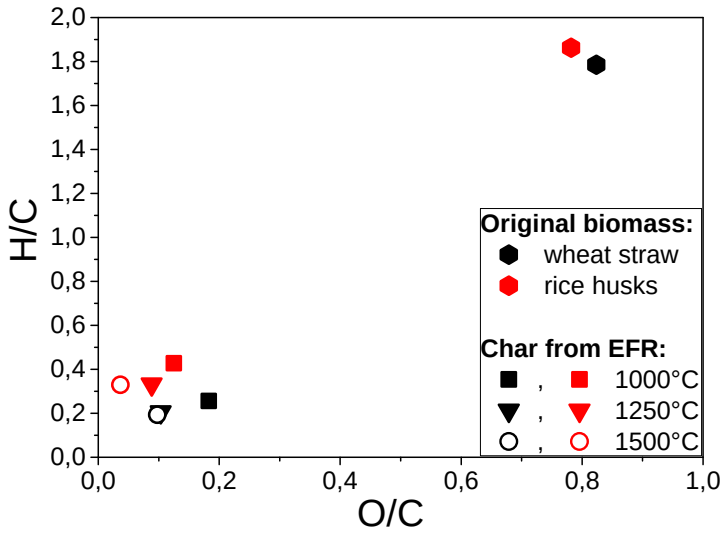

Figure 74: Van Krevelen plot of original rice husk and wheat straw and their chars, pyrolyzed in BabiTER reactor at 1000, 1250 and 1500°C and compared with the WMR chars, reacted at 1000°C.

A.5 Volatile gas composition

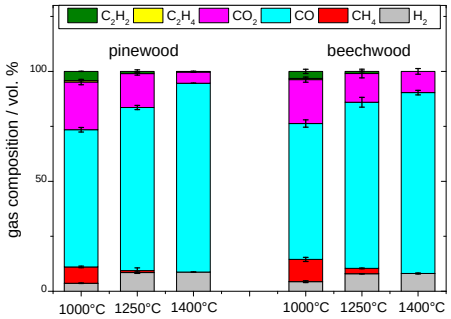

75(a): Pinewood and beechwood

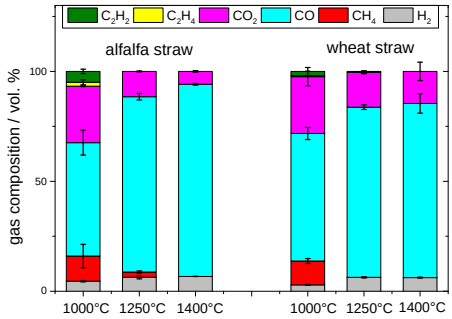

75(b): Alfalfa straw and wheat straw

Figure 75: Gas composition of biomass samples from the DTF (vol. % in inert nitrogen), reacted at 1000, 1250 and 1400°C.

A.6 Factsage simulation results

A.6.1 Drop tube reactor

Table 22: FactSage 6.0 input data for the wheat straw and alfalfa straw calculated in mol %.

Elements	**Wheat straw**	**Alfalfa straw**
Calculation in mol %		
N	0.036	0.021
C	3.533	3.542
H	6.300	6.700
$O_{org.}$	2.457	2.259
$O_{inorg.}$	0.087	0.109
N(pyrolysis)	0.063	0.063
Minerals applied in FactSage simulation		
Si	0.027	0.007
K	0.034	0.072
Ca	0.008	0.032
S	0.005	0.012
Cl	0.016	0.016
Minerals, not applied in FactSage simulation		
Na	0.001	0.004
Mg	0.002	0.006
P	0.002	0.006
Al	$4.6 \cdot 10^{-4}$	$4.3 \cdot 10^{-3}$
Ti	$3.1 \cdot 10^{-5}$	$6.3 \cdot 10^{-5}$
Fe	$6.2 \cdot 10^{-4}$	0

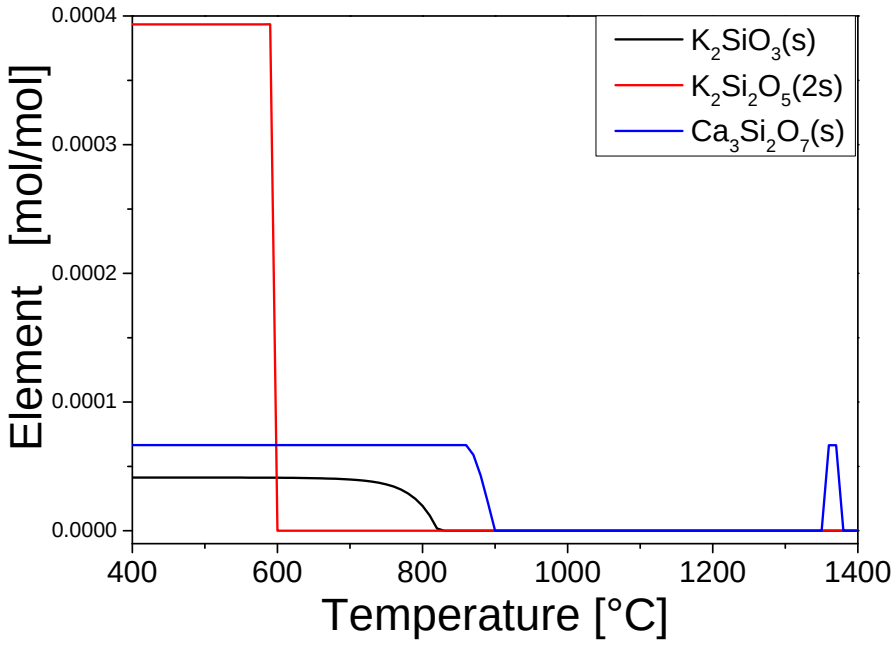

Figure 76: Output results of Factsage calculation with the main inorganic components in the wheat straw.

B Appendix

B.1 ^{13}C CP/MAS and ^{13}C SP/MAS NMR

Table 23: Resonance assignment of ^{13}C CP/MAS and ^{13}C SP/MAS NMR spectra of wheat straw and rice husk.

Chemical shift, ppm	Description
172-174	Carbohydrate; -COO-R, CH_3-COO-
153-154	Lignin; S3(e), S5(e)
145-148	Lignin; S3(ne), S5(ne), G1(e), G4(e)
133-138	Lignin; S1(e), S4(e), G1(e)
121-122	Lignin; G6
105-106	Carbohydrates; C1, Lignin; S2, S6
89-92	C4 in cellulose (cr)
84-85	C4 in cellulose (am)
72-75	C2, C3 in carbohydrates; C5 in cellulose
63-65	CH_2OH (C6 in cellulose, C5 in xylan)
56-57	Lignin, OCH_3
30-38	CH_2 in aliphatics
21	Carbohydrates; CH_3-COO-

Abbreviations: S, syringyl; G, guaiacyl; ne, in non-etherified arylglycerol β-aryl ethers; e, in etherified arylglycerol β-aryl ethers.

B.2 Char morphology and structural transformations in the WMR

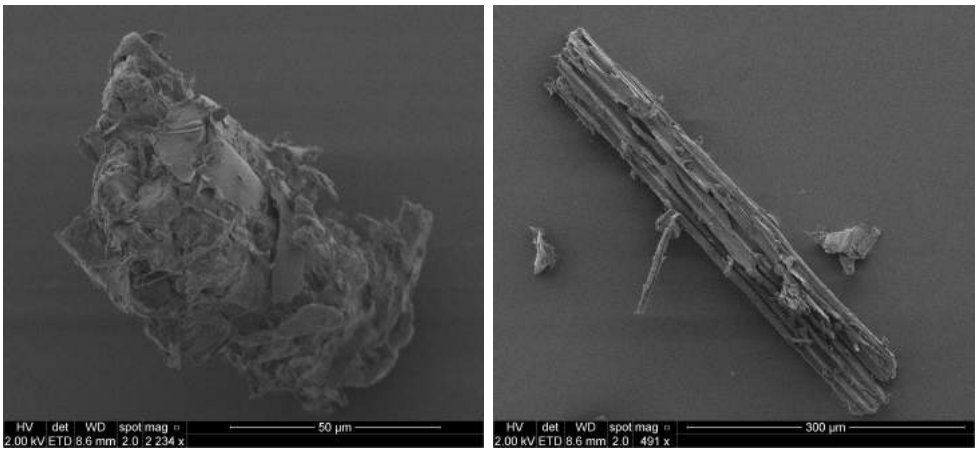

77(a): Pinewood 77(b): Wheat straw

Figure 77: SEM images of non-flattened pinewood and flattened straw particles.

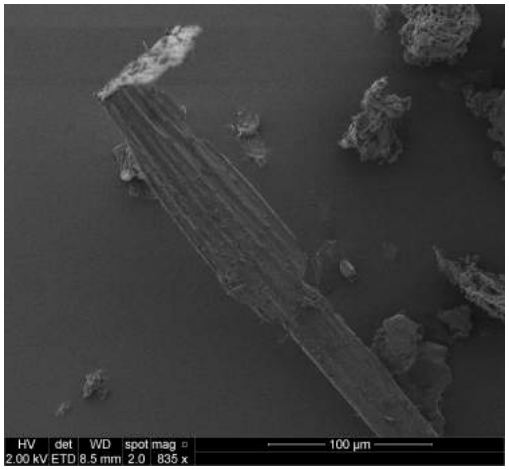

78(a): Original rice husk

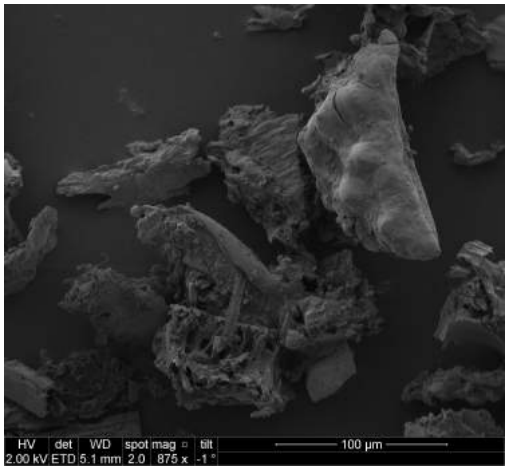

78(b): Char at 1000 °C

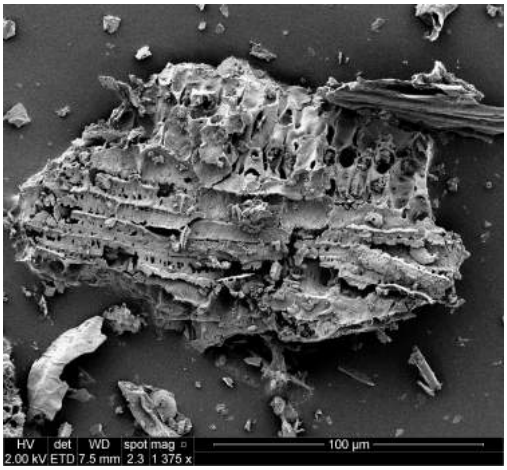

78(c): Char at 1250 °C

Figure 78: SEM images of original rice husk and chars (heat treatment temperature: 1000 and 1250°C, heating rate: 1000 K s^{-1}, holding time: 1 s, particle size: 0.05-0.2 mm (char)).

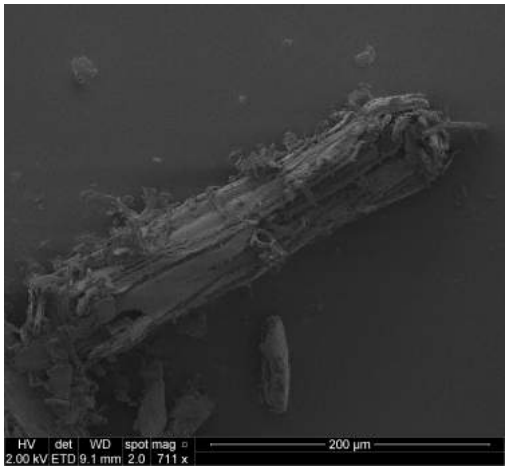

79(a): Original leached straw

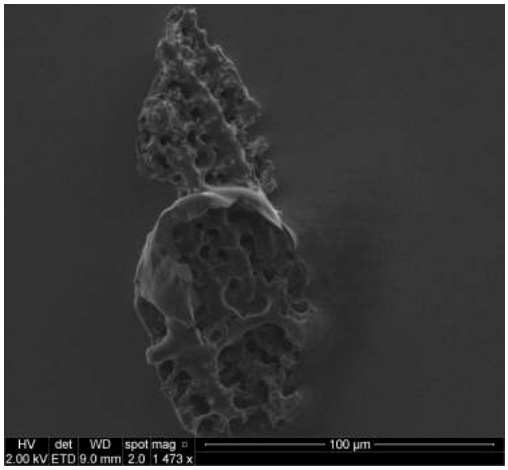

79(b): Char (1000°C, 600 K s^{-1})

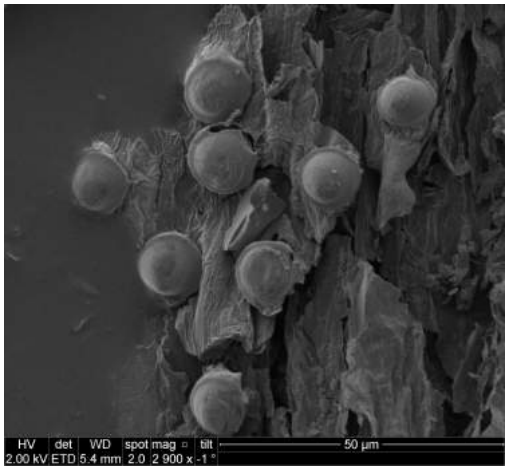

79(c): Char (1000°C, 600 K s^{-1})

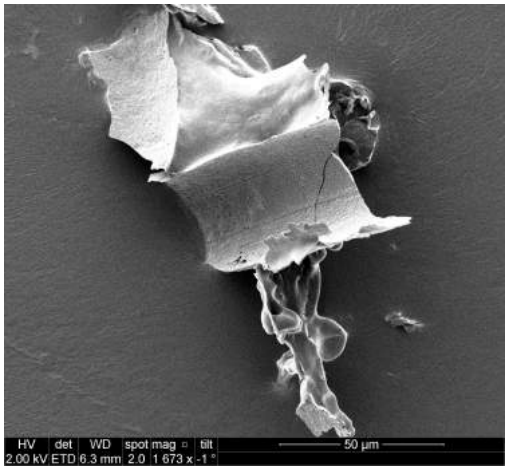

79(d): Char (1250°C, 1000 K s^{-1})

Figure 79: SEM images of original leached wheat straw and their char prepared at (1000 and 1250°C, heating rate: 1000 K s^{-1}, holding time: 1 s, particle size: 0.05-0.2 mm) and (1000°C, heating rate: 600 K s^{-1}, holding time: 1 s, particle size: 0.05-0.2 mm).

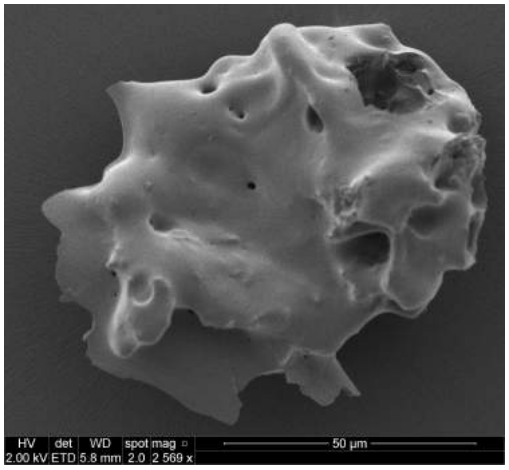

80(a): Pinewood, 350°C

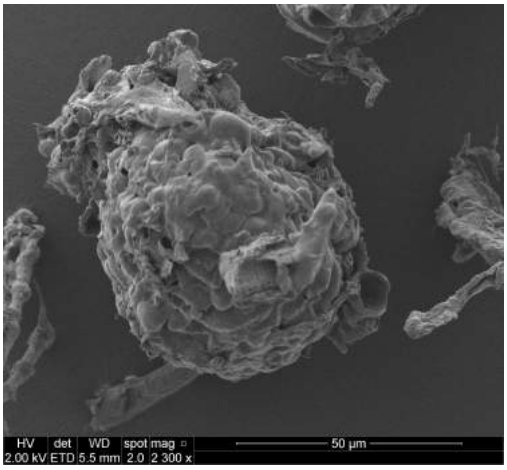

80(b): Wheat straw, 350°C

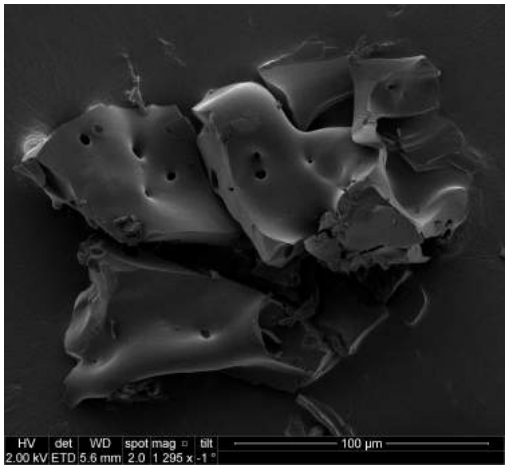

80(c): Pinewood, 600°C

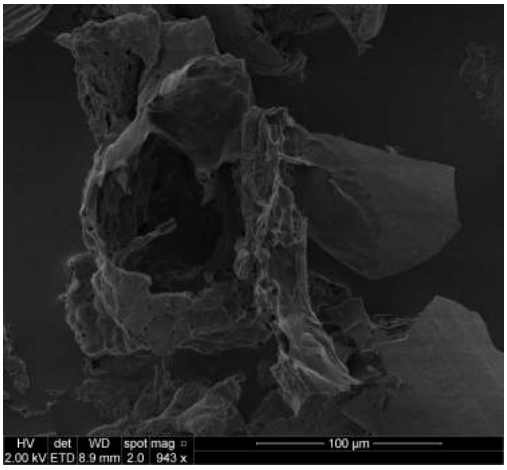

80(d): Wheat straw, 600°C

Figure 80: SEM images of pinewood and wheat straw (heat treatment temperature: 350 and 600°C, heating rate: 1000 K s^{-1}, holding time: 1 s, particle size: 0.05-0.2 mm).

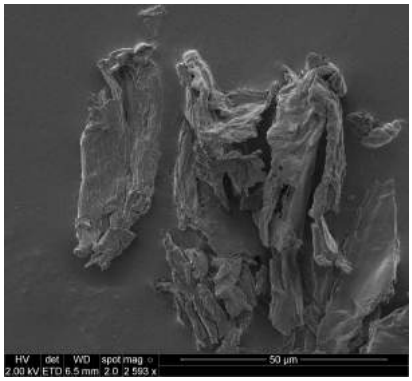

81(a): Cellulose, 350°C

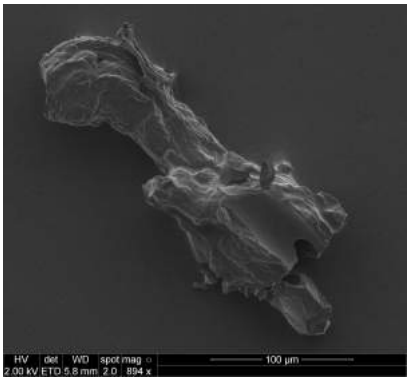

81(b): Cellulose, 600°C

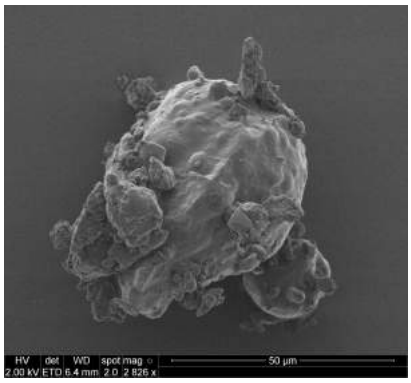

81(c): Hemicellulose, 350°C

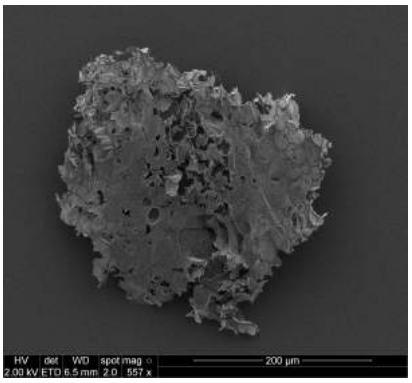

81(d): Hemicellulose, 600°C

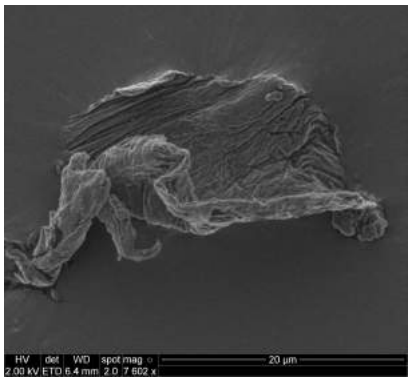

81(e): Lignin, 350°C

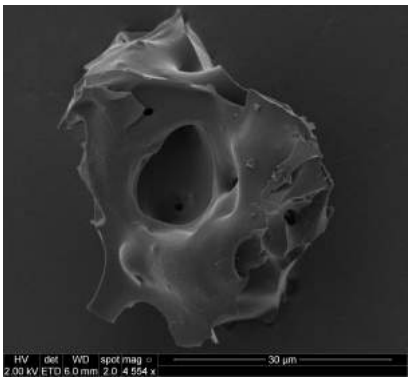

81(f): Lignin, 600°C

Figure 81: SEM images of cellulose, hemicellulose and lignin, pyrolyzed in the WMR (heat treatment temperature: 350 and 600°C, heating rate: 1000 K s^{-1}, holding time: 1 s, particle size: 0.05-0.1 mm).

B.3 Char morphology and structural transformations in the EFR

B.3.1 EDS analysis

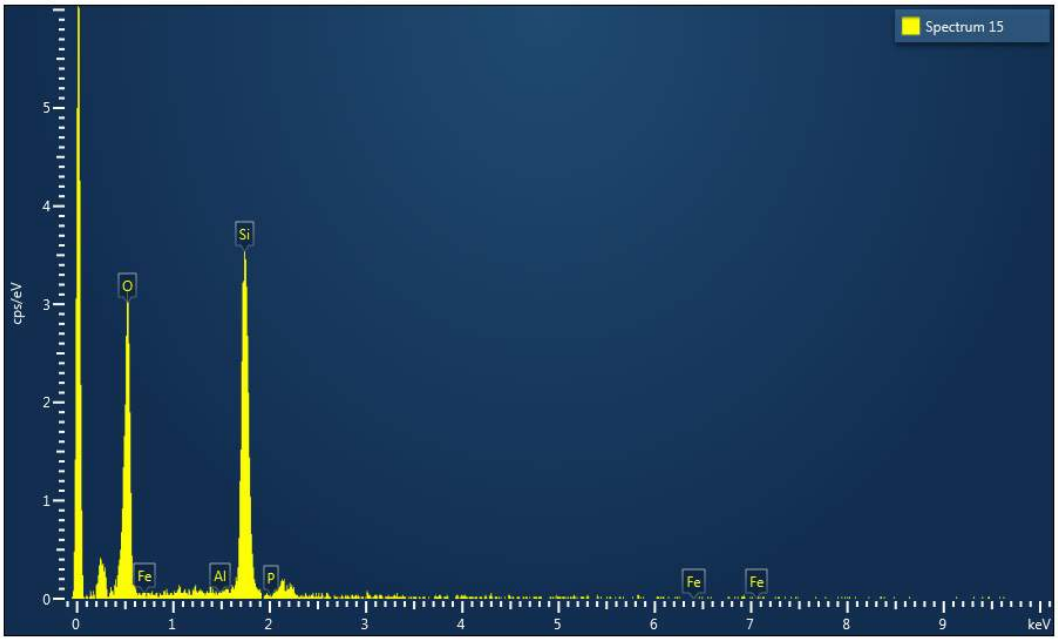

Figure 82: SEM-EDS of the main components in the rice husk chars at 1500°C.

Table 24: SEM-EDS results for C, O and Si present in the rice husk, prepared at 1500°C, shown as an average over 20 points.

Statistics	C	O	Si
Max	68.8	48.5	61.7
Min	19.9	14	16
Average	44.4	33.8	38.3
STDEV	15.5	10.4	16.3

B.4 2D dynamic imaging analysis

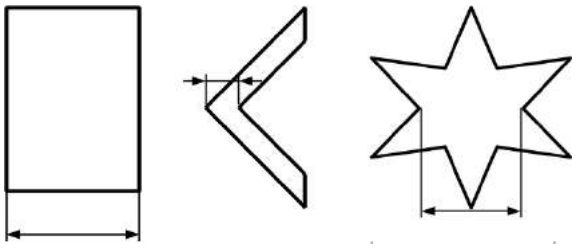

83(a): Martin minimal diameter

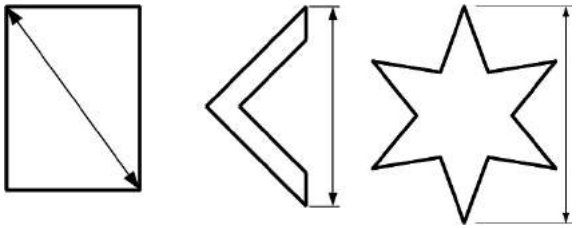

83(b): Feret maximal diameter

Figure 83: Martin minimal ($x_{Ma,min}$) and Feret maximal ($x_{Fe,max}$) diameters of different geometrical figures.

B.5 Elemental analysis

Table 25: Results of the elemental analysis of original wheat straw, rice husk and their chars obtained in the entrained flow reactor shown in %, dry basis.

Biomass	**N**	**C**	**H**	**O**	**Ash**
Wheat straw					
raw	1	42.4	6.3	46.2	4.1
char, 1000°C	0.2	54.6	1	14.2	30
char, 1250°C	-	53	0.6	8.4	38
char, 1500°C	-	50.1	0.4	6.5	43
Rice husk					
raw	0.1	35.5	5.5	37.2	21.7
char, 1000°C	-	22.5	0.8	3.7	73
char, 1250°C	-	15.7	0.4	1.9	82
char, 1500°C	-	9.3	0.3	0.5	90

B.6 ESR-spectra original lignocellulosic materials and their chars

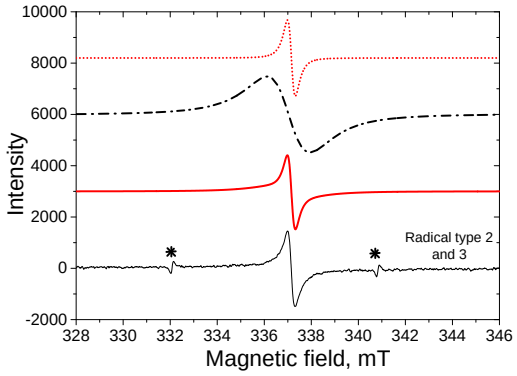

84(a): ESR-spectra of rice husk char (1000°C) from the EFR

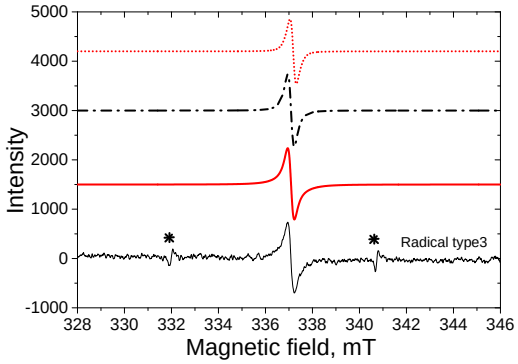

84(b): ESR-spectra of rice husk char (1500°C) from the EFR

Figure 84: Experimental ESR-spectra of (a) rice husk char prepared in the entrained flow reactor at 1000°C and (b) rice husk char prepared in the entrained flow reactor at 1500°C and fitted to simulated data with RMS = 0.989 (rice husk char prepared at 1000°C) and RMS = 0.959 (rice husk char prepared at 1500°C). The experimental ESR-spectra are shown (black line), the simulated spectra (red line), fitting peak 1 (red dotted line) and fitting peak 2 (black dashed line). The Mn (II) internal marker signals are marked by stars.

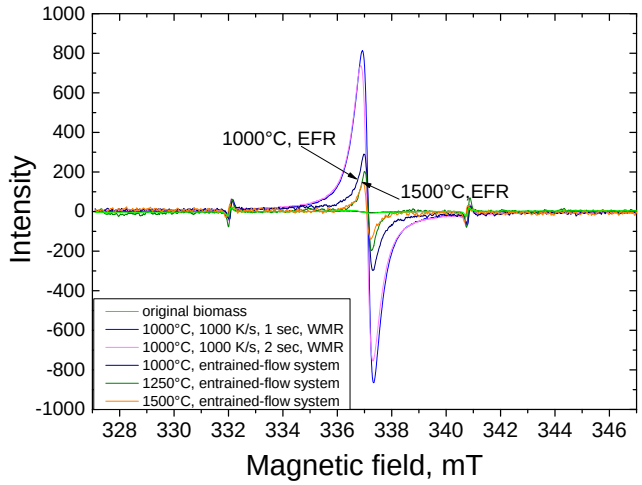

85(a): ESR-spectra of rice husk

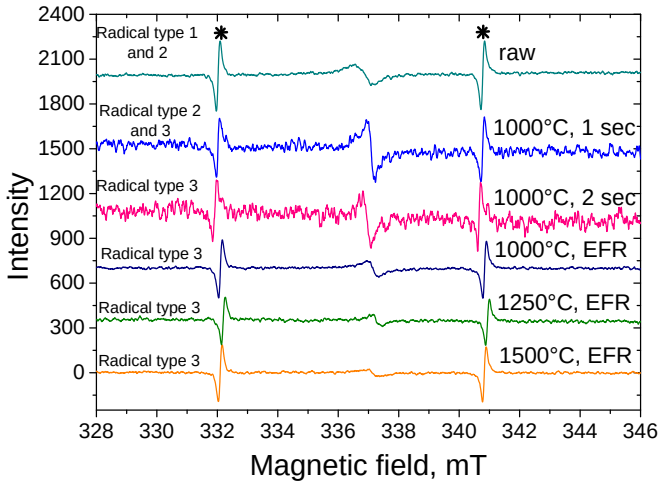

85(b): ESR-spectra of wheat straw

Figure 85: ESR-spectra of (a) **rice husk** (raw (RMS = 0.86) and their chars prepared in the entrained flow reactor at 1000°C (RMS = 0.94), at 1250°C (RMS = 0.85), at 1500°C (RMS = 0.959), and in the wire mesh reactor at (1000°C, 1000 K s^{-1}, 1 s or 2 s (RMS = 0.999))); (b) **wheat straw** (raw (RMS = 0.85) and their chars prepared in the entrained flow reactor at 1000°C (RMS = 0.85), at 1250°C (RMS = 0.86), at 1500°C (RMS = 0.87), and in the wire mesh reactor (1000°C, 1000 K s^{-1}, 1 s or 2 s (RMS = 0.87))). The Mn (II) internal marker signals are marked by stars.

C Appendix

C.1 Reactivity of char prepared at low and intermediate heating rates

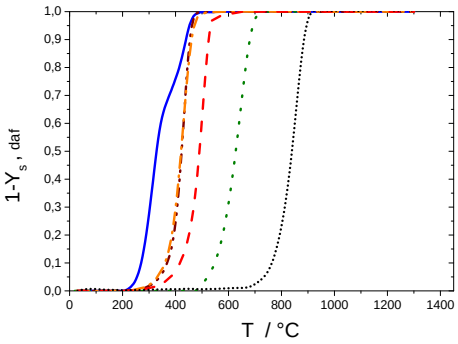

86(a): Beechwood in a O_2 flow

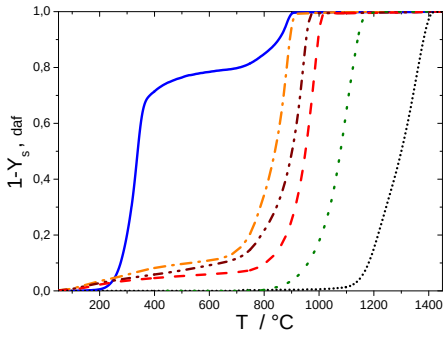

86(b): Beechwood in a CO_2 flow

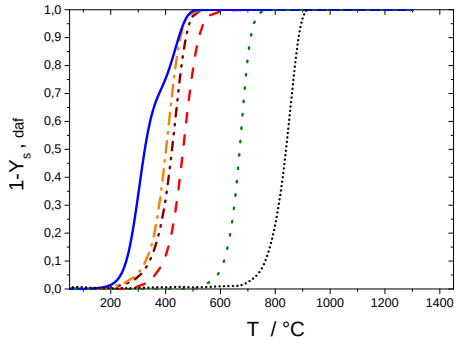

86(c): Wheat straw in a O_2 flow

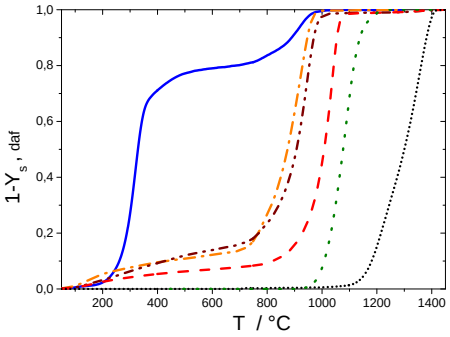

86(d): Wheat straw in a CO_2 flow

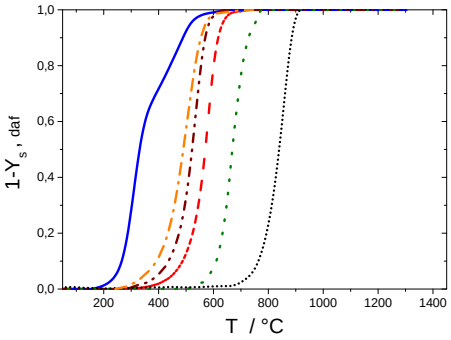

86(e): Rice husk in a O_2 flow

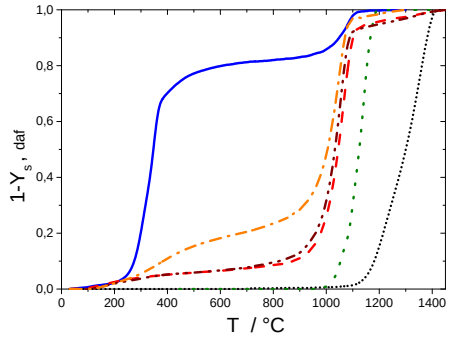

86(f): Rice husk in a CO_2 flow

Figure 86: Conversion in a O_2 and CO_2 flows for original samples ——, char (WMR, 1000°C, 1000 K s^{-1}, 1 s) -·-·-, char (furnace, 1000°C, 10 min) -··-··-, (1000°C, 1.5 h) – – –, char (furnace, 1400°C, 10 min) - - -, graphite •••••.

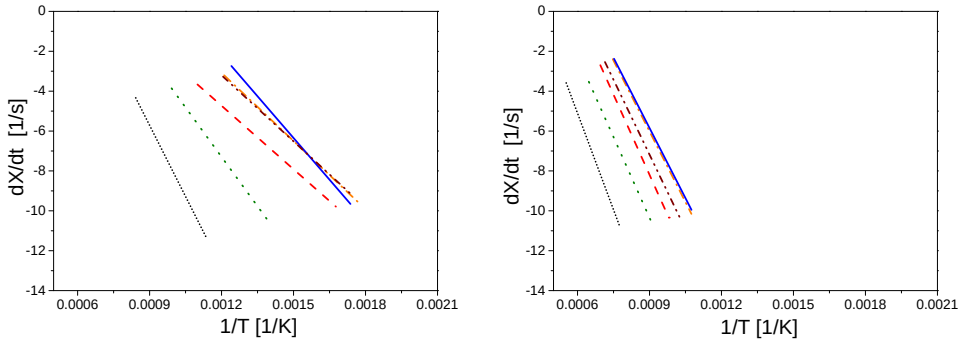

87(a): Beechwood in a O_2 flow

87(b): Beechwood in a CO_2 flow

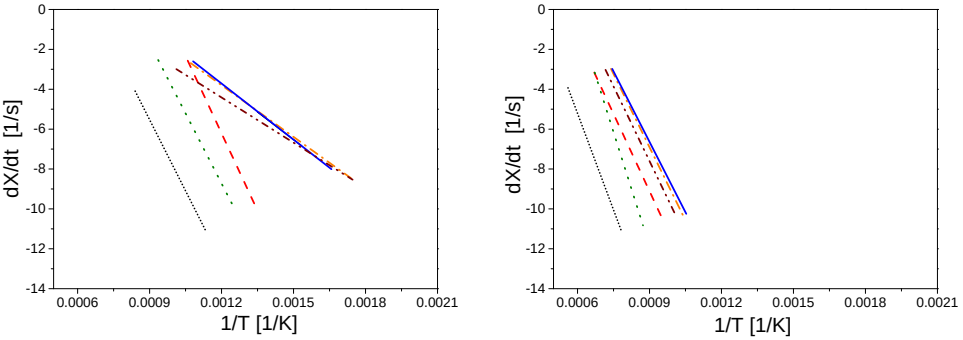

87(c): Wheat straw in a O_2 flow

87(d): Wheat straw in a CO_2 flow

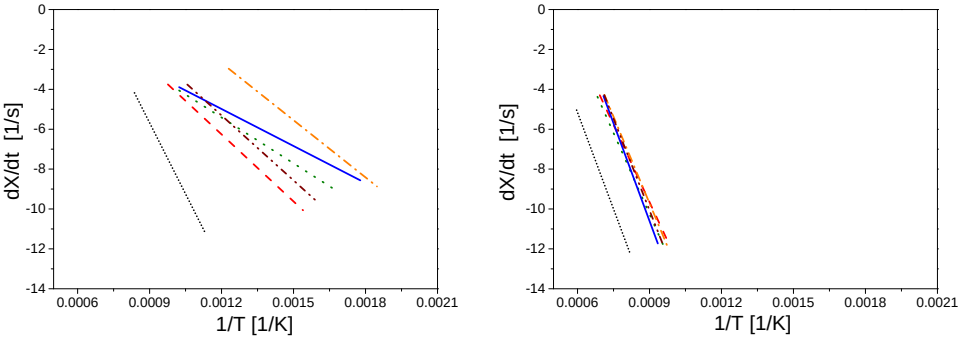

87(e): Rice husk in a O_2 flow

87(f): Rice husk in a CO_2 flow

Figure 87: Arrhenius plot comparing reactivities of beechwood, wheat straw and rice husk in O_2 and CO_2 flows for original samples ——, char (WMR, 1000°C, 1000 K s^{-1}, 1 s) —·—·—, char (furnace, 1000°C, 10 min) —··—··—, (1000°C, 4 h) – – –, char (furnace, 1400°C, 10 min) - - - , graphite ••••• .

C.2 Reactivity of char prepared at fast heating rates

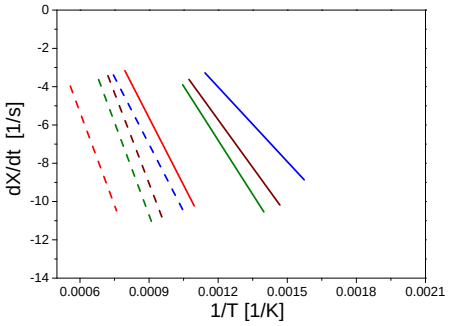

88(a): Pinewood char in O_2 and CO_2

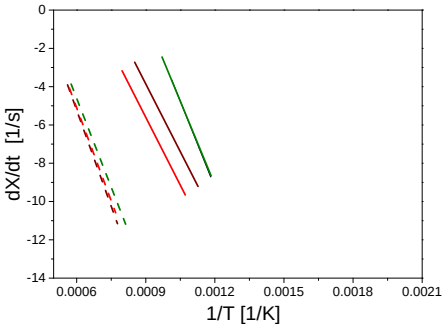

88(b): Pinewood soot in O_2 and CO_2

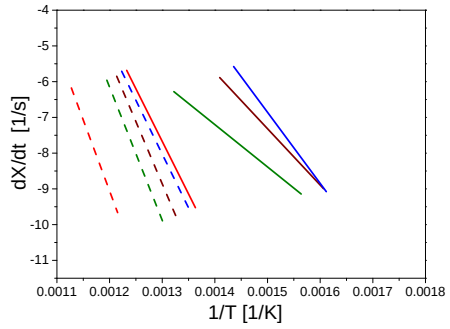

88(c): Beechwood char in O_2 and CO_2

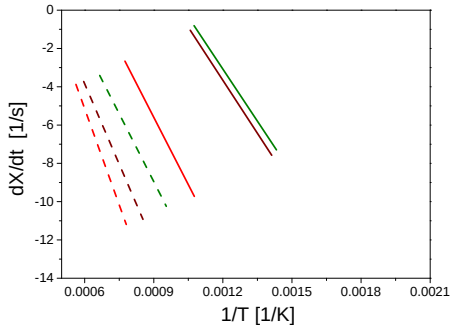

88(d): Beechwood soot in O_2 and CO_2

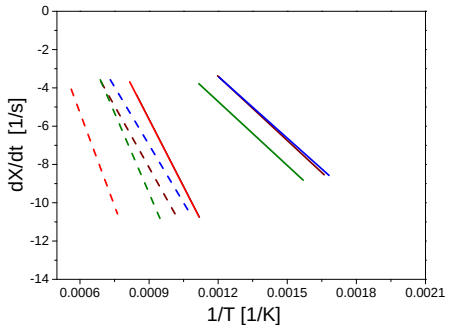

88(e): Straw char in O_2 and CO_2

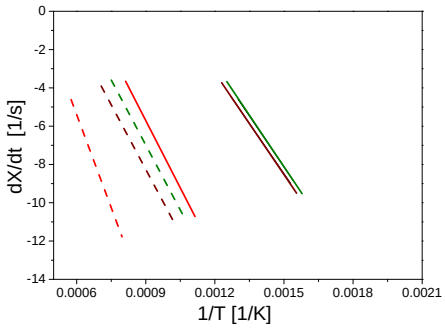

88(f): Straw soot in O_2 and CO_2

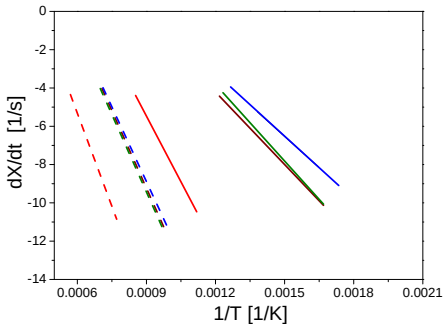

88(g): Leached straw char in O_2 and CO_2

Figure 88: Arrhenius plot comparing reactivities of pinewood, beechwood, wheat straw, leached straw char and pinewood, beechwood and wheat straw soot, obtained in (5 vol. % O_2+95 vol. % N_2) flow at 1000°C ——; 1250°C ——; 1400°C ——; graphite ——; in (5 vol. % CO_2+95 vol. % N_2) flow: 1000°C – – –; 1250°C – – –; 1400°C – – –; graphite – – –.

C.3 Silicates effect on the char reactivity at fast heating rates

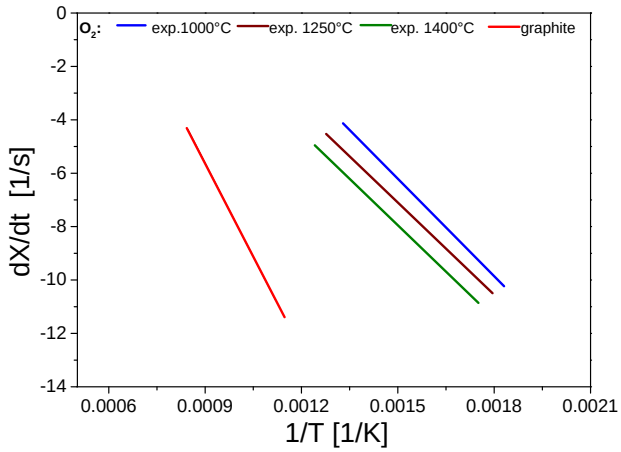

89(a): Wheat straw

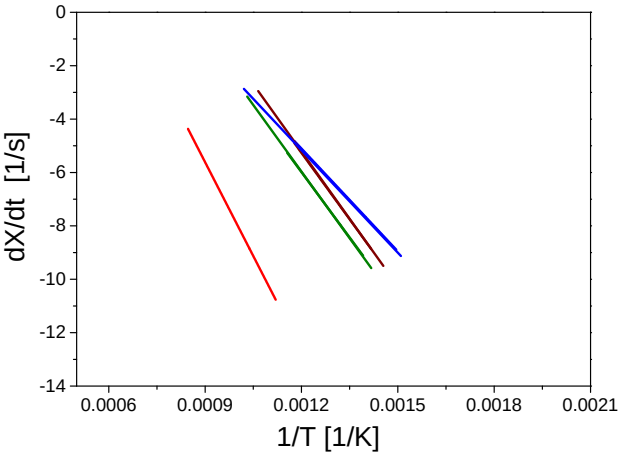

89(b): Rice husk

Figure 89: Arrhenius plot comparing reactivities of wheat straw, rice husk chars and original rice husk raw and beechwood doped with 5 % and 30 % SiO_2, obtained in (5 vol. % O_2+95 vol. % N_2) flow at 1000°C ; 1250°C ; 1400°C ; graphite .

C.4 Reactivity measurements of soot

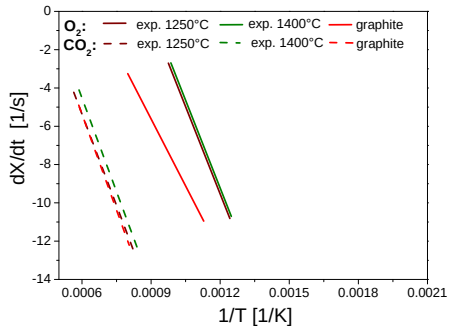

90(a): Pinewood soot in O_2 and CO_2

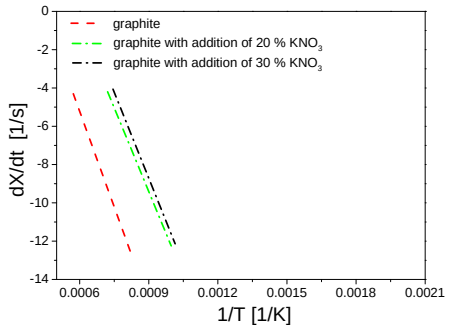

90(b): Graphite with added KNO_3 in CO_2

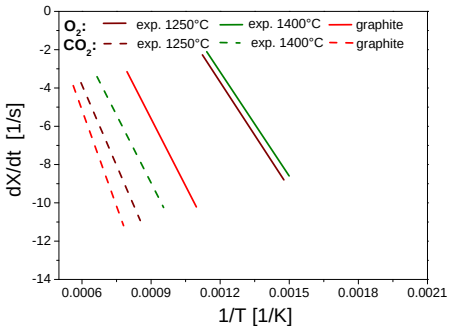

90(c): Beechwood soot in O_2 and CO_2

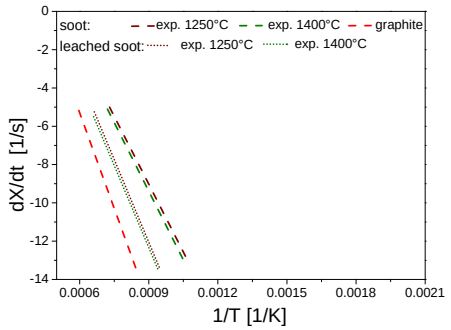

90(d): Leached beechwood soot in CO_2

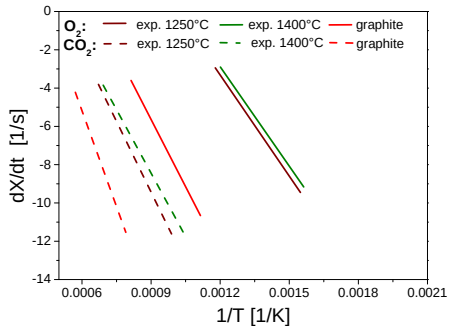

90(e): Straw soot in O_2 and CO_2

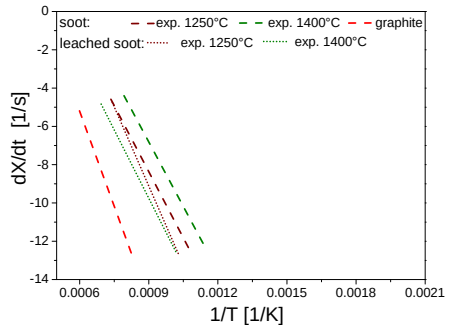

90(f): Leached straw soot in CO_2

Figure 90: (a),(c)-(f) Arrhenius plot comparing O_2 and CO_2 reactivities of pinewood, beechwood, wheat straw, leached beechwood and straw soot prepared at 1250 and 1400°C and graphite; (b) graphite with added 20 wt. % and 30 wt. % KNO_3.

D Appendix

D.1 SEM

Scanning electron microscopy. Analyses were performed on a SEM (FEI Company, Quanta 200 ESEM FEG) fitted with a field emission gun at 30 kV accelerating voltage under high vacuum. For the soot the particle size and surface transformations were characterized. Prior to the analysis, char samples were coated with a thin layer of carbon (40 s, 5 mA) using Cressington 208 Carbon Coater to avoid sample charging.

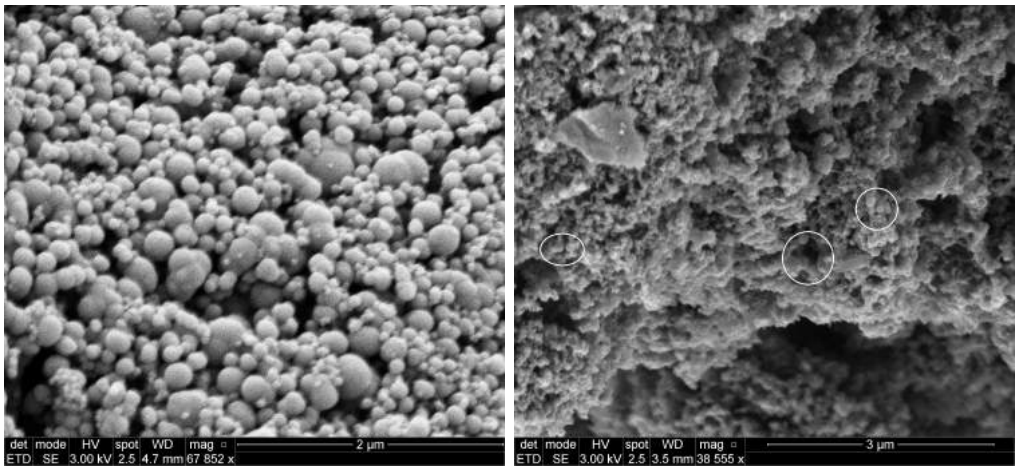

91(a): Pinewood soot particles

91(b): Wheat straw soot mixed with the inorganic particles

Figure 91: SEM images of the pinewood and wheat straw surface at 1250°C. The pinewood char surface was surrounded by soot agglomerates. The white circles represent single soot particles captured by wheat straw silicates.

D.2 Diffusion coefficient calculation

The diffusion coefficient is obtained from correlation of Chapman and Enskog [10]:

$$D_{AB} = \frac{0.00266 \cdot T^{3/2}}{P \cdot M_{AB}^{0.5} \cdot \sigma_{AB}^2 \cdot \Omega_D \cdot 0.0001} \tag{65}$$

where D_{AB} is the diffusion coefficient ($m^2\ s^{-1}$), T is the temperature (K), P is the pressure (bar), σ_{AB} is the characteristic length in (Å) and Ω_D (dimensionless). M_{AB} is defined in equation 66:

$$M_{AB} = \frac{2}{\frac{1}{M_A} + \frac{1}{M_B}} \tag{66}$$

whereas M_A and M_B are the molecular weights of A and B, and σ_{AB} is calculated in equation 67:

$$\sigma_{AB} = (\sigma_A \cdot \sigma_B)^{0.5} \tag{67}$$

Ω_D is defined as a function of $k \cdot T/\varepsilon$ for the Lennard-Jones potential and approximated by Neufield [10] in equation 68:

$$\Omega_D = \frac{A}{(T^*)^B} + \frac{C}{exp(DT^*)} + \frac{R}{exp(FT^*)} + \frac{G}{(HT^*)} \tag{68}$$

with the following parameters:

$$T^* = (k \cdot T)/\varepsilon_{AB} \qquad A = 1.06036 \qquad B = 0.15610 \tag{69}$$

$$C = 0.19300 \qquad D = 0.47635 \qquad E = 1.03587 \tag{70}$$

$$F = 1.52996 \qquad G = 1.76474 \qquad H = 3.89411 \tag{71}$$

N_2-adsorption ($m^2\ g^{-1}$), and recalculated in ($m^2\ kg^{-1}$) for the r''_A determination.

D.3 TEM investigations

The following images of pinewood, beechwood and wheat straw soot were prepared according to Trenikhin [2] and shown in Figure 93. The images were acquired using Gatan Digital Micrograph software, and included the following stages: separation of a region with the sizes of ≈ 90 x 90 nm, staining of the image and transformation into the binary form.

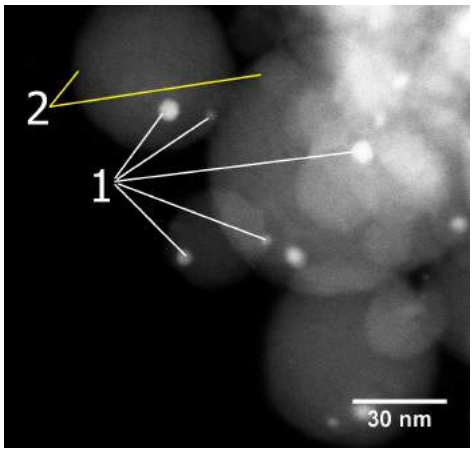

92(a): Wheat straw soot and inorganic matter

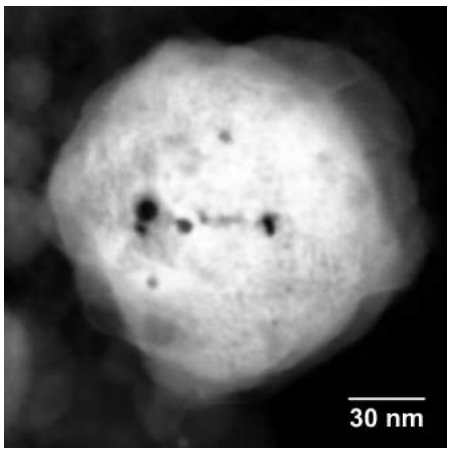

92(b): Inorganic particle

Figure 92: STEM images of wheat straw soot sample from fast pyrolysis at 1400°C. Figure (a) indicates inorganic matter particles (1) in or on soot particles (2) (brighter contrast in the HAADF image); Figure (b) indicates a beam sensitive near-spherical particle.

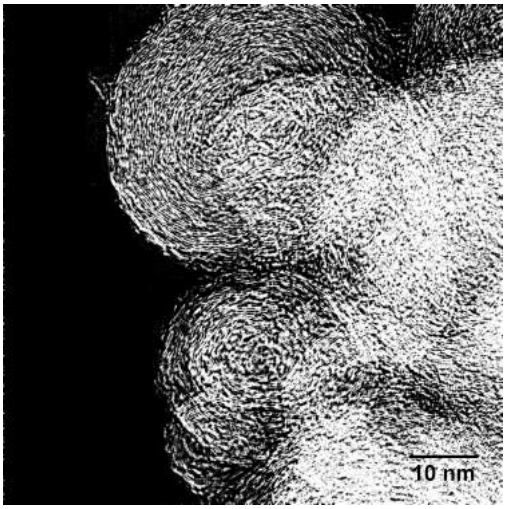

93(a): Pinewood soot (1400°C)

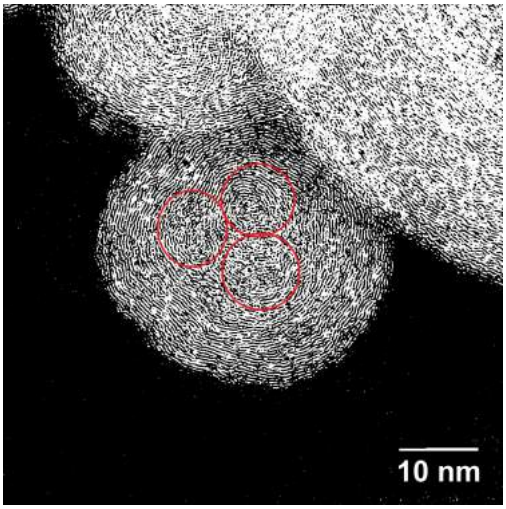

93(b): Beechwood soot (1400°C)

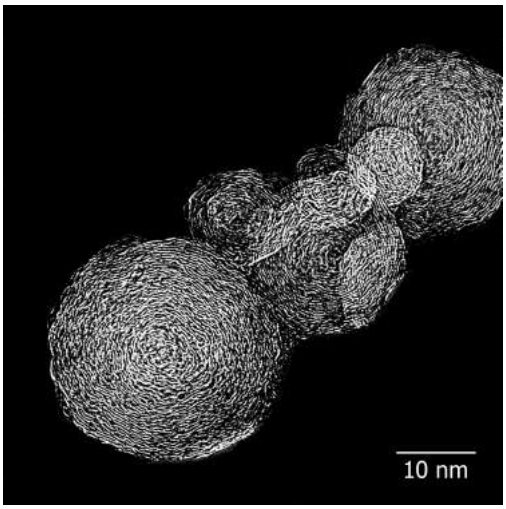

93(c): Wheat straw soot (1400°C)

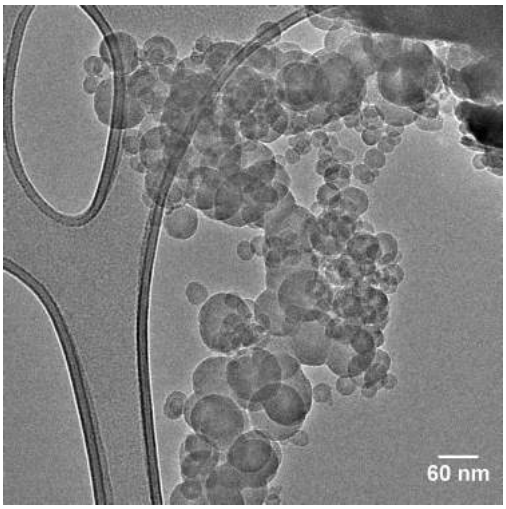

93(d): Pinewood tar balls (1400°C)

Figure 93: TEM images of (a)-(c) pinewood, beechwood and wheat straw soot prepared at 1400°C to show the graphene layer distances. The red marked circles show the multi cores of beechwood soot; (d) Bright-field image of pinewood soot generated at 1400°C.

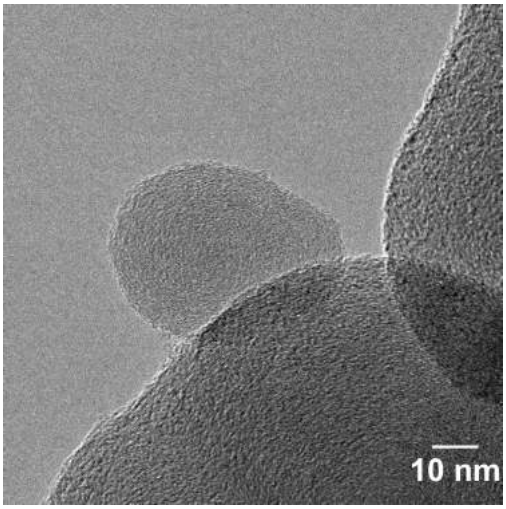

94(a): Pinewood soot (1250°C)

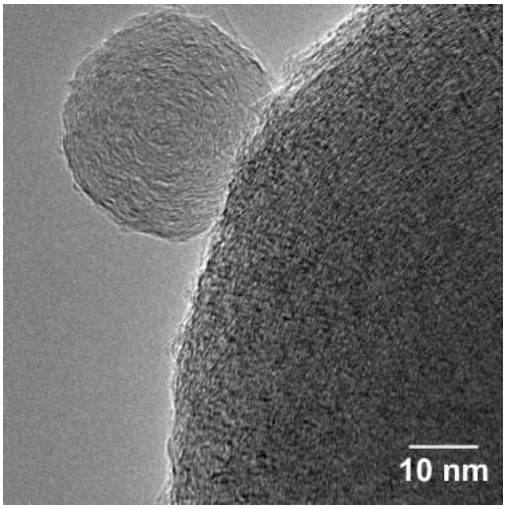

94(b): Pinewood soot (1400°C)

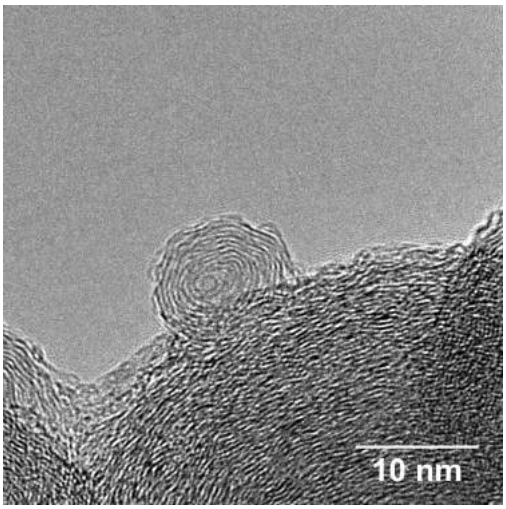

94(c): Beechwood soot (1400°C)

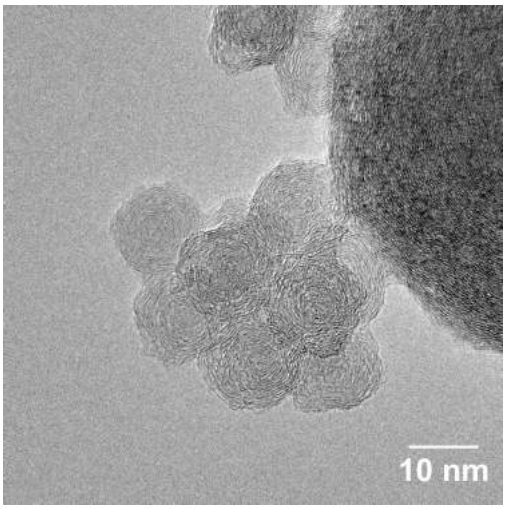

94(d): Wheat straw soot (1400°C)

Figure 94: TEM images of small and large particles of pinewood soot prepared at 1250 and 1400°C, beechwood prepared at 1400°C and wheat straw soot prepared at 1400°C.

D.4 TEM-EELS analysis

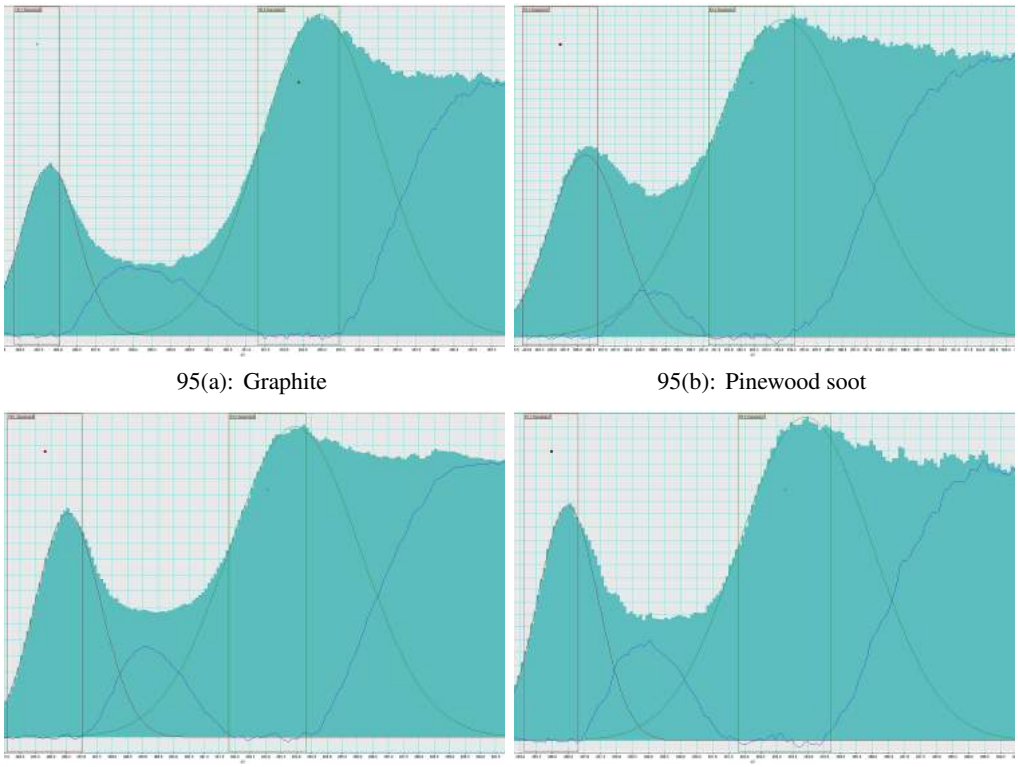

95(a): Graphite

95(b): Pinewood soot

95(c): Beechwood soot

95(d): Wheat straw soot

Figure 95: Gaussian fits of representative EELS data of graphite (a), pinewood soot (b), beechwood soot (c) and wheat straw soot (d). The maxima respresenting s-π* and s-σ* are fitted manually by individual Gaussians in Digital Micrograph (Gatan).

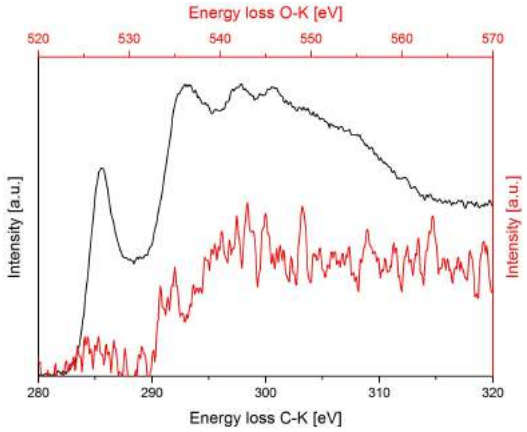

Figure 96: Combined plot of the C-K and O-K edge of the same agglomerate of a wheat straw sample. The carbon edge shows two additional peaks indicating potassium (black plot) and an obvious oxygen edge is visible (red plot).

D.5 XRD measurements of soot

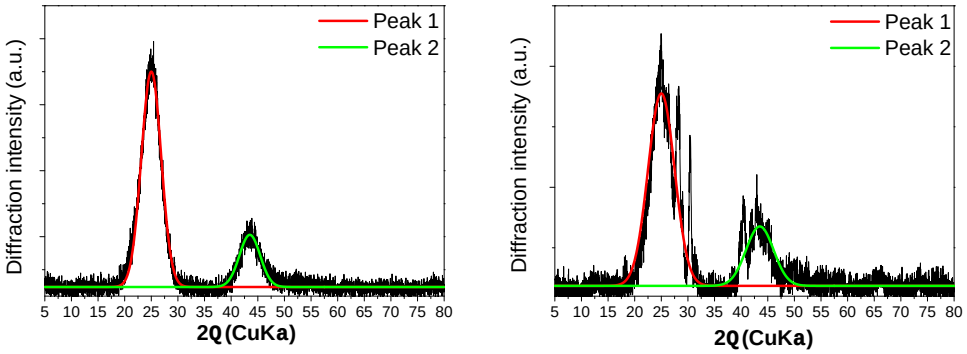

97(a): Beechwood soot at 1250 °C

97(b): Wheat straw soot at 1250 °C

Figure 97: Gauss fitting of XRD peaks (25° and 43.5°) of beechwood soot, prepared at 1250°C, and wheat straw soot, prepared at 1400°C.

D.6 Thermogravimetric measurements

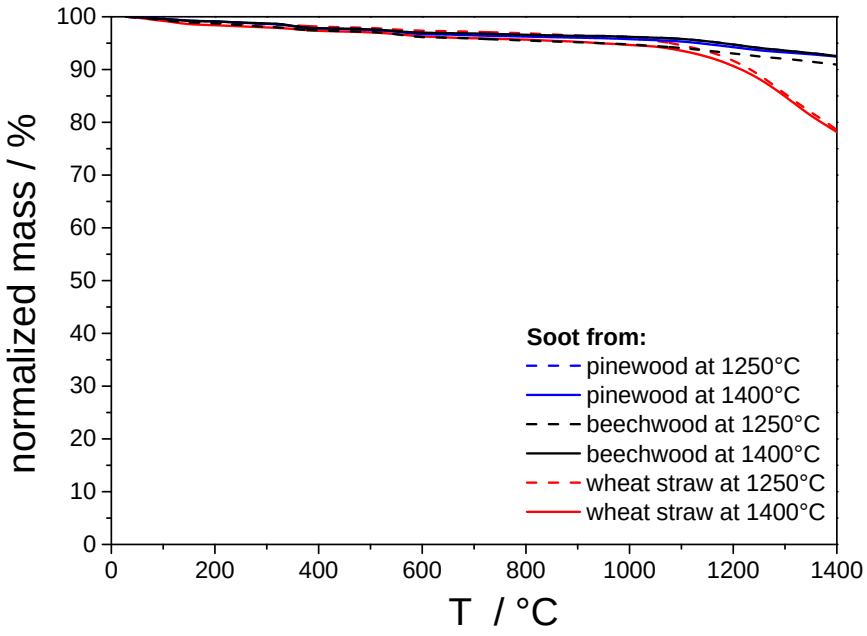

Figure 98: Thermogravimetric analysis in 100 % N_2 flow of pinewood, beechwood and wheat straw soot prepared at 1250 and 1400°C.

D.7 Soot yield and inorganic matter effect

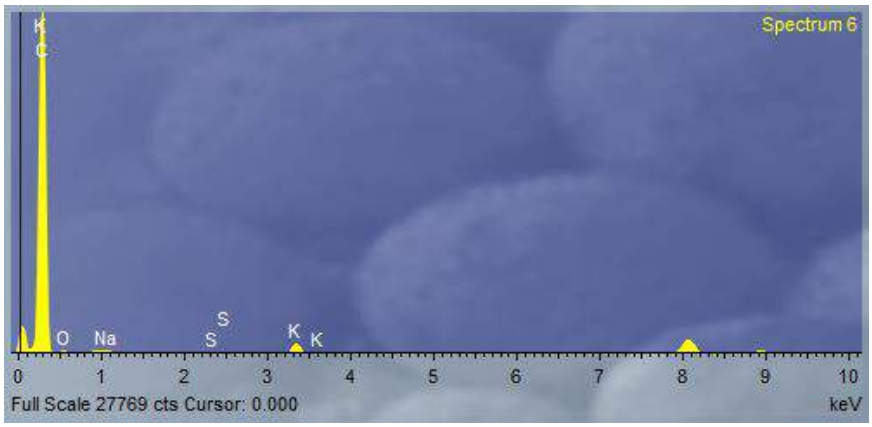

99(a): Beechwood soot

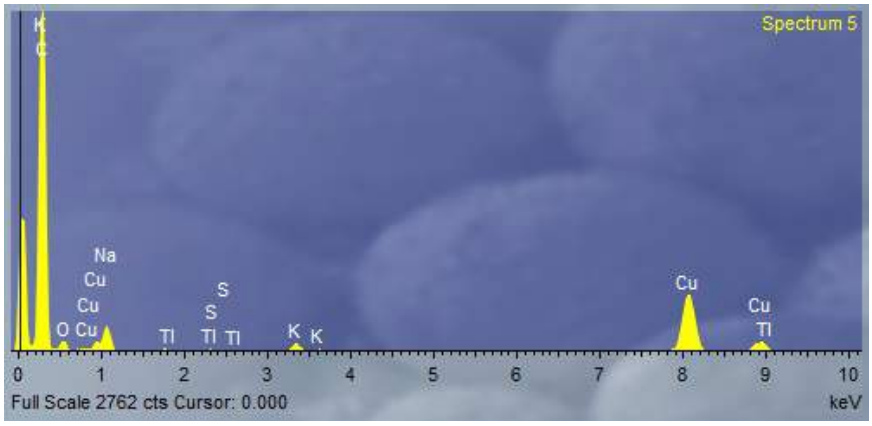

99(b): Wheat straw soot

Figure 99: TEM/EDS analysis of beechwood and wheat straw soot, pyrolyzed at 1250°C.

D.8 Ash composition

Table 26: Inorganic and organic matter fractions of pinewood, beechwood and wheat straw soot shown in wt. % (g g^{-1} biomass).

Temperature, °C	Pinewood		Beechwood		Wheat straw	
	organic	inorganic	organic	inorganic	organic	inorganic
1250	8.36	0	5.86	0.03	2.6	0.06
1400	6.97	0	5.74	0.07	3.1	0.43

Table 27: Ash composition of wheat straw soot prepared at 1250 and 1400°C shown in wt. % (g kg^{-1} solid residue, on dry basis).

Element	1250	1400
g kg^{-1} (db)	°C	°C
Na	0.003	0.02
Si	0.08	0.13
K	0.03	0.19
Ca	0.02	0.03
S	0.01	0.02
Cl	0.03	0.02

D.9 FTIR measurements

Table 28: Summary of IR peak/bands assignment for wheat straw soot, pyrolyzed at 1250 and 1400°C.

Band position, cm^{-1}	Assignment	Reference
3600-3200	OH Hydroxyl	[8, 9]
1550-1500	Chelating bidentate carbonate	[6]
1402	Ionic carbonate	[6]
1354	Chelating bidentate carbonate	[6]
1220	Bicarbonate	[7]
1040	Organic carbonate bond to K^+	[4, 5]

D.10 Van Krevelen plot

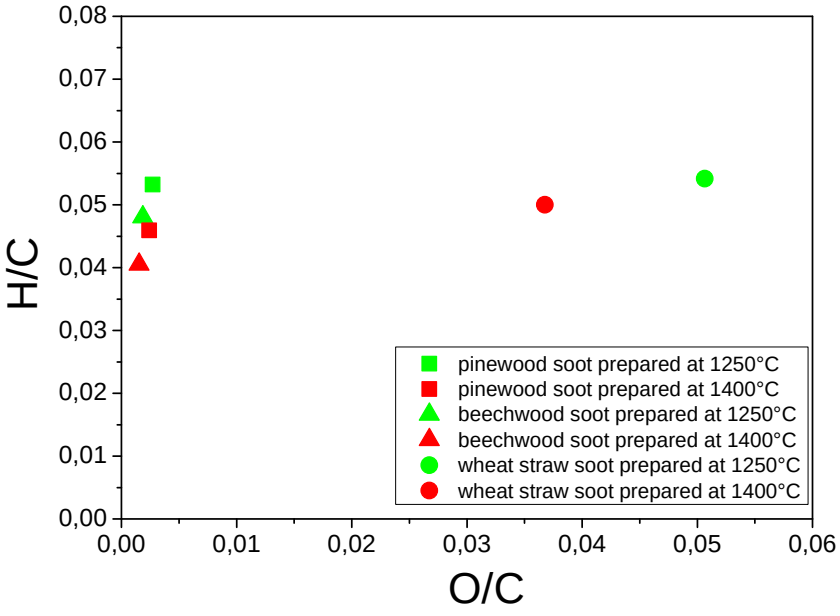

Figure 100: Van Krevelen plot of pinewood, beechwood and wheat straw soot prepared at 1250 and 1400°C.

Table 29: Data applied in Van Krevelen plot of pinewood, beechwood and wheat straw soot, pyrolyzed at 1250 and 1400°C.

Temperature	N	C	H	O	ash
Pinewood soot					
1250°C	0	99.2	0.44	0.36	0
1400°C	0	99.3	0.38	0.32	0
Beechwood soot					
1250°C	0	93.1	0.37	0.23	6.3
1400°C	0	92.5	0.31	0.19	7
Wheat straw soot					
1250°C	0.09	82	0.37	5.54	12
1400°C	0.64	74.4	0.31	3.65	21

References

[1] Akuzawa N, Yoshioka J, Ozaki C, Tokuda M, Ohkura K and Soneda Y, Preparation and characterization of sodium-graphite intercalation compounds, *Mol Cryst Liq Cryst*, 388(1):1-7, 2002.

[2] Trenikhin MV, Protasova OV, Seropyan GM, Zemtsov AE and Drozdov VA, Transmission Electron Microscopy Study of the Graphene Layer Transformation of Carbon Black under Laser Irradiation, *Nanotech Russia*, 9(7):461-5, 2014.

[3] Ibrahim M, Nada A and Kamal DE, Density functional theory and FTIR spectroscopic study of carboxyl group, *Indian J Pure Appl Phys*, 43(12):911-7, 2005. (2005)

[4] Legutko P, Jakubel T, Kaspera W, Stelmachowski P, Sojka Z and Kotarba A, Soot oxidation over K-doped manganese and iron spinels - How potassium precursor nature and doping level change the catalyst activity, *Catal Commun*, 43:34-7, 2014.

[5] Gu B, Schmitt J, Chen Z, Liang L and McCathy JF, Adsorption and Desorption of Natural Organic Matter on Iron Oxide: Mechanisms and Models, *Environ Sci Technol*, 23(1):38-46, 1994.

[6] Zhang Z, Zhang Y, Su Q, Wang Z, Li Q and Gao X, Determination of Intermediates and Mechanism for Soot Combustion with NO_x/O_2 on Potassium-Supported Mg-Al Hydrotalcite Mixed Oxides by In Situ FTIR, Environ Sci Technol, 44(21):8254-8, 2010.

[7] Philipp R, Omata K, Aoki A and Fujimoto K, On the active site of MgO/CaO mixed oxide for oxidative coupling of methane, *J Catal*, 134(2):422-33, 1992.

[8] Guenzler H and Boeck H, *IR-Spektroskopie. Eine Einführung*, Verlag Chemie and Physik, 1983.

[9] Reddy BVR, Chakrapani C, Babu CS, Rao KS, Agarwal K and Prasad M, FT-IR, TG, XRD and SEM Studies of Activated Carbons Prepared from Agricultural Waste, *Asian J Chem*, 22(3):1822-8, 2010.

[10] Poling BE, Prausnitz JM and O'Connell J, *The properties of Gases and Liquids*, McGRAW-HILL, 2000.

E Appendix

E.1 Microscopy investigations

Table 30: Microscopy analysis of the pinewood pellets sieved to fraction 710-1000 μm

Particle size [μm]	**p_3 [%]**	**$x_{Ma,min}$ [μm]**	**$x_{Fe,max}$ [μm]**	**thickness [μm]**	**length/width (a/b)**	**width/thickness (b/c)**
Microscopy						
425-500	5	471.26	2662.66	299.53	5.5	1.5
500-600	18	565.58	2827.87	347.06	5	1.5
600-710	22	651.92	2769.74	350.72	4.5	2
710-850	30	770.96	2967.58	428.13	4	2
850-1000	21	918.08	2733.16	384.44	3	2.5
1000-1400	4	1136.05	2590.17	382.04	3	3

Table 31: Microscopy analysis of the wheat straw sample sieved to fraction 710-1000 μm

Particle size [μm]	**p_3 [%]**	**$x_{Ma,min}$ [μm]**	**$x_{Fe,max}$ [μm]**	**thickness [μm]**	**length/width (a/b)**	**width/thickness (b/c)**
Microscopy						
180-250	0.1	210.7	3100	150.1	15	1.5
425-500	3	454.66	2716.09	272.01	6	2
500-600	16.5	567.05	2746.35	309.13	5	2
600-710	20.4	661.66	2828.99	301.49	4.5	2
710-850	28.2	776.75	2771.26	356.19	3.5	2
850-1000	18.4	914.42	3469.49	366.89	4	2
1000-1400	11.7	1076.59	2592.92	500.23	2.5	2
1400-2000	0.97	1618.33	5890	445.37	3.5	3.5

E.2 CAMSIZER/CAMSIZER XT investigations

Table 32: CAMSIZER analysis of the pinewood pellets (DE 1658-4) sample sieved to fraction 710-1000 μm

Particle size [μm]	**p_3 [%]**	**$x_{Ma,min}$ [μm]**	**$x_{Fe,max}$ [μm]**	**length/width (a/b)**
CAMSIZER				
< 425	12	-	-	
425-500	8.7	464	1699	4
500-600	14.3	553	1774	3
600-710	18	654	1706	3
710-850	23.7	775	1746	2.5
850-1000	15.2	916	1632	2
1000-1400	7.7	1082	1839	1.5
> 1400	0.4	-	-	-

Table 33: CAMSIZER analysis of the wheat straw sample sieved to fraction 710-1000 μm

Particle size [μm]	**p_3 [%]**	**$x_{Ma,min}$ [μm]**	**$x_{Fe,max}$ [μm]**	**length/width (a/b)**
CAMSIZER				
< 180	1.3	-	-	
180-250	2.3	220	2129	10
425-500	9.2	464	2187	5
500-600	14.9	553	2137	4
600-710	19.6	655	2137	3.5
710-850	22.4	775	2196	3
850-1000	12.9	909	2215	2.5
1000-1400	5.5	1087	2705	2.5
1400-2000	0.2	1614	3556	2